

# Short-term and time-dependent flexural behaviour of steel fibre-reinforced reactive powder concrete

**Author:**

Warnock, Robyn Ellen

**Publication Date:**

2006

**DOI:**

<https://doi.org/10.26190/unsworks/23013>

**License:**

<https://creativecommons.org/licenses/by-nc-nd/3.0/au/>

Link to license to see what you are allowed to do with this resource.

Downloaded from <http://hdl.handle.net/1959.4/23027> in <https://unsworks.unsw.edu.au> on 2024-05-04

**SHORT-TERM AND TIME-DEPENDENT  
FLEXURAL BEHAVIOUR OF STEEL-FIBRE REINFORCED  
REACTIVE POWDER CONCRETE BEAMS**



**UNIVERSITY OF NEW SOUTH WALES  
SCHOOL OF CIVIL AND ENVIRONMENTAL ENGINEERING**

**ROBYN WARNOCK**

**DOCTORATE OF PHILOSOPHY  
2005**

## **CERTIFICATE OF ORIGINALITY**

I hereby declare that this submission is my own work and to the best of my knowledge contains no materials previously published or written by another person, or substantial proportions of material which have been accepted for the award of any other degree or diploma at UNSW or any other educational institution, except where due acknowledgement is made in the thesis. Any contribution made to this research by others, with whom I have worked at UNSW or elsewhere, is explicitly acknowledged in the thesis. I also declare that the intellectual content of this thesis is the product of my own work, except to the extent that assistance from others in the project's design and conception or in style, presentation and linguistic expression is acknowledged.

Signed *Robyn Warnock*

## **ABSTRACT**

This thesis presents an experimental and theoretical study of the material and structural behaviour of a Steel-Fibre reinforced Reactive Powder Concrete (SF-RPC). The experimental program consisted of three phases. Phase 1 involved the development of a design mix for use throughout the remainder of the study. Phase 2 consisted of an in-depth investigation into the material properties of the mix. The final phase of the experimental component was the testing of 16 plain and prestressed SF-RPC beams. Twelve beams were tested under short-term loading to determine their cracking and ultimate moment capacity. The remaining 4 beams were used to investigate the time-dependent flexural behaviour of prestressed SF-RPC slabs.

The material properties were measured using a range of short-term tests and included the compressive and flexural behaviour, static chord modulus of elasticity and crack mouth opening. In addition to the short-term tests, investigation into the time-dependent material behaviour was undertaken and included the creep and shrinkage characteristics of the material. The response of the material to various curing conditions was also investigated.

The structural behaviour investigated included the short-term flexural moment-curvature response and load-deflection behaviour of beams and slabs along with the crack patterns of both plain and prestressed SF-RPC members. In addition to the investigations into the short-term flexural behaviour, a study into the time-dependent flexural behaviour was also undertaken.

There are currently 2 available models for predicting the flexural response of plain and prestressed RPC cross-sections. The analytical phase of this investigation involved an evaluation of these models. Based on the experimental findings and analysis, a modified model was proposed for calculating the short-term flexural behaviour of plain and prestressed SF-RPC beams. The applicability of an age-adjusted effective modulus method for calculating the time-dependent deformations of prestressed SF-RPC slabs under various levels of sustained loads was also evaluated and found to be adequate with minor refinements.

## PREFACE

Based on this research, some results have already been published. A short list of the papers published during the course of this study is as follows:

Gowripalan, N., Watters (Warnock), R., Gilbert, R.I., Cavill, B., (2003), *Reactive Powder Concrete (RPC) For Precast Structural Concrete – Research and Development in Australia*, Book of Proceedings, Volume 1, Concrete Institute of Australia 21<sup>st</sup> Biennial Conference, 17 – 19 July 2003

Gowripalan, N., Watters (Warnock), R., (2005), *Very High Strength Fibre Reinforced Concrete for Bridge Super Structures*, Book of Proceedings, Concrete Institute of Australia 22<sup>nd</sup> Biennial Conference, 16 – 19 October 2005  
(Accepted)

## **ACKNOWLEDGEMENTS**

The author wishes to express her sincere thanks to her supervisor, Dr. Nadarajah Gowripalan for his guidance and encouragement throughout the duration of this research. Dr. Gowripalan's generous support and unstinting enthusiasm are gratefully recognized. This study would not have been possible without such assistance. The author would also like to sincerely thank her co-supervisor, Professor Ian Gilbert for his assistance and comments throughout the course of the study.

Thanks must be given to Oliver Fitz-Henry for proof reading of the final document and providing valuable feedback. Thanks are also extended to fellow doctoral students for their assistance and enlightening discussions over the last few years.

The support provided by the remaining academic, technical, administrative and computer staff of the School of Civil and Environmental Engineering is appreciatively recognized. A special vote of thanks goes to William Terry for the tireless contribution of his expertise and time to the experimental aspects of this work. Mention must also be made of the contributions of Tony Macken for his assistance in the experimental phase of this study.

Financial support for this project was gratefully received from VSL through the Australian Postgraduate Award (Industry).

Finally, the author would like to give her heartfelt thanks to my family and friends for their love and support. To my family, this thesis is dedicated.

## TABLE OF CONTENTS

<b>ABSTRACT</b> .....	<b>i</b>
<b>PREFACE</b> .....	<b>ii</b>
<b>ACKNOWLEDGEMENTS</b> .....	<b>iii</b>
<b>TABLE OF CONTENTS</b> .....	<b>iv</b>
<b>NOTATIONS</b> .....	<b>viii</b>
<b>LIST OF FIGURES</b> .....	<b>xi</b>
<b>LIST OF TABLES</b> .....	<b>xv</b>
<b>CHAPTER 1: INTRODUCTION</b> .....	<b>1</b>
1.1 GENERAL INTRODUCTION .....	1
1.2 OBJECTIVES .....	3
1.3 SCOPE OF THESIS.....	3
1.4 LAYOUT OF THESIS.....	4
<b>CHAPTER 2: LITERATURE REVIEW</b> .....	<b>6</b>
2.1 INTRODUCTION .....	6
2.2 DEVELOPMENT OF REACTIVE POWDER CONCRETE .....	9
2.2.1 Homogeneity .....	9
2.2.1.1 Elimination of coarse aggregates .....	10
2.2.1.2 Improved mechanical properties of the paste.....	11
2.2.1.3 Reduction of paste/aggregate ratio.....	11
2.2.2 Density .....	12
2.2.2.1 Optimisation of the granular mixture .....	13
2.2.2.2 Application of pressure .....	14
2.2.3 Microstructure .....	15
2.2.3.1 Increased pozzolanic reaction .....	15
2.2.3.2 Development of crystalline products .....	16
2.2.4 Ductility .....	16
2.3 ADVANTAGES .....	17
2.4 APPLICATIONS .....	20
2.4.1 Bridges .....	20
2.4.1.1 Pedestrian bridges .....	20
2.4.1.2 Vehicular bridges .....	21
2.4.2 Other Applications .....	22
2.5 CURRENT DESIGN GUIDELINES.....	22
2.5.1 Design Guidelines for RPC Prestressed Concrete Beams (2000).....	23
2.5.1.1 Design properties .....	23
2.5.1.2 Strength in flexure.....	28
2.5.1.3 Deflection at service loads .....	30
2.5.2 Interim Recommendations – Ultra High Performance Fibre-Reinforced Concrete (2002).....	31

2.5.2.1 Part 1: Behaviour and mechanical characteristics of UHPFRC.....	32
2.5.2.2 Part 2: Structural design methods .....	33
2.6 RESEARCH NEEDS FOR RPC AND RPC FLEXURAL MEMBERS .....	36
2.6.1 Serviceability .....	36
2.6.2 Short-term Flexural Behaviour .....	37
2.6.3 Time-dependent Flexural Behaviour.....	37
2.7 SUMMARY .....	37
<b>CHAPTER 3: EXPERIMENTAL PROGRAM.....</b>	<b>38</b>
3.1 INTRODUCTION .....	38
3.2 SF-RPC PRODUCTION.....	39
3.2.1 Materials.....	39
3.2.2 Mix Design.....	41
3.2.3 Mixing Procedure.....	41
3.2.3.1 Small-scale batches .....	41
3.2.3.2 Large-scale batches .....	42
3.3 MATERIAL PROPERTIES TESTS.....	43
3.3.1 Specimen Preparation.....	43
3.3.2 Curing.....	44
3.3.3 Test Procedures .....	45
3.3.3.1 Surface preparation of material specimens for testing.....	45
3.3.3.2 Test machine .....	45
3.3.3.3 Compressive strength .....	46
3.3.3.4 Flexural strength .....	46
3.3.3.5 Crack Mouth Opening.....	47
3.3.3.6 Modulus of Elasticity .....	47
3.3.3.7 Stress-strain behaviour in compression.....	47
3.3.3.8 Shrinkage .....	47
3.3.3.9 Creep .....	48
3.3.4 Test results .....	48
3.4 BEAM TESTS .....	49
3.4.1 Beam Construction.....	49
3.4.1.1 Plain beams .....	49
3.4.1.2 Prestressed beams .....	50
3.4.2 Beam Details .....	50
3.4.2.1 Beam Series 1.....	50
3.4.2.2 Beam Series 2.....	52
3.4.2.3 Beam Series 3.....	52
3.4.3 Beam Testing .....	54
3.4.3.1 Loading arrangement .....	54
3.4.3.2 Measurements .....	56
3.4.4 Results .....	57
<b>CHAPTER 4: MATERIAL PROPERTIES .....</b>	<b>58</b>
4.1 INTRODUCTION .....	58
4.2 COMPRESSIVE STRENGTH .....	58
4.2.1 Characteristic Compressive Strength .....	58

4.2.2 Compressive Strength Development.....	60
4.2.3 Heat Treatment Regime .....	62
4.3 FLEXURAL STRENGTH .....	63
4.3.1 Characteristic Flexural Strength.....	63
4.3.2 Flexural Strength Development .....	64
4.3.3 Expressions for Flexural Strength.....	65
4.3.4 Load – Deflection Behaviour .....	66
4.3.4.1 First crack.....	67
4.3.4.2 Post-crack behaviour .....	69
4.3.5 Stress – Crack Width Behaviour.....	72
4.4 MODULUS OF ELASTICITY .....	73
4.4.1 Average Modulus of Elasticity .....	73
4.4.2 Modulus of Elasticity Development .....	74
4.4.3 Expressions for Modulus of Elasticity .....	75
4.5 STRESS-STRAIN RELATIONSHIP IN COMPRESSION .....	76
4.5.1 Expressions for Stress-Strain Relationship.....	78
4.6 SHRINKAGE.....	79
4.6.1 Measured Shrinkage Strains.....	81
4.6.2 Prediction of Shrinkage.....	85
4.7 CREEP .....	88
4.7.1 Measured Creep Strains and Creep Coefficients .....	90
4.7.2 Prediction of Creep Coefficient .....	94
4.8 SUMMARY OF RESULTS.....	98
<b>CHAPTER 5: SHORT-TERM FLEXURAL BEHAVIOUR.....</b>	<b>101</b>
5.1 INTRODUCTION .....	101
5.2 PLAIN SF-RPC BEAMS.....	102
5.2.1 Test Procedures .....	102
5.2.2 Moment – Curvature Behaviour .....	103
5.2.3 Load – Deflection Behaviour.....	105
5.2.4 Cracking Behaviour .....	108
5.2.5 Summary of Test Results for Beam Series 1 .....	109
5.3 PRESTRESSED SF-RPC BEAMS.....	110
5.3.1 Test Procedures .....	110
5.3.2 Moment – Curvature Behaviour .....	111
5.3.3 Load – Deflection Behaviour.....	115
5.3.4 Crack Patterns .....	118
5.3.5 Summary of Test Results for Beam Series 2 .....	121
5.4 ANALYTICAL APPROACH.....	123
5.4.1 Flexural Behaviour Predictions.....	123
5.4.2 Cracking Moment Calculations .....	125
5.4.3 Ultimate Strength Calculations .....	125
5.4.4 Failure Criteria .....	126
5.5 CURRENT THEORETICAL PREDICTIONS .....	127
5.5.1 Effective Moment – Curvature Relationships.....	127

5.5.2 Performance of the Current Models.....	132
5.5.2.1 Plain SF-RPC Beams .....	132
5.5.2.2 Prestressed SF-RPC Beams .....	132
5.6 MODIFIED MODEL .....	136
5.6.1 Adopted Stress-Strain Relationships for the Modified Model.....	138
5.6.1.1 SF-RPC compressive relationship.....	138
5.6.1.2 Concrete tensile relationship .....	139
5.6.1.3 Steel stress-strain relationship.....	141
5.6.1.4 Moment-Curvature Relationship.....	141
5.6.2 Performance of Modified Model.....	142
5.6.2.1 Plain SF-RPC Beams .....	142
5.6.2.2 Prestressed SF-RPC Beams .....	142
5.7 SIMPLIFICATION OF THE MODIFIED MODEL .....	146
5.8 LIMITATION OF MODIFIED MODEL .....	147
5.9 CONCLUSION .....	148
<b>CHAPTER 6: TIME-DEPENDENT FLEXURAL BEHAVIOUR .....</b>	<b>150</b>
6.1 INTRODUCTION .....	150
6.2 TEST PROCEDURES .....	151
6.3 TEST RESULTS .....	152
6.3.1 Slab S5 A .....	152
6.3.2 Slab S5 B.....	153
6.3.3 Slab S5 C.....	154
6.3.4 Slab S5 D .....	155
6.3 CROSS-SECTIONAL ANALYSIS METHOD.....	157
6.4 AEMM APPLIED TO SF-RPC .....	161
6.5 CONCLUSION .....	166
<b>CHAPTER 7: CONCLUSIONS AND RECOMMENDATIONS.....</b>	<b>168</b>
7.1 CONCLUSION.....	168
7.2 RECOMMENDATIONS .....	173
<b>APPENDICES .....</b>	<b>177</b>
<b>REFERENCES.....</b>	<b>198</b>

## NOTATIONS

Symbols used in this thesis are defined where they first appear and are also listed below:

$A_c$	concrete area
$\bar{A}_e$	area of age-adjusted transformed section
$A_g$	cross-sectional area
$A_p$	area of prestressing
$B_c$	first moment of concrete area about the top surface
$\bar{B}_e$	first moment of area about top surface of the age-adjusted transformed section
COV	coefficient of variation
$E, E_{ij}$	elastic modulus of concrete
$E_c$	characteristic modulus of elasticity
$\bar{E}_e$	age-adjusted effective modulus of elasticity
$E_m$	mean 28-day modulus of elasticity
$E_p$	modulus of elasticity of prestressing tendon
$e$	eccentricity
$f'_c$	characteristic 28-day compressive strength
$f'_{cf}$	characteristic 28-days flexural strength
$f_c$	concrete strength at 28 days
$f_c(t)$	strength of concrete at age $t$ days
$f_{f.m}$	characteristic 28-day flexural strength
$f_m$	mean 28-day compressive strength
$f_{ij}$	tensile strength of the cement matrix
$f_{t.m}$	mean 28-day tensile strength
$f_u$	peak stress
$h$	height of flexural strength test specimen
$h_0$	nominal height of flexural strength test specimen (=100mm)
$I$	second moment of area
$\bar{I}_c$	second moment of concrete area about top surface

$\bar{I}_e$	second moment of area about top surface of the age-adjusted transformed section
$l_c$	characteristic length
$M_{cr}$	cracking moment
$M_u$	ultimate moment
$\bar{n}$	age-adjusted modular ratio
$P_e$	effective prestressing force
$R_{fl}$	flexural strength corresponding to loss of elastic behaviour
$R_k$	relaxation in $k$ th tendon layer
$R_t$	tensile strength at which cracking occurs
sd	standard deviation
$t$	time (in days)
$t_h$	hypothetical thickness
$t_0$	age at commencement of drying (shrinkage), age at commencement of loading (creep)
$w$	crack width
w/b	water/binder ratio
w/c	water/cement ratio
$y$	depth below top surface
$Z_b$	section modulus on tension side
$\beta$	dimensionless parameter
$\chi$	ageing coefficient
$\Delta$	deflection
$\Delta_{cr}$	deflection at first cracking
$\delta_m$	deflection at midspan
$\varepsilon$	strain
$\varepsilon_c$	concrete strain at stress $f_c$
$\varepsilon_{cr}$	strain at first cracking
$\varepsilon_{cu}$	concrete strain at stress $f_u$
$\varepsilon_o$	top fibre strain
$\varepsilon_{oi}$	initial top fibre strain
$\varepsilon_{o,u}$	axial strain at peak stress

$\varepsilon_{sh}$	shrinkage strain
$\varepsilon_{sh}(\infty)$	shrinkage strain at time infinity
$\phi_{cc.b}$	basic creep factor
$\phi_{cr}$	creep coefficient
$\gamma_{sh}$	shrinkage correction factor
$\kappa$	curvature
$\kappa_{cr}$	curvature at first cracking
$\kappa_i$	initial curvature
$\kappa_m$	curvature at midspan
$\lambda$	dimensionless parameter
$\rho$	density
$\sigma$	stress
$\sigma_{cr}$	stress at first cracking
$\nu$	Poisson's ratio

## LIST OF FIGURES

<b>Figure 2.1:</b>	Density versus compressive strength (Richard and Cheyrezy, 1995)	12
<b>Figure 2.2:</b>	Improved ductility (Dallaire et al., 1998)	17
<b>Figure 2.3:</b>	Beam cross-section comparisons (from Blais and Couture, 1999)	19
<b>Figure 2.4:</b>	Section comparisons for RPC versus steel (from Dauriac, 1997)	20
<b>Figure 2.5:</b>	Sherbrooke Pedestrian/Bikeway Bridge (Dowd, 2000)	21
<b>Figure 2.6:</b>	Stress-strain relationship in compression (Behloul, 1999)	24
<b>Figure 2.7:</b>	Design stress-strain relationship in compression (Gowripalan and Gilbert, 2000)	24
<b>Figure 2.8:</b>	Behaviour in direct tension (Behloul, 1999)	25
<b>Figure 2.9:</b>	Stress-strain relationship in tension for different beam depths (Behloul, 1999)	25
<b>Figure 2.10:</b>	Design stress-strain relationship in tension (Gowripalan and Gilbert, 2000)	26
<b>Figure 2.11:</b>	Creep plus elastic strain versus time (Behloul, 1999)	27
<b>Figure 2.12:</b>	Shrinkage versus time (Gowripalan and Gilbert, 2000)	28
<b>Figure 2.13:</b>	Stress and strain distribution at ultimate limit state for sections containing bonded reinforcement (Gowripalan and Gilbert, 2000)	29
<b>Figure 2.14:</b>	Stress and strain distribution for plain sections (Gowripalan and Gilbert, 2000)	29
<b>Figure 2.15:</b>	Stress and strain distribution on a cracked section (Gowripalan and Gilbert, 2000)	30
<b>Figure 2.16:</b>	Compressive constitutive law for UHPFRC (AFGC, 2002)	32
<b>Figure 2.17:</b>	Simplified tensile constitutive law for UHPFRC (AFGC, 2002)	33
<b>Figure 2.18:</b>	Stress-strain diagrams for UHPFRC (AFGC, 2002)	35
<b>Figure 3.1:</b>	Grading curve for Sydney Sand	40
<b>Figure 3.2:</b>	Grading curve for Silica 200G (from UNIMIN)	40
<b>Figure 3.3:</b>	Shear mixer	42
<b>Figure 3.4:</b>	INSTRON test machine	46
<b>Figure 3.5:</b>	Creep rig	49
<b>Figure 3.6:</b>	Prestressed beam construction	51
<b>Figure 3.7:</b>	Cross-section for beam series 1	51
<b>Figure 3.8:</b>	Cross-section for beam series 2	53
<b>Figure 3.9:</b>	Cross-section for beam series 3	53
<b>Figure 3.10:</b>	Loading arrangement and moment diagram	55
<b>Figure 3.11:</b>	Test set-up for ultimate moment capacity tests	55
<b>Figure 3.12:</b>	Sustained loading arrangement	56
<b>Figure 3.13:</b>	LVDT arrangement	57
<b>Figure 3.14:</b>	Demec target arrangement	57
<b>Figure 4.1:</b>	Compressive strength development with age (Batch 1)	60
<b>Figure 4.2:</b>	Compressive strength predictions	62
<b>Figure 4.3:</b>	Effect of increased curing temperature on compressive strength	63
<b>Figure 4.4:</b>	Flexural strength development with age (Batch 2)	65
<b>Figure 4.5:</b>	Flexural and compressive strength relationship	66
<b>Figure 4.6:</b>	Load – deflection curve	67

<b>Figure 4.7:</b>	Initial portion of load – deflection curve	68
<b>Figure 4.8:</b>	Matrix – fibre interface	70
<b>Figure 4.9:</b>	Crack propagation	71
<b>Figure 4.10:</b>	Stress – crack width curve	72
<b>Figure 4.11:</b>	Modulus of elasticity development with age (Batch 3)	74
<b>Figure 4.12:</b>	Modulus of elasticity and compressive strength relationship	76
<b>Figure 4.13:</b>	Stress-strain behaviour in compression	76
<b>Figure 4.14:</b>	Poisson’s Ratio versus $\sigma/f_u$	77
<b>Figure 4.15:</b>	Theoretical prediction of stress-strain relationship	78
<b>Figure 4.16:</b>	Simple constitutive model for stress-strain behaviour	79
<b>Figure 4.17:</b>	Shrinkage (Batch 4)	81
<b>Figure 4.18:</b>	Shrinkage (Batch 7)	82
<b>Figure 4.19:</b>	Autogenous shrinkage	82
<b>Figure 4.20:</b>	Shrinkage behaviour of RPC 200 (from Cheyrezy, 1999)	84
<b>Figure 4.21:</b>	Supplementary shrinkage series results	85
<b>Figure 4.22:</b>	Comparison of measured and predicted shrinkage strain	87
<b>Figure 4.23:</b>	Regression analysis of shrinkage results (Batch 4)	87
<b>Figure 4.24:</b>	Regression analysis of shrinkage results (Batch 7)	88
<b>Figure 4.25:</b>	Components of strain (from Gilbert, Mickleborough, 1990)	89
<b>Figure 4.26:</b>	Strain versus time (Batch 4)	91
<b>Figure 4.27:</b>	Strain versus time (Batch 7)	92
<b>Figure 4.28:</b>	Creep coefficient curve for SF-RPC	93
<b>Figure 4.29:</b>	Comparison of measured and predicted creep coefficients (Batch 4)	96
<b>Figure 4.30:</b>	Comparison of measured and predicted creep coefficients (Batch 7)	97
<b>Figure 4.31:</b>	Trend lines for creep coefficients (Batch 4 and 7)	98
<b>Figure 5.1:</b>	P1 moment – curvature relationship	104
<b>Figure 5.2:</b>	P2 moment – curvature relationship	104
<b>Figure 5.3:</b>	Comparison of moment – curvature relationships Beam Series 1	105
<b>Figure 5.4:</b>	P1 load – deflection behaviour	106
<b>Figure 5.5:</b>	P2 load – deflection behaviour	107
<b>Figure 5.6:</b>	Final crack pattern in constant moment region P1 B	108
<b>Figure 5.7:</b>	Final crack pattern in constant moment region P2 B	109
<b>Figure 5.8:</b>	S1 moment – curvature relationship	111
<b>Figure 5.9:</b>	S2 moment – curvature relationship	112
<b>Figure 5.10:</b>	S3 moment – curvature relationship	112
<b>Figure 5.11:</b>	S4 moment – curvature relationship	113
<b>Figure 5.12:</b>	Comparison of moment – curvature relationships Beam Series 2	114
<b>Figure 5.13:</b>	S1 load – deflection behaviour	115
<b>Figure 5.14:</b>	S2 load – deflection behaviour	116
<b>Figure 5.15:</b>	S3 load – deflection behaviour	116
<b>Figure 5.16:</b>	S4 load – deflection behaviour	117
<b>Figure 5.17:</b>	Final crack pattern in constant moment region S1 A	118
<b>Figure 5.18:</b>	Final crack pattern in constant moment region S2 A	119
<b>Figure 5.19:</b>	‘Failure’ crack S2 A	119
<b>Figure 5.20:</b>	Final crack pattern in constant moment region S3 B	120
<b>Figure 5.21:</b>	Final crack pattern in constant moment region S\$ B	120
<b>Figure 5.22:</b>	Left hand shear crack S4 B	121

<b>Figure 5.23:</b>	Typical stress-strain curve for 7-wire strand (Gilbert and Mickleborough, 1990)	124
<b>Figure 5.24:</b>	Bending moment, deflected shape and curvature diagram due to externally applied load	128
<b>Figure 5.25:</b>	P1 moment – curvature relationship comparison	129
<b>Figure 5.26:</b>	P2 moment – curvature relationship comparison	129
<b>Figure 5.27:</b>	S1 moment – curvature relationship comparison	130
<b>Figure 5.28:</b>	S2 moment – curvature relationship comparison	130
<b>Figure 5.29:</b>	S3 moment – curvature relationship comparison	131
<b>Figure 5.30:</b>	S4 moment – curvature relationship comparison	131
<b>Figure 5.31:</b>	Predicted versus experimental moment – curvature relationships (Cross-section P1)	133
<b>Figure 5.32:</b>	Predicted versus experimental moment – curvature relationships (Cross-section P2)	133
<b>Figure 5.33:</b>	Predicted versus experimental moment – curvature relationships (Cross-section S1)	134
<b>Figure 5.34:</b>	Predicted versus experimental moment – curvature relationships (Cross-section S2)	134
<b>Figure 5.35:</b>	Predicted versus experimental moment – curvature relationships (Cross-section S3)	135
<b>Figure 5.36:</b>	Predicted versus experimental moment – curvature relationships (Cross-section S4)	135
<b>Figure 5.37:</b>	Moment – curvature relationship phases for plain SF-RPC sections (P1 B)	136
<b>Figure 5.38:</b>	Moment – curvature relationship phases for prestressed SF-RPC sections (S2 A)	137
<b>Figure 5.39:</b>	SF-RPC stress – strain relationship in compression	138
<b>Figure 5.40:</b>	SF-RPC stress – strain relationship in tension	139
<b>Figure 5.41:</b>	Stress – crack width relationship for SF-RPC	140
<b>Figure 5.42:</b>	P1 modified model performance	143
<b>Figure 5.43:</b>	P2 modified model performance	143
<b>Figure 5.44:</b>	S1 modified model performance	144
<b>Figure 5.45:</b>	S2 modified model performance	144
<b>Figure 5.46:</b>	S3 modified model performance	145
<b>Figure 5.47:</b>	S4 modified model performance	145
<b>Figure 5.48:</b>	Simplified model – plain SF-RPC section	146
<b>Figure 6.1:</b>	Moment – curvature relationship for cross-section S5	153
<b>Figure 6.2:</b>	Change in midspan curvature with time (S5 B)	154
<b>Figure 6.3:</b>	Change in midspan curvature with time (S5 C)	155
<b>Figure 6.4:</b>	Change in midspan curvature with time (S5 D)	156
<b>Figure 6.5:</b>	Actual to age-adjusted transformed section (uncracked)	159
<b>Figure 6.6:</b>	Time-dependent deformations	160
<b>Figure 6.7:</b>	Actual and age-adjusted transformed section (cracked)	160
<b>Figure 6.8:</b>	Predicted long-term deformations (S5 B)	162
<b>Figure 6.9:</b>	Predicted long-term deformations (S5 C)	162
<b>Figure 6.10:</b>	Predicted long-term deformations (S5 D)	163
<b>Figure 6.11:</b>	Refined age-adjusted transformed section	164
<b>Figure 6.12:</b>	Refined predictions for long-term deformations (S5 B)	164
<b>Figure 6.13:</b>	Refined predictions for long-term deformations (S5 C)	165

<b>Figure 6.14:</b>	Refined predictions for long-term deformations (S5 D)	165
<b>Figure 6.15:</b>	Refined AEMM	166

## LIST OF TABLES

<b>Table 2.1:</b>	RPC 200 (from Richard and Cheyrezy, 1994)	7
<b>Table 2.2:</b>	RPC 800 (from Richard and Cheyrezy, 1994)	8
<b>Table 2.3:</b>	Typical RPC Composition – Current (from Cheyrezy, 1999)	9
<b>Table 2.4:</b>	RPC Compared to Conventional Concrete (from Roux et al., 1996)	19
<b>Table 2.5:</b>	Final Creep Coefficients for RPC (Gowripalan and Gilbert, 2000)	27
<b>Table 2.6:</b>	Creep and Shrinkage of RPC (Gowripalan and Gilbert, 2000)	31
<b>Table 3.1:</b>	Mix Design	41
<b>Table 3.2:</b>	Large-scale Batch Mixing Procedure	43
<b>Table 3.3:</b>	Material Specimens	44
<b>Table 3.4:</b>	Designations for Beam Series 1	52
<b>Table 3.5:</b>	Designations for Beam Series 2	52
<b>Table 3.6:</b>	Designations for Beams Series 3	54
<b>Table 4.1:</b>	Compressive Strength Results	59
<b>Table 4.2:</b>	Flexural Strength Results	64
<b>Table 4.3:</b>	Tensile Strength Results	69
<b>Table 4.4:</b>	Modulus of Elasticity Results	73
<b>Table 5.1:</b>	Test Results for Beam Series 1	110
<b>Table 5.2:</b>	Test Results for Beam Series 2	122
<b>Table 5.3:</b>	Parameter $\lambda$	140
<b>Table 6.1:</b>	Initial to time-dependent deflection	157

## **Chapter 1: Introduction**

### **1.1 GENERAL INTRODUCTION**

Concrete is the most widely used construction material in the world today. The historical application of concrete can be dated to the third century where it was first used by the Romans. Examples of these early concrete structures still exist in Rome today. There was a decline in the use of concrete in the Middle Ages and it was not until the late 18<sup>th</sup> Century that concrete re-emerged as a principal building material. The mid 19<sup>th</sup> Century saw the development of reinforced concrete followed by the emergence of the concept of prestress in the late 1800s (Warner et al., 1998).

Over the years, concrete has become considerably more complex than the original crushed stone, tile or brick plus sand, lime and water utilised by the Romans. The use of supplementary cementitious materials and additives designed to enhance the properties of concrete has grown significantly throughout the 20<sup>th</sup> Century. The primary focus of this development has been on the achievement of greater compressive strengths and it is now no longer possible to refer to all concretes as merely “concrete”. Under the generic term, there exists a number of more specific descriptions: normal strength concrete NSC (20 – 50MPa), high strength concrete HSC (50 – 100MPa) and ultra-high strength concrete UHSC (above 100MPa).

This increase in compressive strength introduced a number of additional properties. Properties such as low permeability along with the limited shrinkage and creep that are exhibited by high strength concretes are valuable characteristics for the concrete construction industry. However, increased compressive strength also leads to increased brittleness (or decreased ductility) of the concrete. From the perspective of structural design, this increased brittleness is undesirable as it limits the ability of high strength concrete structures to deform considerably before failure. The introduction of fibres into the cementitious matrix, first seen in the 1950s, is a solution to this problem. The term fibre reinforced concrete (FRC) was adopted to describe concretes

containing short, randomly distributed fibres. The most common material for these fibres is steel.

In the 'race for strength', two distinct lines of research have emerged. The first is compact granular matrix concretes (DSP). DSPs contain high superplasticizer and silica fume contents and may also incorporate ultra-hard aggregates, such as steel aggregates. The principle behind DSPs is that the denser the matrix, the greater the resulting compressive strength. The second line of research concerns macro-defect free (MDF) polymer pastes which exhibit very high tensile strength (above 150MPa), particularly when mixed with aluminous cements (Moranville-Regourd, 2002).

The combination of these two approaches resulted in concretes that can be placed and compacted using conventional placement methods despite having water/cement ratios as low as 0.20. These concretes possessed superior compressive strength, along with superior flexural strength and, when fibres are incorporated in the mix, sufficient ductility. A research program was commenced in France in the early 1990s with the aim of developing and defining these ultra-high performance concretes (UHPC). The result of the program was the development of a class of concretes known as Reactive Powder Concrete (Richard and Cheyrezy, 1995).

Since Reactive Powder Concrete (RPC) first appeared on the world research stage in 1994, it has received considerable attention. The original development of RPC came from the Scientific Division of Bouygues, France. Since then further development of the material has continued throughout the world (for example, Australia, Canada, Japan, Korea and the United States of America) at a frenetic pace. Superior mechanical properties and durability characteristics promise that the material will have a wide and significant impact on the concrete industry.

To date, the greater part of research into RPC has focussed on what the material is and its properties, microstructural analysis, potential applications and preliminary work into the structural behaviour. However investigations into the flexural behaviour of the material, and in particular the time-dependent behaviour, are still in their infancy. This information is required to assist with the

increased use of RPC in practice and to further develop analytical techniques and design standards.

## **1.2 OBJECTIVES**

The main objectives of this study are as follows:

1. To develop an RPC mix design from locally-sourced materials;
2. To investigate experimentally the material properties of this RPC mix including compressive and flexural strength, Young's modulus of elasticity and time-dependent properties relating to creep and shrinkage;
3. To investigate experimentally the ultimate flexural behaviour of plain and prestressed RPC beams including the full range load - deflection response, flexural strength and ductility;
4. To investigate experimentally the time-dependent behaviour of prestressed RPC slabs including the deformation of critical sections;
5. To assess the suitability of existing models and to develop new models, as required, for predicting the structural response of plain and prestressed RPC beams; and
6. To facilitate the introduction of RPC in practice in Australia, as well as to advance existing design guidelines for structural members made from RPC.

## **1.3 SCOPE OF THESIS**

The experimental component of this thesis consisted of two sections:

1. A detailed material properties investigation; and
2. Investigations into the flexural behaviour of plain and prestressed RPC beams.

A steel fibre reinforced RPC mix consisting of locally-sourced materials was developed and a range of tests were conducted to determine its mechanical properties. In addition, investigations into the time-dependent properties of creep and shrinkage as well as the effect of various curing conditions were conducted.

The investigations into the flexural behaviour of plain and prestressed RPC beams involved testing 3 series of beams/slabs. All beams/slabs were 3m in length with varying cross-sectional dimensions. Beams series 1 and 2 consisted of 4 plain beams and 8 prestressed beams respectively. The beams were tested for ultimate moment capacity at an age of between 25 – 35 days. Beam series 3 consisted of 4 prestressed slabs. The slabs were tested under sustained load with loading commencing at an age of 28 days. The time-dependent behaviour including the change in curvature and deflection of these slabs were obtained from these tests.

The analytical component of this thesis involved the evaluation and modification of existing models proposed for RPC. There are currently 2 available models for the flexural behaviour of plain and prestressed RPC beams. Both models use a strain compatibility approach to predict the flexural behaviour of RPC sections. Therefore, a strain compatibility approach was adopted for the analysis of the short-term flexural behaviour of the beams tested as part of this investigation. Gilbert's (1990) Age-adjusted Effective Modulus Method (AEMM) was used in the analysis of the time-dependent behaviour of prestressed RPC slabs. Refinements specific to RPC were considered for the application of the AEMM to the slabs tested.

#### **1.4 LAYOUT OF THESIS**

Chapter 2 presents a detailed literature review which summarises the results of research conducted thus far into the behaviour of RPC. Included in this chapter is a detailed description of the 2 currently available models for the structural behaviour of RPC sections.

Chapter 3 outlines the experimental program undertaken as part of this research and includes details pertaining to the procedures of the various materials and beam tests. Chapter 4 presents the results of the material properties investigation covering both the short-term and time-dependent aspects.

Chapter 5 contains the experimental results and analysis of the ultimate flexural strength of plain and prestressed RPC beams (Series 1 and 2). The performance of the 2 currently available models was assessed in this chapter along with details of a modified model designed to provide greater accuracy in predicting the structural behaviour of plain and prestressed RPC sections. Chapter 6 contains the results and analysis of the time-dependent behaviour of the prestressed RPC slabs (Series 3). The ability of the AEMM to provide a reasonable estimate of the time-dependent deformations of prestressed RPC slabs is considered. Details of proposed refinements to the AEMM for greater accuracy are also included.

Chapter 7 presents a summary and conclusions of the investigation and recommendations for future research.

## **Chapter 2: Literature Review**

### **2.1 INTRODUCTION**

Reactive Powder Concretes (RPCs) are ultra-high strength cementitious materials composed of very fine powders with a maximum particle size of approximately 800 $\mu$ m. In addition to the absence of the traditional coarse aggregates used to produce normal and high strength concrete, RPCs are characterized by very high silica fume content and very low water-cement (w/c) ratios (Cheyrezy et al., 1995). The low w/c ratios are achieved through the use of new generation superplasticizers in large doses, typically in excess of 20L per cubic metre of concrete. The large dose of superplasticizer is required to achieve a workable mix.

A typical RPC has a compressive strength in excess of 150MPa, flexural strength of between 20 and 50MPa and Young's modulus of elasticity in the range of 45 – 65GPa. With the inclusion of steel fibres to overcome the brittleness of the cementitious matrix, RPCs exhibit superior ductility to even high performance concretes. Hence RPCs are often referred to as ultra-high performance concretes. They also have an extremely low porosity resulting in an extremely durable material. Due to the fineness of the constituent materials and the workability of the mix, RPC can take any shape required with a high quality surface finish (Dauriac, 1997).

The original development of RPC came from the Scientific Division of Bouygues, France. Development began in the early 1990s with the first published report on the material appearing in 1994 (Richard and Cheyrezy, 1994). Two distinct classes of RPCs were developed: RPC 200 and RPC 800, which have nominal compressive strengths of 200MPa and 800MPa respectively. Each class requires different fabrication processes, possess different characteristics and can be used for a variety of structural and non-structural applications. The fibre type used as part of this original research were straight, smooth steel fibres 12.5mm in length and 0.18mm in diameter given them an aspect ratio (length/diameter) of approximately 70.

RPC 200 can be produced and placed in a similar manner to conventional high performance concretes. Typical mix proportions and the resulting mechanical properties are detailed in Table 2.1. The lower compressive strength (170MPa) results from curing the concrete at ambient temperatures whilst the upper strength (230MPa) results from hot water or steam curing at 80 – 90°C for 48 hours after two days of pre-curing at ambient temperatures. RPC 200 can be used in a wide variety of structural applications with or without prestress.

**Table 2.1:** RPC 200 (from Richard and Cheyreyzy, 1994)

<u>Composition</u>	
	Per m <sup>3</sup>
Portland cement – Type V	955 kg
Fine sand (150 – 400µm)	1051 kg
Silica fume (18m <sup>2</sup> /g)	229 kg
Precipitated silica (35m <sup>2</sup> /g)	10 kg
Superplasticizer (polyacrylate)	13 kg
Steel fibres	191 kg
Total water	153 L
<u>Mechanical Properties</u>	
Compressive strength $f_{ck}$ of cylinders	170 – 230 MPa
Flexural strength	30 - 60 MPa
Fracture energy	20000 – 40000 J/m <sup>2</sup>
Ultimate tensile strain	5000 - 7000 µε
Young's modulus	54 - 60 GPa

RPC 800 requires air-drying at elevated temperatures in excess of 250°C. The material is pressurised before and during setting. The mix proportions and resulting mechanical properties are detailed in Table 2.2. The mechanical properties are for pressurised specimens cured at 400°C. Steel powder can be used to replace the quartz sand resulting in compressive strengths up to 810MPa. Due to the complex fabrication processes required, RPC 800 is suitable for small to medium scale prefabricated elements or as a steel replacement e.g. anchorage heads or protective panels for impact resistance.

**Table 2.2:** RPC 800 (from Richard and Cheyrezy, 1994)

<u>Composition</u>	
	Per m <sup>3</sup>
Portland cement – Type V	1000 kg
Fine sand (150 – 400µm)	500 kg
Silica fume (18m <sup>2</sup> /g)	229 kg
Ground quartz (4µm)	390 kg
Superplasticizer (polyacrylate)	18 kg
Steel fibres	630 kg
Total water	180 L
<u>Mechanical Properties</u>	
Compressive strength $f_{ck}$ of cylinders	490 – 680 MPa
Flexural strength	45 – 141 MPa
Fracture energy	1200 – 2000 J/m <sup>2</sup>
Young's modulus	65 - 75 GPa

Since its inception in 1994, the composition of a typical RPC with a nominal compressive strength in the vicinity of 200MPa has been modified slightly from the composition of RPC 200. The component materials have remained the same but the mix proportioning has been adjusted. The main difference is a reduction in cement content. The composition of a current RPC mix is given in Table 2.3. The mix has a mean compressive strength of 200MPa, a mean flexural strength of 40MPa, a Young's modulus of 50GPa and fracture energy of 30000J/m<sup>2</sup>.

**Table 2.3:** Typical RPC Composition – Current (from Cheyrezy, 1999)

<u>Composition</u>	
	Per m <sup>3</sup>
Cement	710 kg
Silica fume	1020 kg
Sand	230 kg
Quartz powder	215 kg
Steel fibres	160 kg
Superplasticizer	10 kg
Total water	140 L

## 2.2 DEVELOPMENT OF REACTIVE POWDER CONCRETE

It is clear from their constituent materials that RPCs have some fundamental differences from conventional concretes, i.e. the absence of coarse aggregates and the presence of well-graded aggregates down to sub-micron sizes. The superior mechanical properties exhibited by RPCs result from the principles used in their development. These principles fall into four key areas of improvement (Richard and Cheyrezy, 1995):

1. Homogeneity
2. Density
3. Microstructure
4. Ductility

The fifth principle that was adopted in the original development program for RPC was to maintain mixing and casting procedures as close as possible to existing practices.

### 2.2.1 Homogeneity

Conventional concrete is a heterogeneous material consisting of constituents from fine cement to coarse aggregate. Each component material exhibits a different strength and modulus of elasticity. At a macroscopic level concrete consists of two main components – hardened cement paste (cement and water) and inclusions (aggregates). It is accepted that the performances of these two main components will not be fully retained when the two are combined. In

RPCs, the problems relating to heterogeneity are substantially reduced for the following reasons (Richard and Cheyrezy, 1995):

- Elimination of coarse aggregates,
- Improved mechanical properties of the paste, and
- Reduction in the aggregate/paste ratio.

#### *2.2.1.1 Elimination of coarse aggregates*

Aggregates form the bulk of conventional normal and high strength concrete. These aggregates form a rigid skeleton of granular elements in the cementitious matrix. When compressive force is applied, tensile and shear stresses appear at the paste-aggregate interface and generate cracks in the weak interface zone between the aggregates and the paste. In normal strength concrete, where the strength of the paste is less than the strength of the aggregates, these cracks will propagate through the paste only as the applied stress increases resulting in a tortuous crack surface. In high strength concretes where the strength of the paste is similar to or in some cases exceeds the strength of the aggregates, cracks will propagate through the aggregates as well as the paste resulting in a smoother crack surface. In cases where the strength of the paste exceeds the strength of the aggregates, cracks may initiate from within the aggregates themselves.

The crack size is related to the extent of the zone under tensile stress. In the case of a spherical inclusion, the size of the equatorial crack is directly proportional to the diameter of the inclusion. For normal and high strength concrete, the maximum aggregate size is 40mm and 20mm respectively. For a typical RPC mix, sand is the largest inclusion with a maximum size of 600 – 800 $\mu$ m. With this reduction in size of the coarsest particle by a factor of 50, there is a major reduction in the size of microcracks of the following origins (Richard and Cheyrezy, 1995):

- Mechanical (external loads),
- Chemical (autogenous shrinkage), and
- Thermo-mechanical (differential expansion between the paste and aggregate under the effect of heat treatment)

### *2.2.1.2 Improved mechanical properties of the paste*

In conventional concrete there is a large mismatch in the Young's modulus of the aggregates (45 – 70GPa) and the paste (18 – 22GPa). This mismatch tends to magnify the effects associated with disturbance in the mechanical stress field. When external force is applied, the components of conventional concrete will deform at different rates. This differential movement produces strains between the component materials and cracking will occur once the tensile strain capacity of the concrete is reached (O'Neil et al, 2002).

The increase of Young's modulus for a typical RPC paste, by comparison with that of conventional cementitious pastes, tends to moderate the effects associated with the disturbance in the mechanical stress field. The Young's modulus of RPC paste generally exceeds 45GPa and, in some cases, can reach 75GPa. Thus, the global modulus of the paste and aggregates is similar to the modulus of the aggregate (sand) alone. The effect of mechanical heterogeneity is therefore significantly reduced and in some cases completely removed (Richard and Cheyrezy, 1995).

### *2.2.1.3 Reduction of paste/aggregate ratio*

In conventional concrete, the aggregates (sand and gravel) form the majority of the volume of the composite material. As a rigid skeleton of adjacent granular elements, these aggregates effectively block a major proportion of the paste shrinkage. When shrinkage occurs, the paste that is trapped inside the cavities between the aggregate particles will decrease in volume and, as a result, air voids will be created. As air voids are considered to be a form of inclusion in concrete, their presence leads to greater heterogeneity. In addition to this, increased air voids lead to increased porosity and subsequent decreased compressive strength (see Section 2.2.2).

For RPC, the volume of the paste is at least 20% greater than the voids ratio of the non-compacted sand (aggregate). Thus, the aggregates do not form a rigid skeleton but are rather a set of inclusions in the continuous cementitious matrix. The paste shrinkage is locally restrained around the sand particles but global shrinkage is unrestrained unless by external means (Richard and Cheyrezy, 1995). Therefore, shrinkage of RPC does not result in a significant increase in

the number of air voids and subsequent increase in heterogeneity or decreased strength due to increased porosity.

### 2.2.2 Density

It is accepted for concrete that an increase in the density (or decreased porosity) will result in an increase in the compressive strength (Neville, 1995). Figure 2.1 shows the strength values obtained for different relative densities for both plain and fibre reinforced RPC 200. It can be seen that there is an increase in compressive strength with increasing relative density. Relative density is the ratio between the density at demoulding and the solid density of the granular mixture assumed to be compacted, i.e. no water or air. In addition to illustrating the effect of density on strength, Figure 2.1 also shows the advantageous effect of heat treatment (see Section 2.2.3).

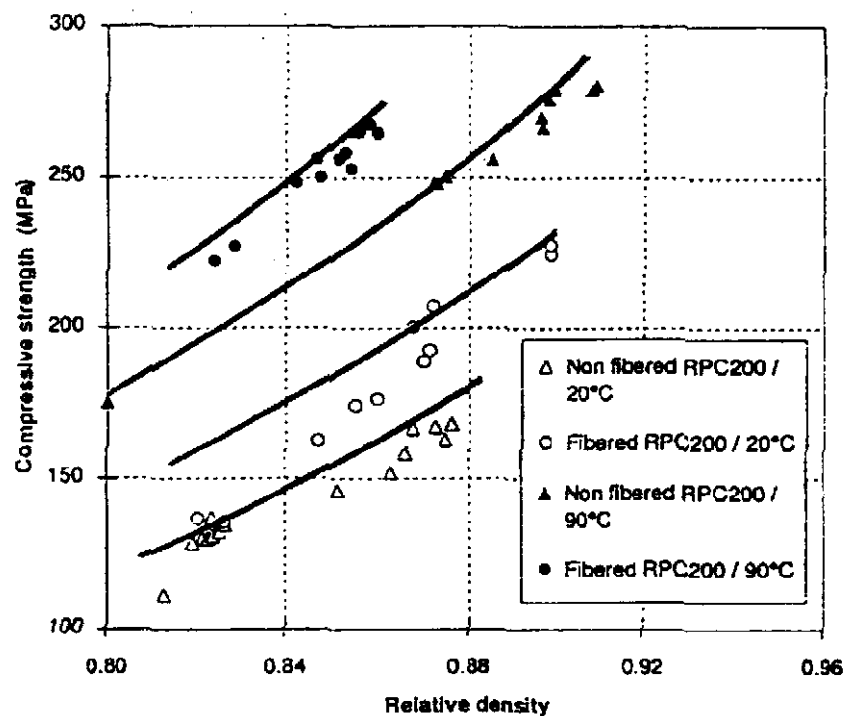


**Figure 2.1:** Density versus compressive strength (Richard and Cheyrezy, 1995)

One key factor governing the density of a concrete mix is the amount of water used (Neville, 1995). For two conventional concretes having the same mix proportions for the dry constituents and identical production procedures, the concrete with the lower water to cement ratio ( $w/c$ ) will have a higher compressive strength. Therefore, excess water in a concrete mix is clearly

detrimental to the compressive strength. In a typical RPC mix, the volume of water is kept low to ensure that there is no excess. The water to binder ratio (w/b) is less than what is required for full hydration to ensure that all the water is consumed in the hydration/pozzolanic reaction process. (Binder refers to all cementitious materials, i.e. cement plus silica fume.) Typical w/b ratios for RPC vary from 0.15 – 0.22. However if the w/b ratio is less than 0.12, there is a decrease in strength resulting from poor compaction of the resulting concrete (O'Neil et al., 2002).

The key factor governing the amount of water required for fluidizing a concrete mix is the compacted dry density of the solids. With conventional concrete, this compaction is improved by the use of superplasticizers and particles smaller than cement grains such as silica fume. For RPC, the granular mixture is carefully optimised to ensure that the maximum compacted dry density of the solids is obtained. Another technique used to increase the density of RPC is the application of pressure before and during setting to remove excess water.

#### *2.2.2.1 Optimisation of the granular mixture*

The granular mixture can be optimised by the use of a packing model. The following principles apply to the selection of the granular components (Richard and Cheyrezy, 1995):

- Obtain a mixture containing several granular classes, with a tight granular range within each class. Select materials that give a high ratio (13+) between mean particle diameter ( $d_{50}$ ) for consecutive classes,
- Determine the optimum ratio of cement to superplasticizer by rheological analysis and check their compatibility, and
- Select the least agglomerated fine powders.

According to Richard and Cheyrezy (1995), several parameters apply to the selection of the individual granular components of an RPC mix in order to obtain optimum packing:

### Sand

The particle size distribution should fall into the range 150 – 600 $\mu$ m. The upper limit is determined by homogeneity requirements and the lower limit is set to avoid interference with the largest particles of the next granular class – cement. A  $d_{50}$  of approximately 250 $\mu$ m is desirable as cement has a  $d_{50}$  of 11 - 15 $\mu$ m. Rounded sand is preferable due to the slightly lower water demand.

### Cement

Due to their high water demand, over-ground cements with a high Blaine fineness (e.g. high early strength cements) are generally unacceptable. Cements with low  $C_3A$  content have been found to give better strength results. The selection of the cement type cannot be dissociated from the selection of the superplasticizer. Polyacrylate-based superplasticizers give the best dispersing results and therefore allow the greatest reduction in w/c ratio but they can retard the setting of the concrete.

### Silica Fume

The silica fume performs the following functions:

- 1) Fills the voids between the cement particles,
- 2) Enhances the rheological characteristics of the mix as a result of the perfect sphericity of the particles, and
- 3) Produce secondary hydrates.

The silica fume should be relatively free from particle aggregation and impurities. Undensified silica fume is therefore desirable.

### Quartz

A  $d_{50}$  between 5 – 25 $\mu$ m provides maximum reactivity during heat treatment. This results in the crushed quartz being in the same granular class as the cement.

#### *2.2.2.2 Application of pressure*

The application of pressure has three beneficial effects:

1. Reduction of entrapped air

The application of pressure for a few seconds to the fresh mix virtually eliminates air bubbles in the RPC.

## 2. Removal of excess water

If the pressure is applied over several minutes, excess water can be “squeezed” out of the concrete. In the case of an RPC, this has only a slight effect, as there is minimal water in the mix to start with.

## 3. Compensating for chemical shrinkage

When the applied pressure is maintained throughout the setting phase for the fresh RPC (6 – 12 hours), part of the porosity resulting from chemical shrinkage can be eliminated.

When the three above principles are applied to RPC, increases in density in excess of 6% can result. Since compressive strength is highly dependent on density at time of demoulding, this results in a significant gain in strength. However, there is only a marginal increase in the tensile strength of the material resulting from any increase in the density (Richard and Cheyrezy, 1995).

### 2.2.3 Microstructure

The application of heat treatment after setting has occurred substantially enhances the microstructure, and subsequently the mechanical properties, of RPC. Heat treatment involves heating the concrete after initial setting. There are two different improvements that can be made through the application of heat. Results depend on the temperature and the duration of the heat treatment (Richard and Cheyrezy, 1995). These improvements are:

1. Increased pozzolanic reaction; and
2. Development of crystalline products

#### 2.2.3.1 Increased pozzolanic reaction

Portland cement, silica fume, crushed quartz and to a lesser extent sand react chemically during the different processing stages of the material. Heating RPC for two days at 90°C, once setting has occurred, accelerates these pozzolanic reactions and modifies the hydrate structure. Zanni et al. (1996) investigated the hydration and pozzolanic reactions in RPC using <sup>29</sup>Si NMR (Nuclear Magnetic Resonance) spectrometry. The results of their investigation showed that increasing the temperature and duration of heat treatment led to the development of longer calcium-silicate-hydrate (CSH) chains in larger volumes. A larger amount of CSH increases the strength of the binder improving the bond

between the cement and the aggregates and subsequently results in increased strength. At a heat treatment temperature of 90°C, these hydrates remain amorphous.

#### *2.2.3.2 Development of crystalline products*

High temperature heat treatment such as autoclaving (250 - 400°C), which can only be applied to RPC containing steel fibres and crushed quartz, results in the formation of crystalline hydrates (xonotlite). Richard and Cheyrezy (1994) used XRD analysis to show the presence of xonotlite. The formation of xonotlite results in a major dehydration of the cement paste. Compressive strengths in excess of 480MPa have been recorded on specimens that have undergone high temperature heat treatment.

#### **2.2.4 Ductility**

The first three principles for enhancing the mechanical properties of RPC result in a very high strength but brittle material. The cementitious matrix is nearly as brittle as an industrial ceramic with fracture energy as low as 30J/m<sup>2</sup>, which leads to the RPC matrix behaviour being virtually purely linear and elastic. For RPC to be able to be used for structural applications, it is necessary to achieve ductile behaviour.

There are 2 techniques available for improving the ductility of RPC. The first method involves the inclusion of steel fibres into the matrix. This leads to an increase in the load to first crack and improves the post-peak behaviour. The large number of small fibres that cross the path of potential cracks, coupled with good bond between fibre and matrix, provides high resistance to fibre pullout during tensile cracking, and greatly increases the ductility of the material (O'Neil et al., 2002).

The second method is to confine the cementitious matrix in a steel tube. This not only improves ductility but also has the additional advantage of increased compressive strength due to the confining effect. Figure 2.2 shows the increased ductility that can be achieved by these methods. As can be seen in the figure, significant improvements in post-peak behaviour are obtained by the

addition of fibres or confinement. Figure 2.2 also shows the superior ductility of RPC when compared with normal strength and high-performance concretes.

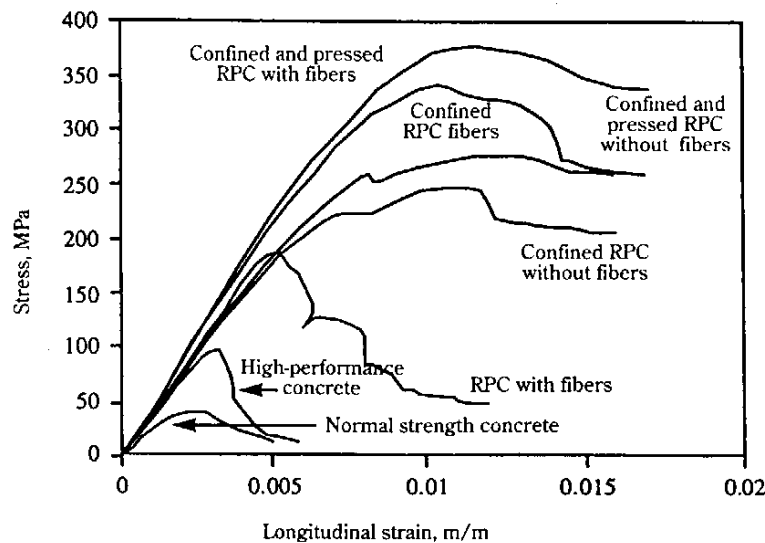


**Figure 2.2:** Improved ductility (Dallaire et al., 1998)

### 2.3 ADVANTAGES

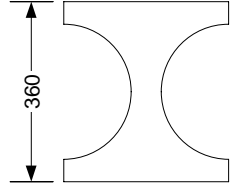
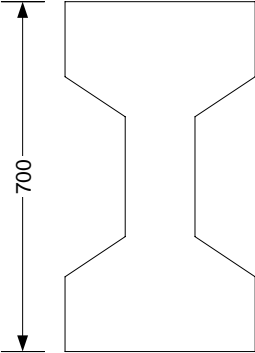
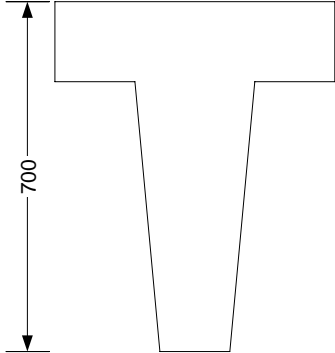
With its superior mechanical properties, the use of RPC has a number of advantages when compared with currently used conventional and high performance concretes. These advantages are listed below:

- Superior compressive and tensile strength
  - Superior strength can lead to more slender structures resulting in a significant dead load reduction. This can lead to an increase in the usable floor space within high-rise buildings as a result of decreased column size or decreased substructure requirements for bridges containing RPC superstructures. For example, the older decks of existing bridges can be replaced with RPC decks leading to an increased load carrying capacity through the reduction in dead load.
  - Superior strength also results in an optimisation of material usage. Figure 2.3 shows a comparison in the section depth and weight for three types of concrete beam cross sections having equal moment carrying capacity. As can be seen from the diagram, RPC sections

are approximately one-third the weight of their prestressed or reinforced counterparts.

- The superior tensile strength of RPC is such that the concrete itself can carry all but the primary tensile stresses. This elimination of shear and other auxiliary reinforcing steel allows nearly limitless freedom of shape for structural members. In addition to this, major cost savings can be realised from the absence of supplemental reinforcing steel as the fixing of such steel has significant labour costs associated with it.
- Superior durability
  - Due to the optimisation of the granular materials, RPCs have extremely low porosity and are virtually impermeable to liquids and gases. Roux et al (1996) carried out a number of tests to verify this. Their findings are summarised in Table 2.4. These properties make RPC an ideal material for use in chemically aggressive environments i.e. marine splash-zones, de-icing salts or areas prone to freezing and thawing. Its low porosity also makes RPC suitable for containment purposes i.e. nuclear waste storage.
  - RPC also has a high resistance to abrasive wear (Roux et al, 1996), which is ideal in applications where physical wear greatly limits the life of more conventional concrete, i.e. bridge decks and industrial floors.

The enhancements required to produce the superior characteristics of RPC, however, come with a substantial cost increase. In a typical RPC formulation the least expensive components of a conventional concrete mix (aggregates) have been replaced by more expensive components. The cost of producing 1 cubic metre of steel fibre reinforced RPC is 3 – 5 times the cost to produce 1 cubic metre of conventional concrete. With increasing use, the cost is gradually decreasing but RPCs are not expected to replace conventional concretes where the latter can economically meet the performance criteria.

<b>Cross Section</b> (Reinforcing bars and tendons omitted)			
	RPC X-Shaped	Prestressed Concrete	Reinforced Concrete
	Weight 130 kg/m	470 kg/m	530 kg/m

(Ultimate moment capacity 675 kN.m)

**Figure 2.3:** Beam cross-section comparisons (from Blais and Couture, 1999)

**Table 2.4:** RPC Compared to Conventional Concretes (from Roux et al, 1996)

<u>Durability Indicator</u>	<u>Comparison</u>
Porosity	4 – 6 times lower
Air Permeability	20 – 50 times lower
Water Absorption	7 – 10 times lower
Corrosion Velocity	10 – 25 times lower
Carbonation Rate	Undetected in RPC

However, with properties nearing those of some metals, it is more likely that RPC will compete with structural steel. Figure 2.4 shows the size of an RPC X-shape cross-section compared to a steel section of equal moment capacity. The cost comparison of RPC should be made with steel on a volumetric basis as the two materials have similar compressive strengths. The cost of 1 cubic metre of steel is approximately 10 times that of 1 cubic metre of RPC.

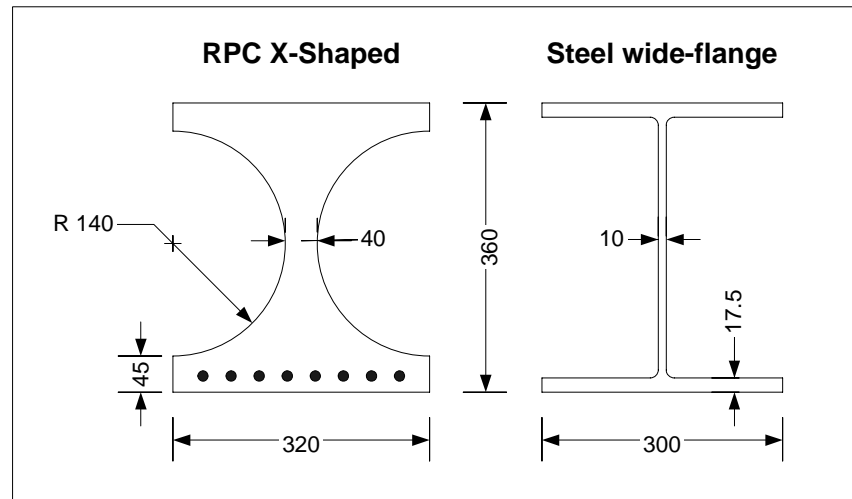


**Figure 2.4:** Section comparisons for RPC versus steel (from Dauriac, 1997)

## 2.4 APPLICATIONS

### 2.4.1 Bridges

RPC has already been used in a number of bridge structures throughout the world. The first RPC structure was a pedestrian bridge built in Sherbrooke, Canada. Pedestrian bridges have since followed in a number of other countries, i.e. France, South Korea and Japan. The first RPC vehicular bridge has recently been constructed in Australia.

#### 2.4.1.1 Pedestrian bridges

The Sherbrooke pedestrian/bikeway bridge was the first major structure built using RPC. It was completed in July 1997. The bridge superstructure is a post-tensioned open-web space truss. Unconfined RPC, with a compressive strength of 200MPa, was used in the deck and top and bottom chord elements of the truss. RPC confined in stainless steel tubes, with a compressive strength of 350MPa, was used for the construction of the diagonal web members. The bridge consisted of 6 pre-fabricated match-cast segments. The segments were assembled on site using internal and external post-tensioning (Blais and Couture, 1999).

The 60m long bridge spans the Magog River in a circular arch in central Sherbrooke. The bridge is shown in Figure 2.5.



**Figure 2.5:** Sherbrooke Pedestrian/Bikeway Bridge (Dowd, 2000)

Following the success of the Sherbrooke Pedestrian/Bikeway Bridge, RPC pedestrian bridges have been built in several other countries. The Seonyu Footbridge is a 120m long and quite slender arch bridge on the Han River near Seoul, Korea. It is a post-tensioned segmental bridge consisting of 6 segments, each 20m in length, with a walkway thickness of 30mm (Semioli, 2001). The Maeta Footbridge is a 50m long bridge in Japan. The bridge is post-tensioned and consists of castellated beam elements. Both the Seonyu and the Maeta footbridges were fabricated using steel-fibre reinforced RPC.

#### *2.4.1.2 Vehicular bridges*

The bridge at Shepherd's Gully Creek (New South Wales, Australia) is the first RPC bridge structure in the world that has been constructed for normal highway traffic. The bridge is a single span bridge, 15m in length with a width of 21m containing four traffic lanes plus a footway. The superstructure consists of precast, pretensioned RPC beams along with precast, pretensioned RPC deck slabs. An in-situ connection is designed to provide composite action between the deck slabs and beams.

The beams are I-shape cross-sections with a depth of 600mm and a weight of 280kg/m. The spacing between adjacent beams is 1.3m. The slab sections are each 2m wide with a depth of 110mm and a weight of 275kg/m<sup>2</sup>. The total weight of the superstructure will be 490kg/m<sup>2</sup>. This is approximately 40% of the weight of a conventional concrete bridge superstructure (Cavill and Chirgwan, 2003).

### 2.4.2 Other Applications

Giving its superior mechanical and durability properties, RPC is currently being used, or is envisaged to be used, in a wide variety of other structural and non-structural applications. In these cases, the material is chosen for its ability to withstand high stresses, both from a load and an environmental perspective. These applications are listed below:

- Current Applications
  - Architectural panels for sound proofing, France
  - Beams in the Cattenom Nuclear Power Plant, France
  - Seawall anchors, Portugal
- Envisaged Applications
  - High pressure pipes for liquid and gas transportation
  - Isolation and containment of nuclear waste
  - Blast resistant structures
  - Seismic applications
  - High strength liners for tunnels and mining shafts
  - Industrial flooring
  - Wide open enclosures e.g. stadium domes

### 2.5 CURRENT DESIGN GUIDELINES

With RPC already being used in practice, a number of documents have been produced to provide guidelines for its use. They are:

1. Design Guidelines for RPC Prestressed Concrete Beams – 2000 (Gowripalan and Gilbert, 2000)
2. Interim Recommendations: Ultra High Performance Fibre-Reinforced Concretes – 2002 (AFGC, 2002)

Both documents deal with a range of structural effects including flexure, shear and torsion. As the focus of this thesis is on the flexural behaviour of RPC, only those sections pertaining to this structural aspect are discussed.

### **2.5.1 Design Guidelines for RPC Prestressed Concrete Beams (2000)**

Gowripalan and Gilbert (2000) prepared this document with the aim of providing guidelines for the design of prestressed beams using RPC. The guidelines, where possible, adopt a limit state approach consistent with the design requirements of the Australian Standard for Concrete Structures AS3600 - 1994.

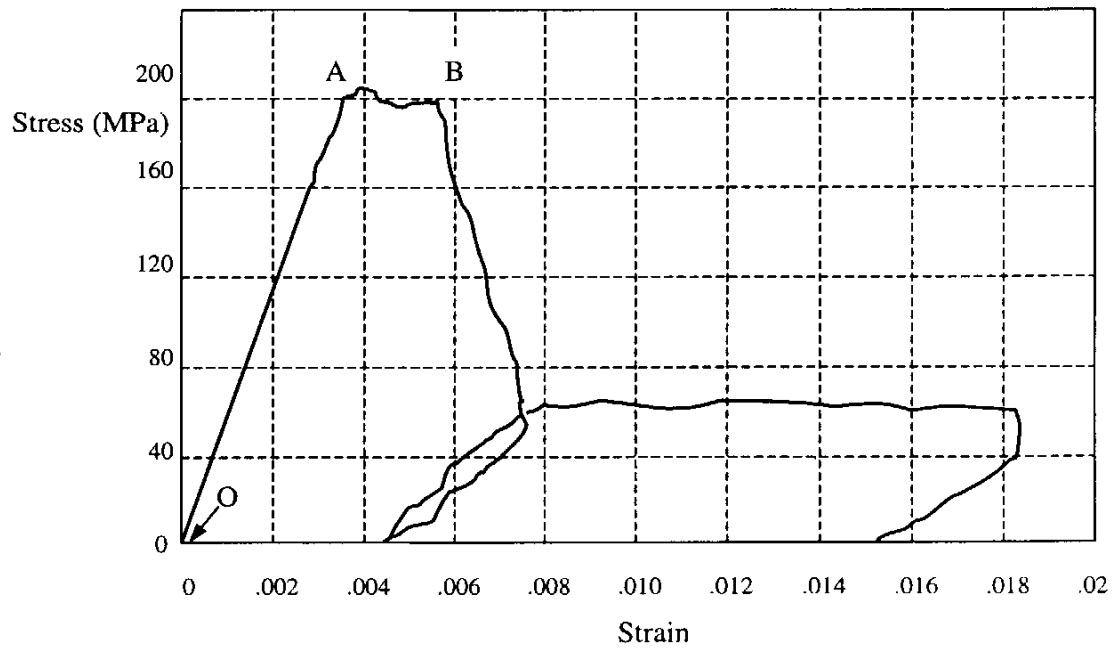
The document was produced to provide guidelines for the design of beams fabricated using a specific commercially available RPC product and as such have a limited range of application. The RPC for which the document was formulated has a compressive strength at 28 days of 150 – 220MPa and a minimum fibre content of 2% by volume. Any specific values referred to are applicable to this RPC only.

#### *2.5.1.1 Design properties*

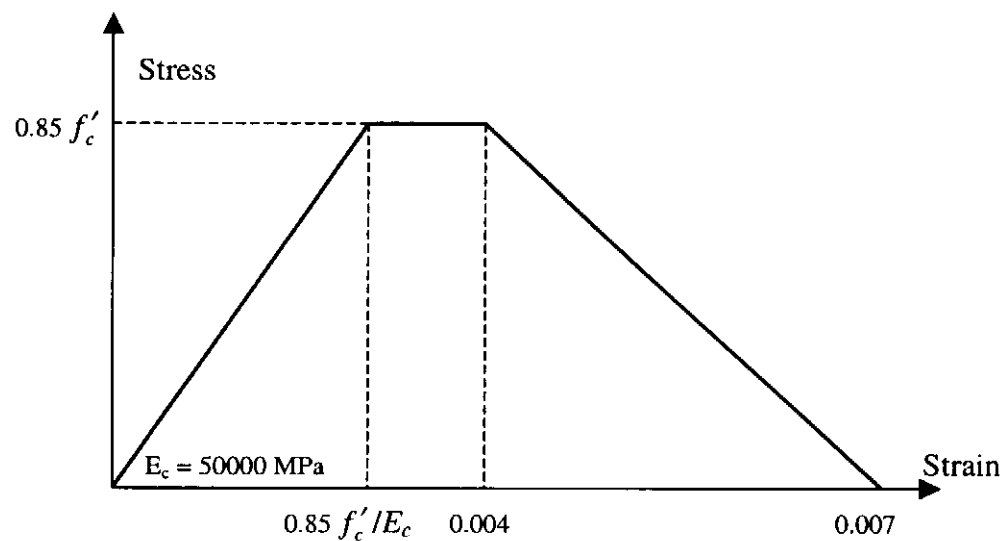
##### **COMPRESSION**

A typical stress-strain curve for RPC in compression is shown in Figure 2.6. The curve was obtained from measurements taken in a standard compression test on a 70mm diameter cylinder. As can be seen from the curve, the ascending part of the curve is essentially linear up until the peak stress is reached. Once peak has been reached, the steel fibres provide ductility resulting in the plateau AB. The length of the plateau and the shape of the descending portion of the stress-strain curve depend on the type and quantity of the fibres.

From this curve, an idealised stress-strain relationship in compression was proposed as shown in Figure 2.7.



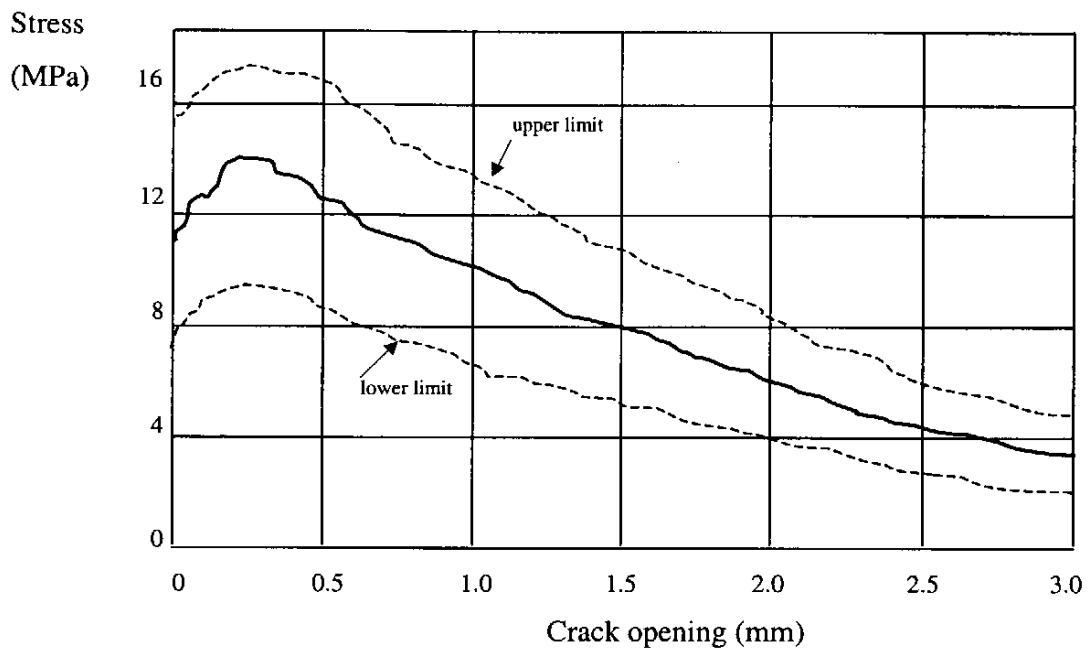
**Figure 2.6:** Stress-strain relationship in compression (Behloul, 1999)



**Figure 2.7:** Design stress-strain relationship in compression (Gowripalan and Gilbert, 2000)

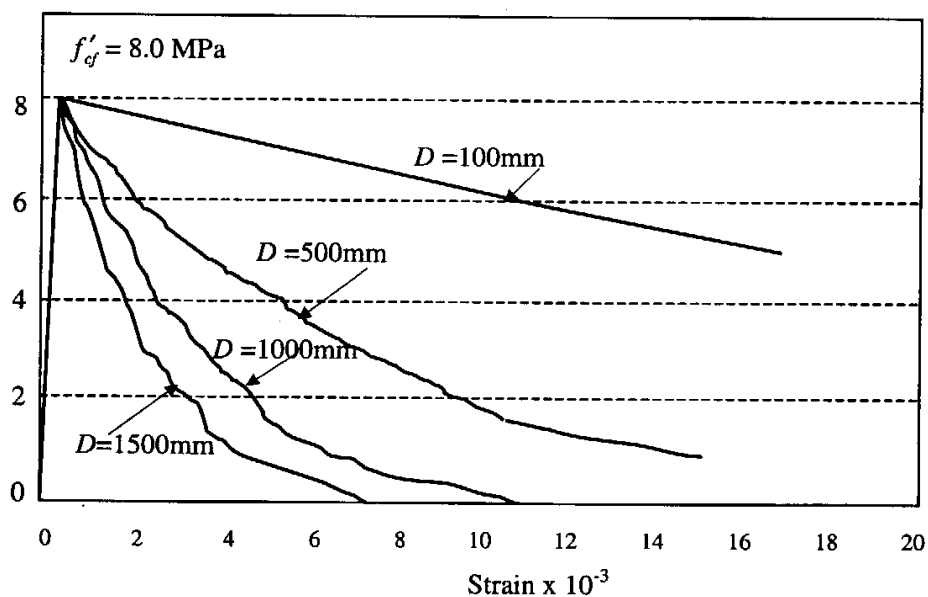
## TENSION

Figure 2.8 presents the typical results of a direct tensile test conducted on a 70mm diameter RPC cylinder, as well as the range of variability to be expected. It should be noted that the average tensile stress on the cracked surface increases after first cracking. With increasing crack width, fibres are gradually pulled out of the crack surface and the average tensile stress subsequently decreases once a crack width of approximately 0.2mm is reached.



**Figure 2.8:** Behaviour in direct tension (Behloul, 1999)

As with conventional concrete, the flexural tensile strength of RPC is higher than the direct tensile strength with values in excess of 40MPa having been recorded. The flexural strength may be determined from standard 3-point or 4-point modulus of rupture tests. A typical stress-strain curve for RPC in tension for various beam depths is shown in Figure 2.9.



**Figure 2.9:** Stress-strain relationship in tension for different beam depths (Behloul, 1999)

The tension capacity across a crack inevitably relies on not only the type of fibre and the depth of the beam as shown in Figure 2.9 but also on the quantity of fibres crossing the crack. Since this is highly variable, the resulting tension capacity is also highly variable and hence, a high factor of safety is recommended. Overseas practice (Behoul, 1999) uses a factor of safety of 4 when determining the design tensile stress at which cracking first occurs. The characteristic flexural tensile stress ( $f'_{ct}$ ) at which cracking is initiated may be taken as

$$f'_{ct} = 8.0 \text{MPa}$$

For design purposes, the idealised stress-strain relationship shown in Figure 2.10 is proposed.  $D$  is the overall depth of the beam and  $L_f$  is the length of the fibres.

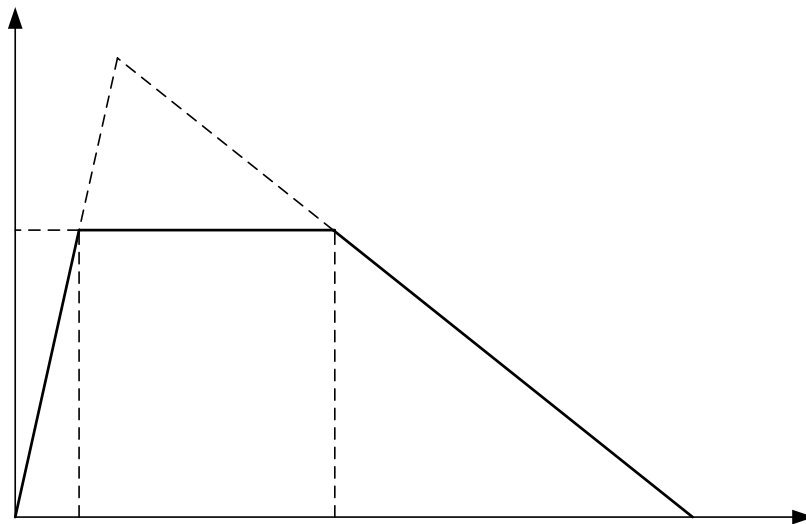


**Figure 2.10:** Design stress-strain relationship in tension (Gowripalan and Gilbert, 2000)

#### POISSON'S RATIO

According to Behloul (1996), Poisson's ratio for a typical RPC varies between 0.16 and 0.24. It is proposed that, in the absence of any specific test data, Poisson's ratio may be taken as 0.2. This is consistent with the Poisson's ratio for conventional and high strength concretes.

## CREEP

The creep of RPC is, like conventional concrete, dependent on the age at first loading and the duration of applied stress. In addition to this, it is also dependent on the curing regime. RPCs that have undergone curing at 90°C for a period of 48 hours exhibit little creep. If no curing is applied, the creep coefficient (ratio of creep strain to initial elastic strain) can range between 1.2 and 1.8 depending on the age of first loading. Figure 2.11 shows a typical set of elastic and creep strain (per unit stress) for an RPC loaded at different ages.

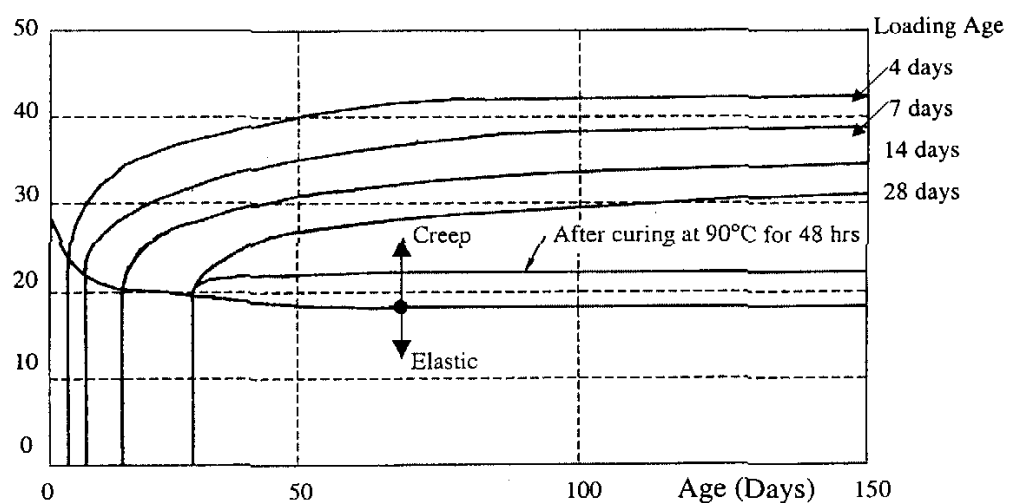


**Figure 2.11:** Creep plus elastic strain versus time (Behloul, 1999)

The guidelines propose the final creep coefficients as detailed in Table 2.5.

**Table 2.5:** Final Creep Coefficients for RPC (Gowripalan and Gilbert, 2000)

Time of first loading	Final creep coefficient, $\Phi^*$	
	Without steam curing	With steam curing for 48 hrs
4 days	1.8	0.5
28 days	1.2	0.3

## AUTOGENOUS SHRINKAGE

RPCs suffer an endogenous shrinkage strain of approximately 500 $\mu\epsilon$  due to higher cementitious content and the absence of coarse aggregates and the restraint that these aggregates provide to shrinkage of the paste. If steam curing is initially applied, almost all this shrinkage occurs during the curing process, with no shrinkage subsequently taking place. If steam curing is not

applied, shrinkage will take place over a longer period. As shrinkage in RPC is the result of chemical reactions and not through a process of drying (as in conventional concretes), almost all shrinkage occurs within the first 28 days. Figure 2.12 shows the shrinkage of specimens with or without heat treatment.

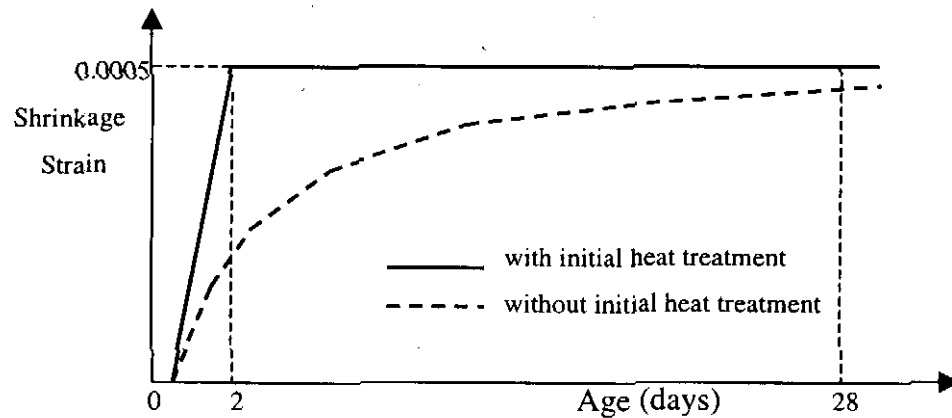


**Figure 2.12:** Shrinkage versus time (Gowripalan and Gilbert, 2000)

#### 2.5.1.2 Strength in flexure

Information on calculating the strength of both plain and prestressed RPC cross-sections in flexure is becoming available (Gowripalan and Gilbert, 2000). Typical stress and strain distributions at ultimate limit state for a singly reinforced cross-section are shown in Figure 2.13. It is proposed that for a prestressed section containing bonded tendons in the tensile zone, the extreme fibre compressive strain at ultimate limit state may be taken as  $\epsilon_{o,u} = 0.0035$ . This figure is slightly higher than what is used for conventional concrete in current Australia design codes but is similar to ultimate strain figures used in current UK and European design codes.

Typical stress and strain distributions at ultimate limit state for a cross-section containing no bonded reinforcement are shown in Figure 2.14. It is proposed that the ultimate bending strength of a plain section may be assumed to occur when the extreme fibre tensile strain equals  $\epsilon_{t,p}$  (as defined by Figure 2.10).

As with AS3600 – 1994, the design strength in bending is obtained by multiplying the ultimate strength  $M_u$  by a strength reduction factor,  $\Phi$ . It is proposed that  $\Phi = 0.8$ , when  $k_u \leq 0.4$ , for sections containing bonded

reinforcement or tendons. Where flexural strength is provided solely by the steel fibres i.e. a plain section,  $\Phi$  should be reduced to 0.7.

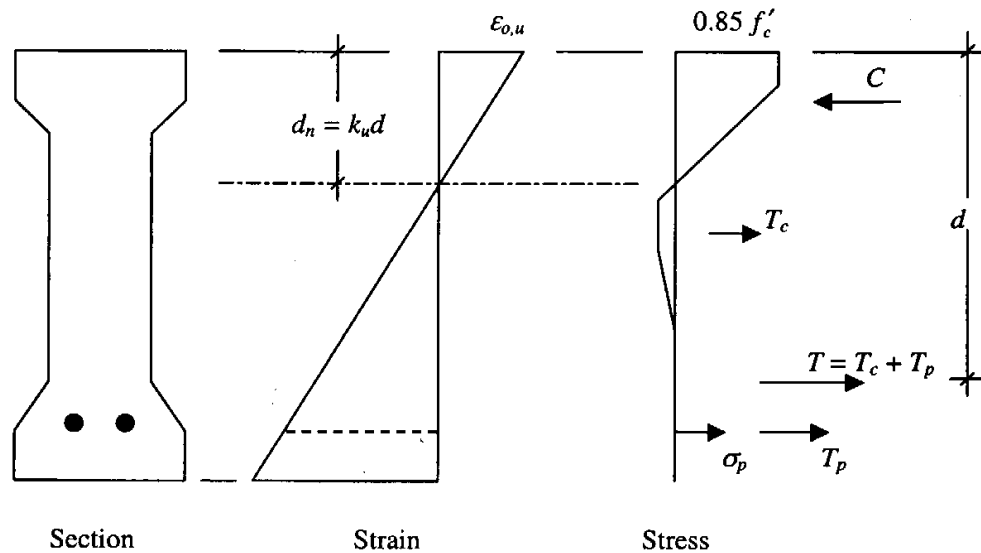


**Figure 2.13:** Stress and strain distribution at ultimate limit state for sections containing bonded reinforcement (Gowripalan and Gilbert, 2000)

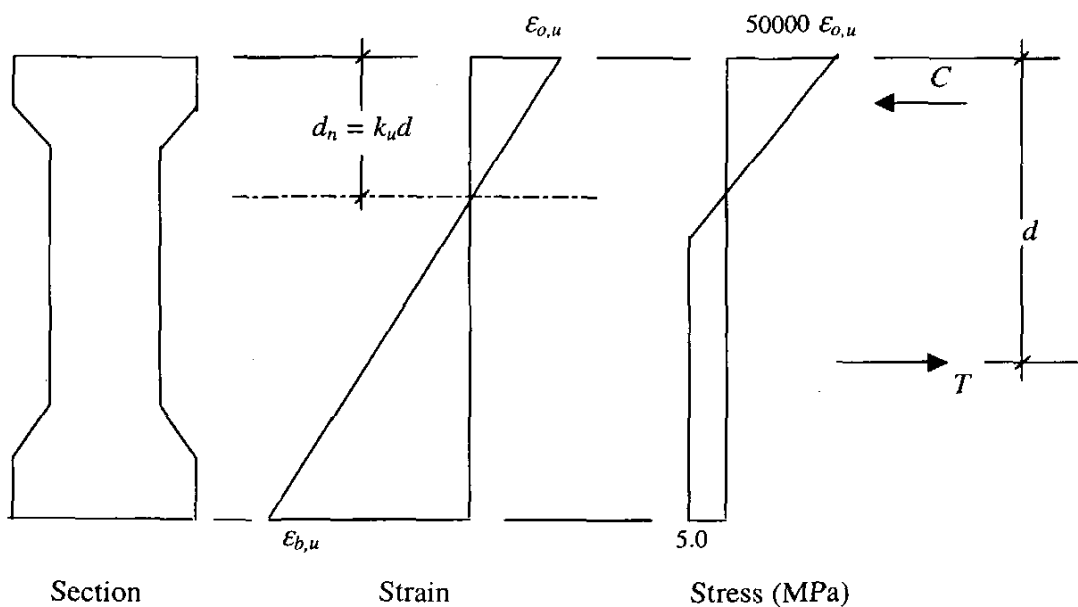


**Figure 2.14:** Stress and strain distribution at ultimate limit state for plain sections (Gowripalan and Gilbert, 2000)

### 2.5.1.3 Deflection at service loads

Section 9 of the guidelines provides information on calculating both the short and long term deflections of RPC beams.

For beams that remain uncracked under service load, the short-term deflection may be calculated assuming an elastic modulus of 50GPa and a second moment of area of the gross section about the centroidal axis. If cracking occurs under service loads, the instantaneous curvature,  $\kappa_i$ , at the cracked cross-section may be calculated assuming the stress distribution shown in Figure 2.15. The short-term deflection is then the result of integrating the curvature at selected cross-sections along the beam.

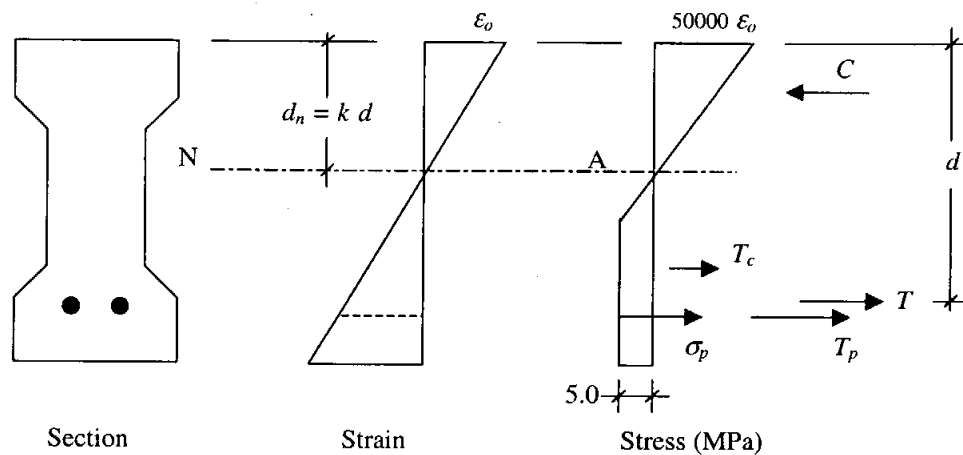


**Figure 2.15:** Stress and strain distribution on a cracked section (Gowripalan and Gilbert, 2000)

For long-term deflections, it is proposed that a reliable estimate may be obtained by integrating the final curvatures obtained from time analyses of the critical cross-sections, using a well-established age-adjusted effective modulus method (Gilbert, 1988).

Table 2.6 presents the proposed creep and shrinkage data for use in the long-term analyses:

**Table 2.6:** Creep and Shrinkage of RPC (from Gowripalan and Gilbert, 2000)

Initial Curing Condition	Coefficient		Shrinkage Strain ( $\mu\epsilon$ )	
	Final Creep	Ageing	Final	Autogenous
Without heat treatment	1.2 – 1.8	0.8	500	-
With heat treatment	0.3 – 0.5	0.8	100	500

### 2.5.2 Interim Recommendations – Ultra High Performance Fibre-Reinforced Concrete (2002)

The recommendations proposed by the Association Française de Génie Civil are intended to constitute a reference document for the use of RPC in civil engineering applications. The term Ultra High Performance Fibre-Reinforced Concrete (UHPFRC) refers to materials with a cement matrix and a characteristic compressive strength in excess of 150MPa, possibly attaining 250MPa, and containing steel fibres in order to achieve ductile behaviour under tension.

The recommendations contain three parts. The first part concerns the characterization of UHPFRC. The second part deals with the design and analysis of UHPFRC structures. It was drafted in accordance with the plan of Chapter 6 and 7 of the BPEL 91 design code (1991 edition of the Rules for Use of Prestressed Concrete at Ultimate Limit State revised in 1999) which it modifies and complements to integrate the participation of fibres and the existence of non-prestressed and/or non reinforced elements. The third part deals with the durability of UHPFRC and will not be discussed within the scope of this thesis.

Unlike the Australian Guidelines, the French Recommendations are not specific to a particular RPC formulation. The following section contains a brief summary of the recommendations.

### 2.5.2.1 Part 1: Behaviour and mechanical characteristics of UHPFRC

#### COMPRESSION

Compressive behaviour is defined by the characteristic compressive strength and the modulus of elasticity. For calculations regarding ultimate limit state (ULS) bending, a conventional linear constitutive law with a yield plateau will be used. The start of the yield plateau corresponds to a maximum stress of  $0.85f_{ck}/\theta_{\gamma_b}$ . A reduction factor of 0.85 and a safety factor of 1.3 are applied to the characteristic compressive strength  $f_{ck}$ . The factor  $\theta$  is dependent on the duration of the application of the load  $t$ . Figure 2.16 contains an example of the compressive constitutive law of a UHPFRC.

#### TENSION

The tensile behaviour of UHPFRC is characterized by an initial elastic stage limited by the tensile strength  $f_{ij}$  and a post-cracking stage characterized by the tensile strength of the composite material after the matrix has cracked. Figure 2.17 shows an example of the simplified tensile strength law of a UHPFRC.

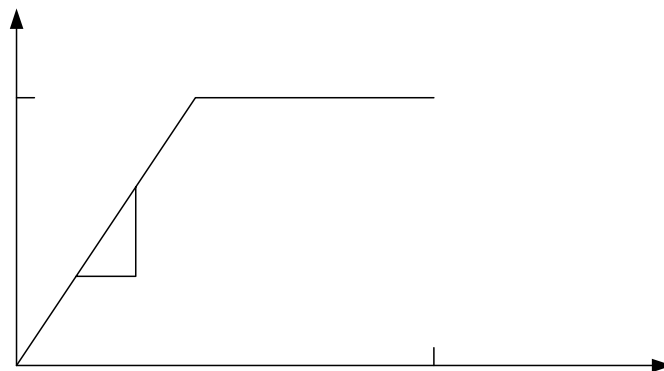


**Figure 2.16:** Compressive constitutive law for UHPFRC (AFGC, 2002)

#### STATIC MODULUS OF ELASTICITY and POISSON'S RATIO

Experimental data to date for UHPFRCs indicate that there is no usable simple formula for calculating the static modulus of elasticity based on compressive strength. Thus, it is recommended that the modulus of elasticity be determined experimentally. At a preliminary design stage, a value of 55GPa may be used.

For Poisson's ratio, a value of 0.2 may be considered if no other figure is determined experimentally.

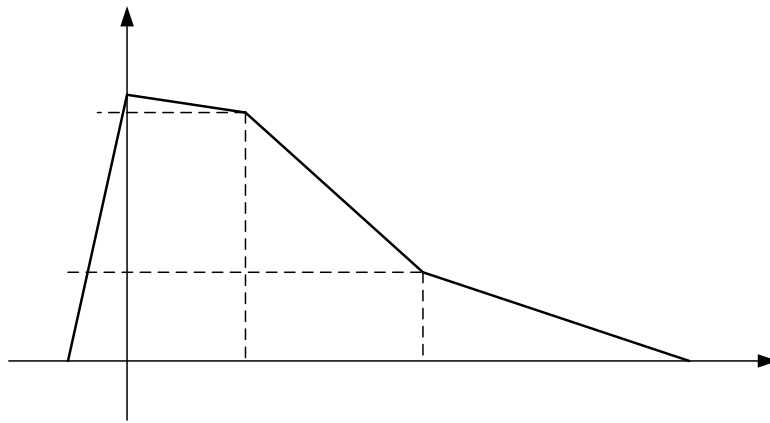


**Figure 2.17:** Simplified tensile constitutive law for UHPFRC (AFGC, 2002)

### CREEP-SHRINKAGE

UHPFRC shrinkage is mainly autogenous. When it is heat treated, UHPFRC has no further shrinkage. A guideline value of  $550\mu\text{m}$  can be considered if no other value is determined experimentally.

Heat treatment significantly reduces creep of UHPFRC. A guideline long-term creep coefficient,  $\Phi$ , of 0.8 can be considered if there is no heat treatment and 0.2 with heat treatment if no other value is determined experimentally.

For RPC, creep tests under high stress checked the long-term strength of the material under high sustained loads and gave reassurance regarding the 0.85 reduction factor on the compressive strength of the material.

#### 2.5.2.2 Part 2: Structural design methods

The analysis of standard sections is carried out with the following two fundamental assumptions:

- plane sections remain plane, and
- stresses in the uncracked part of the concrete are proportional to strains.

For calculations of uncracked prestressed sections, the following additional assumptions apply:

- the concrete withstands tensile stress, and
- the constituent materials are subject to no relative slippage, i.e. normal stresses due to all actions other than permanent actions can be calculated for the entire section made uniform using equivalence ratios  $n_i$

Elastic s

$\sigma$

$\sigma(1\%$

and  $n_v$ . (It is assumed that  $n_i = 4$  and  $n_v = 8$  without heat treatment and  $n_v = 5$  with heat treatment.)

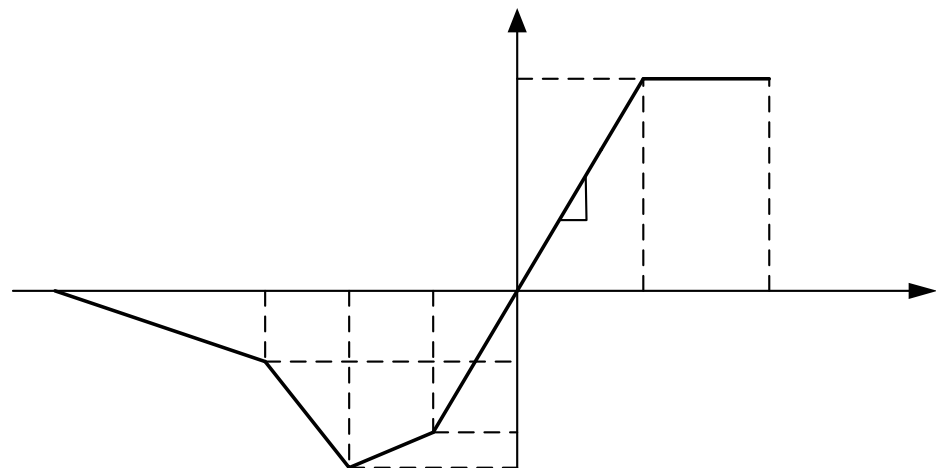
For calculations of cracked prestressed sections, the following additional assumptions apply:

- the constituent materials are subject to no relative slippage, and
- when the strain in the concrete is eliminated at a reinforcement bar, the tension in the reinforcement is;
  - 0 if it is passive reinforcement,
  - $\sigma_{pd} + n_i \sigma_{bpd}$  (with  $n_i = 4$ ) if it is prestressing reinforcement ( $\sigma_{bpd}$  representing the concrete stress at the reinforcement considered, under the effect of permanent actions and prestress assumed to be  $P_d$ ).
- the stress in passive reinforcement and the variation of overstress in the prestressing reinforcement which appears after decompression of the concrete are evaluated from the equivalence coefficient  $n_v = 8$  without heat treatment and  $n_v = 5$  with heat treatment.

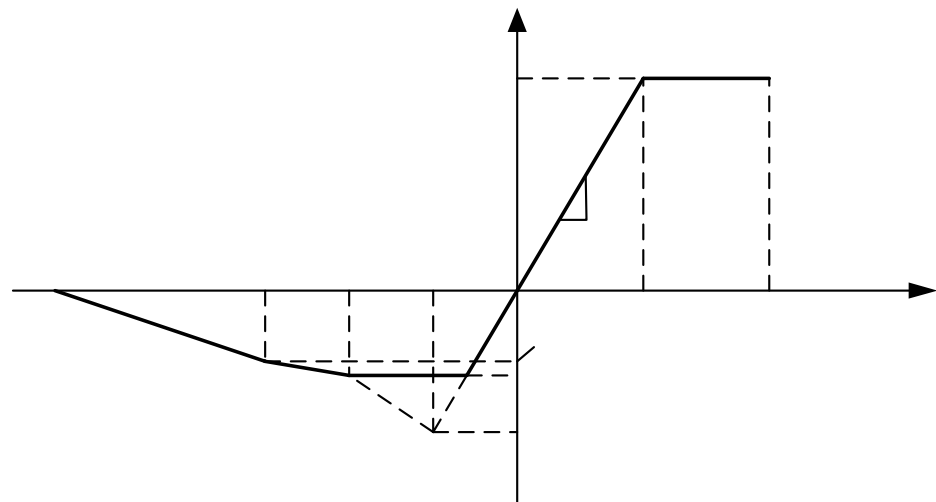
#### CALCULATION OF ULTIMATE BENDING MOMENT CAPACITY

The design assumptions are:

- the concrete, passive reinforcement and the pre-tensioned prestressing reinforcement are not subject to any relative slippage, and
- the stress-strain diagram for UHPFRC is as shown in Figure 2.18.



Strain harden



Limits:  $\epsilon_u = 3\%$  (0.003)

$$\epsilon_{u\ 0.3} = w_{0.3}/l_c + f_{tj}/\gamma_{bf}E_{ij} , \text{ with } w_{0.3} = 0.3\text{mm}$$

$$\epsilon_{u\ 1\%} = w_{1\%}/l_c + f_{tj}/\gamma_{bf}E_{ij} , \text{ with } w_{1\%} = 0.01H$$

$$\epsilon_{lim} = l_f/4l_c$$

$$\sigma_{bcu} = 0.85f_c/\theta\gamma_b$$

$$\sigma_{btu} = \sigma(w_{0.3})/K\gamma_{bf}$$

$$\sigma_{u\ 1\%} = \sigma(w_{1\%})/K\gamma_{bf}$$

where  $l_c$  is the characteristic length such that  $\epsilon = f_{tj}/E_{ij} + w/l_c$

$l_f$  is the fibre length

$H$  is the height of the bending test specimen

$K$  is the orientation or local effects coefficient

$\sigma(w)$  is the material's characteristic stress-crack width curve

$\epsilon_{lim}$

Figure 2.18: Stress-strain diagrams for UHPFRC (AFGC, 2002)

## **2.6 RESEARCH NEEDS FOR RPC AND RPC FLEXURAL MEMBERS**

RPC is a relatively new material and the first structure fabricated using RPC (beams in the Cattenom Nuclear Power Plant – France) is approximately 10 years of age. The research needs in regards to RPC can be categorized into two groups:

1. Material Properties
2. Analysis and design guidelines

The majority of research conducted to date has focused on the material properties of RPC. As such, the behaviour of the material is relatively well understood. The major deficiencies in this area concern the time-dependent material properties of shrinkage and creep. Whilst preliminary investigations into shrinkage have taken place, there have been few studies into the creep of RPC. These shortcomings can pose a problem with regards to predicting the time-dependent behaviour of RPC structures. Therefore, studies are needed to improve the understanding of these properties for RPC.

Limited studies have been conducted into the behaviour of plain and prestressed RPC beams. Additional studies are required to create a database for development of design equations. All structural aspects of this new material require further investigation. In particular, the following areas require further investigation.

### **2.6.1 Serviceability**

RPC exhibits compressive strengths approaching that of steel. However, its modulus of elasticity (40 – 65GPa) is approximately one-quarter the modulus of elasticity of steel (200GPa). Therefore, the aspects of serviceability (in particular, deflections) are more likely to govern the design of RPC structural members. Current design guidelines for predicting the deflections of concrete members need to be considered and modified as appropriate to predict the behaviour of RPC beams.

Due to the exceptional mechanical properties of RPC, RPC members can have quite slender components (particularly web elements). As a result, buckling may

become an issue and research into this area is also needed but is outside the scope of this study.

### **2.6.2 Short-term Flexural Behaviour**

The current design guidelines for predicting the short-term flexural behaviour of RPC beams have several deficiencies. Within the elastic range, where the material properties and how they relate to flexural behaviour are well understood, the current models give close agreement with experimental results. However, based on this research, the current design guidelines do not show good agreement in the post-cracking range. The predictions for ultimate strength, deflections at ultimate and post-peak behaviour in this study tend to vary widely from the theoretical predictions of the current models. Therefore, investigations into the short-term flexural behaviour of both plain and prestressed RPC beams are needed to address this situation.

### **2.6.3 Time-dependent Flexural Behaviour**

Little research has been carried out into the time-dependent flexural behaviour of plain and prestressed RPC beams. Studies need to be conducted in order to develop a database of information. At present, current models rely heavily on the standard models available for predicting the time-dependent deformations of conventional concrete members. The suitability of these standard models needs to be determined and modified as appropriate.

## **2.7 SUMMARY**

From the literature review presented above, it is clear that more research is needed to facilitate the increased use of RPC in structural applications. Primarily, the time-dependent behaviour of RPC structural members is the most important and urgently needed.

## **Chapter 3: Experimental Program**

### **3.1 INTRODUCTION**

The purpose of the experimental program conducted as part of this research was to investigate both the material properties and structural behaviour of a steel fibre reinforced reactive powder concrete (SF-RPC) produced from locally-sourced materials and based on a commercially available RPC mix design. Seven large-scale batches along with several smaller batches were completed. From these batches, a large number of material specimens along with 16 beam specimens were produced.

The material properties investigated included compressive strength, flexural strength and modulus of elasticity. These properties were investigated over a period of 365 days to determine their development with age. The time-dependent properties of creep and shrinkage were also examined. Various curing conditions were adopted to determine their effect on the material properties of SF-RPC.

The major objective of this experimental study was to investigate both the short-term and time-dependent behaviour of plain and prestressed SF-RPC beams. Three series of plain and prestressed beams were conducted. Beam series 1 and 2 involved the short-term ultimate moment capacity tests of 4 plain and 8 prestressed SF-RPC beams, respectively. The moment-curvature behaviour over the full range of loading and ultimate flexural strength of the beams was determined. Series 3 involved sustained load tests conducted on 4 prestressed SF-RPC slabs. As part of the sustained load tests, the time-dependent change in curvature was monitored.

This chapter contains details of the component materials, the final mix design and the batching procedures used for the production of the SF-RPC. The chapter also contains details pertaining to the production of the material specimens and the material properties tests undertaken. The final section of the chapter includes details of the beam construction and designations along with a

description of the loading arrangement and experimental techniques adopted for the beam tests.

## 3.2 SF-RPC PRODUCTION

The component materials and production techniques required to produce an SF-RPC differ from those required to produce conventional concrete. This section contains details of the materials used, the final mix design and the batching procedures used as part of the experimental program.

### 3.2.1 Materials

The granular components of the mix were sourced locally in the Sydney region. The selection of the granular materials was based on the method for optimising the granular mixture outlined in Section 2.2.2.1. The properties of the granular materials used in the present investigation are specified below:

➤ Cement

Type GP cement manufactured by Blue Circle Southern Cement was used. The cement has an approximate specific gravity of 3.15, a  $d_{50}$  (mean particle diameter) of  $11\mu\text{m}$  and a fineness of  $360\text{m}^2/\text{g}$ .

➤ Silica Fume

Undensified silica fume manufactured by SIMCOA was used. The silica fume has a specific gravity of 2.20, a  $d_{50}$  of approximately  $0.5\mu\text{m}$  and a fineness of  $19000\text{m}^2/\text{g}$ .

➤ Sydney Sand

Sydney sand has a specific gravity of 2.65 and a  $d_{50}$  of approximately  $320\mu\text{m}$ . For quality control, all particles greater than  $800\mu\text{m}$  were removed and the sand was oven dried at  $105^\circ\text{C}$  for a period of 48 hours before being used. A typical grading curve for this sand is shown in Figure 3.1.

➤ Silica Flour

Silica flour was used as a crushed quartz replacement as there is no readily available source of crushed quartz within the local Sydney market. The silica flour used was Grade 200 Silica manufactured by UNIMIN. It has a specific gravity of 2.60, a maximum particle size of  $75\mu\text{m}$  and a  $d_{50}$  of

approximately 15 $\mu$ m. A typical grading curve (supplied by the manufacturer) is presented in Figure 3.2.

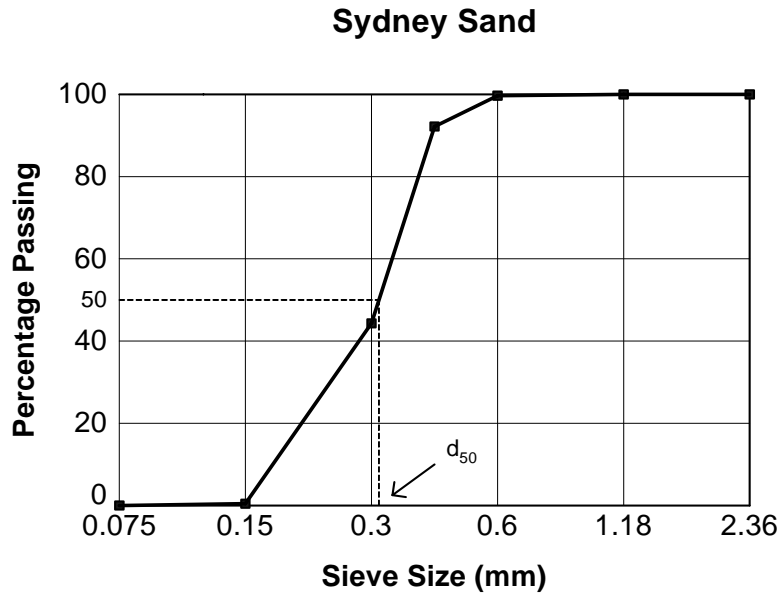


**Figure 3.1:** Grading curve for Sydney Sand

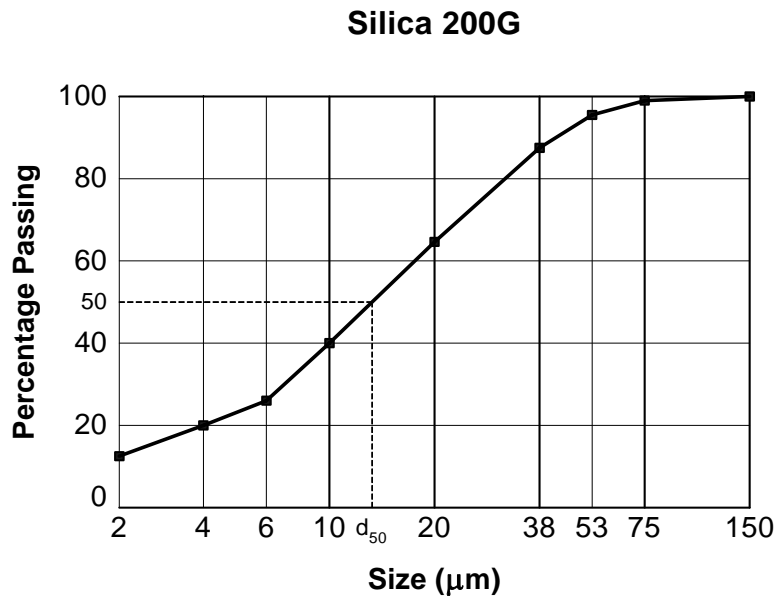


**Figure 3.2:** Grading curve for Silica 200G (from UNIMIN)

Steel fibres manufactured by Bekaert were used. They were imported from Belgium as there are no locally produced, small diameter, short, straight steel fibres. The fibres are 0.2mm in diameter with a length of 13mm giving them an aspect ratio (length/diameter) of 65. The fibre dosage adopted corresponds to approximately 2% by volume

The superplasticizer used was a modified Carboxylic ether manufactured and supplied by MBT under the commercial name Glenium 51.

### 3.2.2 Mix Design

The final mix design adopted is shown in Table 3.1. It is based on a commercially available RPC mix design similar to that found in Table 2.3. The proportions given in Table 3.1 are “batch quantities” representing the actual amount of each material as added, i.e. oven-dried sand, and represent a concrete volume of approximately 1m<sup>3</sup>. Unlike the batching of conventional concrete, the aggregates (sand and silica flour) were not in a saturated surface dry condition before being added to the mix. Completely dry aggregates were required to enable the use of pre-blended bags for large-scale batches. Therefore for quality control, dry aggregates were adopted for small-scale batches as well. The “batch” water/cement ratio (w/c) and water/binder ratio (w/b) are 0.22 – 0.24 and 0.17 – 0.19, respectively.

**Table 3.1:** Mix Design

<u>Component</u>	<u>Mass</u> (kg/m <sup>3</sup> )
Cement	700
Silica Fume	210
Sand	1000
Silica Flour	210
Fibres	160
Water	154 – 168 L
Superplasticizer	40 L

### 3.2.3 Mixing Procedure

#### 3.2.3.1 Small-scale batches

Batches less than 0.1m<sup>3</sup> in volume were mixed in a 50-litre capacity pan mixer. After all materials were measured, the initial step in the mixing process was to pre-blend the granular components for a duration of 3 – 5 minutes. Once homogeneity of the granular mixture was achieved, the water and superplasticizer were added in a single dose. Mixing durations between 8 – 10

minutes were required to achieve a fluid (plastic) mix. The final step was the addition of fibres. Fibres were added in a “sprinkling” motion and mixing continued for a further 5 – 8 minutes to ensure even fibre distribution.

### 3.2.3.2 Large-scale batches

Seven large-scale batches, in excess of 0.5m<sup>3</sup> each, were cast using a special 1.5m<sup>3</sup> capacity shear mixer. Figure 3.3 shows the shear mixer used. From each large-scale batch, a minimum of two 3m beams were cast along with a large number of accompanying material specimens. Given the volumes required for a large-scale batch, it was deemed necessary to have the granular materials pre-blended separately and supplied in bulk bags of 500kg. As mentioned, it was for this reason that the mix design volumes are given in “batch quantities”. The presence of water in the aggregates (sand and silica flour) in the pre-blended bags could start the hydration process of the cementitious materials (cement and silica fume). The procedure used for a large-scale batch is presented in Table 3.2.



**Figure 3.3:** Shear mixer

**Table 3.2:** Large-scale Batch Mixing Procedure

<u>Process</u>	<u>Mix Speed</u> (rpm)	<u>Duration</u> (minutes)
1. Bulk bags loaded	-	-
2. Pre-mix of granular materials	1800	8
3. Water + half superplasticizer added	1800	3
4. Remaining superplasticizer added	1800	5
5. Fibres added	1600	9
6. De-gassing	750	3
7. Discharge	-	-

### 3.3 MATERIAL PROPERTIES TESTS

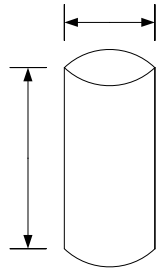
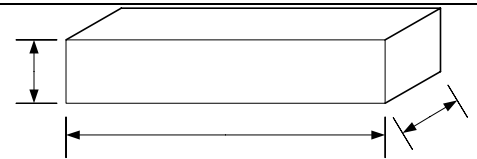
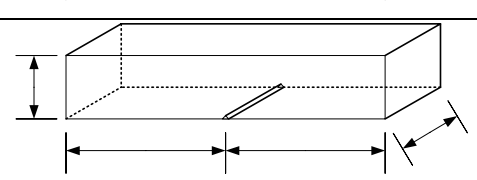
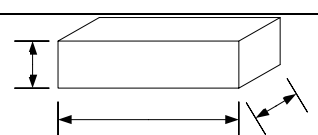
#### 3.3.1 Specimen Preparation

All material specimens were cast in accordance with AS 1012.8.1 – 2000 with vibration being applied by means of an external vibrating table. Cylindrical specimens for compressive strength, modulus of elasticity and creep tests were cast in two layers in steel moulds with a diameter of 100mm and a height of 200mm. Prismatic specimens for modulus of rupture tests were cast in a single layer in 100 x 100 x 500mm steel moulds. Notched prismatic specimens for crack mouth opening (CMO) tests were cast in a single layer in a 100 x 100 x 500mm wooden mould with a 5mm triangular wedge centrally located on the left hand vertical edge to provide the notch. Prismatic specimens for shrinkage tests were cast in a single layer in 75 x 75 x 285mm steel moulds. The shrinkage moulds satisfied the criteria specified by AS 1012.13 – 1992.

Table 3.3 contains a summary of the material specimens used. Details of the various material properties tests are given in Section 3.3.3.

After casting, the specimens were covered with a plastic sheet to minimise any moisture loss. All mixing and casting was carried out under standard laboratory conditions at  $23 \pm 2^\circ\text{C}$  and  $50 \pm 5\%$  relative humidity (RH). The specimens were demoulded within  $24 \pm 2$  hours from the completion of casting.

**Table 3.3: Material Specimens**

<u>Specimen</u>	<u>Test</u>	
Cylindrical	Compression Modulus of Elasticity Creep	
Flexural Prism	Modulus of Rupture	
CMO Prism	CMO	
Shrinkage Prism	Shrinkage	

### 3.3.2 Curing

Three separate curing conditions were investigated. Details are as follows:

➤ Curing Condition 1 (SC – Standard Cure)

After demoulding, specimens were placed in an environmental control room set at  $23 \pm 2^\circ\text{C}$  and  $100 \pm 5\%$  RH until time of testing.

➤ Curing Condition 2 (HT – Hot Water Cure)

After demoulding, specimens were placed in a large hot water bath for a period of 5 days. The volume of the water bath is approximately  $8\text{m}^3$ . Due to a variable power supply, it was not possible to maintain the temperature in this hot water bath at a constant  $90^\circ\text{C}$ . Power was supplied to the bath for a period of 12 hours from 6pm each night. The temperature gradient for this water bath is  $7^\circ\text{C}/\text{hour}$ . The water in the bath reached a maximum temperature of  $80^\circ\text{C}$ . The temperature dropped to  $50 - 55^\circ\text{C}$  during the day. Upon removal from the water bath, specimens were stored in the laboratory until the time of testing.

➤ Curing Condition 3 (CHT – Comparative Hot Water Cure)

After demoulding, the specimens were placed in a small hot water bath for a period of 48 hours. The volume of the water bath is approximately 0.5m<sup>3</sup>. The temperature gradient for this water bath is 12°C/hour. Once a temperature of 90°C has been reached, the water bath maintains this temperature at 90 ± 4°C for the duration of the curing due to constant power supply. Upon removal from the water bath, specimens were stored in the laboratory until time of testing.

### 3.3.3 Test Procedures

#### 3.3.3.1 Surface preparation of material specimens for testing

To provide a smooth surface for testing of cylindrical specimens, it was necessary to either cap or grind the unfinished end of the cylinders. As SF-RPC specimens, with the exception of those tested at an early age without heat treatment, have compressive strengths in excess of 100MPa, sulphur capping was unsuitable for the end preparation of the majority of cylinders. According to AS 1012.9 – 1999, molten sulphur as a capping material should only be used on samples with compressive strengths up to 80 MPa. Therefore, sulphur capping was used only on specimens that had undergone standard curing conditions and were less than an age of 7 days. All remaining cylinders had the unfinished end ground to produce a smooth surface for testing.

Flexural prism specimens were tested at 90 degrees to the as cast position to provide a smooth testing surface.

#### 3.3.3.2 Test machine

An INSTRON 3000kN test machine with stiff loading platens was used to conduct the materials testing for compressive and flexural strength along with modulus of elasticity.



**Figure 3.4:** INSTRON test machine

#### 3.3.3.3 Compressive strength

Cylindrical specimens for compressive strength tests were tested at a rate of 20MPa/min in accordance with AS 1012.9 – 1999. Specimens from Batch 1 were tested at various ages to determine the strength development of SF-RPC. The 28-day compressive strength for all other batches was also determined.

#### 3.3.3.4 Flexural strength

Prismatic specimens for flexural strength tests were tested under 4-point bending at a rate of 1.1MPa/min (extreme fibre tensile stress) in accordance with AS 1012.11 – 2000. A Linear Variable Displacement Transducer (LVDT) was used to measure the deflection at midspan. The deflection was taken as the movement of the loading jack. Specimens from Batch 2 were tested at various ages to determine the flexural strength development of SF-RPC. The 28-day flexural strength of all other batches was also determined.

### 3.3.3.5 Crack Mouth Opening

Notched prismatic specimens for CMO tests were tested under 3-pt bending at a CMO displacement rate of 2.5mm/min. An LVDT was used to monitor the crack width. The specimens were from Batch 1 and tested at an age of 28 days.

### 3.3.3.6 Modulus of Elasticity

Cylindrical specimens for static chord modulus of elasticity tests were tested at 15 MPa/min to a stress of approximately 40% of the compressive strength in accordance with AS 1012.17 - 1997. The axial strain was measured by an averaging transducer. This transducer consists of two LVDTs located on diametrically opposite sides of the specimen. The strain measurement is the average of the two readings. Specimens from Batch 3 were tested at various ages to monitor the elastic modulus of SF-RPC with age. The 28-day static chord modulus of elasticity was determined for all other batches.

### 3.3.3.7 Stress-strain behaviour in compression

Cylindrical specimens were tested to determine the stress-strain behaviour of SF-RPC in compression. The axial strain and circumferential strain were measured by an averaging transducer and a circumferential LVDT respectively. The test was run under displacement control taken as the movement of the ram of the test machine. The ascending displacement rate was 0.2mm/min. The rate was reduced to 0.005mm/min near peak to avoid sudden failure of the test specimen.

### 3.3.3.8 Shrinkage

Prismatic shrinkage specimens from batches 4 and 7 were used to monitor the shrinkage of SF-RPC. Three shrinkage series were conducted:

1. Standard Shrinkage

Specimens were cured and tested in accordance with AS1012.13 – 1992. Initial readings were taken at an age of 7 days.

2. Hot water curing Shrinkage

Initial measurements were taken at an age of 1 day immediately after specimens were demoulded. The specimens were then cured in accordance with Curing Condition 2. At the completion of hot water

curing, the specimens were stored in the drying room ( $23\pm 2^{\circ}\text{C}$ ,  $50\pm 5\%$  RH) throughout the duration of testing.

### 3. Autogenous Shrinkage

Initial measurements were taken at an age of 1 day immediately after the specimens were demoulded. The specimens were then stored in a water tank at  $23\pm 2^{\circ}\text{C}$  throughout the duration of testing.

All measurements were carried out in a vertical comparator with a resolution of 0.002mm which corresponds to a resolution of  $8\mu\epsilon$  for the specimens used.

#### 3.3.3.9 Creep

Cylindrical specimens from batch 4 and 7 were placed in creep rigs and monitored throughout the duration of the corresponding sustained load beam tests. The creep rig consisted of a floating steel plate attached to a hydraulic ram (fitted with a pressure transducer) and connected by macalloy bars to a fixed steel top plate. The pressure transducer controlled the stress at  $\pm 2\%$  of the initial applied load. The creep rig is shown in Figure 3.5.

The specimens were loaded at an age of 28 days to a sustained stress of approximately 40% of the concrete strength. The strains on both the loaded and control specimens were measured using a demec strain gauge with a resolution of  $16.2\mu\epsilon$ . Standard curing (Curing Condition 1) and hot water curing (Curing Condition 2) specimens were tested. All creep tests were carried out in accordance with AS1012.16 – 1996.

### 3.3.4 Test results

The results of the material properties tests conducted are presented and discussed in Chapter 4 and were also used in the analyses of the beams.

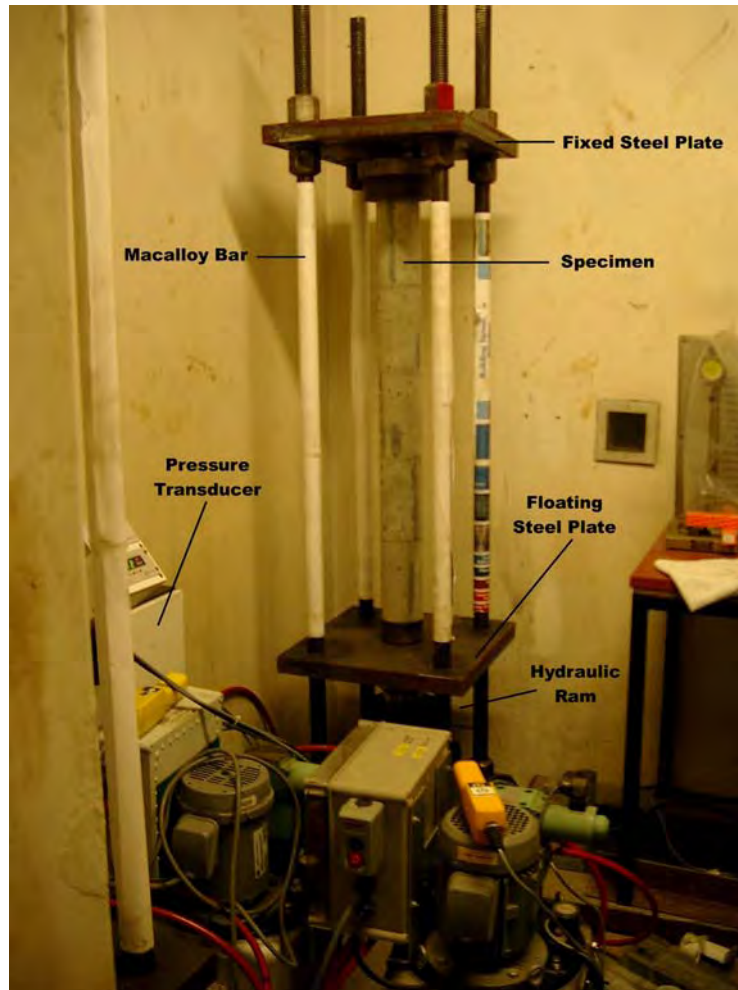


Figure 3.5: Creep rig

### 3.4 BEAM TESTS

As part of this experimental program, 3 series of beam tests were conducted. This section contains details of the beam construction, designation, loading arrangements and monitoring procedures.

#### 3.4.1 Beam Construction

##### 3.4.1.1 Plain beams

Four plain beams were cast as part of Series 1. Steel moulds of the required cross-sections were constructed for the casting of these beams. The concrete was placed in the moulds via a suspended hopper and sleeve arrangement that was steadily moved from one end of the mould to the other as the concrete was poured. Steel moulds as opposed to moulds constructed from formwork were required to enable the use of external vibrators. External vibration was applied

as the moulds were being filled and for a minimum period of 15 minutes after completion. The beams were then covered with wet hessian and plastic sheets to prevent any moisture loss. The beams were demoulded after 2 days and underwent hot water curing in accordance with Curing Condition 2 (see Section 3.3.2). Upon removal from the hot water bath, all beams were stored in the laboratory until time of testing.

#### *3.4.1.2 Prestressed beams*

Eight prestressed beams and 4 prestressed slabs were cast as part of Series 2 and 3, respectively. The members were constructed in an 8m long prestressing bed using steel moulds. A load cell was used to monitor the force in each tendon during jacking. Figure 3.6 shows the prestressing bed and construction procedure. As with the plain beams, a suspended hopper and sleeve arrangement was used to pour the concrete and vibration was applied by means of external vibrators clamped to the side of the moulds. External vibration was applied during filling and for a minimum period of 15 minutes after completion. The beams were then covered with wet hessian and plastic sheets to prevent moisture loss. The beams were demoulded after 2 days. Transfer of prestress occurred at an age of either 2 or 3 days depending on the size of the prestressing force. The prestressing force was transferred to the concrete by cutting the tendons at one end. After transfer of prestress had occurred, the beams underwent hot water curing in accordance with Curing Condition 2. Upon removal from the hot water bath, all beams were stored in the laboratory until time of testing.

### **3.4.2 Beam Details**

#### *3.4.2.1 Beam Series 1*

Four 3m long plain beams of 2 differing cross-sections were cast as part of this series. The beams were tested for ultimate moment capacity (UMC) at an age of 26 – 30 days. Figure 3.7 contains details of the 2 cross-sections and Table 3.3 lists the beam designations and details.



**Figure 3.6:** Prestressed beam construction

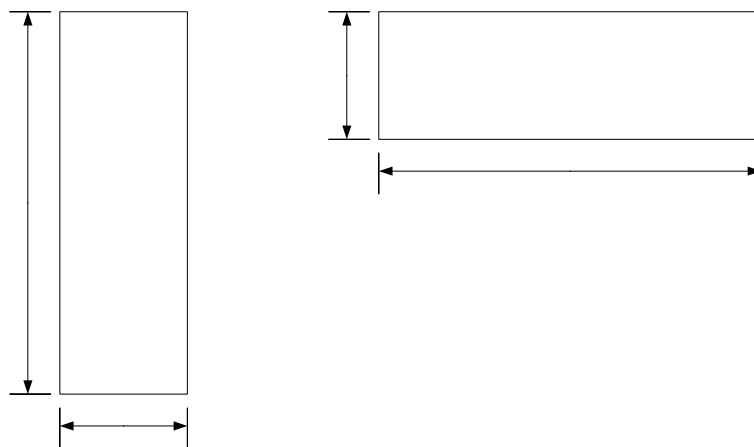


**Figure 3.7:** Cross-sections for beam series 1

**Table 3.4:** Designations for Beam Series 1

Beam	No. of Beams cast	Beam Designations	Batch Number	Test Type
1	2	P1 A P1 B	2	UMC
2	2	P2 A P2 B	1	UMC

#### 3.4.2.2 Beam Series 2

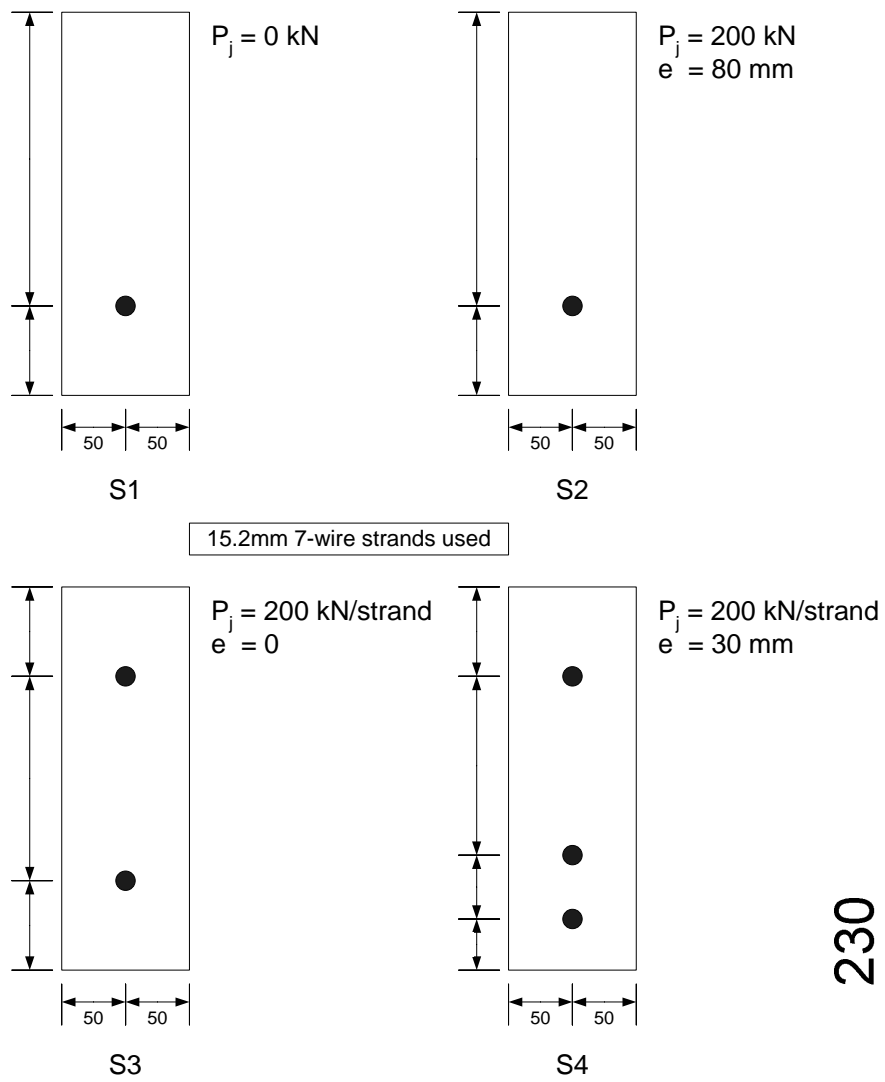
Eight 3m long prestressed beams of 4 differing cross-sections were cast as part of this series. The beams were tested for ultimate moment capacity at an age of 26 – 30 days. Figure 3.8 contains details of the 4 cross-sections and Table 3.5 lists the beam designations and details.

**Table 3.5:** Designations for Beam Series 2

Beam	No. of Beams cast	Beam Designations	Batch Number	Test Type
1	2	S1 A S1 B	5	UMC
2	2	S2 A S2 B	5	UMC
3	2	S3 A S3 B	6	UMC
4	2	S4 A S4 B	6	UMC

#### 3.4.2.3 Beam Series 3

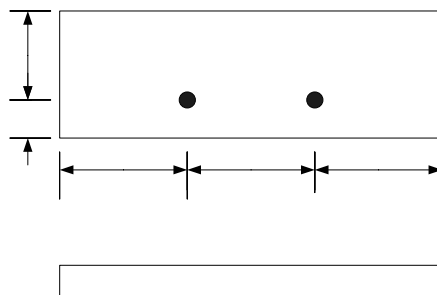
Four identical 3m long prestressed slabs were cast as part of this series. The first beam was tested for ultimate moment capacity at an age of 26 days to determine the cracking load and ultimate moment capacity of the cross-section. The remaining 3 beams underwent sustained loading commencing at an age of 28 days. Figure 3.9 contains details of the cross-section and Table 3.6 lists the beam designations and details. As the beams sustained a load greater than the cracking load  $P_{cr}$ , all beams displayed visible cracks from the commencement of the sustained load tests.



230

(Dimensions in millimetres)

**Figure 3.8:** Cross-sections for beam series 2



70

**Figure 3.9:** Cross-section for beam series 3

**Table 3.6:** Designations for Beam Series 3

No.	No. of Beams cast	Beam Designations	Load	Batch Number	Test Type
1	4	S5 A		7	UMC
		S5 B	$1.2P_{cr}$		SL
		S5 C	$1.4P_{cr}$		SL
		S5 D	$1.8P_{cr}$		SL

### 3.4.3 Beam Testing

#### 3.4.3.1 Loading arrangement

All beams were simply supported over a span of 2.7m and loaded with 2 equal point loads applied at one-third span. Figure 3.10 contains an illustration of the loading arrangement and corresponding bending moment. For ultimate moment capacity tests (Beam series 1 and 2), the load was applied via a hydraulic ram as can be seen in Figure 3.11. The beams in Series 1 were tested under displacement control from the deflection at mid-span. Section P1 and P2 were tested at loading rates of 0.2 and 0.4mm per minute. The beams in Series 2 were tested under load control. The loading rate for section S1 was 0.36mm per minute and 0.6mm per minute for the remaining beams in Series 2. The difference in test procedure between the plain and prestressed SF-RPC beams was to ensure that the post-peak behaviour of the plain beams in Series 1 could be captured.

For the time-dependent tests (Series 3), the sustained loads were applied through dead load blocks. Figure 3.12 shows the dead load arrangement for slab S5 B tested as part of Beam Series 3. The sustained load level remained constant throughout the duration of the test.

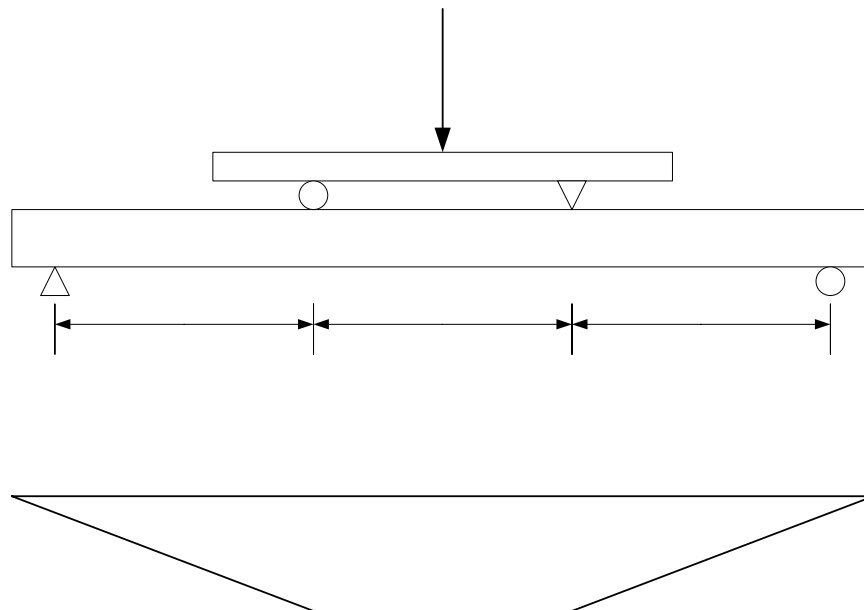


**Figure 3.10:** Loading arrangement and moment diagram



**Figure 3.11:** Test set-up for ultimate moment capacity tests

(Dimen



**Figure 3.12:** Sustained loading arrangement

#### 3.4.3.2 Measurements

The following data was collected for each beam specimen during the ultimate moment capacity tests conducted as part of Beam Series 1 and 2. LVDTs were located at the midspan and under the load points to electronically measure the deflections of the beam. Figure 3.13 shows the arrangement of the LVDTs. At various load levels during the ascending portion of the load-deflection curve, surface strain measurements using a demec gauge were taken throughout the constant moment region. The demec gauge had a gauge length of 250mm and a resolution of  $6.3\mu\epsilon$  per division. Figure 3.14 shows the arrangement of the demec targets. The demec targets were equally spaced around the centre line of the beam. For beams with a depth of 300mm (Sections P1, S1 – S4), the targets were located along horizontal lines at a depth of 10mm, 150mm and

290mm. For beams with a depth of 100mm (Sections P2 and S5), the targets were located along horizontal lines at a depth of 10mm and 90mm.

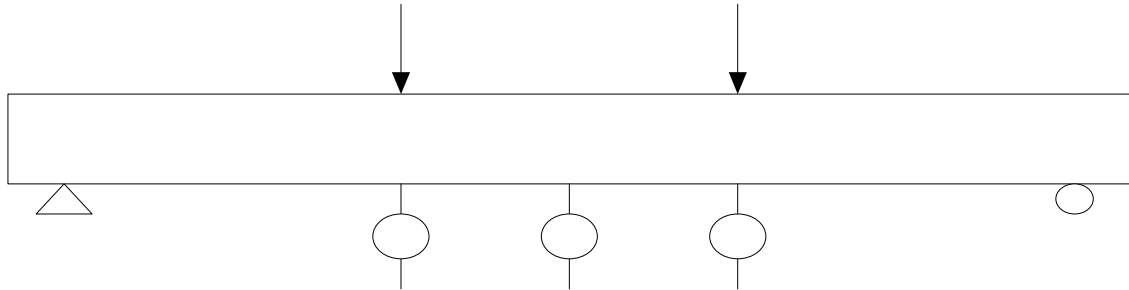


**Figure 3.13:** LVDT arrangement

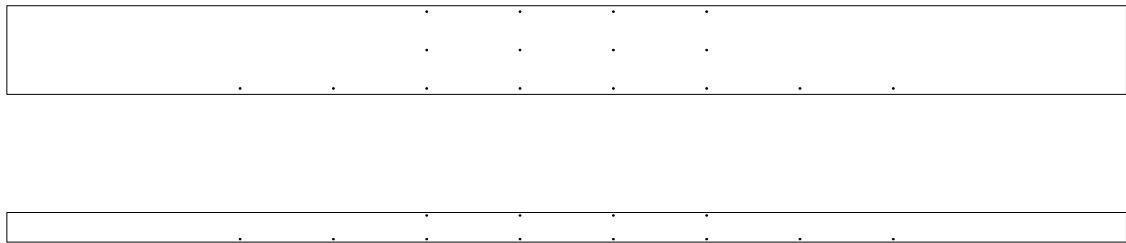


**Figure 3.14:** Demec target arrangement

In addition to this, once cracks were visible on the surface of the member, the cracks were marked and digital images were taken of the crack pattern. The surface of the beam specimens was painted in white acrylic paint in order to facilitate the detection of cracks and to provide clear crack markings for the digital photos. No attempt was made to implement digital imaging technology in the analysis of the crack patterns.

For the sustained load tests (Beam Series 3), the deflections at midspan and under the load points was monitored using dial gauges. The arrangement of the dial gauges was identical to the arrangement of the LVDTs during the ultimate moment capacity tests (see Figure 3.13). Digital images were also taken during the test period to monitor the crack patterns of the slabs under sustained load.

#### 3.4.4 Results

The results of the flexural strength tests on both the plain and prestress beams (Series 1 and 2, respectively) are discussed in Chapter 5. The results of the time-dependent slab tests (Series 3) are discussed in Chapter 6.

## **Chapter 4: Material Properties**

### **4.1 INTRODUCTION**

In order to predict the flexural behaviour of SF-RPC structural members, it is necessary to know and understand the properties of the material. Therefore as part of this research, a detailed investigation into the material properties of SF-RPC was conducted. The results of this investigation are presented and discussed in this chapter.

The material properties investigated include compressive strength, flexural strength and modulus of elasticity. The 28-day mean and characteristic value of these properties was determined as well as their development over a period of 365 days. The stress-strain behaviour in compression and the load-deflection behaviour in flexure were also determined. These properties were used in the prediction of the short-term flexural behaviour of plain and prestressed SF-RPC beams.

The time-dependent material properties of creep and shrinkage were also investigated. The deformation of SF-RPC is both instantaneous and time-dependent. The time-dependent deformations occur as a result of creep and shrinkage. Therefore, knowledge of the magnitude and the rate of development of these properties is necessary in order to predict the time-dependent flexural behaviour of plain and prestressed SF-RPC beams.

As discussed in Section 2.2.3, the application of heat treatment has an effect on the material properties of RPC. Therefore, various curing conditions were adopted in order to determine the effect that heat treatment has on both the short-term and time-dependent material properties of the SF-RPC studied.

### **4.2 COMPRESSIVE STRENGTH**

#### **4.2.1 Characteristic Compressive Strength**

The mean 28-day compressive strength ( $f_m$ ) for all large-scale batches was determined and the results along with the standard deviation (sd) and coefficient of variation (COV) are shown in Table 4.1.

**Table 4.1:** Compressive Strength Results

Batch	w/c	$f_m$ (MPa)	sd (MPa)	COV (%)
1	0.220	140.0	2.75	1.96
2	0.239	160.9	3.32	2.06
3	0.230	160.5	3.49	2.17
4	0.230	163.7	9.69	4.09
5	0.234	169.1	7.65	4.52
6	0.234	176.7	4.93	2.79
7	0.234	164.5	5.96	3.62

The w/c ratios given in Table 4.1 correspond to the amount of water to cement used in the mixing process. This does not account for any water being absorbed by the dry sand. No attempt was made to quantify this loss. Thus, actual w/c ratios will be slightly lower than those given.

Despite Batch 1 having a lower w/c ratio than all other batches, lower strength values were obtained. This lower strength can be attributed to poor compaction of the specimens. The vibration table used to compact the specimens was malfunctioning during the casting of Batch 1 and together with the fact that the mix was dry resulted in poorly compacted specimens and hence, lower strength values.

The compressive strength values are lower than those reported elsewhere (Bonneau et al., 1997 and Cheyrezy, 1999). This can be attributed to a number of key factors. As mentioned in Section 2.2.3, the dry granular mix was pre-packed and supplied in 500kg bulk bags making quality control with regards to w/b ratios difficult as the amount of cementitious materials in each batch was assumed to be identical. In addition to this, one of the key ingredients used overseas (crushed quartz) is not readily available in Australia. The closest alternative to crushed quartz available in Australia is Silica Flour, which has a higher water demand. As a result, slightly higher w/c ratios were required to facilitate proper mixing. In addition to this, the silica flour has a larger mean particle diameter than the crushed quartz and therefore does not lead to the same level of packing being achieved when

used as a replacement. These factors together result in the lower strength values obtained.

For this SF-RPC, the mean 28-day compressive strength is 167.0MPa with a standard deviation of 8.4MPa and a coefficient of variation of 5%. A 28-day characteristic compressive strength ( $f'_c$ ) of 153MPa was calculated using Equation 4.1 for a 5% confidence level. Batch 1 results were excluded for the reason stated previously.

$$f'_c = f_m - 1.64sd \quad (4.1)$$

#### 4.2.2 Compressive Strength Development

The compressive strength development of SF-RPC was monitored over a period of 365 days. Specimens for compressive strength development were taken from Batch 1 and the results are presented in Figure 4.1. For clarity, these results are also presented in Table A.1. As can be seen from the figure, as with conventional concretes, the strength of SF-RPC cured under standard conditions continues to increase with time. It can also be seen that there is an initial rapid strength gain (in the first 3 days) followed by a much slower, gradually decreasing rate of strength gain.

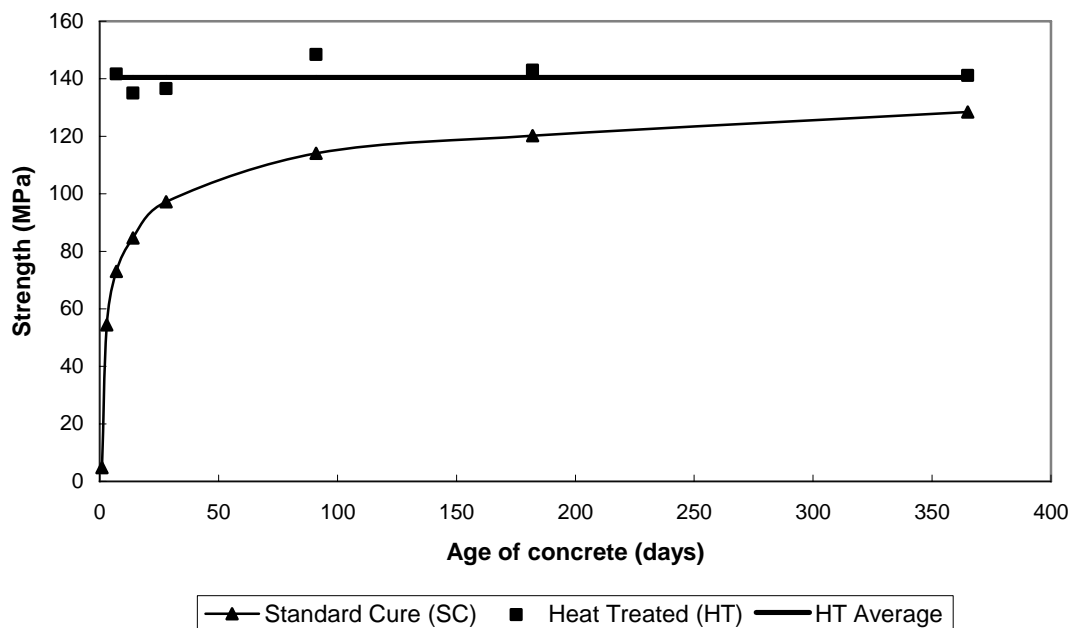


**Figure 4.1:** Compressive strength development with age (Batch 1)

The beneficial effects of heat treatment discussed in Section 2.2.3 can also be seen in Figure 4.1. Specimens that have undergone hot water curing have reached their maximum strength at the completion of the curing period (curing was provided for a period of no less than 48 hours). The long-term strength of specimens that have undergone standard curing conditions is expected to reach 90 – 95% of the strength of hot water cured specimens.

ACI 209 (1992) recommends the following expression for predicting the strength at any time from a measured 28-day value for normal and high strength concrete containing ordinary Portland cement and cured under standard conditions ( $23\pm 2^{\circ}\text{C}$ ,  $100\pm 5\%$  RH);

$$f_c(t) = \frac{t}{4.0 + 0.85t} f_c \quad (4.2)$$

where  $f_c(t)$  is the strength of the concrete at age  $t$  in days,  
 $f_c$  is the concrete strength at 28 days.

Figure 4.2 shows the comparison between the strength development predicted by Equation 4.2 and the actual strength values obtained. It can be seen that the experimental results are comparable to the ACI equation in the range of 0 – 28 days. It should be noted that the 3- and 7-day predictions are slightly lower than the actual strength results. This is because of the effect of w/c ratio on strength development. Concrete mixes with a lower w/c ratio (i.e. RPC mixes) will gain strength more rapidly than mixes with higher w/c ratios (conventional concretes) as the cement grains are closer together and a continuous system of gel is established more rapidly (Neville, 1995).

However, the ACI equation fails to predict the strength gains occurring after 28 days. Due to the low w/c ratios of a typical RPC mix, there is a greater proportion of unhydrated cementitious material in the hardened cement paste than there is for conventional concretes. Since the strength of concrete increases with the progress of hydration of cement (Neville 1995), it is expected that standard cured RPCs will continue to display strength gains for a greater period of time than conventional concretes as the remaining unhydrated cementitious material continues to hydrate with time.

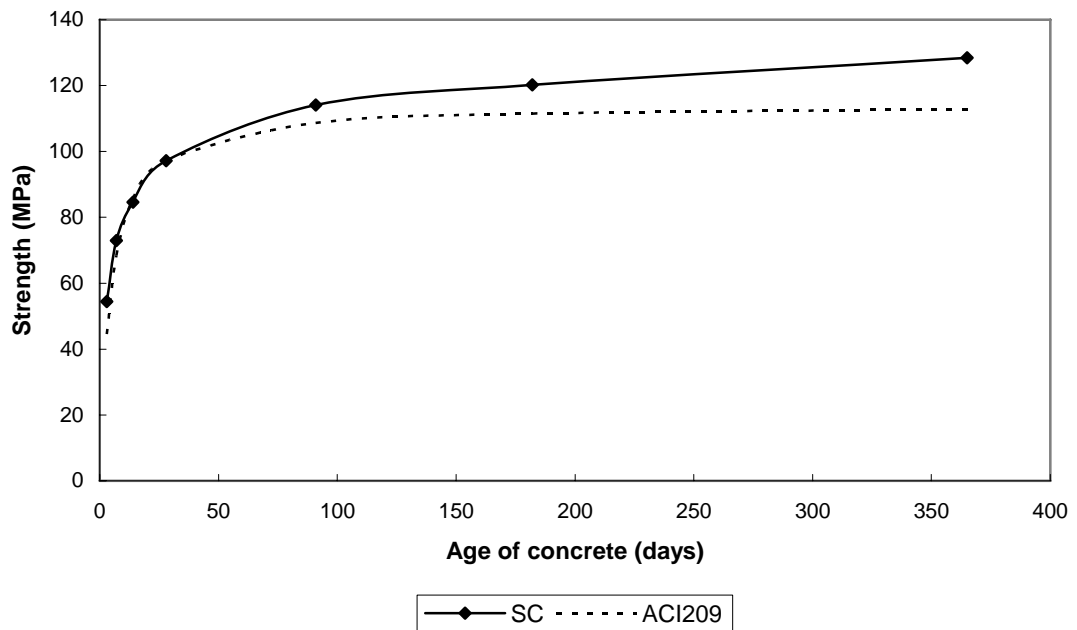


**Figure 4.2:** Compressive strength predictions

From the experimental results for strength development from this research, it is unreasonable to present an equation for the prediction of the strength of an SF-RPC for a given age. The long-term compressive strength of an SF-RPC cured under standard conditions may be conservatively taken as 90% of the compressive strength of specimens that have undergone heat treatment.

#### 4.2.3 Heat Treatment Regime

Figure 4.3 shows the comparison between Curing Conditions 2 and 3 (see Section 3.3.2). With the exclusion of Batch 1 results, the mean compressive strength of specimens having undergone Curing Condition 3 (CHT) is greater than the mean compressive strength of specimens cured under Curing Condition 2 (HT). This can be attributed to the effect of curing temperature and duration on strength discussed in Section 2.2.3.1. Increased curing temperature and duration have beneficial effect on the compressive strength of RPC. Due to the cyclic nature of the power supply to the large hot water bath the water was unable to reach 90°C nor be maintained at constant temperature throughout the duration of Curing Condition 2. Although a longer curing period was adopted to compensate for this lower average temperature, the effect is not the same as reaching and maintaining a temperature of 90°C

(Curing Condition 3). Hence, slightly lower strengths resulted from Curing Condition 2 when compared to Curing Condition 3.

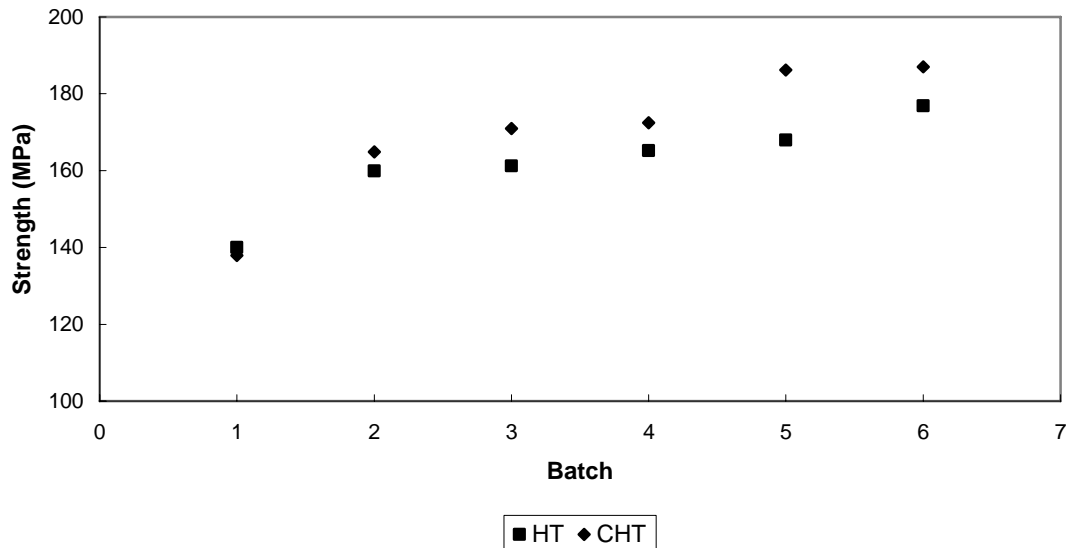


**Figure 4.3:** Effect of increased curing temperature on compressive strength

## 4.3 FLEXURAL STRENGTH

### 4.3.1 Characteristic Flexural Strength

The mean 28-day flexural strength ( $f_{f,m}$ ) for 6 batches was determined and the results along with the standard deviation (sd) and coefficient of variation (COV) are shown in Table 4.2.

The large scatter in the results of Batch 4, 5 and 6 (as indicated by the coefficient of variation for these batches) can be attributed to the variable nature of fibre reinforced concrete. Lee and Barr (2003) reported similar scatter in the flexural strength of steel fibre reinforced concrete. It is not possible to achieve perfect distribution and orientation of short fibres in the concrete matrix and as a result, some cross-sections within a beam specimen will have fewer fibres available to bridge developing cracks and these fibres may also be at an ineffective angle to arrest crack development. These sections of weakness govern the flexural strength of the prism. It is for this reason, that it is necessary to adopt a high factor of safety when dealing with the flexural and tensile capacity of fibre reinforced concretes.

**Table 4.2:** Flexural Strength Results

Batch	$f_{f,m}$ (MPa)	sd (MPa)	COV (%)
1	20.1	1.35	6.69
2	20.3	0.27	1.33
4	20.3	2.44	12.04
5	21.9	3.15	14.37
6	25.4	2.97	11.68
7	28.0	0.79	2.83

The flexural strength values obtained are lower than those reported elsewhere (Cheyrezy, 1999). This can be attributed to the lower compressive strength of this SF-RPC when compared to other RPC formulations (see Section 4.2.1).

The mean flexural strength for the SF-RPC studied is 23.0MPa with a standard deviation of 4.0MPa. A characteristic flexural strength ( $f'_{cf}$ ) of 16.5MPa was calculated using Equation 4.3. Although the same confidence level is applied to the flexural strength equation as the compressive strength equation, there is a high factor of safety due to the large standard deviation.

$$f'_{cf} = f_{m,f} - 1.64sd \quad (4.3)$$

#### 4.3.2 Flexural Strength Development

The flexural strength development for SF-RPC was monitored over a period of 365 days. Specimens for flexural strength development were taken from Batch 2 and the results are presented in Figure 4.4. For clarity, these results are also presented in Table A.2. The flexural strength of SF-RPC cured under standard conditions continues to develop with time whilst specimens that have undergone hot water curing have reached their final strength at the completion of curing, as is the case for compressive strength. However, unlike the results for compressive strength, there appears to be no beneficial effect of hot water curing on flexural strength.

The absence of any benefit from hot water curing on flexural strength can be attributed to several factors. The flexural strength of fibre reinforced concrete

is related to the strength and geometry of the fibre used as well as the bond between fibre and matrix. The application of heat treatment to RPC results in an improved microstructure. However, the application of heat treatment has no influence on fibre type and geometry plus little effect on the bond between the fibres and the matrix. These factors are considered dominant factors for the flexural strength of fibre reinforced concrete (Chunxiang and Patnaikuni 1999). Therefore, heat treatment has little to no effect on the flexural strength of SF-RPC.

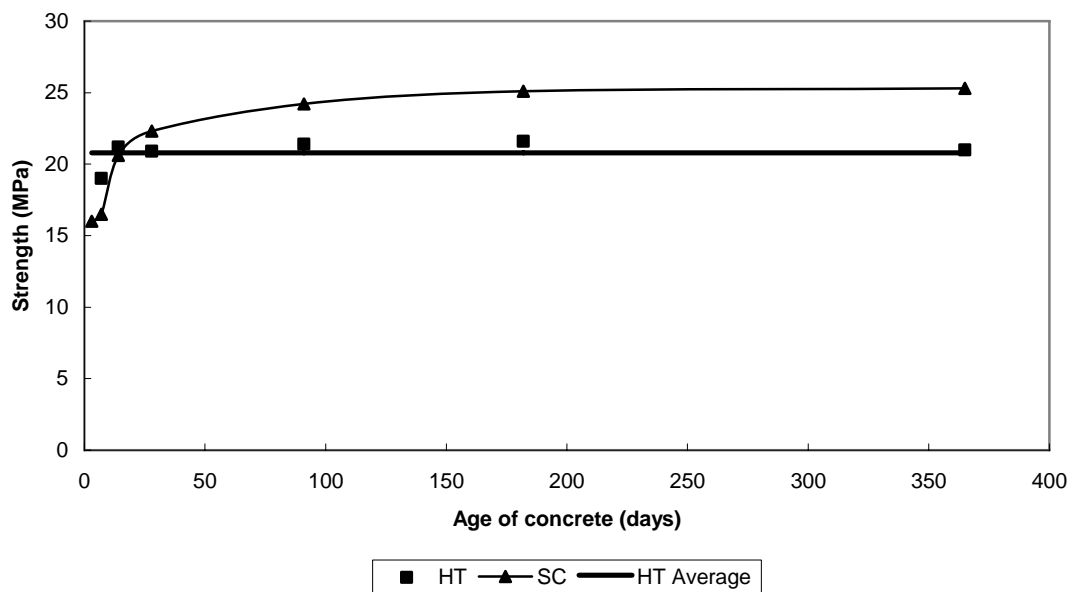


**Figure 4.4:** Flexural strength development with age (Batch 2)

### 4.3.3 Expressions for Flexural Strength

For structural design purposes, the compressive strength is the material property most commonly considered. Therefore, most concrete design codes contain relationships for the flexural strength based on the compressive strength. The flexural strength of plain concrete usually lies within the range of the following equation:

$$f_{cf} = 0.6\sqrt{f_c} \sim 1.0\sqrt{f_c} \quad (4.4)$$

The lower end of this range is usually specified in design codes, such as ACI 318 (95) and AS 3600 (2001).

Figure 4.5 shows the relationship between flexural and compressive strength for the SF-RPC investigated along with the lower and upper bound predictions based on Equation 4.4. As can be expected, SF-RPC has a greater proportion of flexural strength in relation to its compressive strength than normal strength concretes. This is a direct result of the inclusion of fibres.

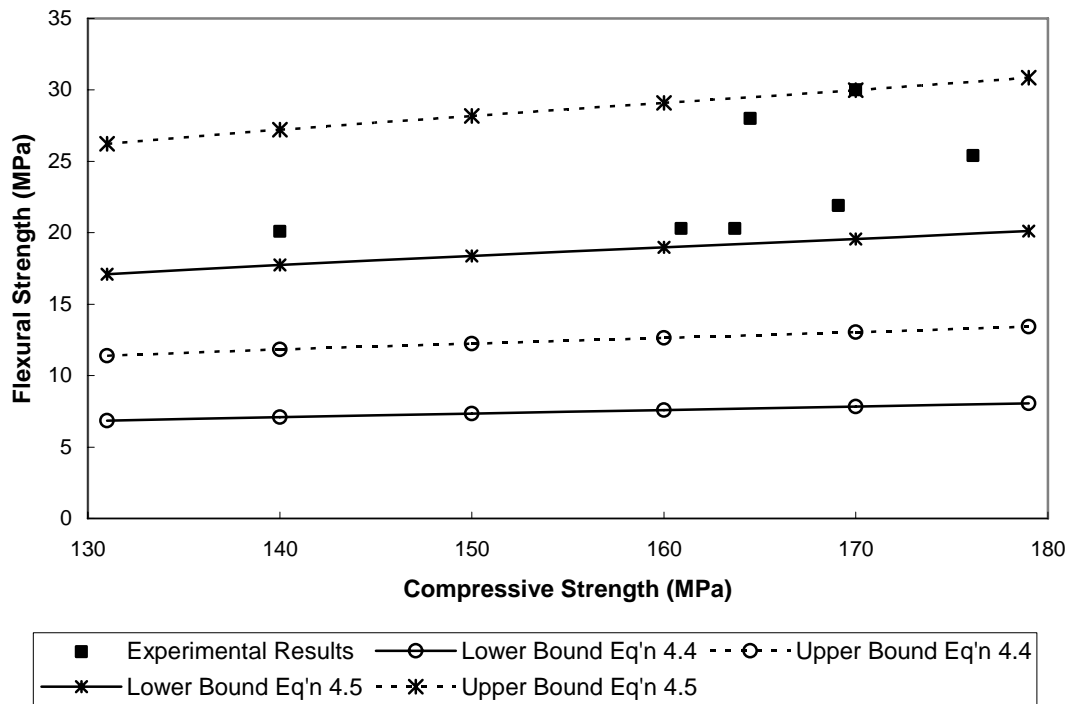


**Figure 4.5:** Flexural and compressive strength relationship

For this SF-RPC, the flexural strength usually lies within the range given by Equation 4.5 as can be seen in Figure 4.5. The lower end of this range may be taken as the flexural strength of SF-RPC for design purposes.

$$f_{cf} = 1.5\sqrt{f_c} \sim 2.3\sqrt{f_c} \quad (4.5)$$

#### 4.3.4 Load – Deflection Behaviour

A typical load-deflection curve for a beam constructed from this material is presented in Figure 4.6. The load-deflection curve was obtained from a standard modulus of rupture test. It can be seen from the figure that SF-RPC beams exhibit linear behaviour up to first cracking, a post first crack strain hardening phase up to the peak flexural load, and a post peak load strain

softening phase. SF-RPCs exhibit significant deformability in the post-peak range of the load deflection curve.

#### 4.3.4.1 First crack

The end of linearity of the load-deflection curve occurs as a result of the cementitious matrix cracking. This first crack occurs when the tensile strain limit of the matrix is exceeded. As the first crack load is dependent on the tensile strength of the matrix, the stress at which this occurs in SF-RPC (10 – 12MPa) is only slightly higher than that of high performance concretes (8 – 10MPa) as the two materials have similar matrices. The corresponding strain value at first cracking calculated using respective modulus of elasticity ( $E$ ) values are in the range of 200 – 300 $\mu\epsilon$  for both materials.

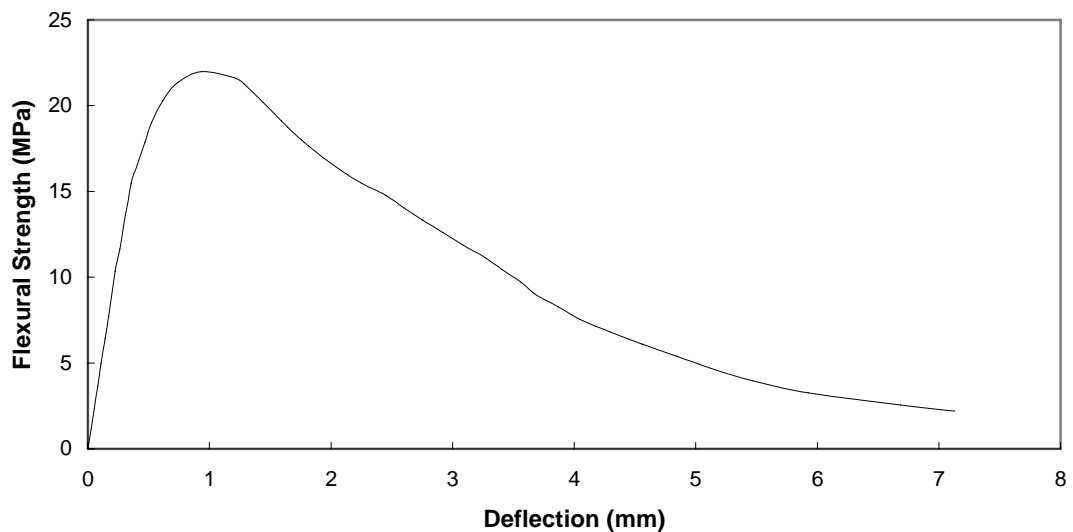


**Figure 4.6:** Load – deflection curve

In order to see the point of first cracking more clearly, it is sometimes necessary to expand the ascending portion of the load-deflection curve as shown in Figure 4.7.

According to the AFGC Interim Recommendations (2002) for RPC, in the absence of direct tensile strength results, the tensile strength can be approximated from the results of a flexural test by determining the value of the flexural strength corresponding to the loss of linearity of elastic behaviour,  $R_{fl}$  (see Figure 4.7).

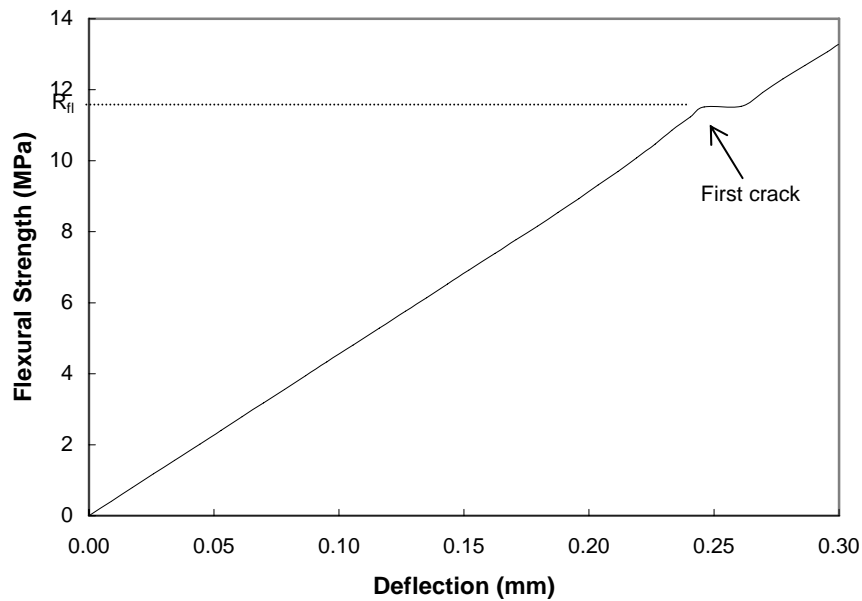


**Figure 4.7:** Initial portion of load-deflection curve

The direct tensile stress at which cracking occurs,  $R_t$ , can be estimated from  $R_{ft}$  using Equation 4.6 (as from the CEB – FIP Code) to account for size effects.

$$R_t = \frac{R_{ft} \times 2.0 \times \left(\frac{h}{h_0}\right)^{0.7}}{1 + 2.0 \times \left(\frac{h}{h_0}\right)^{0.7}} \quad (4.6)$$

where  $h$  is the height of the test specimen and  $h_0 = 100\text{mm}$

Using the above equation, the mean 28-day tensile strength ( $f_{t,m}$ ) for 6 batches was determined and the results along with the standard deviation (sd) and coefficient of variation (COV) are shown in Table 4.3.

The large scatter in the results (as indicated by the coefficients of variation) can be attributed to the variable nature of fibre reinforced concrete. The mean tensile strength for the SF-RPC studied is 8.3MPa with a standard deviation of 1.37MPa. These figures are comparable to direct tensile strength reported elsewhere for RPCs containing similar fibres (Toutlemonde et al., 1998).

**Table 4.3:** Tensile Strength Results

Batch	$f_{t,m}$ (MPa)	sd (MPa)	COV (%)
1	7.4	0.92	12.43
2	7.4	0.71	9.70
4	7.3	0.52	7.16
5	9.6	1.34	13.98
6	9.4	1.43	15.32
7	8.8	1.35	15.43

#### 4.3.4.2 Post-crack behaviour

The major difference between SF-RPC and high performance concretes in flexure occurs in the post-cracking region of their respective load-deflection curves. For concrete reinforced with short, strong fibres such as the fibres used in the present study, there are three types of failure that can occur after the matrix has cracked (Gopalaratnam and Shah, 1987). The first type of failure, where the composite fractures immediately after the matrix has cracked, is the result of either insufficient fibre content at the critical cross-section or insufficient fibre lengths to transfer tensile stresses across the matrix crack. The composite strength is approximately equal to the strength of the cementitious matrix alone. This type of behaviour is brittle in nature.

In the second type of failure there is again little difference between the maximum load the composite can carry compared to the load the matrix can carry alone but the composite continues to carry decreasing load after peak. Fibres pulling out from the cracked surfaces provide this post-cracking resistance resulting in a considerable increase in the fracture energy of the composite. Hence, this type of failure is more ductile in nature.

For the third type of failure, the composite continues to carry increasing tensile stresses after the matrix has first cracked. The peak stress and corresponding deformation are greater than those of the matrix alone. This type of failure is exhibited by the SF-RPC investigated in the present study. For the specimens

tested, the ultimate load was 1.5 – 2.5 times the load at which the matrix first cracked. For this type of behaviour, sufficient fibres with adequate strength and length as well as adequate bond between fibres and matrix are required to carry tensile stresses across the propagating crack surfaces.

In order to explain Type 3 behaviour, consider a fibre crossing a crack surface as shown in Figure 4.8. When the matrix cracks, there is a small area of frictional slip and debonding but the majority of the fibre is still “bonded” to the cementitious matrix as shown in (a). Tensile stresses are transmitted through bond stress and the material can sustain increasing load. As the load increases, subsequent frictional slip and debonding will occur as shown in (b). Eventually the fibre will be pulled out of the crack surface as shown in (c) which corresponds to the peak load. In addition to the progressive debonding and frictional slip occurring at the matrix-fibre interface, some additional matrix cracking may also occur. Final failure occurs due to unstable crack propagation when fibres pull out of the crack surface completely and the interfacial shear stress along the fibre-matrix interface reaches the ultimate bond strength.

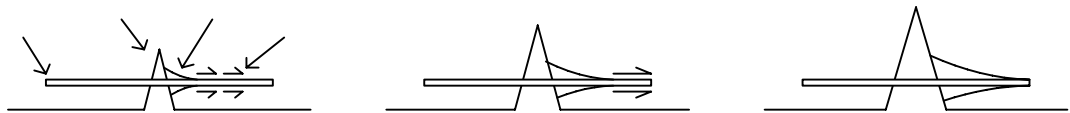


**Figure 4.8:** Matrix – fibre interface

Figure 4.9 contains images taken from a flexural test. The figure shows the propagation of the major crack at various stages of loading. As can be seen in the various images of this figure, for this SF-RPC additional matrix cracks occur as the load increases. Image F and G show the fibres beginning to be pulled out of the crack surface.

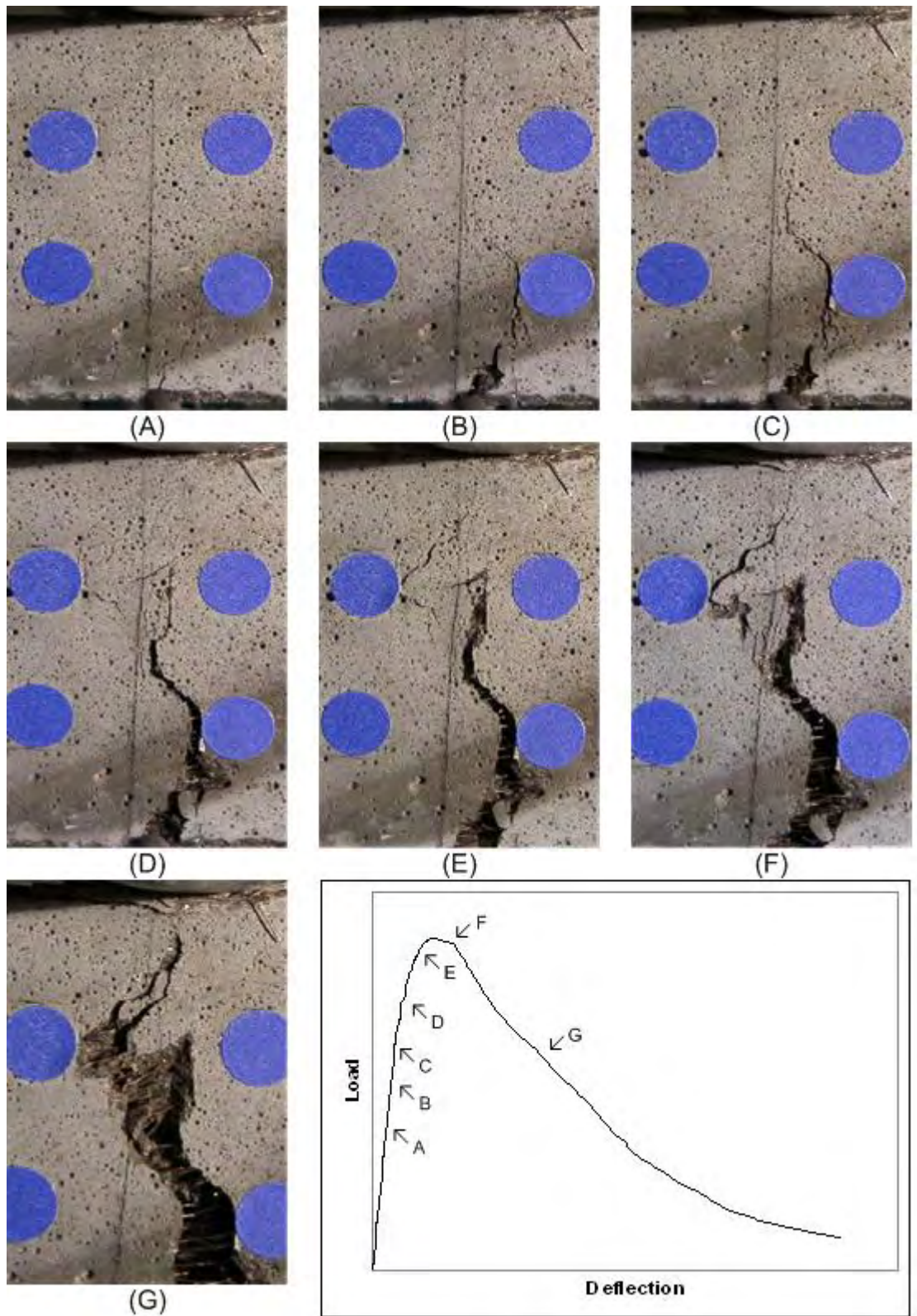
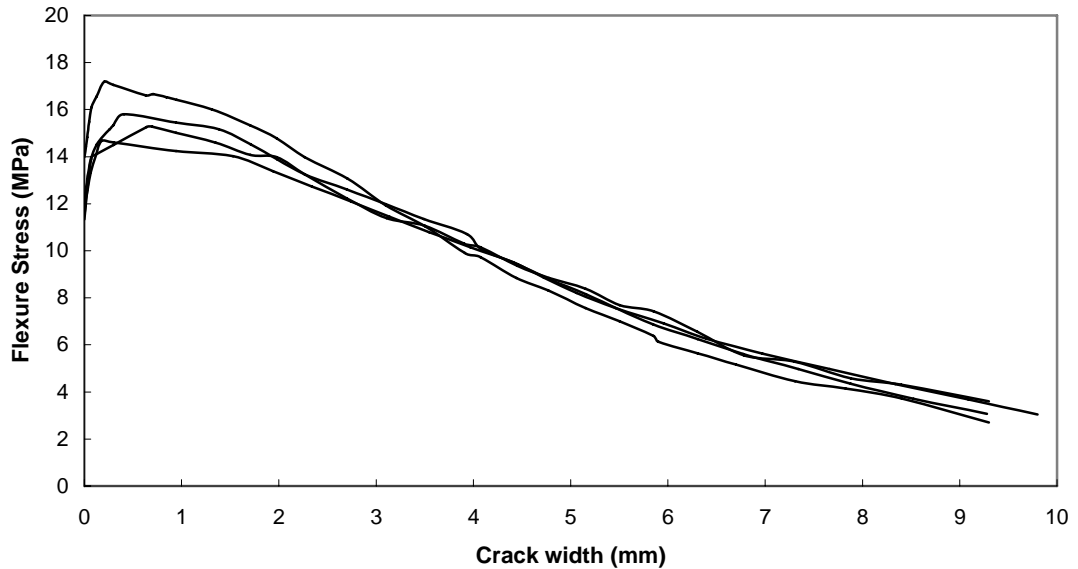


Figure 4.9: Crack propagation

### 4.3.5 Stress – Crack Width Behaviour

The results of the crack mouth opening (CMO) tests performed on specimens from Batch 1 are presented in Figure 4.10. For details of CMO test, see Section 3.3.3.5. As can be seen in the figure, the shape of the curve is similar to the load-deflection curve shown in Figure 4.6.



**Figure 4.10:** Stress – crack width curve

The French Interim Recommendations (2002) for RPC suggest the use of a characteristic length  $l_c$  to transform from a constitutive law of the  $\sigma = f(w)$  (stress–crack width) type to a constitutive law of the  $\sigma = f(\varepsilon)$  (stress–strain) in order to simplify calculations. This gives the following equation:

$$\varepsilon = \frac{f_{ij}}{E_{ij}} + \frac{w}{l_c} \quad (4.7)$$

where  $f_{ij}$  is the tensile strength of the cement matrix; and  
 $E_{ij}$  is the elastic modulus.

The value of  $l_c$  depends on the sectional area. For a rectangular section, the following expression is given:

$$l_c = \frac{2}{3}h \quad (4.8)$$

where  $h$  is the depth of the section.

For Equation 4.7, the first term on the right hand side  $f_{ij} / E_{ij}$  is the strain at which first cracking occurs according to *Hooke's law*. The remaining term on the right hand side  $w/l_c$  uses the characteristic length for the cross-section to transform crack widths into equivalent strains.

## 4.4 MODULUS OF ELASTICITY

### 4.4.1 Average Modulus of Elasticity

The average 28-day modulus of elasticity ( $E_m$ ) for all 7 batches was determined and the results along with the standard deviation ( $\sigma$ ) and coefficient of variation (COV) are shown in Table 4.3.

**Table 4.4:** Modulus of Elasticity Results

Batch	$E_m$ (GPa)	sd (GPa)	COV (%)
1	41.0	0.84	2.06
2	44.5	1.33	3.00
3	45.6	0.16	0.36
4	45.2	1.60	3.55
5	45.9	0.38	0.83
6	46.9	0.94	2.00
7	46.0	1.35	3.01

The modulus of elasticity values obtained are lower than those reported elsewhere (Cheyrezy, 1999). This can be attributed to the lower compressive strength of this SF-RPC when compared to other RPC formulations (see Section 4.2.1). The general trend of increased compressive strength leading to increased modulus of elasticity (Neville, 1995) is shown in the results of the 7 batches. Batch 1 with lowest compressive strength has the lowest modulus of elasticity whereas Batch 6 with the highest compressive strength has the greatest modulus of elasticity.

The average modulus of elasticity for the SF-RPC investigated is 45.5GPa with a standard deviation of 1.44GPa. A characteristic modulus of elasticity ( $E_c$ ) of 43.1GPa was calculated using the following equation:

$$E_c = E_m - 1.64sd \quad (4.9)$$

#### 4.4.2 Modulus of Elasticity Development

The modulus of elasticity development for SF-RPC was monitored over a period of 365 days. The samples were from Batch 3 and the results are presented in Figure 4.11. For clarity, these results are also presented in Table A.3. The modulus of elasticity of SF-RPC cured under standard conditions continues to develop with time whilst specimens that have undergone hot water curing have reached their final modulus of elasticity at the completion of curing, as is the case for compressive strength. However, unlike the results for compressive strength, there appears to be no beneficial effect of hot water curing on modulus of elasticity. This appears to be contradictory to the general conclusion for cementitious materials that increased strength results in an increase in modulus of elasticity. However, the modulus of elasticity of RPC is governed not only by the cementitious matrix but also by the fibres. Since the application of heat treatment has no effect on the stiffness of the fibres, it has a limited effect on the modulus of elasticity of the composite.

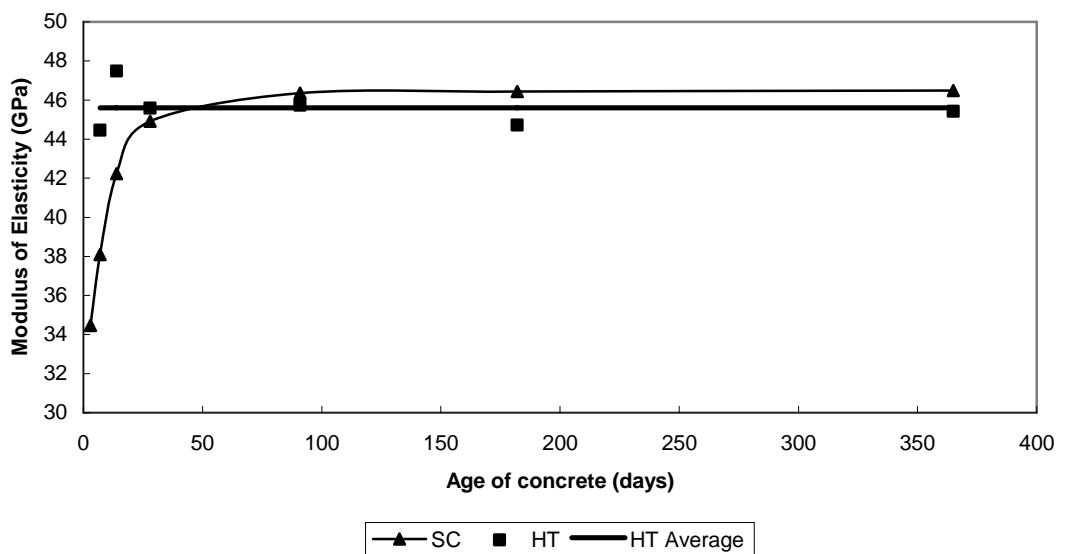


**Figure 4.11:** Modulus of elasticity development with age (Batch 3)

#### 4.4.3 Expressions for Modulus of Elasticity

Concrete design codes commonly deal with the modulus of elasticity in a similar manner to the flexural strength, i.e. the modulus of elasticity is a function of the compressive strength. AS 3600 (2001) gives the following equation for calculating the modulus of elasticity of normal strength concrete based on the density ( $\rho$ ) and the compressive strength ( $f_c$ ).

$$E_c = \rho^{1.5} \times 0.043 \sqrt{f_c} \quad (4.10)$$

The equation was developed for concrete with strength ranging from 20 – 50MPa. When applied to concretes with strengths above this range, the equation over-estimates the modulus of elasticity.

In the range of strengths from 80 – 140MPa, it was found that the modulus of elasticity (in GPa) is approximately related to the compressive strength (in MPa) by the following expression (Neville, 1995):

$$E_c = 3.65 \sqrt{f_c} \quad (4.11)$$

Figure 4.12 shows the relationship between modulus of elasticity and compressive strength for the SF-RPC investigated along with the predictions based on Equation 4.12. As can be seen from the figure, Equation 4.11 over-estimates the modulus of elasticity of SF-RPC.

For this SF-RPC, the modulus of elasticity (in GPa) usually lies within the range given by Equation 4.12 as can be seen in Figure 4.12. The lower end of this range may be taken as the modulus of elasticity of SF-RPC for design purposes.

$$E_c = 3.4 \sqrt{f_c} \sim 3.6 \sqrt{f_c} \quad (4.12)$$

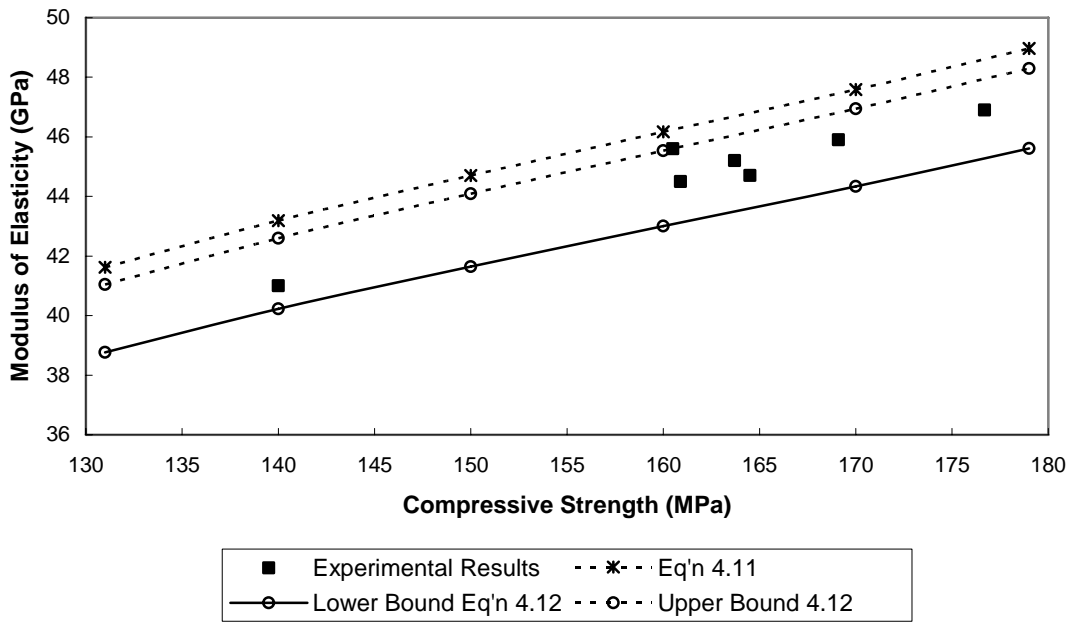


Figure 4.12: Modulus of elasticity and compressive strength relationship

#### 4.5 STRESS-STRAIN RELATIONSHIP IN COMPRESSION

A typical compressive stress-strain relationship for the SF-RPC investigated is shown in Figure 4.13. The results shown are for a cylinder from Batch 6. A stress-strain test was performed on one cylinder from each batch (excluding Batch 3). From the results of these tests, the axial strain at peak stress ( $\epsilon_{o,u}$ ) lies between  $3500 - 4500\mu\epsilon$ . The average value of Poisson's ratio ( $\nu$ ) was 0.17.

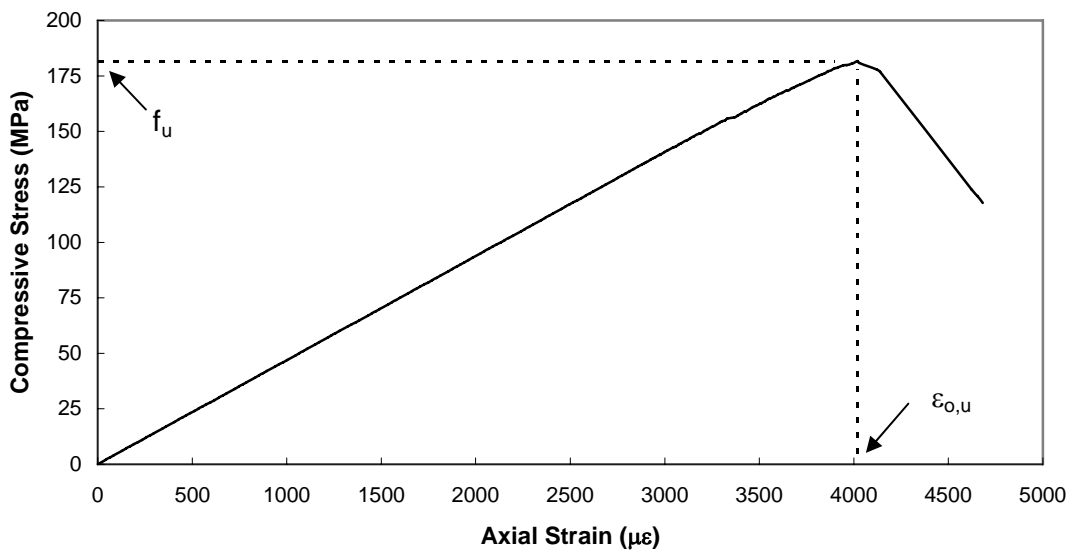
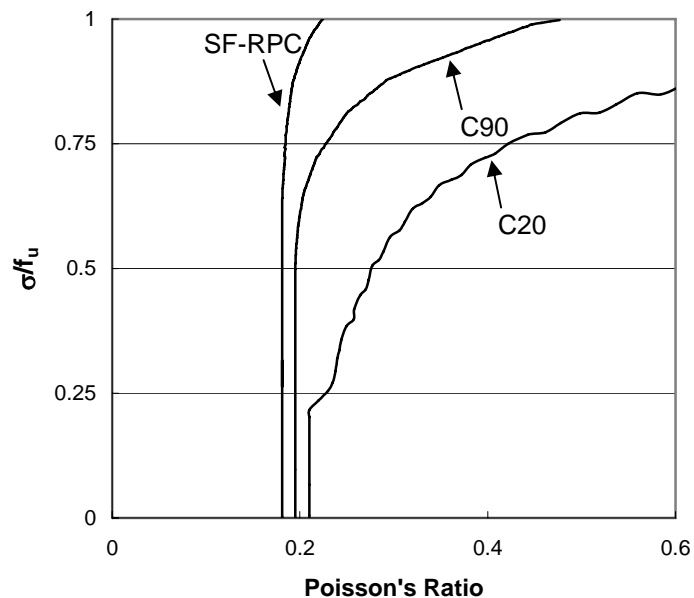


Figure 4.13: Stress-strain behaviour in compression

From Figure 4.13, it can be seen that SF-RPC exhibits linear elastic stress-strain behaviour up to approximately 95% of the peak stress,  $f_u$ . For conventional concretes, deviation from linearity begins at  $0.65 - 0.8 f_u$ . This increase in the linear behaviour in SF-RPC is the effect of the delay in the growth of internal microcracks resulting from the increased homogeneity of the material above that of conventional concrete. Figure 4.14 shows the Poisson's Ratio plotted against the stress-strength ratio ( $\sigma / f_u$ ) for both the SF-RPC investigated and various concrete strengths (20 and 90 MPa). It can be seen in this figure that the circumferential (lateral) strain for the 20MPa concrete deviates from linearity at a much lower stress-strength ratio than for the 90MPa concrete. Similarly, the lateral strain of the 90MPa concrete deviated from linearity at a lower stress-strength ratio than for the SF-RPC. This results in the earlier deviation and point of discontinuity of the volumetric strain. The discontinuity point of the volumetric strain corresponds to the onset of the fast crack propagation stage and the deviation of linearity in the axial stress-strain behaviour (Neville, 1995).



**Figure 4.14:** Poisson's Ratio versus  $\sigma / f_u$

### 4.5.1 Expressions for Stress-Strain Relationship

There are a number of equations available for predicting the stress-strain curve of concrete. A widely used suggested by Carreira and Chu (1985) for plain concrete and modified for fibre reinforced concrete is as follows:

$$\frac{f_c}{f_{cu}} = \frac{\beta \left( \frac{\varepsilon_c}{\varepsilon_{cu}} \right)}{\beta - 1 + \left( \frac{\varepsilon_c}{\varepsilon_{cu}} \right)^\beta} \quad (4.13)$$

where  $f_c$  is the stress in the concrete at strain  $\varepsilon_c$

$f_{cu}$  is the compressive strength of the fibre reinforced concrete

$\varepsilon_{cu}$  is the strain at  $f_{cu}$

$\beta$  is the material parameter that depends on the shape of the stress-strain diagram

For the SF-RPC studied, the parameter  $\beta$  is approximately 20 as can be seen in Figure 4.15.

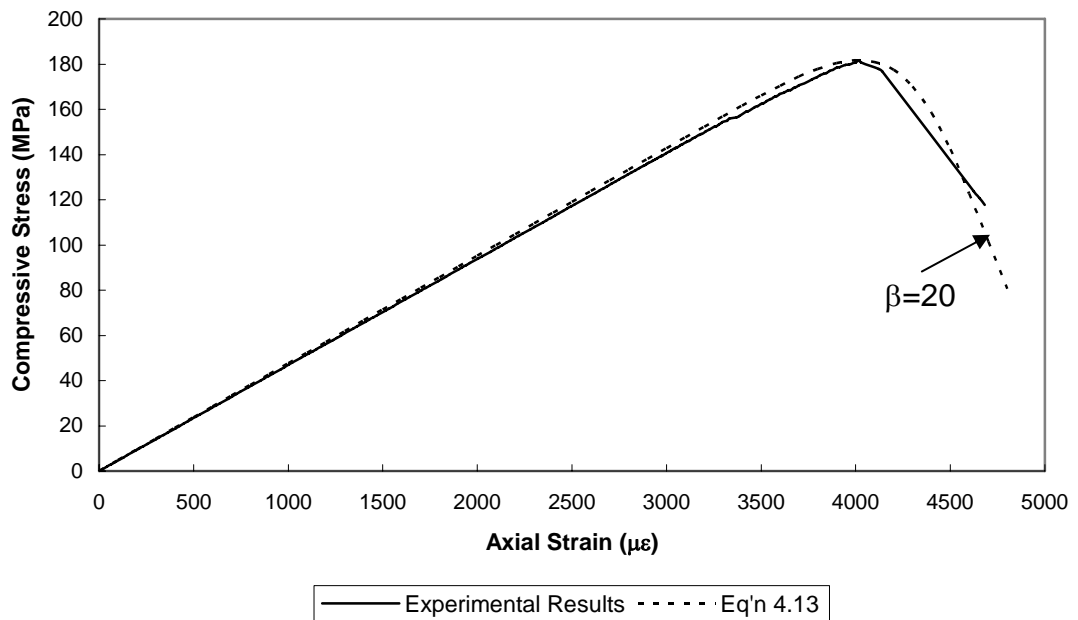


**Figure 4.15:** Theoretical prediction of stress-strain relationship

For design purposes, the simplified constitutive model shown in Figure 4.16 can be used. The compressive behaviour is then defined by the characteristic strength and the modulus of elasticity with the maximum strength corresponding to a stress of  $0.85f'_c$  and a maximum strain of  $4000\mu\epsilon$ .

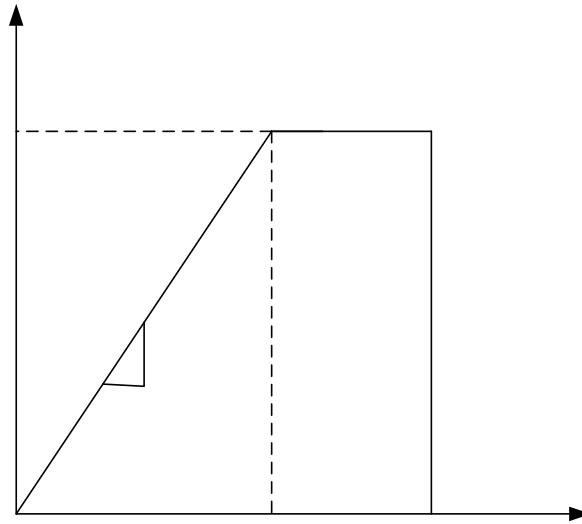


**Figure 4.16:** Simple constitutive model for stress-strain behaviour

#### 4.6 SHRINKAGE

Shrinkage is the time-dependent strain of an unloaded and unrestrained concrete specimen. For conventional concrete, shrinkage commences with drying and continues to increase with time at a decreasing rate. There are two main forms of shrinkage: (1) drying shrinkage and (2) autogenous (chemical) shrinkage (Neville, 1995). A third component due to carbonation of concrete is very small in high performance concrete (less than  $50\mu\epsilon$ ) due to its low permeability and hence is not considered in this chapter.

Drying shrinkage results from the withdrawal of water from concrete stored in unsaturated air. The change in the volume of drying concrete is not equal to the volume of water removed. The loss of free water, which takes place first, causes little or no shrinkage. As drying continues, adsorbed water is removed and there is a reduction in the volume of the unrestrained hydrated cement paste resulting in drying shrinkage. Drying shrinkage is therefore dependent

on the factors that affect the drying of concrete including relative humidity, the water content and w/c ratio of the mix as well as the size and shape of the member. Typical values for the drying shrinkage strain of normal and high strength concretes are in the range of 500 – 850 $\mu\epsilon$  and 200 – 350 $\mu\epsilon$ , respectively.

When the w/c ratio of a concrete mix is less than about 0.32, there is insufficient water available to ensure the complete hydration of all the cement particles present. As a result, there remain unhydrated cement particles after setting has occurred. For conventional concretes, continued hydration when a supply of water is present leads to expansion but, when no moisture movement to or from the cement paste is permitted, shrinkage occurs. This shrinkage occurs as a result of the withdrawal of water from the capillary pores by the hydration of the remaining unhydrated cement particles in a process known as self-desiccation. This form of shrinkage is called autogenous (chemical) shrinkage. As self-desiccation is greater at lower w/c ratios, autogenous shrinkage could be expected to increase but this may not occur due to the more rigid structure of the hydrated cement paste at low w/c ratios. For normal strength concretes, autogenous shrinkage values are in the range of 40 - 100 $\mu\epsilon$  (Neville, 1995).

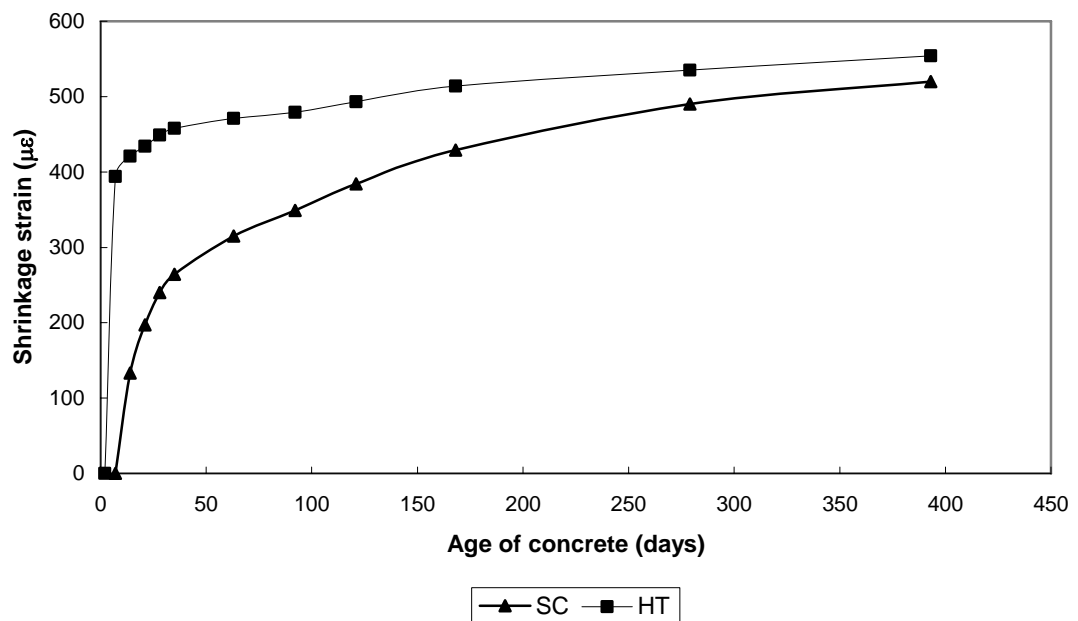
As mentioned in the previous paragraph, the continued hydration of a conventional concrete when a supply of water is present leads to expansion or swelling. This swelling is due to the absorption of water by the cement gel. The water molecules act against the cohesive forces and tend to force the gel particles further apart. Typical values of swelling for a conventional concrete with a cement content of 300kg/m<sup>3</sup> are approximately 100 – 150 $\mu\epsilon$  (Neville, 1995).

As the component materials of SF-RPC are similar to those of conventional concretes, the material is expected to shrink in a similar manner. As part of this research, the shrinkage of SF-RPC under various curing conditions was monitored to verify this. The specimens were taken from Batch 4 and 7 as accompanying specimens to the beams placed under sustained loading. This section presents the results of the various tests.

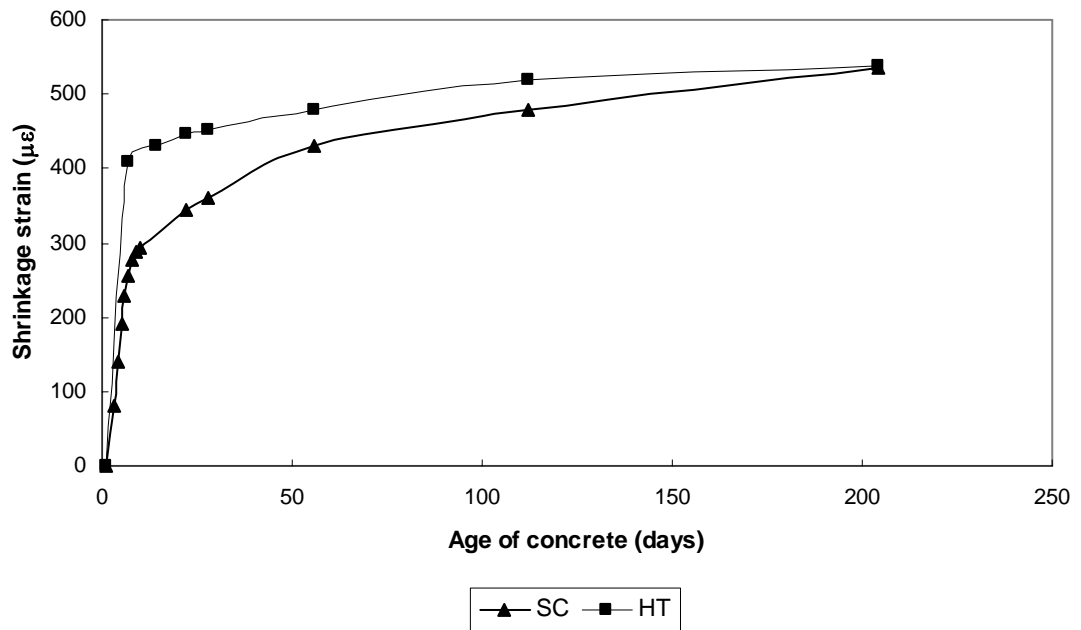
#### 4.6.1 Measured Shrinkage Strains

Figure 4.17 and 4.18 show the measured shrinkage strains of specimens from Batch 4 and 7, respectively. Initial shrinkage readings for the HT specimens (Curing Condition 2) took place at the time of demoulding. The specimens were then placed in the large hot water bath and continued readings took place upon completion of hot water curing. For the SC specimens, initial shrinkage readings took place at an age of 7 days in accordance with AS 1012.13 – 1992. The results for both batches are included in Table A.4.

Figure 4.19 shows the measured shrinkage strains for specimens from Batch 4 that were placed in a water bath at 23°C immediately after demoulding and were stored in the bath throughout the duration of the shrinkage test. Initial shrinkage readings took place at the time of demoulding. The purpose of this test was to identify the autogenous shrinkage component for this SF-RPC. The results are also included in Table A.4.



**Figure 4.17:** Shrinkage (Batch 4)



**Figure 4.18:** Shrinkage (Batch 7)

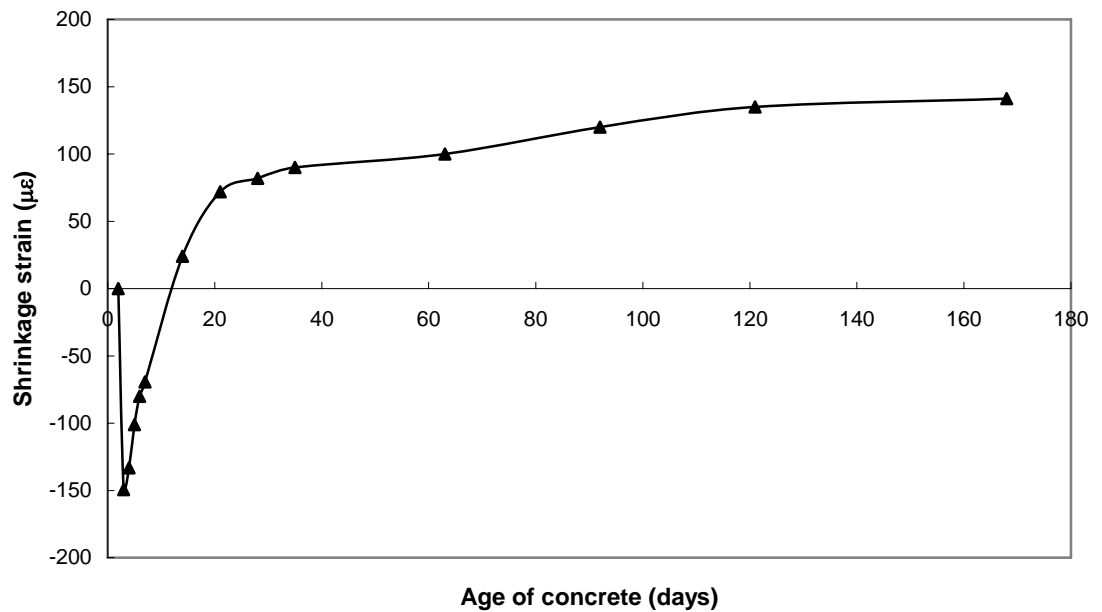


**Figure 4.19:** Autogenous shrinkage

From Figure 4.19, it can be seen that after an initial swelling of up to  $150\mu\epsilon$ , the net autogenous shrinkage component for this SF-RPC is  $100 - 150\mu\epsilon$  and the total shrinkage is  $300 - 400\mu\epsilon$ . The autogenous shrinkage for HT specimens from Batch 4 and 7 is  $300 - 400\mu\epsilon$  as can be seen in Figures 4.17 and 4.18. According to Neville (1995), increased curing temperature results in increased autogenous shrinkage as shown by these results. It can also be

seen in Figures 4.17 and 4.18 that the majority of shrinkage when this SF-RPC is heat treated occurs during the period of hot water curing. Approximately 70 -75% of the total shrinkage occurred during this period. The remaining 25 – 30% of the total shrinkage that occurs after the completion of hot water curing is either the result of drying shrinkage or continued autogenous shrinkage due to self-desiccation.

For specimens that have not undergone a period of initial hot water curing (SC specimens), it can be seen in Figures 4.17 and 4.18 that the shrinkage developed rapidly at an early age and continued to increase at a decreasing rate. About 60% of the total shrinkage occurred in the first 2 months. After a period of 1 year, the rate of shrinkage development was small. It can also be seen in these two figures that the total shrinkage after a long period of time (200 – 500 days) is similar regardless of whether the specimens have undergone a period of hot water curing or not.

The shrinkage of this SF-RPC is therefore different from conventional concretes although the two materials undergo similar shrinkage mechanisms. As mentioned previously, conventional concrete will continue to swell when stored in water. However SF-RPC when stored in water, after an initial swelling, will shrink. This is due to both the low w/c ratio and the large proportion of cementitious materials present in SF-RPC. At the completion of setting, due to the low w/c ratio only a small proportion of the cement particles have hydrated. In the presence of a supply of water these particles will continue to hydrate. The products of the hydration process (calcium silicate hydrates) are smaller than the reactants (cement particles and water) and therefore continued hydration results in autogenous shrinkage. In conventional concrete, where there is considerably less cementitious materials, the swelling due to the absorption of water is greater than the shrinkage due to continued hydration. However for SF-RPC where there is a greater number of cement particles, the shrinkage due to continued hydration of these particles is greater than the swelling due to the absorption of water and thus, SF-RPC will shrink even when stored in water.

Preliminary work done in the area of shrinkage of RPC indicates that after a period of heat treatment (48h hours at 90°C), RPCs exhibit no residual shrinkage (Cheyrezy, 1999). Figure 4.20 shows the shrinkage behaviour of an RPC with a w/c ratio of 0.20 and a cement content of 710kg/m<sup>3</sup>. As can be seen in the figure, heat-treated RPC 200 does not display residual shrinkage and the shrinkage of concrete without initial heat treatment approaches the value of the heat treated concrete. From this study, Cheyrezy concluded that the shrinkage of RPC is the result of autogenous shrinkage and not drying shrinkage as in conventional concretes.

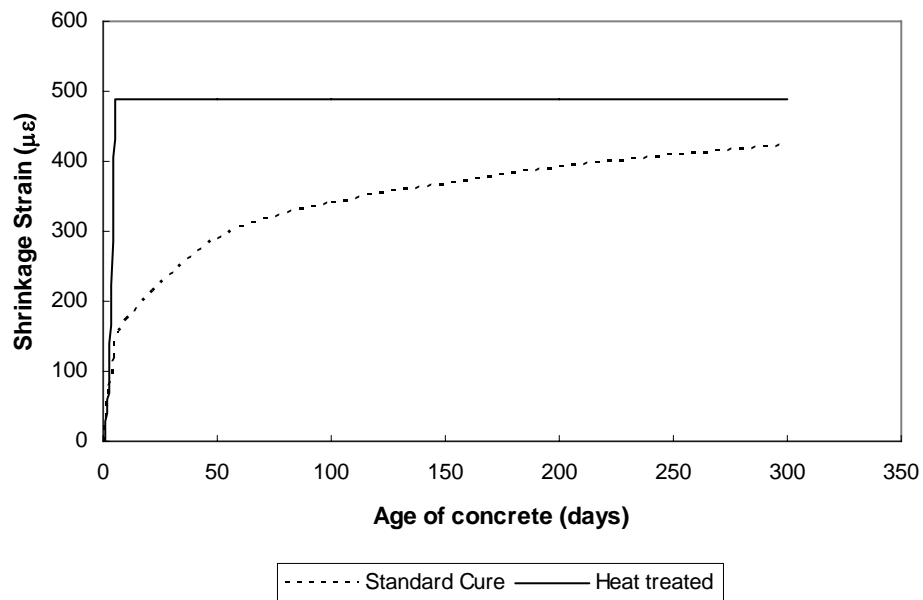


**Figure 4.20:** Shrinkage behaviour of RPC 200 (from Cheyrezy, 1999)

In order to determine whether the lower average temperature of the hot water bath used for Curing Condition 2 had an effect on the shrinkage behaviour of this SF-RPC, i.e. the appearance of residual shrinkage, a supplementary shrinkage series was conducted. The concrete had the same mix design as Batch 4 and the specimens were cast using the small-batch procedure detailed in Section 3.2.3.1. The compressive strength results from this batch were comparable with the results from Batches 2 – 7. Initial shrinkage readings took place at the time of demoulding. The specimens then underwent hot water curing for a period of 48 hours at a temperature of 90°C

(Curing Condition 3). Figure 4.21 shows the results of this supplementary shrinkage series.

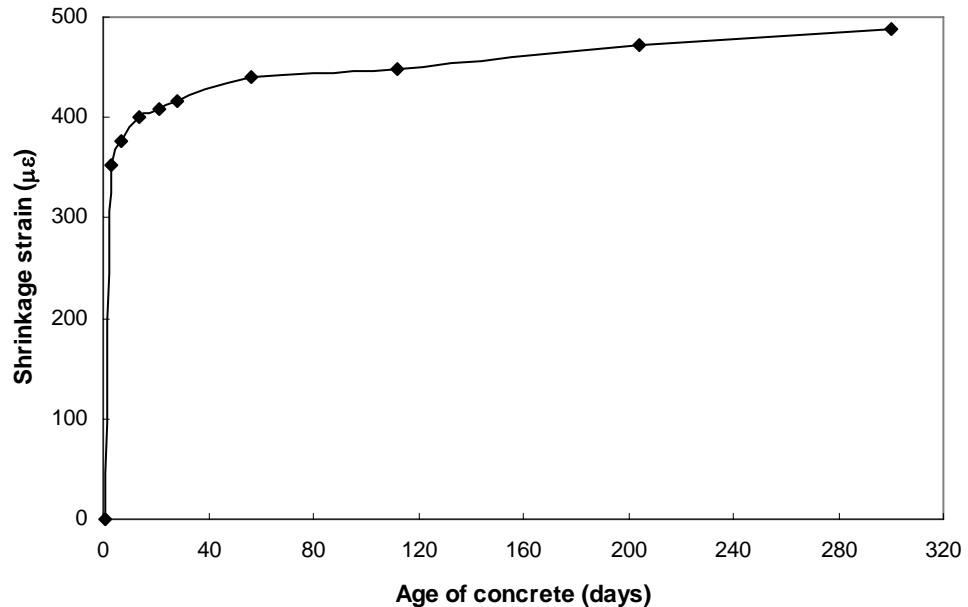


**Figure 4.21:** Supplementary shrinkage series results

As can be seen in Figure 4.21, the material although having undergone identical conditions to the RPC 200 investigated by Cheyrezy (1999), displayed residual shrinkage after the completion of hot water curing. This indicates that the residual shrinkage displayed by this SF-RPC is a function of the mix and not a result of the curing procedures adopted. As the w/c ratio of this mix (w/c = 0.23) is greater than the w/c of the RPC 200 investigated, these results may indicate that the residual shrinkage is actually an additional component of drying shrinkage due to a higher w/c ratio.

#### 4.6.2 Prediction of Shrinkage

Most concrete design codes include expressions for predicting the shrinkage strain of concrete. These expressions are developed for concretes that have not undergone any form of initial heat treatment.

The shrinkage strain is assumed to reach a limiting value at time infinity ( $\varepsilon_{sh}(\infty)$ ). ACI 209 (1992) suggests the following expression for the shrinkage strain,  $\varepsilon_{sh}$ , of moist cured conventional concrete:

$$\varepsilon_{sh}(t, t_0) = \frac{(t - t_0)}{35 + (t - t_0)} \varepsilon_{sh}(\infty) \quad (4.14)$$

$$\text{where } \varepsilon_{sh}(\infty) = -0.00078 \gamma_{sh} \quad (4.15)$$

$\gamma_{sh}$  is a correction factor depending on the age when drying commences and may be taken as

$$\gamma_{sh} = 1.25 t_0^{-0.118} \quad (4.16)$$

AS3600 (2001) also proposes an equation for shrinkage strain at any time  $t$  after the commencement of drying:

$$\varepsilon_{sh}(t, t_0) = 0.00085 k_1 \quad (4.17)$$

where  $k_1$  may be taken as (Gilbert, 1988)

$$k_1 = \frac{k_4 k_5 (t - t_0)^{0.7}}{(t - t_0)^{0.7} + k_6} \quad (4.18)$$

$$\text{and } k_4 = 0.62 + 1.5 e^{-0.005 t_h} \quad (4.19)$$

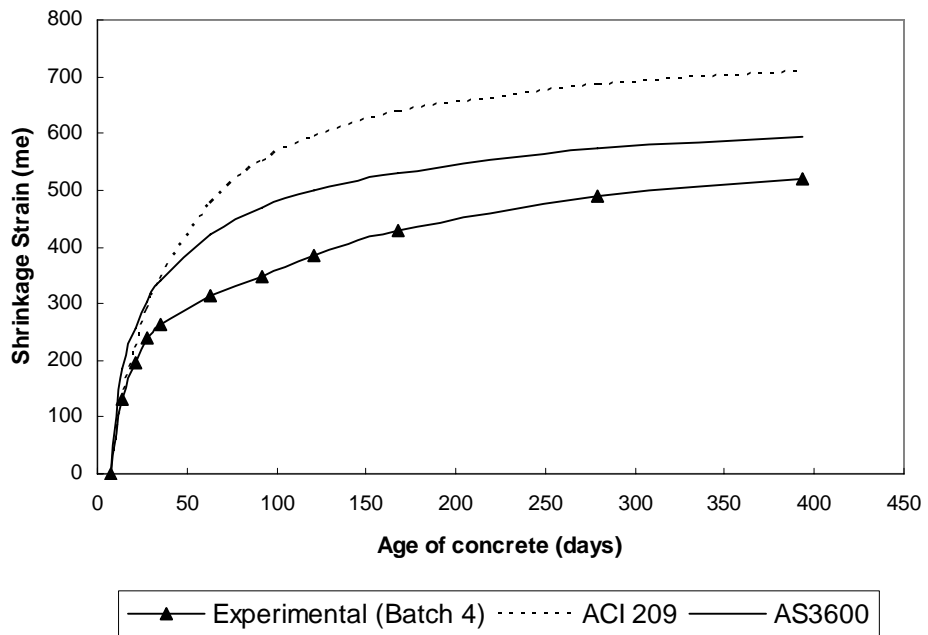
$$k_5 = \frac{4.0 - 0.04 h}{3} \quad (4.20)$$

$$k_6 = \frac{t_h}{7} \quad (4.21)$$

where  $t_h$  is the hypothetical thickness

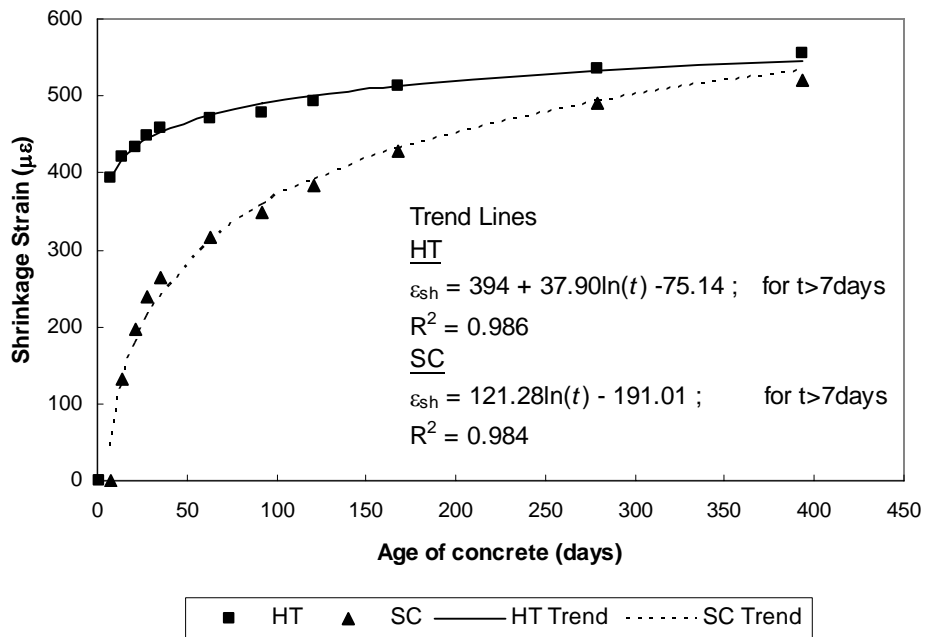
$h$  is the average relative humidity

Figure 4.22 shows the comparison between the measured shrinkage strain for SF-RPC without heat treatment to the shrinkage strain predicted by Equations 4.14 and 4.17. It can be seen from the figure that both equations overestimate the shrinkage of SF-RPC. This is to be expected as both equations were developed for conventional concretes that have a higher w/c ratio and thus are expected to display increased shrinkage.



**Figure 4.22:** Comparison of measured and predicted shrinkage strain

Figures 4.23 and 4.24 show the regression lines, together with the equations for the trend lines for the shrinkage results from Batch 4 and 7, respectively. The HT equations for Batch 7 are used to model the shrinkage of the concrete in the time dependent analysis of the prestressed slabs in Chapter 6.



**Figure 4.23:** Regression analysis of shrinkage results (Batch 4)

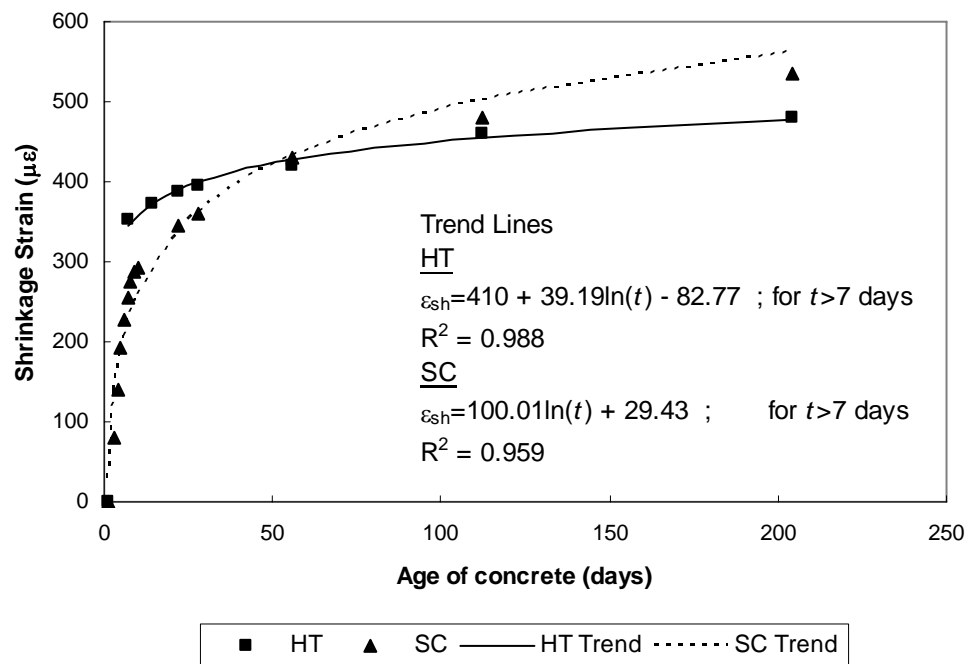


**Figure 4.24:** Regression analysis of shrinkage results (Batch 7)

From the regression analysis of these two batches, the following equation can be used to calculate the shrinkage of SF-RPC that has undergone initial hot water curing. The first component in the equation is the shrinkage that occurs during the period of heat treatment. The remainder of the equation predicts the shrinkage that occurs after the completion of heat treatment.

$$\varepsilon_{sh}(t, t_0) = 400 + 38.5 \ln(t) - 79 \quad (4.22)$$

where  $t$  is the age of concrete (days)

#### 4.7 CREEP

Creep can be defined as the increase in strain under a sustained stress. For conventional concrete, creep commences upon the application of load and continues to increase with time at an appreciably decreasing rate. Approximately 50% of the final creep develops in the first 2 – 3 months and about 90% after 2 – 3 years. In practical applications, creep and shrinkage occur simultaneously and it is assumed that the two are additive. Creep is therefore calculated as the difference between the total time-dependent deformation of the loaded specimen and the shrinkage of a similar unloaded specimen stored under the same conditions (Neville, 1995). Figure 4.25

illustrates diagrammatically the individual components of strain for a specimen under constant compressive stress.

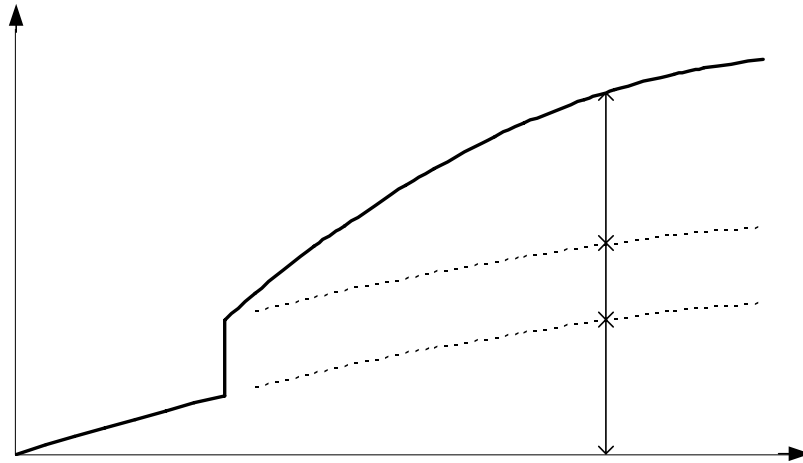


**Figure 4.25:** Components of strain (from Gilbert and Mickleborough 1990)

Many factors influence the magnitude and rate of development of creep including environmental factors, the properties of the concrete mix and the loading history. Environmental conditions such as relative humidity and average temperature affect the creep of concrete. In general, lower relative humidity and higher temperature will increase the magnitude and rate of development of creep. As far as the properties of the concrete are concerned, the higher the quality of the concrete the lower the capacity to creep is and therefore creep in higher strength concretes is lower than that in lower strength concrete. Creep also decreases as the w/c ratio is reduced. Another significant factor affecting the creep of concrete is the loading history, in particular the magnitude of the stress and the age of the concrete when the stress is first applied. Concrete loaded at an early age creeps more than concrete loaded at a later age (Gilbert and Mickleborough, 1990).

The capacity of concrete to creep is usually defined in terms of the creep coefficient. The creep coefficient  $\phi_{cr}(t, t_0)$  at time  $t$  after loading can be obtained from the following equation:

Strain

$\tau_d$   
 $\tau_0$

$$\phi_{cr}(t, t_0) = \frac{\varepsilon_{cr}(t, t_0)}{\varepsilon_e(t_0)} \quad (4.23)$$

where  $\varepsilon_{cr}(t, t_0)$  is the creep strain at time  $t$

$\varepsilon_e(t_0)$  is the instantaneous strain

$t_0$  is the concrete age at first loading

The time-dependent strain at time  $t$  caused by a constant sustained stress  $\sigma_o$  is the sum of the elastic and creep components and may be expressed as:

$$\varepsilon_e(t_0) + \varepsilon_{cr}(t, t_0) = \frac{\sigma_o}{E_c(t_0)} [1 + \phi_{cr}(t, t_0)] = \frac{\sigma_o}{E_e(t, t_0)} \quad (4.24)$$

where  $E_e(t, t_0)$  is known as the effective modulus of concrete and is given by:

$$E_e(t, t_0) = \frac{E_c(t_0)}{1 + \phi_{cr}(t, t_0)} \quad (4.25)$$

If the stress is applied gradually to the concrete, the effect of ageing can be taken into account by multiplying the creep coefficient by a reduction or ageing coefficient  $\chi$ . Hence, the effective modulus is adjusted and is often called the age-adjusted effective modulus given by

$$\bar{E}_e(t, t_0) = \frac{E_c(t_0)}{1 + \chi\phi_{cr}(t, t_0)} \quad (4.26)$$

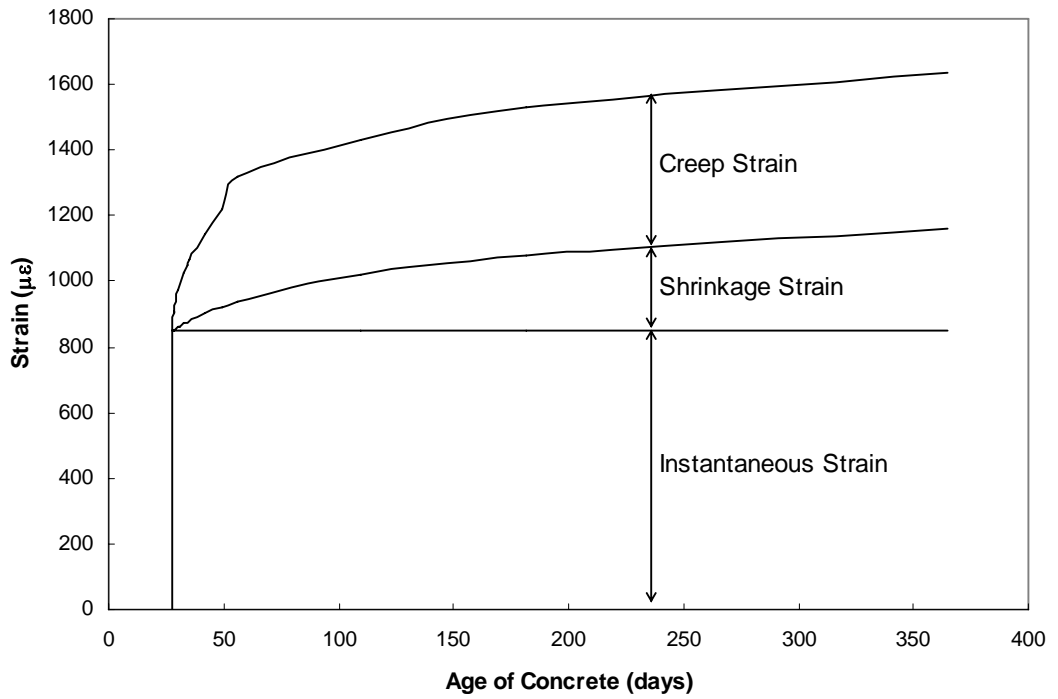
If the environmental conditions remain constant, then it is expected that SF-RPC will exhibit lower creep than conventional concrete i.e. will have a lower creep coefficient. As part of this research, the creep of SF-RPC under various curing conditions was monitored to verify this. The specimens were taken from Batch 4 and 7 accompanying the beams placed under sustained loading. This section presents the results of the creep tests.

#### 4.7.1 Measured Creep Strains and Creep Coefficients

Figure 4.26 shows the concrete strain versus time for cylinders from Batch 4 under a constant compressive stress of 38MPa. The stress level applied was approximately 35% of the concrete strength of specimens cured under standard curing conditions (Curing Condition 1) and 23% for specimens that

had been heat treated (Curing Condition 2) at the time of loading. For clarity, these results are also included in Table A.5.

**Standard Cure (Curing Condition 1)**



**Heat treated (Curing Condition 2)**

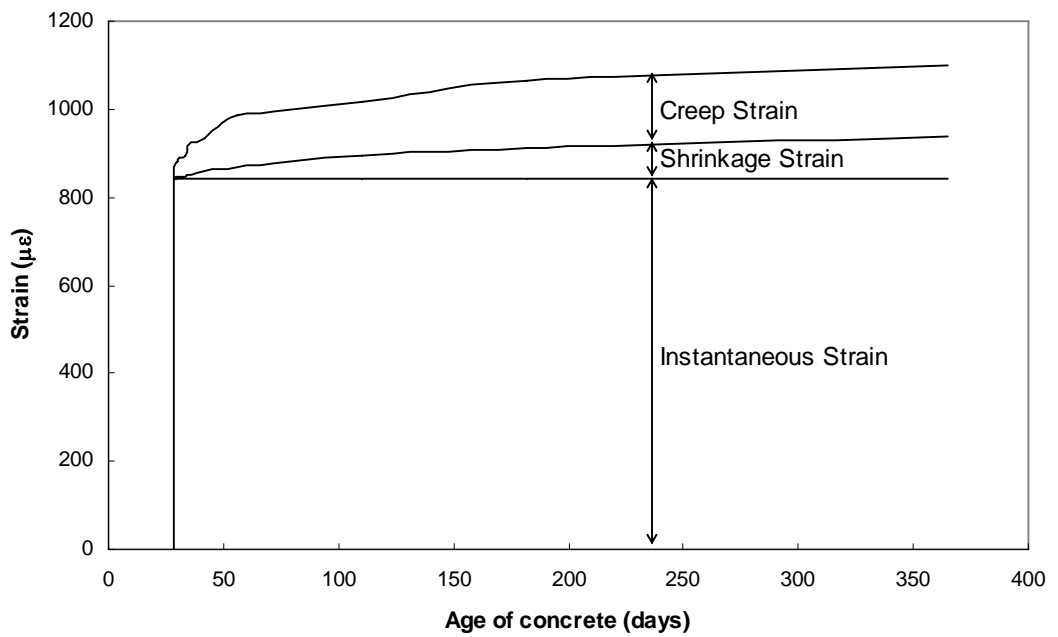


**Figure 4.26:** Strain versus time (Batch 4)

Figure 4.27 shows the concrete strain versus time for cylinders from Batch 7 under a constant compressive stress of 65MPa. The stress level applied was approximately 40% of the concrete strength. For clarity, these results are also included in Table A.5.

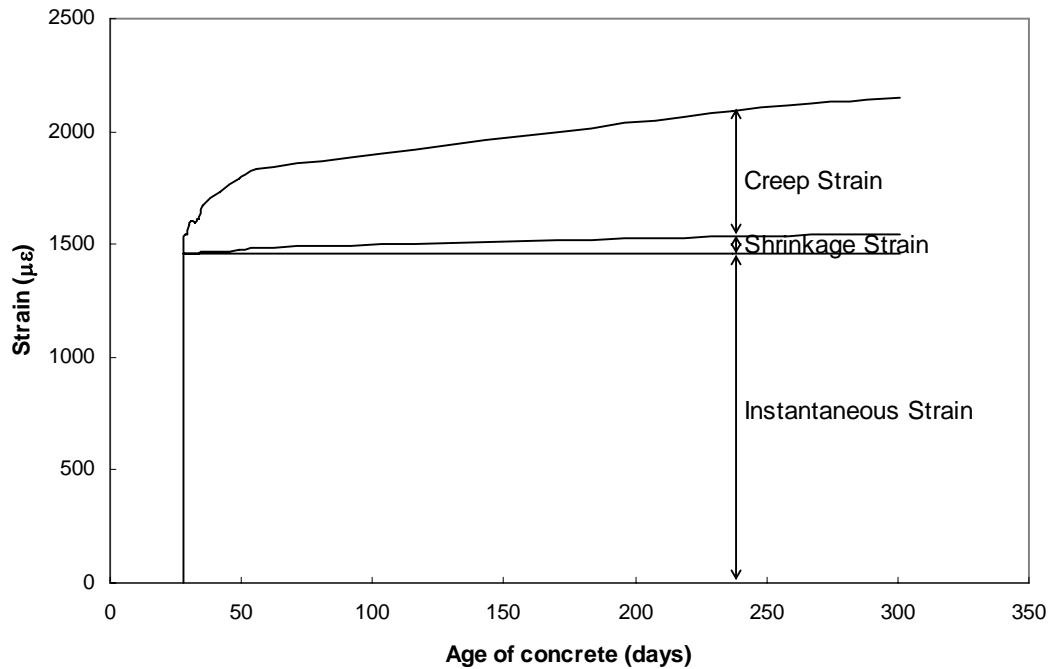


**Figure 4.27:** Strain versus time (Batch 7 Results)

From these figures, it can be seen that the creep behaviour of SF-RPC with or without initial heat treatment is similar to that of conventional concrete, i.e. the creep strains develop rapidly upon application of load and continue to increase at an appreciably decreasing rate with time. In both cases, approximately 75 – 80% of the creep measured over 365 days occurred in the first 28 days after the load was applied. It can also be seen that heat-treated SF-RPC specimens suffer less creep than SF-RPC specimens cured under standard conditions. Heat treated SF-RPC specimens have reached their final strength at the completion of curing and therefore the effect of age of loading on creep has been negated. The specimens cured under standard curing conditions are still maturing.

Figure 4.28 illustrates the creep coefficients of the SF-RPC investigated. From the comparison between the results for Batch 4 – SC (specimens without

initial heat treatment) and Batch 4 – HT (heat treated specimens), it can be seen that heat treatment significantly reduces the creep coefficient of SF-RPC. The effect of increased stress level on the creep coefficient can also be seen in the figure. The sustained stress level for heat treated specimens from Batch 4 and 7 was 23% and 40% respectively and as a result, the creep coefficients for heat treated specimens from Batch 7 (Batch 7 – HT) are higher than those of heat treated specimens from Batch 4 (Batch 4 – HT).

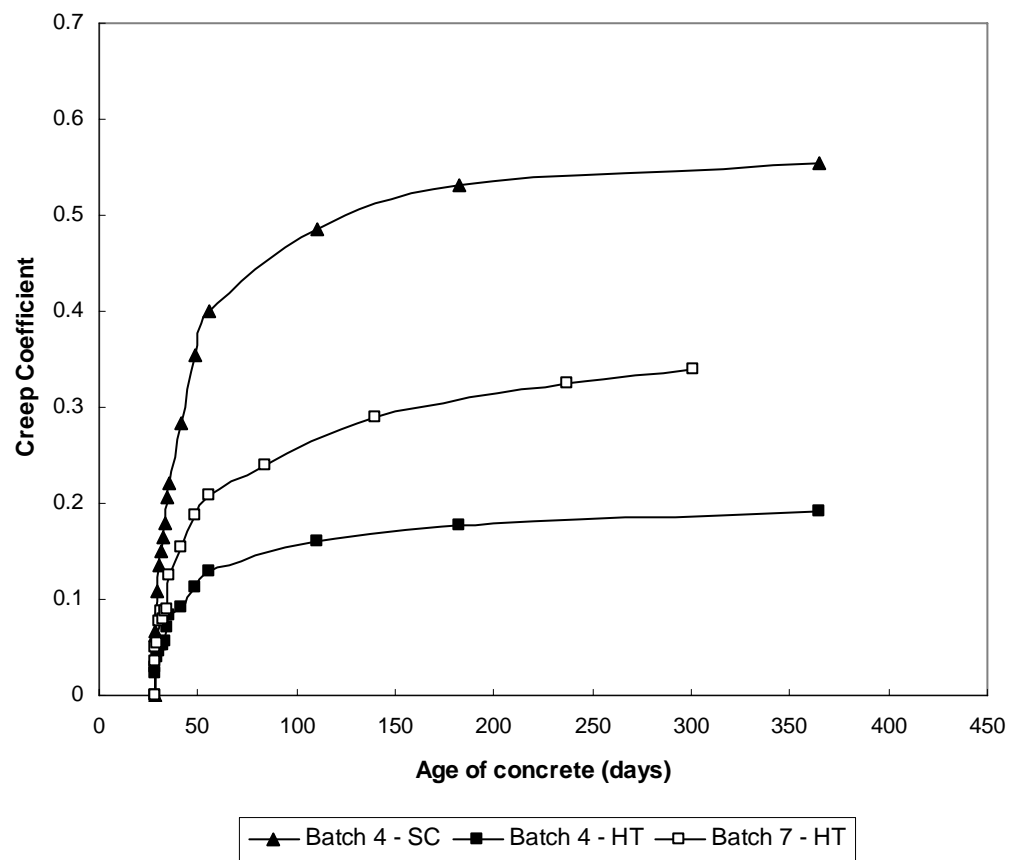


**Figure 4.28:** Creep coefficient curve for SF-RPC

### 4.7.2 Prediction of Creep Coefficient

Based on 28-day measurements  $\phi_{cr}(28)$ , the ACI Committee 209 (1992) suggests the following expression for the creep coefficient at any time  $t$  after first loading ( $t_0$ ):

$$\phi_{cr}(t, t_0) = \frac{2.35(t - t_0)^{0.6}}{10 + (t - t_0)^{0.6}} \phi_{cr}(28) \quad (4.27)$$

AS3600 (2001) suggests the following expression for the creep coefficient at time  $t$  due to a sustained stress first applied at age  $t_0$ :

$$\phi_{cr}(t, t_0) = k_2 k_3 \phi_{cc,b} \quad (4.28)$$

where  $\phi_{cc,b}$  is the basic creep factor

Constant  $k_2$  depends on the hypothetical thickness  $t_h$ , the relative humidity  $h$ , and the duration of load ( $t - t_0$ ) and may be calculated from (Gilbert, 1988)

$$k_2 = \frac{k_7 k_8 (t - t_0)^{0.7}}{(t - t_0)^{0.7} + k_9} \quad (4.29)$$

$$\text{where } k_7 = 0.76 + 0.9e^{-0.008t_h} \quad (4.30)$$

$$k_8 = 1.37 - 0.011h \quad (4.31)$$

$$k_9 = 0.15t_h \quad (4.32)$$

Constant  $k_3$  depends on the age of the concrete at the time of loading ( $t_0$ ) and can be determined from the ratio of the strength at first loading ( $f_c(t_0)$ ) to the strength at 28 days ( $f_c'$ ).

For a strength ratio in the range of 0.5 to 1.0,  $k_3$  may be expressed as:

$$k_3 = -0.8 \left( \frac{f_c(t_0)}{f_c'} \right) + 1.9 \quad (4.33)$$

For the strength ratio in the range of 1.0 to 1.4,  $k_3$  may be expressed as:

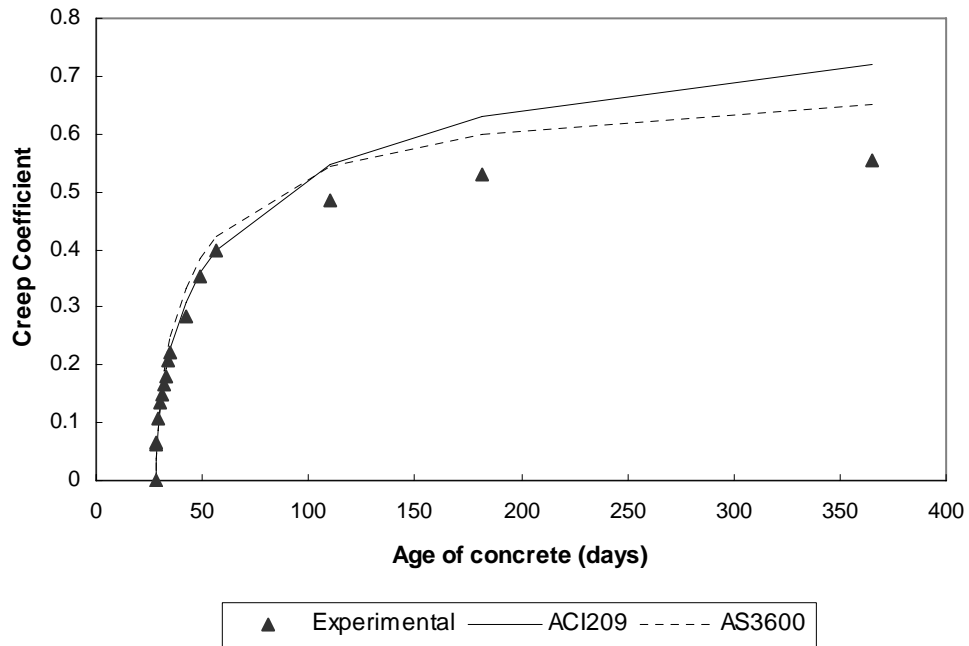
$$k_3 = -0.5 \left( \frac{f_c(t_0)}{f'_c} \right) + 1.6 \quad (4.34)$$

AS3600 (2001) is applicable to concretes with strengths ranging from 20 – 50MPa. The basic creep factors given in this code are therefore not applicable to SF-RPC. The basic creep factors used for the predictions of the creep coefficient of SF-RPC based on Equation 4.28 were 0.3 and 1.2 for specimens with and without initial heat treatment respectively. These creep factors are those proposed in the Design Guidelines for RPC Prestressed Concrete Beams (Section 2.5.1.1).

Figures 4.29 and 4.30 show the suitability of both the ACI 209 (1992) and AS3600 (2001) methods for predicting the creep coefficient with time for the SF-RPC investigated. As can be seen in this figure, the ACI 209 (1992) method provides a reasonable estimate for the creep coefficient of SF-RPC provided that the creep coefficient at 28 days ( $\phi_{cr}(28)$ ) is known. For this study, the creep coefficient at 28 days was determined experimentally. The AS3600 (2001) method using modified basic creep factors over-estimates the creep coefficient with time for specimens with or without initial heat treatment from Batch 4 but provides a reasonable estimate for the heat treated specimens from Batch 7. The over-estimate for specimens without initial heat treatment from Batch 4 is the result of using a basic creep factor of 1.2. At an age of 365 days, the measured creep coefficient for these specimens was 0.55 indicating that a basic creep factor of approximately 0.6 would have been more appropriate. The over-estimate for heat-treated specimens from Batch 4 is the result of the sustained stress level. Basic creep factors are for a sustained stress of 40% of the concrete strength. The heat-treated specimens from Batch 4 were under a sustained stress level of only 25% of the concrete strength. The reduced percentage of the sustained stress level used was to necessitate the use of a single creep rig for both standard cure and heat treated specimens from Batch 4. The standard cure specimens were at a sustained stress level of 40% which was approximately a sustained stress

level of 25% for the heat treated specimens. For heat-treated specimens from Batch 7, the sustained stress level was 40% of the concrete strength and therefore there is only a slight difference between the predicted and actual results.

### Standard Cure (Curing Condition 1)



### Heat treated (Curing Condition 2)

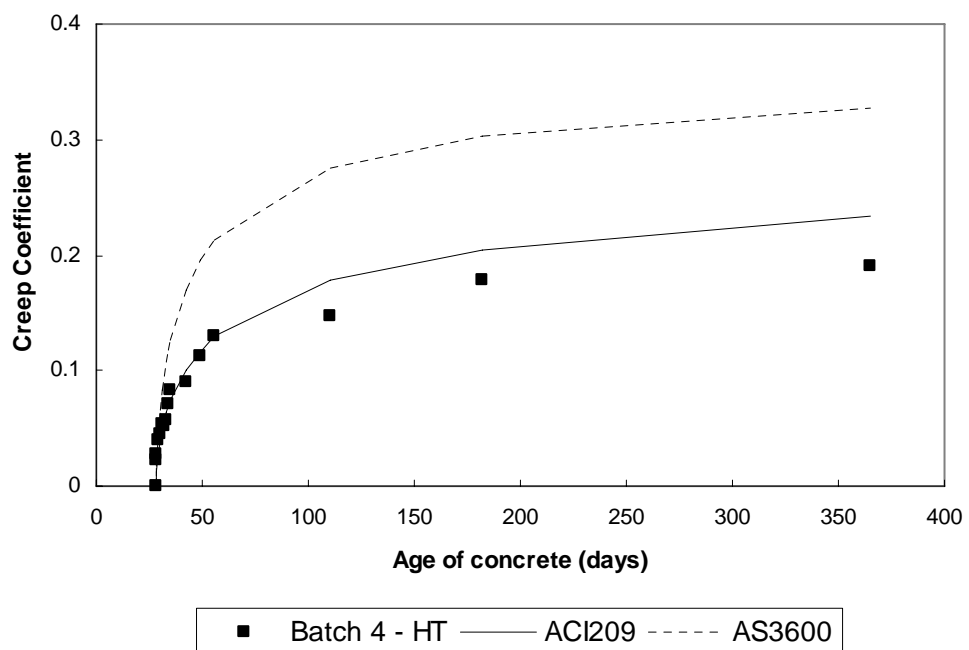


**Figure 4.29:** Comparison of measured and predicted creep coefficients  
(Batch 4)

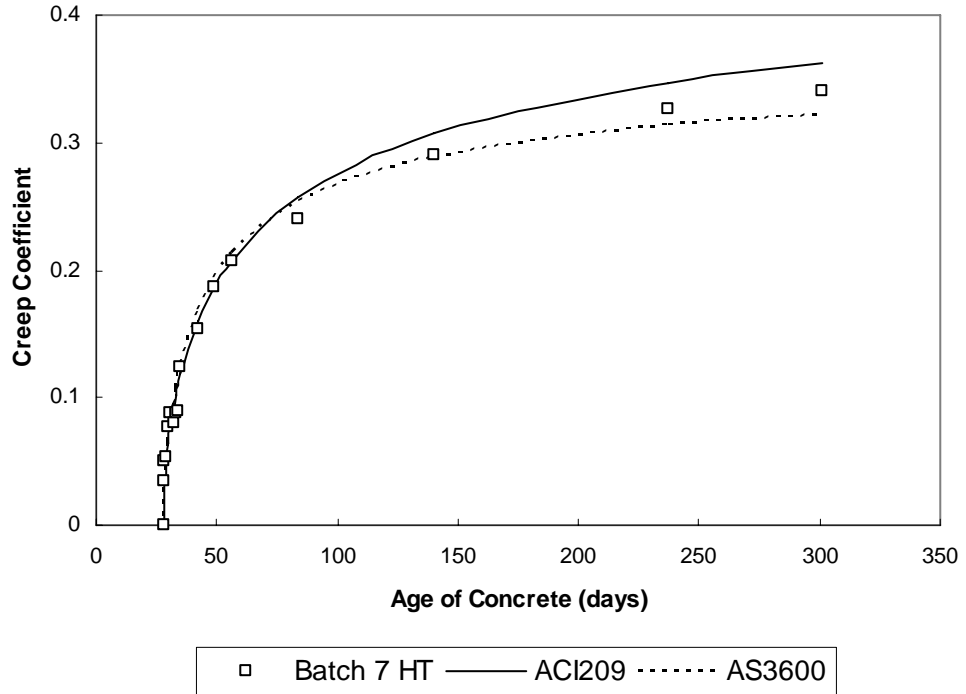


**Figure 4.30:** Comparison of measured and predicted creep coefficients  
(Batch 7)

From Figures 4.29 and 4.30, it can be seen that shape of the creep coefficient curves for the SF-RPC investigated is similar to the shape of the curves predicted by AS3600 (2001). Therefore, an equation of the following form was used for the trend lines for the creep coefficient results:

$$\phi_{cr}(t, t_0) = \frac{X(t - t_0)^{0.7}}{Y + (t - t_0)^{0.7}} \phi_{cc.b} \quad (4.35)$$

where  $X$  and  $Y$  are values determined from the experimental data

Figure 4.31 shows the trend lines, together with the value of the parameters  $X$ ,  $Y$  and  $\phi_{cc.b}$  for the creep coefficient results from Batch 4 and 7. The HT parameters for Batch 7 are used to model the creep of the concrete in the time-dependent analysis of the prestressed slabs in Chapter 6.

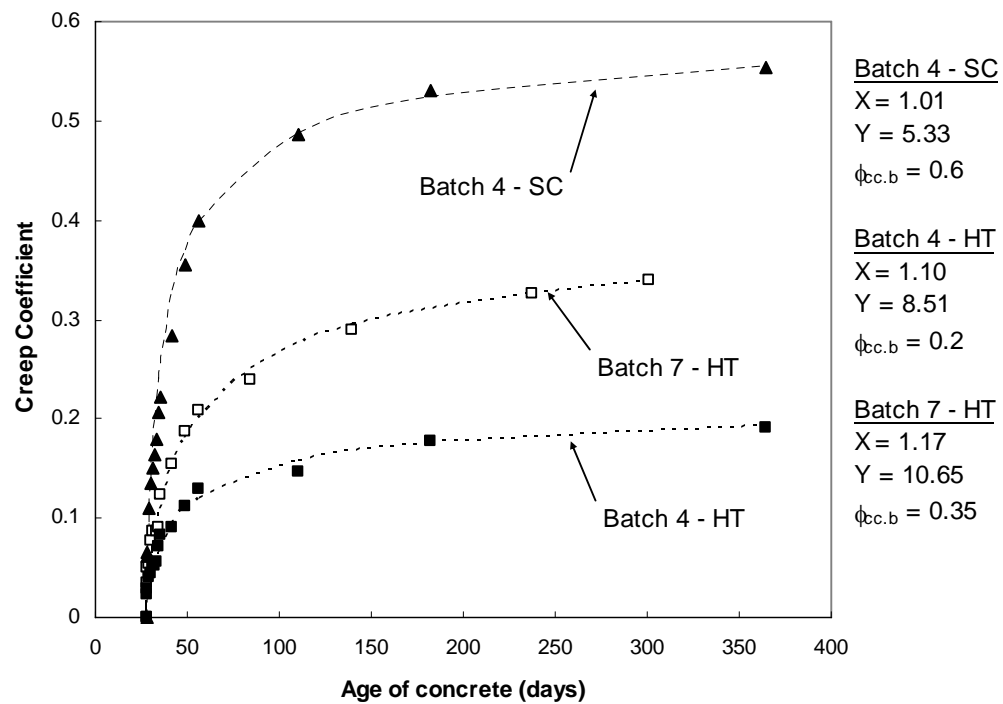


**Figure 4.31:** Trend lines for creep coefficients (Batch 4 and 7)

#### 4.8 SUMMARY OF RESULTS

From the experimental results presented here and the comparisons made between test results and theoretical predictions, the following points summarise the properties of the SF-RPC used in this study:

1. The material has an average 28-day compressive strength of 167.0MPa and a characteristic compressive strength of 153.0MPa for specimens that have undergone heat treatment.
  - a. For heat treated SF-RPC, the compressive strength obtained at the end of heat treatment can be taken as the final strength. The temperature that the heat treatment is carried out at, has a greater effect on compressive strength than the duration of curing.
  - b. For SF-RPC without initial heat treatment, the rate of compressive strength development is greatest at early age. The final strength is about 1.3 times the strength at 28 days when the specimens undergo standard moist curing conditions.

2. The material has an average 28-day flexural strength of 23.0 MPa and a characteristic flexural strength of 16.5MPa for specimens that have undergone heat treatment. The material displays considerable ductility in the post-peak range of the load-deflection curve.
  - a. For heat treated SF-RPC, the flexural strength obtained at the end of heat treatment can be taken as the final strength. The flexural strength lies in the range of 1.5 to 2.3 times the square root of the compressive strength.
  - b. For SF-RPC without initial heat treatment, the rate of flexural strength development is greatest at early age. The final strength is about 1.1 times the strength at 28 days when the specimens undergo standard moist curing conditions.
3. The material has an average 28-day estimated direct tensile strength of 8.3MPa for specimens that have undergone heat treatment. The range of calculated tensile strengths is 6.3 to 11.1MPa.
4. The material has an average 28-day modulus of elasticity of 45.5GPa and a characteristic modulus of elasticity of 43.1GPa.
  - a. For heat treated SF-RPC, the modulus of elasticity obtained at the end of heat treatment can be taken as the final value. The modulus of elasticity (in GPa) lies in the range of 3.4 to 3.6 times the square root of the compressive strength.
  - b. For SF-RPC without initial heat treatment, the rate of modulus of elasticity development is greatest at early age. The final value is about 1.1 times the strength at 28 days when the specimens undergo standard moist curing conditions.
5. The stress-strain behaviour of SF-RPC is best determined experimentally. A conservative model for the stress-strain behaviour may be taken as that shown in Figure 4.16. The Poisson's Ratio of SF-RPC may be conservatively taken as 0.2.
6. The majority of shrinkage that occurs in heat treated SF-RPC is autogenous. The autogenous shrinkage of heat treated SF-RPC is about 400 $\mu\epsilon$  with a small proportion (100 - 150 $\mu\epsilon$ ) of shrinkage strain

occurring post heat treatment. Like conventional concrete, the rate of drying shrinkage for heat treated SF-RPC develops rapidly at early age and continues to increase at a decreasing rate.

7. The shrinkage of non heat-treated SF-RPC, like conventional concrete, develops rapidly at early age and continues to increase at a decreasing rate. Current equations available for predicting the shrinkage of concrete over-estimate the shrinkage of non heat-treated SF-RPC.
8. Using regression analysis, the shrinkage of SF-RPC may be expressed as a function of time by the following equation:

$$\varepsilon_{sh}(t, t_0) = 400 + 38.5 \ln(t) - 79$$

For design purposes, the long-term shrinkage for the SF-RPC studied may be estimated as  $720\mu\epsilon$ .

9. The creep of SF-RPC with or without initial heat treatment, like conventional concrete, develops rapidly at early age and continues to increase at an appreciably decreasing rate with time. Initial heat treatment significantly reduces the creep of SF-RPC. Creep coefficients for SF-RPC are smaller than those of conventional concrete.
10. The equation for the creep coefficients with time found in ACI 209 (1992) gives reasonable values provided the creep coefficient at 28 days is known. The method found in AS3600 (2001), with modified basic creep factors, gives reasonable predictions for the creep coefficient curves of SF-RPC with time.

## **Chapter 5: Short-term Flexural Behaviour**

### **5.1 INTRODUCTION**

Flexural behaviour, especially the ultimate flexural strength, is a key consideration for the design of any structure in bending. The behaviour of a member under service load is important as it is the observable behaviour of the structure throughout its life. The ultimate flexural strength is the most important design objective for a member as failure to provide adequate strength usually involves considerable costs to repair and in extreme situations can have dire consequences. Therefore, it is important to understand the flexural behaviour of structures in order to be able to provide adequate strength and behaviour under service loads.

This chapter presents the experimental results and analysis of the short-term flexural behaviour and ultimate flexural strength of both the plain and prestressed SF-RPC beams (Series 1 and 2, respectively). Series 1 consisted of 4 plain SF-RPC beams of 2 different cross-sections. The beams were tested for ultimate flexural strength under displacement control at an age of approximately 28 days. Series 2 consisted of 8 prestressed beams of 4 different cross-sections. The beams in this series were tested for ultimate strength under displacement control at an age of approximately 28 days.

The first two sections of the chapter present the test results for both Beam Series 1 and 2. These test results include the moment-curvature relationships, load-deflection behaviour, the crack patterns and the cracking loads and the ultimate flexural strengths of all beams tested, along with a qualitative discussion of the results. The remainder of the chapter provides details of the analysis of the results. The performance of existing models (see Section 2.5) is evaluated, and details of a modified model are presented. Details pertaining to the modified model include its development, performance evaluations and simplifications along with the limitations and recommendations for further research.

## 5.2 PLAIN SF-RPC BEAMS

### 5.2.1 Test Procedures

The aim of Beam Series 1 was to gain some insight into the flexural behaviour of plain SF-RPC beams. The series consisted of 4 beams of 2 different cross-sections. Details of the beam cross-sections can be found in Figure 3.7, beam designations in Table 3.4 and loading arrangement in Figure 3.10. The beams were tested at an age of between 26 – 30 days. Identical cross-sections (e.g. Beams P1 A and P1 B) were produced from a single batch. Details of the batch during which any given beam was produced can be found in Section 3.4. The results of the material tests conducted on companion specimens from each batch can be found in Chapter 4.

In order to capture the full flexural behaviour including the descending portion of the load-deflection curve, the beams were tested under displacement control measured from the midspan deflection. Testing in this mode allows for load reduction while the deformation of the specimen increases uniformly. In this way, the loading rate is reduced automatically when the specimen is approaching its ultimate flexural strength and thus, sudden failure is avoided. The displacement rate was 0.2mm per minute for cross-section P1 and 0.4mm per minute for cross-section P2.

The following data was collected for each beam specimen: At various load levels during the ascending portion of the load-deflection curve, surface strain measurements (using a demec gauge with a gauge length of 250mm) were taken at various depths throughout the constant moment region. The demec gauge used had a gauge length of 250mm. In addition to this, once cracks were visible on the surface of the member, the cracks were marked and digital images were taken of the crack pattern. Throughout the duration of the test, a complete load–deflection curve was recorded electronically using a load cell and three LVDTs located at midspan and under the application of the point loads.

For plain SF-RPC beams, failure can occur by either crushing of the concrete in the compression zone or by unstable crack propagation. Therefore failure is sudden and for safety reasons, the tests in this series were stopped when the

load had dropped to about one-third of the peak load. This allowed for a substantial amount of post-peak data to be collected without the risk of sudden catastrophic failure. Therefore, the mode of failure was not verified.

### **5.2.2 Moment – Curvature Behaviour**

For the moment-curvature relationships shown in this section, the curvature was obtained from strain measurements at various depths throughout the constant moment region of the beams. The arrangement of the demec targets can be seen in Figure 3.14.

#### **P1 BEAMS**

The moment-curvature relationships of the two beams of cross-section P1 tested as part of Series 1 are shown in Figure 5.1. As can be seen from this figure, the beams behave linearly before cracking. After cracking occurred, the beams continued to carry increasing load with decreasing stiffness as the cracks propagating in depth up to the peak moment which was 1.5 – 1.7 times the cracking moment.

#### **P2 BEAMS**

The moment-curvature relationships of the two beams of cross-section P2 tested as part of Series 1 are shown in Figure 5.2. As can be seen in the figure, the behaviour of the beams was similar to that of the beams of cross-section P1. The beams behaved linearly prior to cracking and after cracking, the beams continued to carry increasing load with decreasing stiffness up to the peak moment which was 1.9 – 2.0 times the cracking moment.

Cross-section P2 A and P2 B were cast from the same batch (Batch 1). Despite this, there is a slight variation in the moment-curvature response of the two sections. The small variation in the results of the two identical cross-sections can be attributed to the natural variations in fibre reinforced concrete.

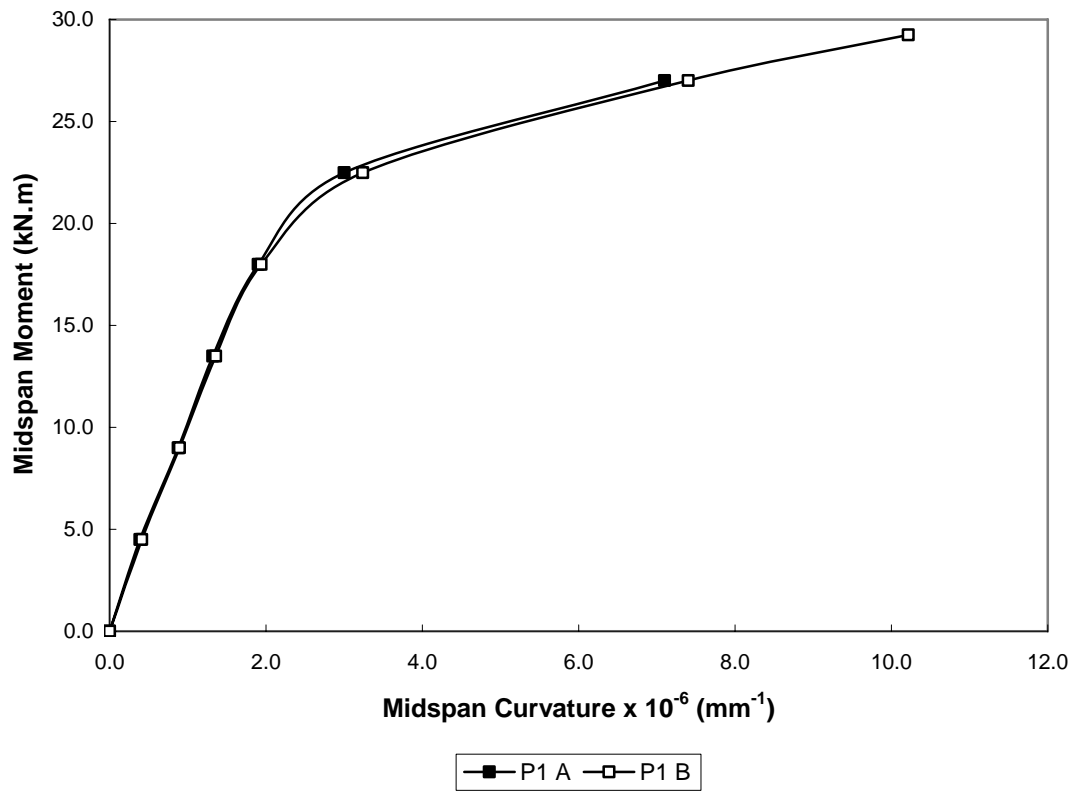


Figure 5.1: P1 moment – curvature relationship

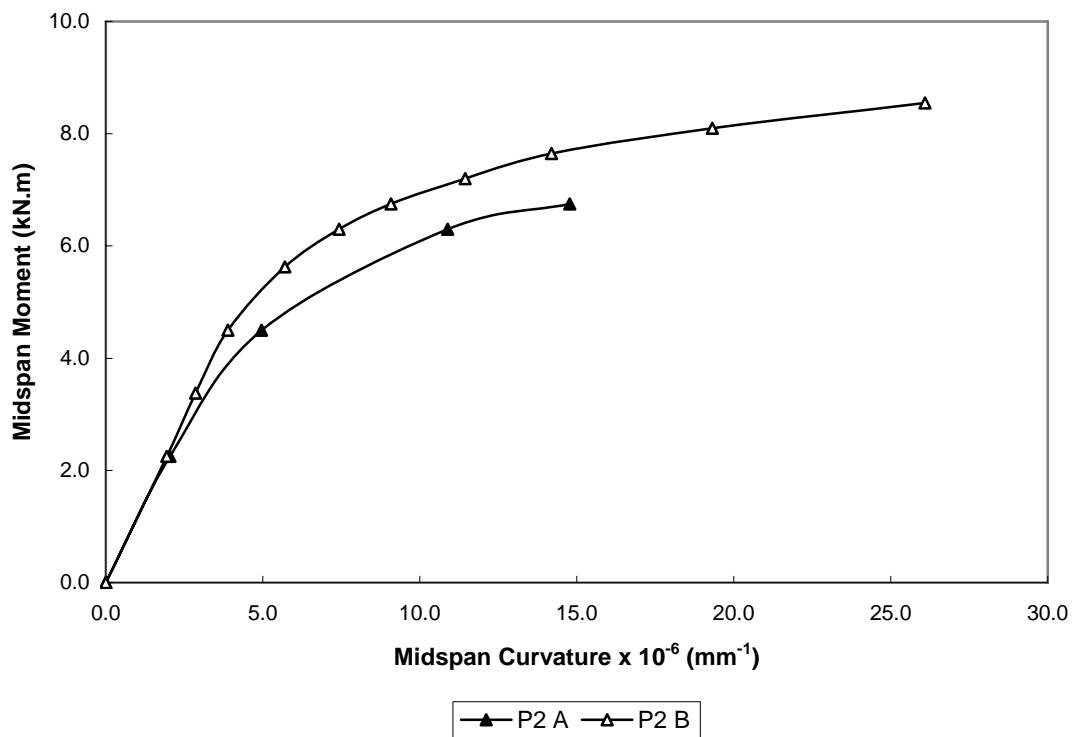
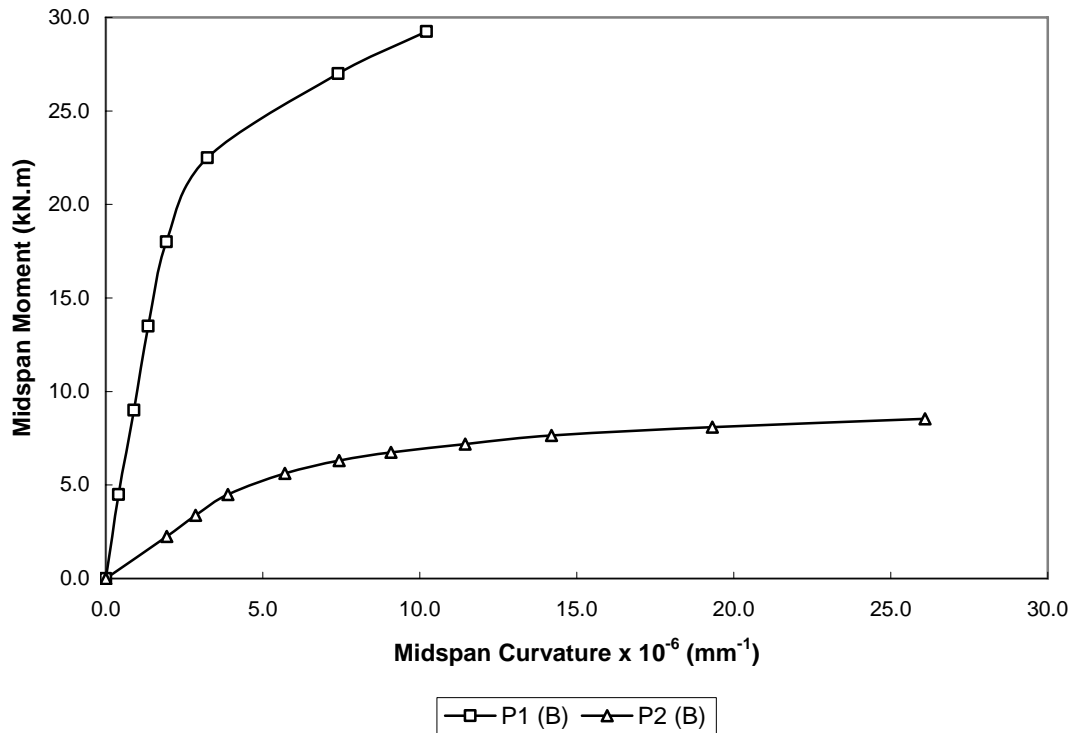


Figure 5.2: P2 moment – curvature relationship

Figure 5.3 shows a comparison of the moment-curvature relationships for the two cross-sections investigated. It can be seen in this figure that P1 beams have a greater stiffness i.e. lower curvatures than P2 beams as expected due to their cross-sectional geometry.



**Figure 5.3:** Comparison of moment – curvature relationships Beam Series 1

### 5.2.3 Load – Deflection Behaviour

#### P1 BEAMS

The load-deflection curves of the two beams of cross-section P1 tested as part of Series 1 are shown in Figures 5.4. The load-deflection behaviour was linear before cracking and increasingly non-linear after cracking as the stiffness of the section continued to decrease with increasing crack depth. The deflection at the peak load was at least 2.5 times the deflection at first cracking. The beams were still carrying a significant portion (approximately 30%) of the peak load despite deflections exceeding 6 times the deflection at first cracking (or about 4 times the deflection at the peak load).

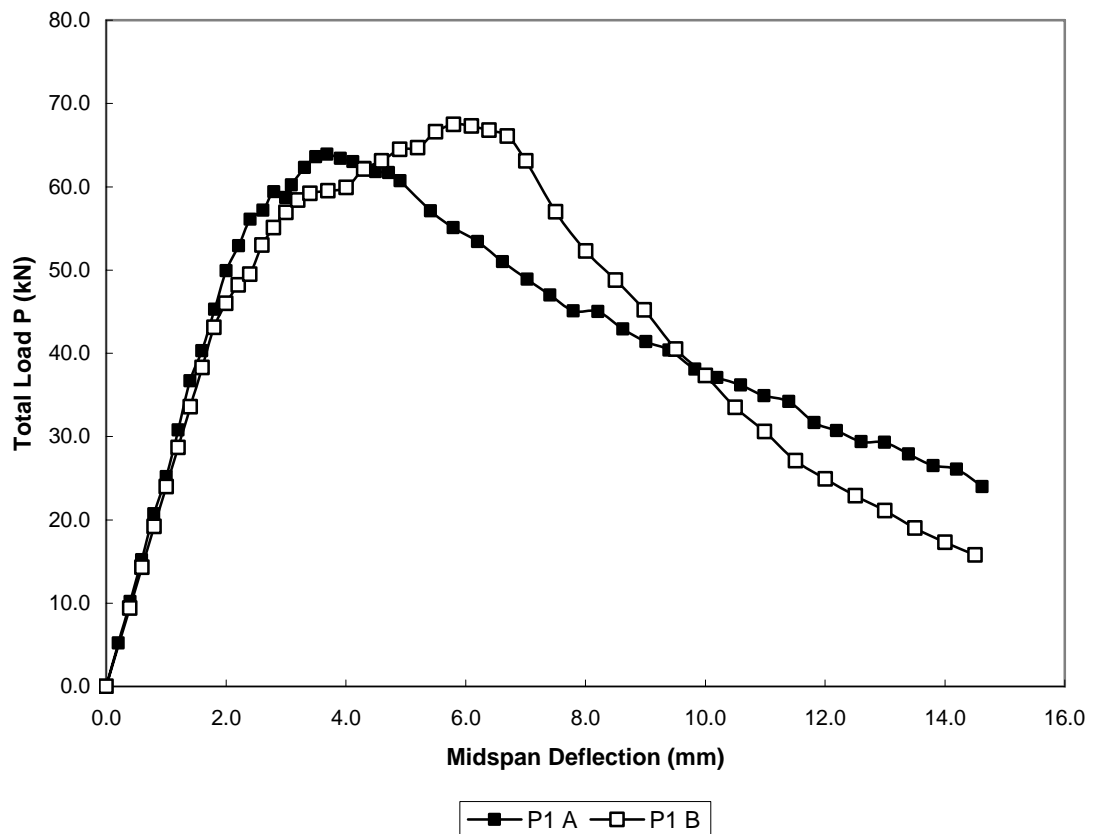


**Figure 5.4:** P1 load – deflection behaviour

### P2 BEAMS

The load-deflection curves of the two beams of cross-section P2 tested as part of Series 1 is shown in Figure 5.5. As can be seen in the figure, the shape of the load-deflection curves of the beams was similar in shape to the curves for cross-section P1. Cross-section P2 had a lower initial stiffness and therefore, as expected, the P2 beams exhibited lower strength but greater deflections. The deflection at the peak load was at least 4 times the deflection at first cracking. As with the beams of cross-section P1, the beams of cross-section P2 were still able to carry a significant portion of the peak load despite deflections exceeding almost 10 times the deflection at first cracking (or about 2 times the deflection at the peak load).

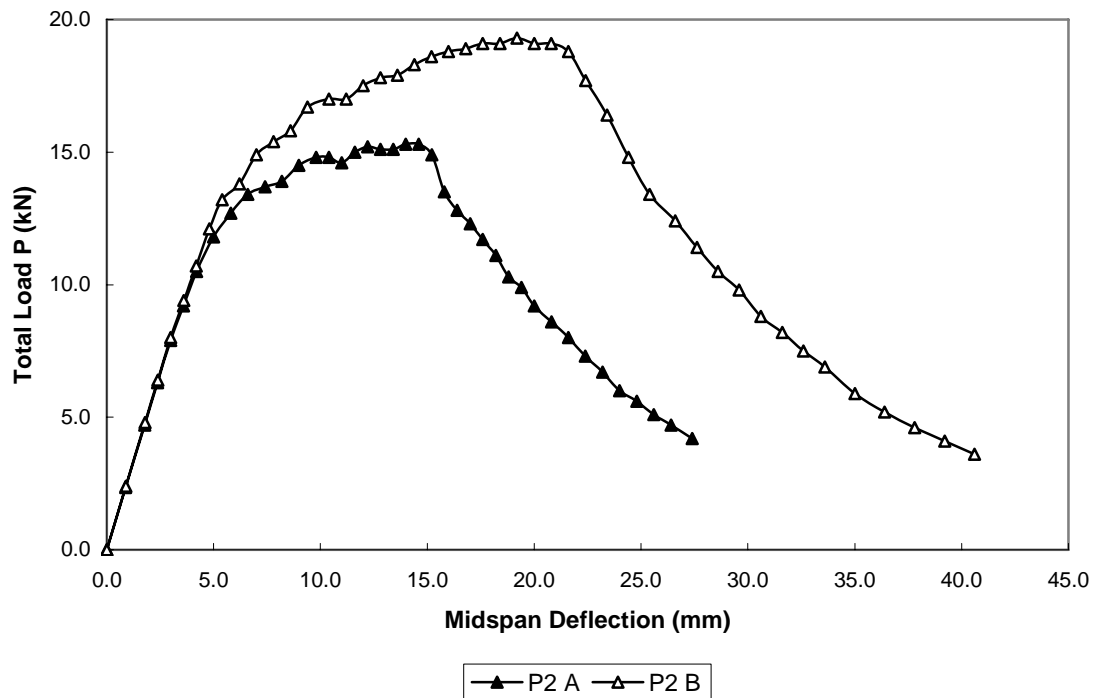


**Figure 5.5:** P2 load – deflection behaviour

The differences in the load-deflection curves for both plain beam cross-sections tested are the result of the natural variations present in all fibre-reinforced concrete. To a limited extent, this was also seen in the moment-curvature result for cross-section P1. In the absence of any traditional longitudinal reinforcement or prestressing steel, the flexural tensile capacity of the SF-RPC governs the behaviour of the beams after first cracking. As this property of the material can be highly variable (see Section 4.3) due to the random distribution of fibres, it is to be expected that this variation will appear in the moment-curvature and load-deflection beam results for the plain cross-sections tested. The effect is more pronounced in the load-deflection behaviour than in the moment-curvature behaviour as the load-deflection data was more detailed and covered a greater duration of the tests than the moment-curvature data.

It is due to this natural variation in the material properties of all fibre-reinforced concretes including SF-RPC that makes modelling the structural behaviour of these materials difficult. These variations may be accounted for by considering upper and lower bound curves. For design purposes, the lower bound curve along with an applied safety factor may be used.

### 5.2.4 Cracking Behaviour

In order to examine the cracking behaviour of the beams tested, digital images of each beam specimen were taken throughout the ultimate moment tests. The surface of each beam was painted with white acrylic paint in order to facilitate the detection of cracks and to provide clear crack markings for the digital photos. No attempt was made to implement digital imaging technology in the analysis of the digital photos.

For both P1 beams, the first visible cracks appeared on the surface of the member at a load of approximately 50kN. In each case, a single crack could be seen somewhere within the constant moment region of the beam. As the load level was increased, an increasing number of cracks appeared and these cracks continued to extend through the depth of the cross-section. As the peak load was reached, crack development become localised to a single crack. Both the depth and the width of the 'failure crack' increased whilst all other cracks remained essentially the same. As there was little difference between the responses of the two P1 beams, only the final crack pattern for P1 B is shown in Figure 5.6.

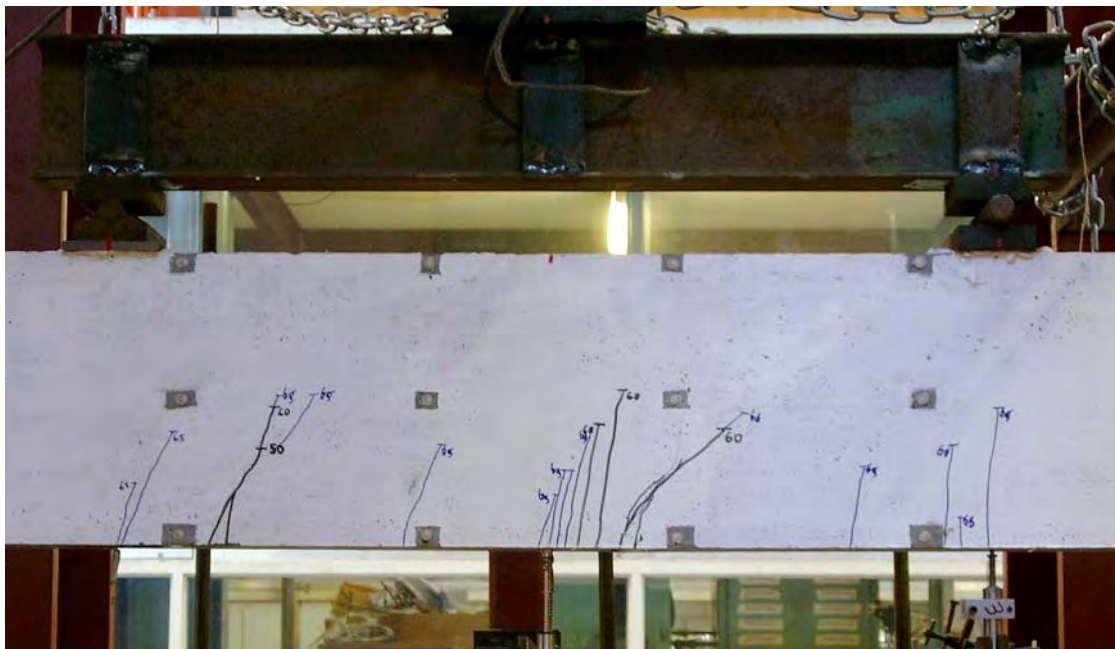


**Figure 5.6:** Final crack pattern in constant moment region P1 B

For both P2 beams, the first visible cracks appeared on the surface of the member at a load of approximately 14kN. At a load of 14kN, 5 cracks were visible on beam P2 A and 1 crack was visible on beam P2 B. The cracking behaviour of the P2 beams was similar in nature to that of the P1 beams. The final crack pattern for P2 B is shown in Figure 5.7.

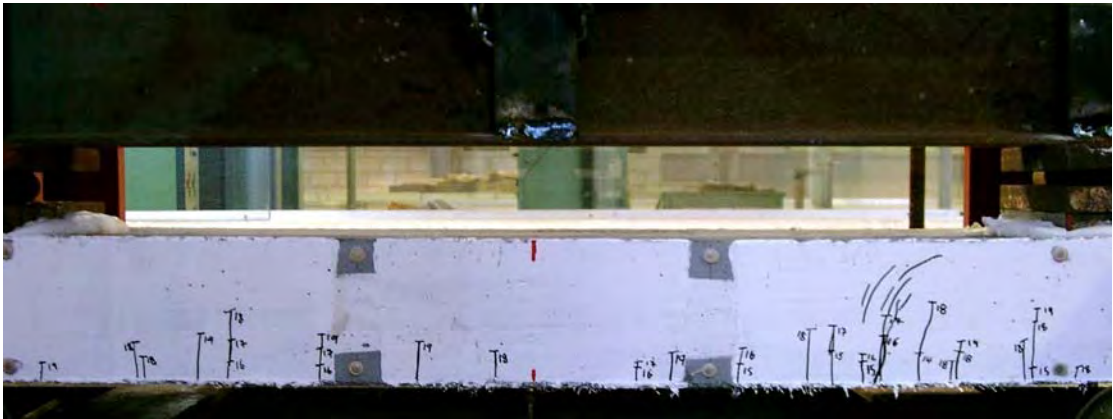


**Figure 5.7:** Final crack pattern in constant moment region P2 B

As can be seen in Figures 5.6 and 5.7, the crack pattern of a plain SF-RPC beam is similar in nature to a conventional reinforced concrete beam i.e. the formation of numerous cracks throughout the constant moment region. The cracks develop slowly and the beams are still able to carry increasing load after first crack. This is different to a plain concrete beam in which a single crack develops and rapidly leads to failure with little or no increase in load.

### 5.2.5 Summary of Test Results for Beam Series 1

Table 5.1 is a summary of the 4 beam tests conducted as part of Series 1. The table shows the cracking moment, ultimate moment, deflection at first cracking as well as deflection at ultimate. The average ratio of ultimate moment to cracking moment is 1.60 for P1 beams and 1.97 for P2 beams. The average ratio for deflection at ultimate to deflection at cracking is 2.83 and 4.83 for P1 and P2 beams, respectively.

**Table 5.1:** Test Results for Beam Series 1

Beam ID	P1 A	P1 B	P2 A	P2 B
Cracking moment (kNm), $M_{cr}$	17.1	20.1	3.6	4.3
Ultimate moment (kNm), $M_u$	28.8	30.6	6.9	8.7
$M_u/M_{cr}$	1.68	1.52	1.92	2.02
Deflection at first cracking (mm), $\Delta_{cr}$	1.47	1.93	3.04	3.7
Deflection at ultimate (mm), $\Delta_u$	3.79	5.92	13.48	19.36
$\Delta_u/\Delta_{cr}$	2.58	3.07	4.43	5.23

The behaviour of plain SF-RPC beams is significantly different from the behaviour of plain conventional concrete beams i.e. despite the absence of any traditional steel reinforcement SF-RPC beams display considerable ductility. For plain conventional concrete beams, steel reinforcement is essential to obtain the level of ductility required for a flexural element. The ductility of plain SF-RPC beams is the result of the addition of the fibres making their inclusion necessary if the member is to be used as a flexural element. In this way, plain SF-RPC beams behave in a similar manner to conventional reinforced concrete beams.

### 5.3 PRESTRESSED SF-RPC BEAMS

#### 5.3.1 Test Procedures

In order to gain some insight into the flexural behaviour of prestressed SF-RPC beams, 8 beams of 4 different cross-sections were tested as part of Beam Series 2. Details of the beam cross-sections are shown in Figure 3.8 and beam designations are specified in Table 3.6. The beams were tested at an age of 26 – 32 days. The loading arrangement is shown in Figure 3.10.

The beams were tested under displacement control measured from the movement of the hydraulic loading jack. The displacement rate was 0.36mm per minute for cross-section S1 and 0.6mm per minute for cross-sections S2, S3 and S4. The tests were stopped when the load had dropped by 5% from the peak load for safety reasons. It was observed that all beams displayed

some crushing of the concrete in the compression zone at the completion of each test indicating a typical flexural failure.

The data collected for each beam specimen was identical to the data collected for the beams in Series 1.

No data was collected on the beams at transfer or from transfer up to the application of load. These details were approximated from existing principles for prestressed beams and are contained in Appendix B.

### 5.3.2 Moment – Curvature Behaviour

#### S1 BEAMS

The moment-curvature relationships of the two beams of cross-section S1 tested as part of Series 2 are shown in Figures 5.8.

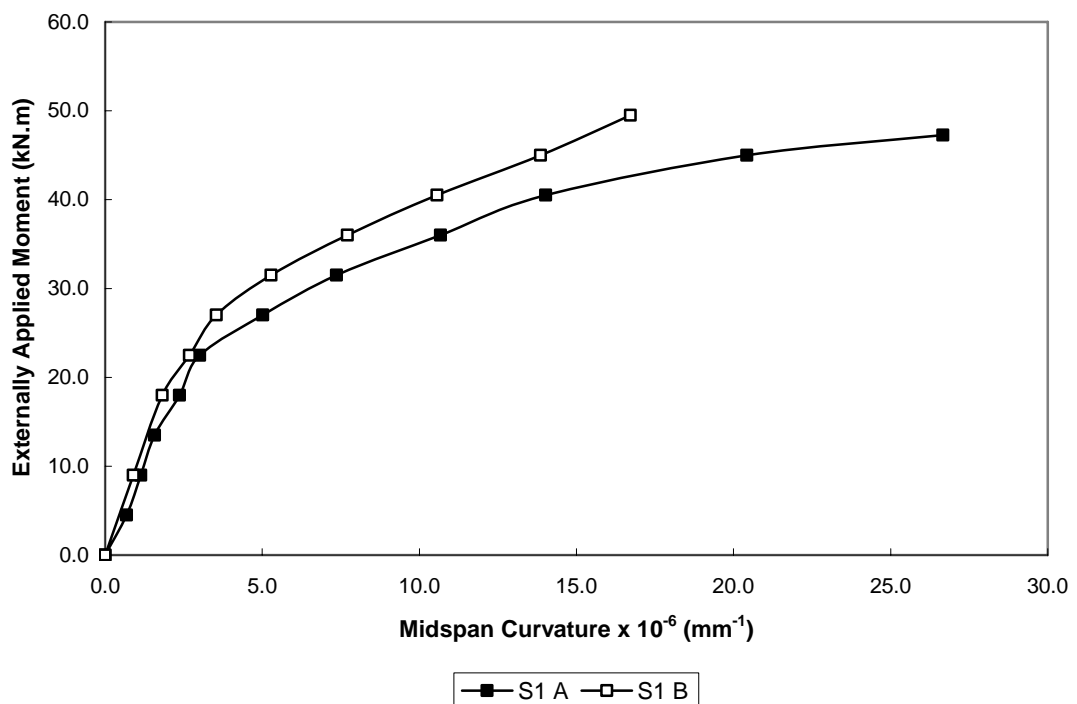


**Figure 5.8:** S1 moment – curvature relationship

#### S2 BEAMS

The moment-curvature relationships of the two beams of cross-section S2 tested as part of Series 2 are shown in Figure 5.9.

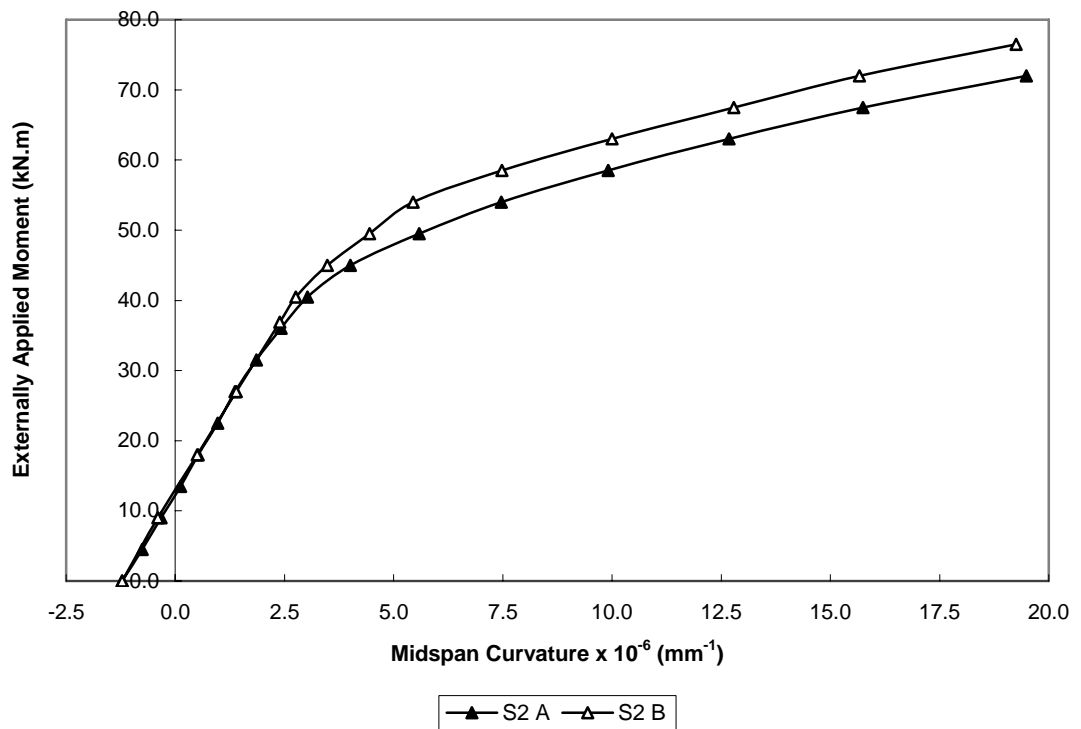


**Figure 5.9:** S2 moment – curvature relationship

### S3 BEAMS

The moment-curvature relationships of the two beams of cross-section S3 tested as part of Series 2 are shown in Figure 5.10.

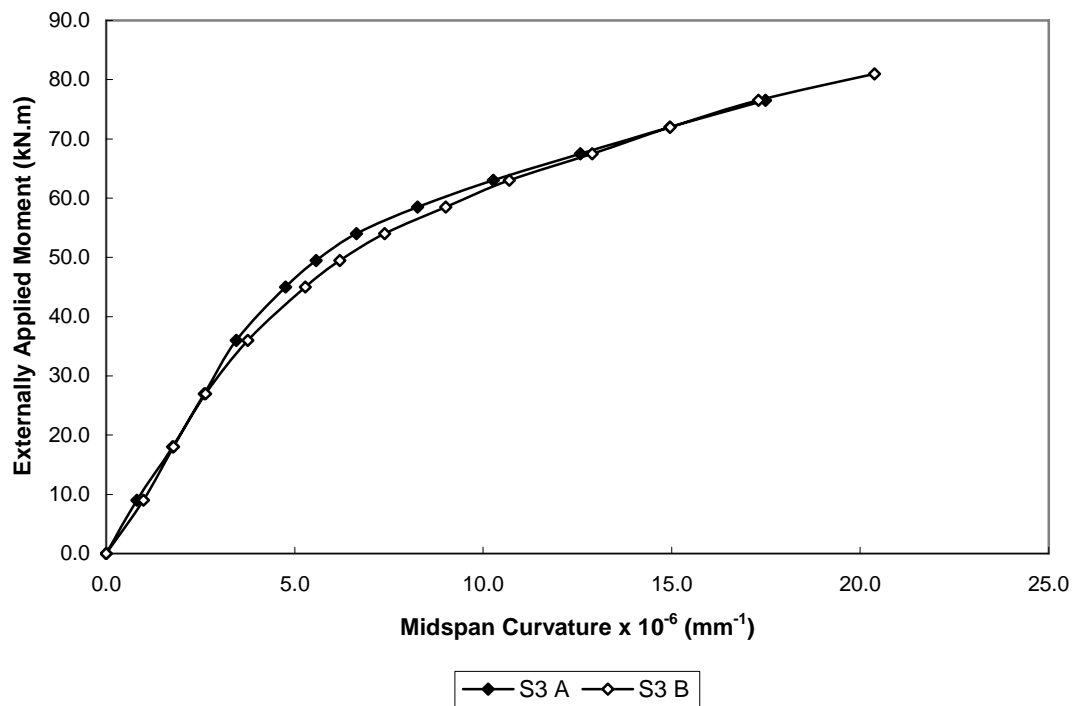


**Figure 5.10:** S3 moment – curvature relationship

## S4 BEAMS

The moment-curvature relationships of the two beams of cross-section S4 tested as part of Series 2 are shown in Figure 5.11.

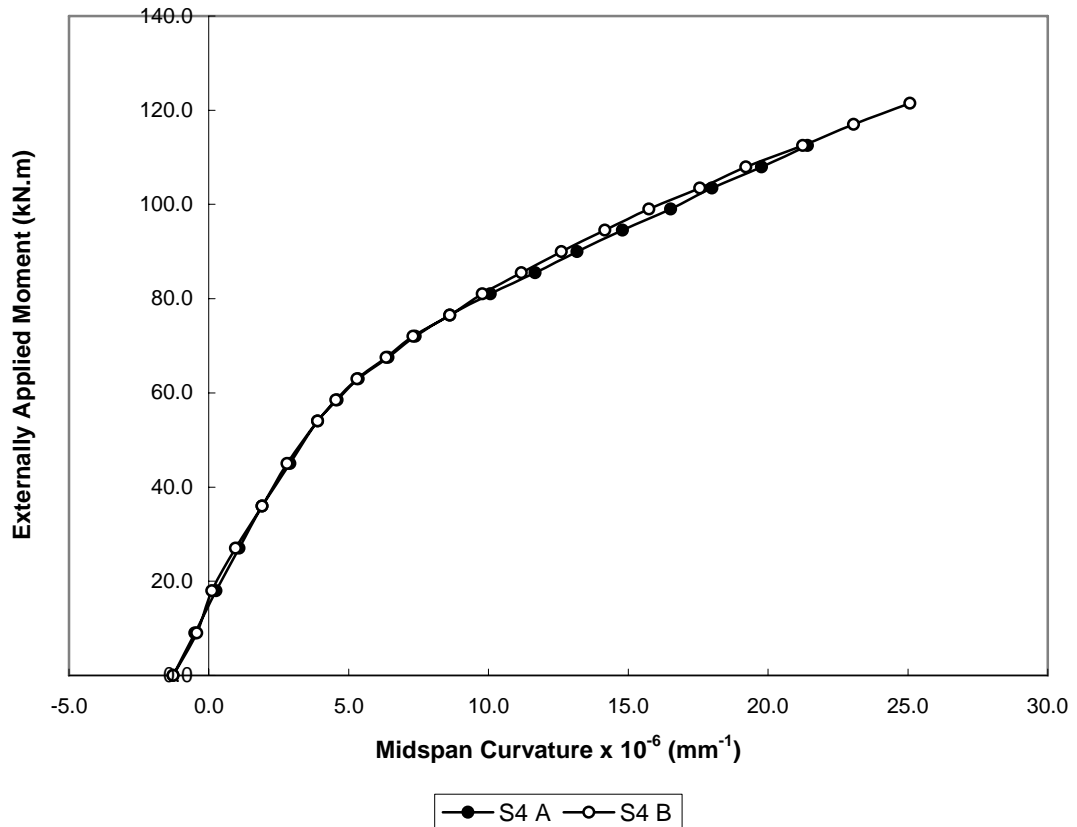


**Figure 5.11:** S4 moment – curvature relationship

It can be seen from Figures 5.8 – 5.11 that prestressed SF-RPC beams behave linearly before cracking and almost linearly after cracking with a reduced stiffness up to approximately 85% of the ultimate moment capacity of the section. After cracking has occurred, the beams continue to carry increasing load with decreasing stiffness as the cracks propagate in depth up to the peak moment which was at least 1.8 times the moment at which first crack occurred.

Figure 5.12 shows a comparison of the moment-curvature relationships for the four cross-sections investigated as part of Series 2. It can be seen that as the steel ratio (area of steel/gross cross-sectional area) increases the ultimate moment capacity of the section also increases. An increase in steel ratio also results in an increase in the cross-sectional stiffness after cracking has

occurred as indicated by the increase in the slope of the post-cracking portion of the moment-curvature relationships for the four cross-sections from S1 to S4.

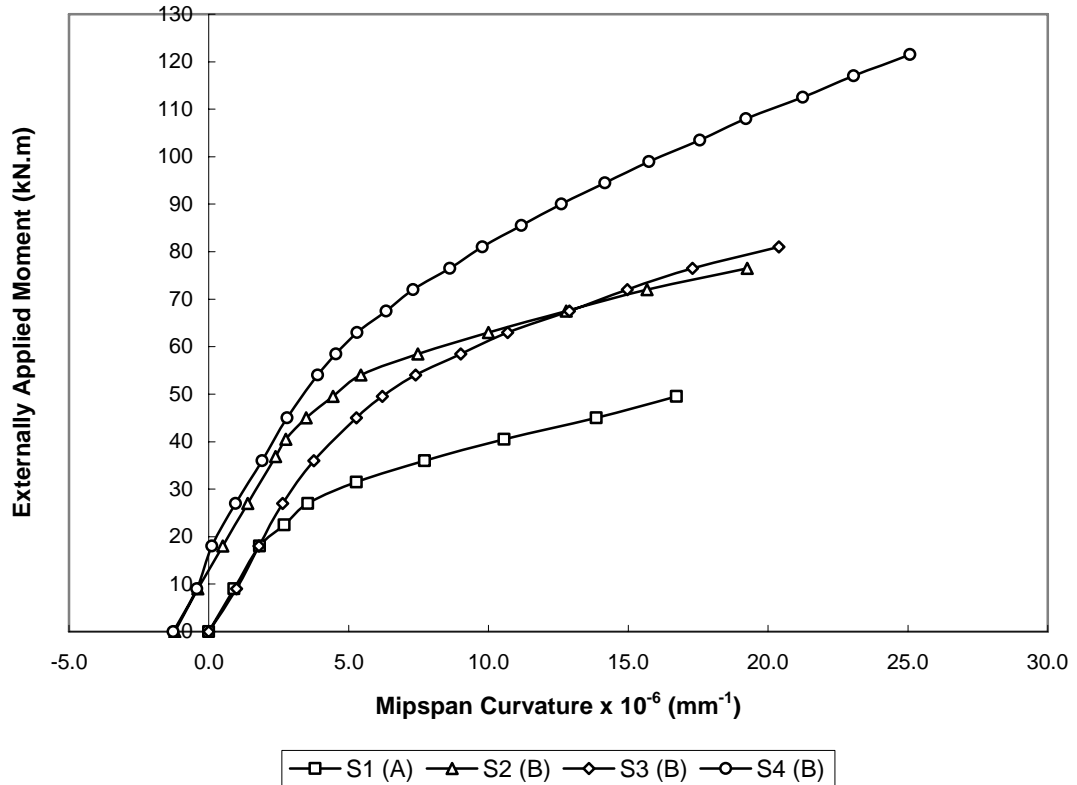


**Figure 5.12:** Comparison of moment – curvature relationships Beam Series 2. Cross-sections S1 and S2 are geometrically identical and therefore, the shape of the moment-curvature relationship for these two sections is similar. The difference between the two sections was that no initial prestress was applied to cross-section S1. From the results for these two sections, the effect of prestress can be seen. The application of prestress leads to an increase in the load to first crack and ultimate moment capacity. However, after cracking has occurred, the beams have a similar cross-sectional stiffness and therefore, the slope of the post-crack portion of the two curves is almost identical.

### 5.3.3 Load – Deflection Behaviour

#### S1 BEAMS

The load-deflection curves of the two beams of cross-section S1 tested as part of Series 2 is shown in Figures 5.13.

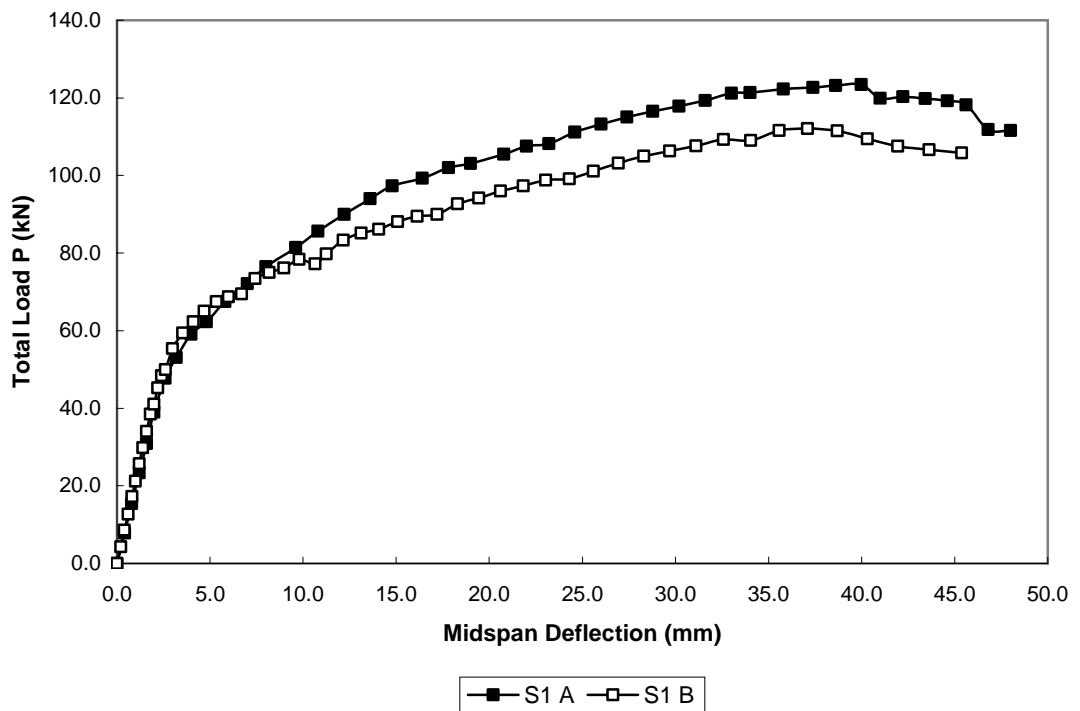


**Figure 5.13:** S1 load – deflection behaviour

#### S2 BEAMS

The load-deflection curves of the two beams of cross-section S2 tested as part of Series 2 is shown in Figure 5.14.

#### S3 BEAMS

The load-deflection curves of the two beams of cross-section S3 tested as part of Series 2 is shown in Figure 5.15.

#### S4 BEAMS

The load-deflection curves of the two beams of cross-section S4 tested as part of Series 2 is shown in Figure 5.16.

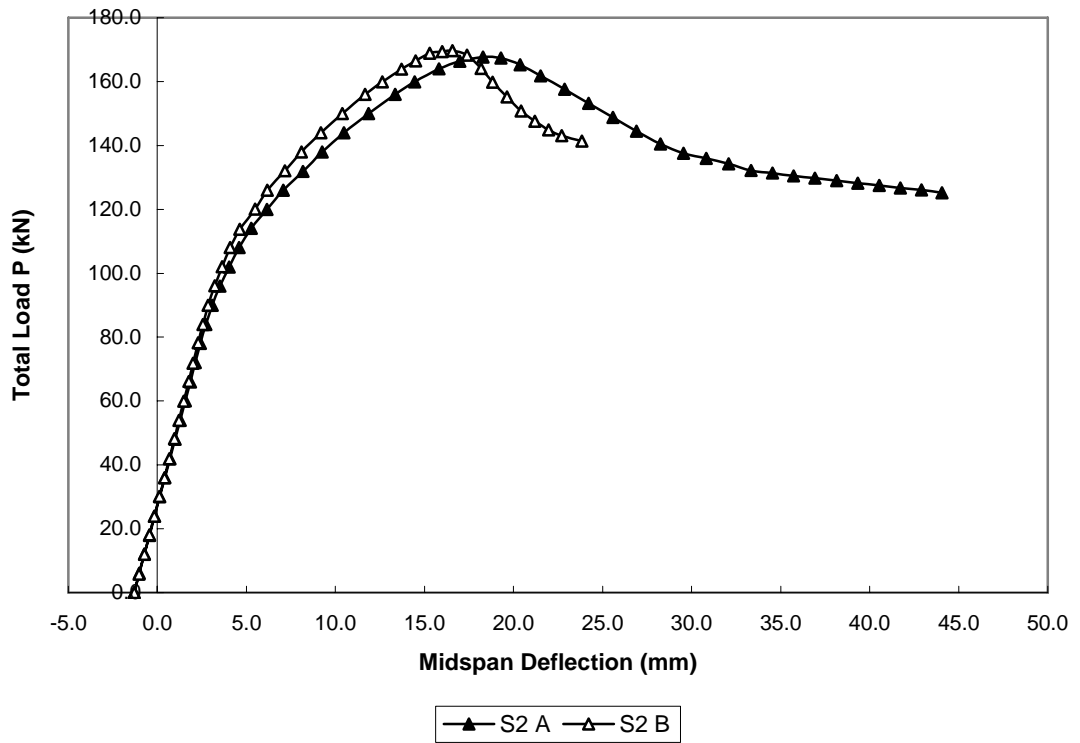


Figure 5.14: S2 load – deflection behaviour

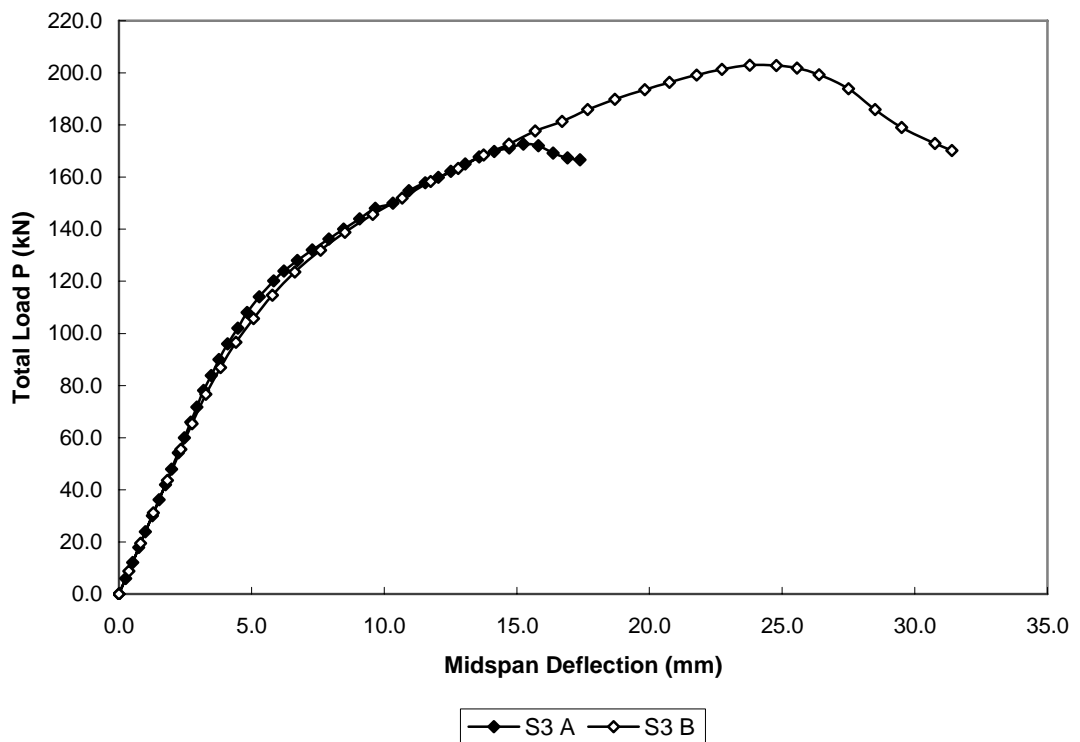
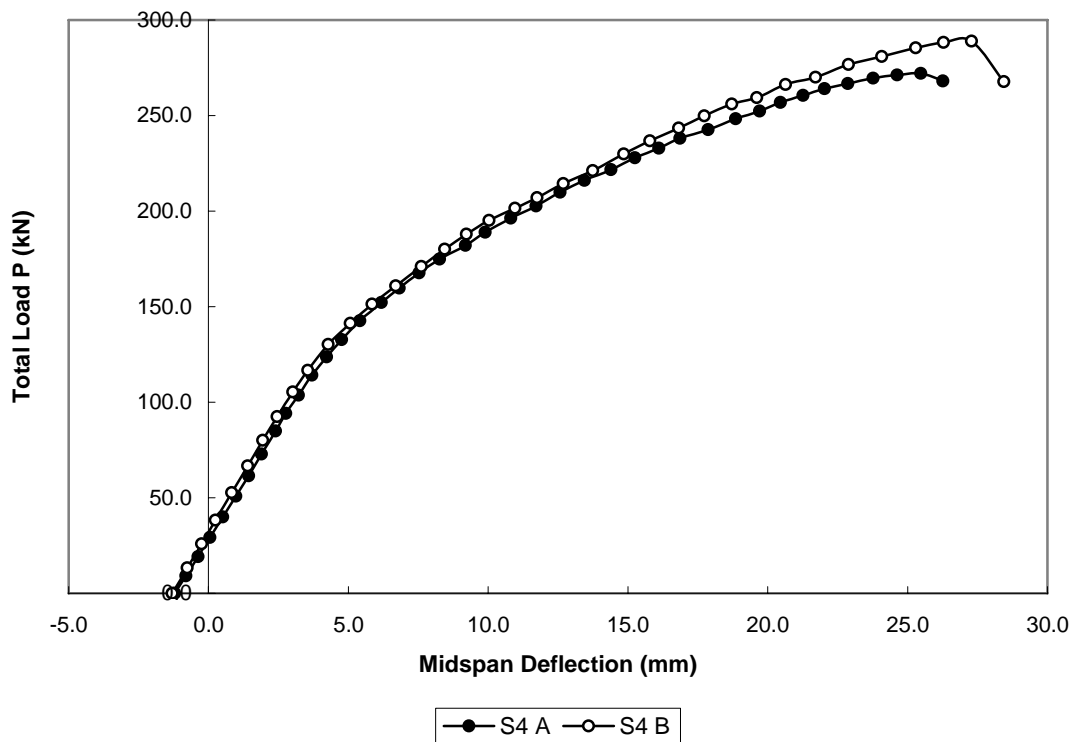


Figure 5.15: S3 load – deflection behaviour



**Figure 5.16:** S4 load – deflection behaviour

It can be seen from Figure 5.13 – 5.16 that the load-deflection behaviour of prestressed SF-RPC beams is linear before cracking and almost linear after cracking with a reduced stiffness up to approximately 80 – 85% of the ultimate load capacity. As the load approached the peak load, the beam behaviour becomes increasingly non-linear as the strain in the bonded prestressing tendons approaches its yield value and the concrete behaviour in the compressive zone becomes increasingly non-linear.

The moment-curvature and load-deflection diagrams for the prestressed SF-RPC beams show considerably less variation between two identical cross-sections than the plain SF-RPC beams. This is because the majority of the tensile capacity is now being provided by the prestressing steel and not by the SF-RPC. As the tensile capacity of the prestressing steel does not show the same natural variations as the tensile capacity of SF-RPC, the reduction in variations between identical specimens is to be expected.

### 5.3.4 Crack Patterns

For cross-sections S1 A and S1 B, the first visible cracks appeared on the surface of the member at an external load of approximately 40kN and 60kN, respectively. Several cracks were visible in the constant moment region of the beam. As the load level increased, the number of cracks visible increased rapidly and these cracks continued to extend through the depth of the cross-section. By the time the peak load was reached, there were numerous cracks spaced evenly throughout the constant moment region of the beam and beyond. For cross-section S1 A, two 'failure cracks' appeared with evidence of concrete crushing in the compression zone visible above both. For cross-section S1 B, there was a single 'failure' crack with evidence of concrete crushing in the compression zone above. The evidence of crushing in the compression zone of the beam indicates a typical flexural failure. Figure 5.17 shows the final crack pattern for cross-section S1 A.



**Figure 5.17:** Final crack pattern in constant moment region S1 A

For cross-sections S2 A and S2 B, the first visible cracks appeared on the surface of the member at an external load of approximately 100kN and 90kN, respectively. Similarly to cross-section S1, several cracks were visible in the constant moment region of the beam at first cracking. Additional cracks appeared with increasing load, and by peak load numerous cracks spaced evenly throughout the constant moment region and beyond were evident. Both S2 beams had a single 'failure' crack with evidence of concrete crushing in the compression zone indicating a flexural failure. Figure 5.18 shows the final crack pattern for cross-section S2 A. Figure 5.19 is a detailed image of

the ‘failure’ crack. The crushing of the concrete in the compression zone can be seen clearly in this image.



**Figure 5.18:** Final crack pattern in the constant moment region S2 A

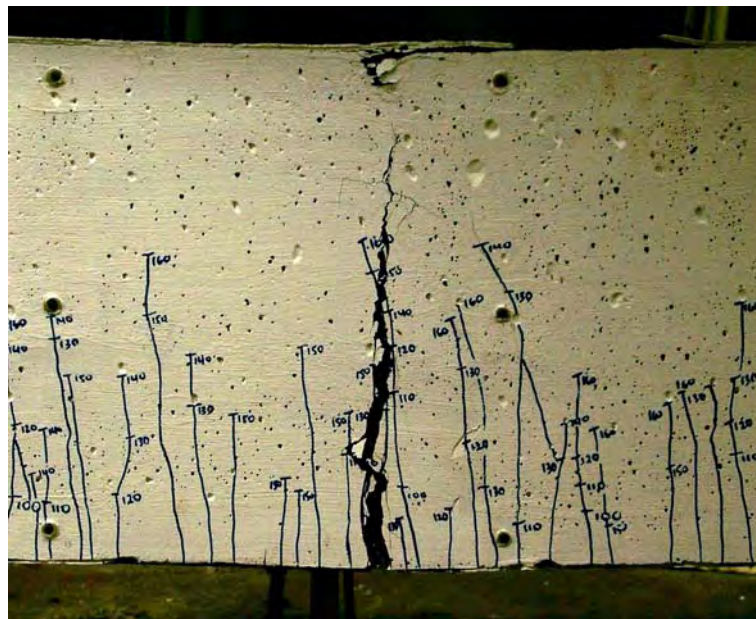


**Figure 5.19:** ‘Failure’ crack S2 A

For cross-sections S3 A and S3 B, the first visible cracks appeared on the surface of the member at an external load of approximately 100kN and 110kN, respectively. Similarly to cross-sections S1 and S2, several cracks were visible in the constant moment region of the beam at first cracking. Additional cracks appeared with increasing load, and by peak load numerous cracks spaced evenly throughout the constant moment region and beyond were evident. Both S3 beams had a single ‘failure’ crack with evidence of

concrete crushing in the compression zone indicating a flexural failure. Figure 5.20 shows the final crack pattern for cross-section S3 B.



**Figure 5.20:** Final crack pattern in constant moment region S3 B

For cross-sections S4 A and S4 B, the first visible cracks appeared on the surface of the member at an external load of approximately 140kN. Similar to cross-sections S1 – S3, several cracks were visible in the constant moment region of the beam at first cracking. Additional cracks appeared with increasing load and at peak load; numerous cracks spaced evenly throughout the constant moment region and beyond were evident. However, unlike cross-sections S1 – S3, the failure mode of both cross-sections S4 A and S4 B indicated a shear failure as evident by a large diagonal crack extending from the left hand support to the left hand point of load application. Figure 5.21 shows the final crack pattern for cross-section S4 A. Figure 5.22 is a detailed image of the shear crack seen in member S4 A as the peak load was reached. As the load decreased, this crack opened considerably.



**Figure 5.21:** Final crack pattern in constant moment region S4 B



**Figure 5.22:** Left hand shear crack S4 B

As can be seen in Figures 5.17 – 5.22, the crack patterns of prestressed SF-RPC is similar to conventional prestressed concrete beams i.e. numerous small cracks spaced evenly throughout the beam. The effect of increasing prestress in the tensile zone of the beam can be seen with the increasing load required to cause first crack in beams S1, S2 and S4.

### 5.3.5 Summary of Test Results for Beam Series 2

Table 5.2 is a summary of the 8 beam tests conducted as part of Series 2. The table shows the cracking moment, ultimate moment, deflection at first cracking as well as deflection at ultimate. The average ratio of ultimate moment to cracking moment is 2.65 for section S1, 1.82 for section S2, 2.35 for section S3 and 2.74 for section S4.

**Table 5.2:** Test Results for Beam Series 2

Beam ID	S1 A	S1 B	S2 A	S2 B
Cracking moment (kNm), $M_{cr}$	20.7	19.3	40.8	42.4
Ultimate moment (kNm), $M_u$	55.5	50.5	75.6	76.5
$M_u/M_{cr}$	2.68	2.62	1.85	1.80
Deflection at first cracking (mm), $\Delta_{cr}$	2.4	2.0	3.1	3.2
Deflection at ultimate (mm), $\Delta_u$	39.1	37.1	18.5	16.0
$\Delta_u/\Delta_{cr}$	16.3	18.6	6.0	5.0
Beam ID	S3 A	S3 B	S4 A	S4 B
Cracking moment (kNm), $M_{cr}$	36.1	36.0	45.0	47.4
Ultimate moment (kNm), $M_u$	77.9	91.4	122.9	130.6
$M_u/M_{cr}$	2.16	2.54	2.73	2.76
Deflection at first cracking (mm), $\Delta_{cr}$	3.4	3.3	3.1	3.0
Deflection at ultimate (mm), $\Delta_u$	15.5	24.1	25.8	27.2
$\Delta_u/\Delta_{cr}$	4.6	7.3	8.3	9.1

## 5.4 ANALYTICAL APPROACH

A strain compatibility approach was used for the analysis of the plain and prestressed SF-RPC beams. For this approach, the following assumptions are made:

- a. Bernoulli's assumption that plane sections remain plane in flexure i.e. the concrete is subjected to uniform strain over the entire width of the cross-section and the strains are linear over the depth of the section; and
- b. Where a prestressing tendon is present, perfect bond exists between the tendon and the concrete.

The strain compatibility method is used in both existing design guidelines for RPC and is also widely used to predict the flexural behaviour of prestressed concrete beams (e.g. Gilbert and Mickleborough, 1990). The cracking moment, deflection at first crack, ultimate load and deflection at ultimate load can be determined using this approach.

### 5.4.1 Flexural Behaviour Predictions

As mentioned, both existing design guidelines for RPC have used the strain compatibility approach to predict the flexural behaviour of plain and prestressed RPC beams. The Australian Guidelines (2000) uses actual or idealized stress-strain relationships for the component materials. The AFGC Interim Recommendations (2002) uses idealized stress-strain relationships for the component materials and also makes use of equivalence ratios to transform areas of steel into equivalent areas of concrete in order for the cross-section to be analysed. For this study, the method used within the Australian Guidelines has been adopted.

The main steps of the method are listed below (Gowripalan and Gilbert, 2000):

1. Assume a strain at the extreme compressive fibre of the concrete ( $\epsilon_o$ );
2. Assume a depth to the neutral axis ( $d_n$ );

3. From the strain profile, calculate the internal forces in the compression and tension zones from the stress-strain relationships adopted for both the concrete and the tendons;
4. Check the equilibrium of the forces on the cross-section and adjust  $d_n$  accordingly until equilibrium is satisfied;
5. Calculate the moment and curvature of the cross-section; and
6. Calculate the moment-curvature relationship for the cross-section by performing steps 1 – 5 for a range of  $\epsilon_o$ .

The assumed stress-strain behaviour for the concrete is shown in Figures 2.7 and 2.10 for the Australian Guidelines and Figure 2.18 for the AFGC Recommendations. The equivalence ratios for the AFGC model are  $n_i$  and  $n_v$  are 4 and 5 respectively. The assumed stress-strain behaviour of the steel tendons is shown in Figure 5.23:

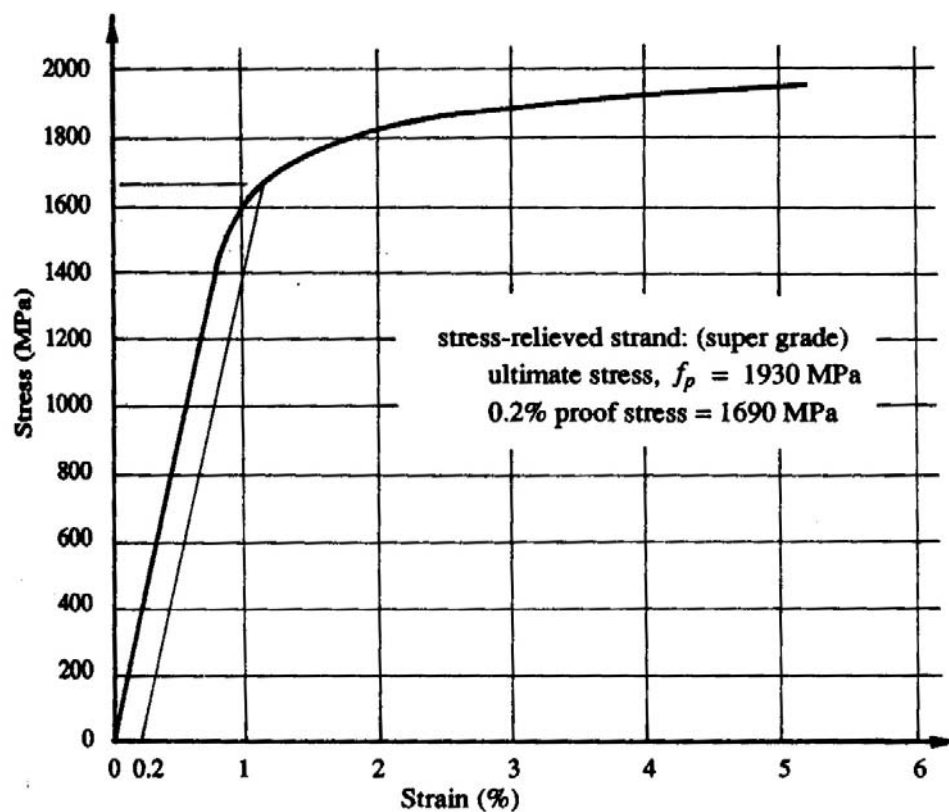


**Figure 5.23:** Typical stress-strain curve for 7-wire strand (Gilbert and Mickleborough, 1990)

### 5.4.2 Cracking Moment Calculations

The cracking moment for both plain and prestressed SF-RPC beams can be calculated based on the gross cross-sectional properties. Equation 5.1 and Equation 5.2 are for plain and prestressed beams, respectively.

$$M_{cr} = \sigma_{cr} Z_b \quad (5.1)$$

$$M_{cr} = P_e e + \left( \sigma_{cr} + \frac{P_e}{A_g} \right) Z_b \quad (5.2)$$

where

- $M_{cr}$  is the cracking moment;
- $\sigma_{cr}$  is the cracking stress of the concrete;
- $Z_b$  is the section modulus of the tension side;
- $P_e$  is the effective prestressing force;
- $e$  is the eccentricity of the prestressing tendons; and
- $A_g$  is the cross-sectional area

### 5.4.3 Ultimate Strength Calculations

For calculations relating to ultimate strength of a cross-section, the Australian models for a plain RPC section assumes the ultimate strength in bending occurs when the extreme tensile fibre reaches a strain of  $\varepsilon_{t,p}$ . For sections containing bonded prestress or conventional reinforcement, ultimate strength in bending is assumed to be reached when the extreme compressive fibre reaches a strain of 0.0035. For the AFGC model, no ultimate strain is imposed and the ultimate strength in bending is determined iteratively.

For this study, an iterative approach has been used to determine the ultimate bending moment. This approach was adopted as it was found that the ultimate moment in bending was under-estimated by imposing strain limits. The application of strain limits in order to determine the ultimate bending capacity of a cross-section is suitable for use in preliminary design procedures but for detailed analysis of a section, the full moment-curvature diagram should be considered.

#### 5.4.4 Failure Criteria

As mentioned previously, for plain SF-RPC beams failure is either the result of crushing of the concrete in the compression zone or unstable crack propagation. As this would result in a sudden failure, the ultimate moment tests of the plain SF-RPC beams conducted in this study were stopped after the peak moment was reached but before failure occurred. This allowed for a substantial amount of the post-peak behaviour to be captured without the risk of sudden, catastrophic failure of the beam specimen.

For prestressed SF-RPC, there are three failure modes that may occur, they are (1) crushing of the concrete, (2) rupture of the steel tendons and (3) simultaneous crushing of the concrete and rupture of the steel tendons (balanced failure). Therefore, the failure of SF-RPC prestressed beams is controlled by either the compressive strain of the concrete at the extreme compression fibre or the tensile strain of the tendon farthest from the neutral axis. In particular, the failure criteria of prestressed SF-RPC beams may be any one of the following:

1. For an over-reinforced member: Crushing of the concrete when the concrete strain in compression reaches the compressive strain limit of the concrete. The compressive strain limits of RPC are assumed to be 0.0035 and 0.003 according to the Australian model and the AFGC model, respectively ;
2. For an under-reinforced member: Rupture of the tendon when the tensile strain of the tendon at the layer farthest from the neutral axis reaches the tensile strain limit of the tendon. The tensile strain limit for stress-relieved strands such as those used within this study is approximately 5% (Gilbert and Mickleborough, 1990).
3. For a balanced reinforced member: Balanced failure can occur if the tendon achieves its ultimate tensile strain value simultaneously with the concrete reaches its ultimate compressive strain at the extreme fibres.

## 5.5 CURRENT THEORETICAL PREDICTIONS

### 5.5.1 Effective Moment – Curvature Relationships

In addition to being able to calculate the curvature on a cross-section of a beam from strain readings taken at various depths (as in Sections 5.2.2 and 5.3.2), the curvature can also be estimated from the midspan deflection results. As the midspan deflection measurement was taken electronically by LVDT, it was possible to monitor the beams throughout the full load-deflection curve. By estimating the curvature from the midspan deflection, it is therefore possible to get a full moment-curvature relationship for each beam.

In order to be able to calculate the curvature from the midspan deflection, it is practical to assume a constant cross-sectional stiffness ( $I$ ) for the entire span. The assumption of constant stiffness leads to constant flexural rigidity ( $EI$ ) and thus, as shown in Figure 5.24, the bending moment and curvature diagrams due to externally applied load are identical in shape. The deflection at midspan can then be calculated using the second moment-area theorem (see Beer and Johnston, 1992).

Figures 5.25 to 5.30 show the comparisons between the moment-curvature relationships from both strain measurements and midspan deflection for the 6 cross-sections investigated in the ascending portion of the load-deflection curve. As can be seen in these figures, the assumption of constant cross-sectional stiffness provides a reasonable estimate of the midspan curvature for all beams with the exception of P1. Prior to cracking, slight variations in the curvature results from strain and deflection measurements can be accounted for by localised variations in the modulus of elasticity,  $E$  across the span of the beam.

Variations between the measurements after cracking are the result of the localised nature of the strain measurements. The curvature calculated from strain measurements is the localised curvature within a small section of the beam with a length equal to the gauge length of the demec gauge used (i.e. 250mm). The curvature estimated from the midspan deflection based on the assumption of constant flexural rigidity for the entire beam is the curvature throughout the constant moment region.

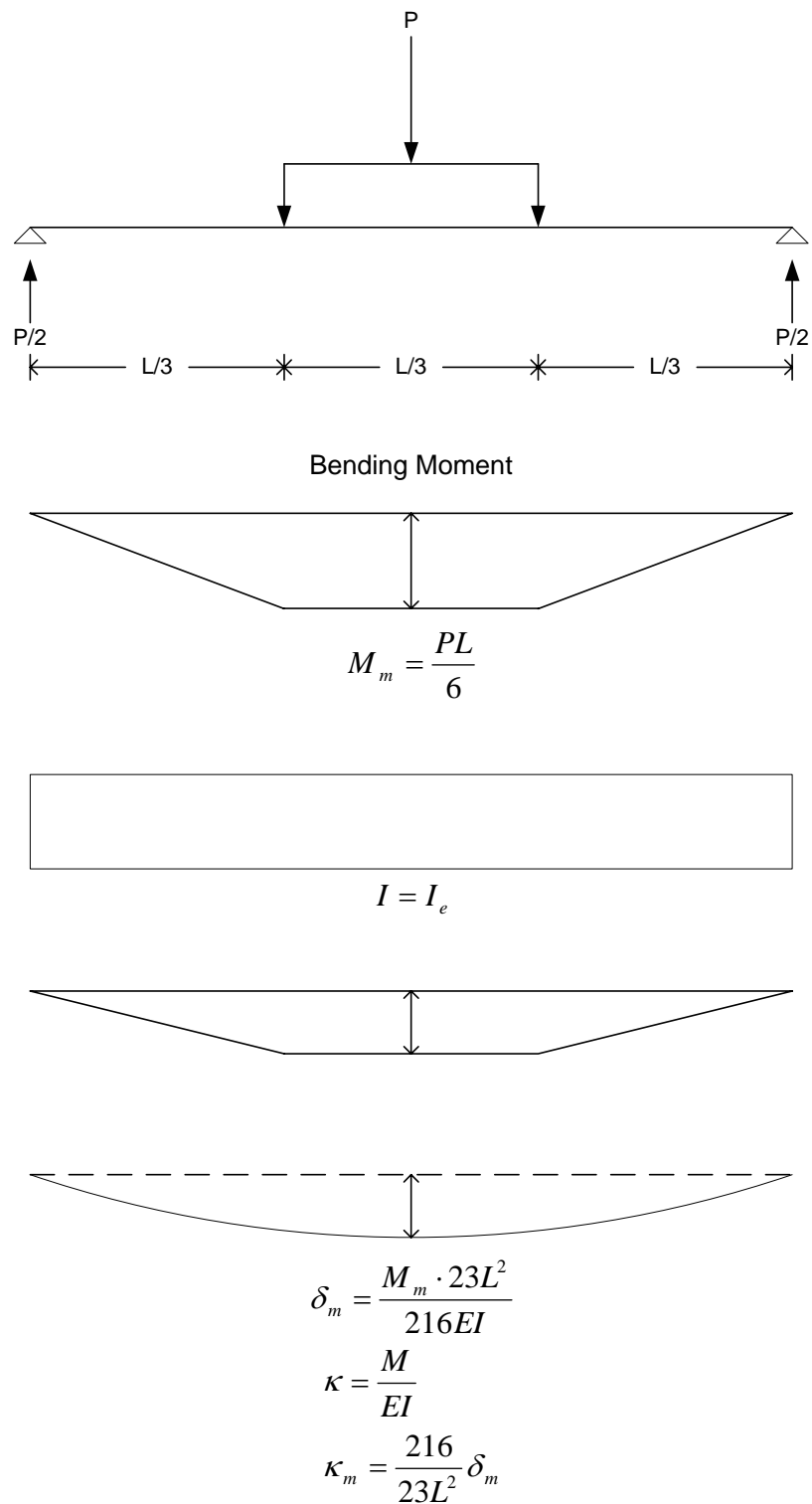


**Figure 5.24:** Bending moment, deflected shape and curvature diagram due to externally applied load

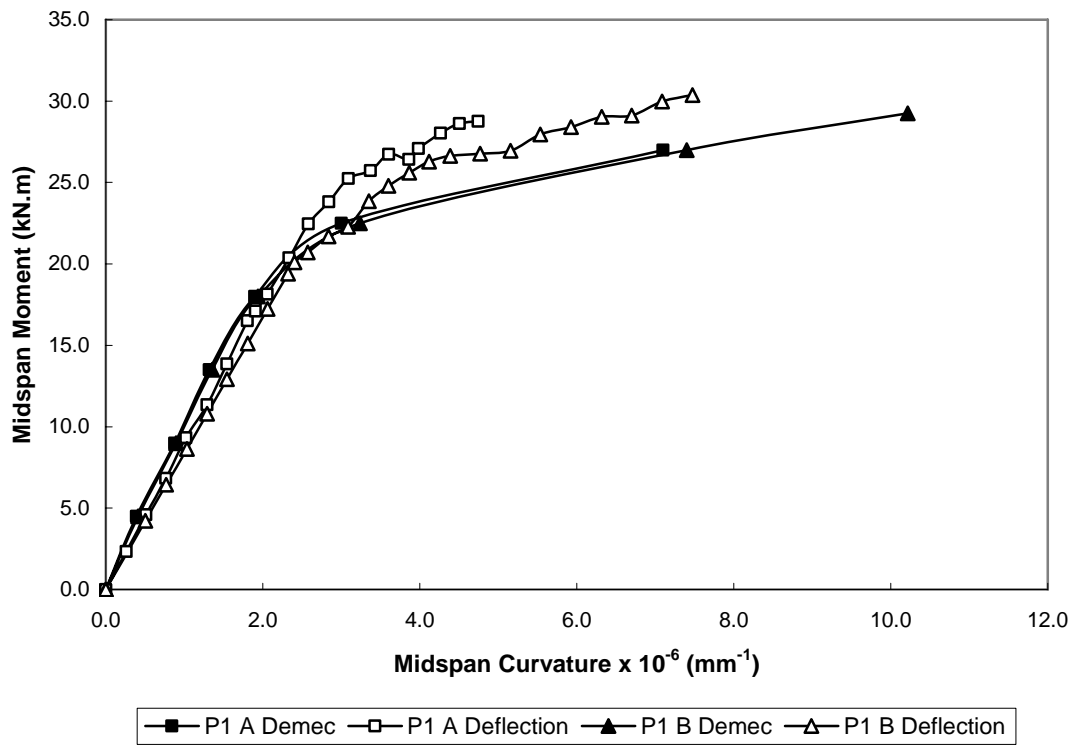


Figure 5.25: P1 moment – curvature relationship comparison

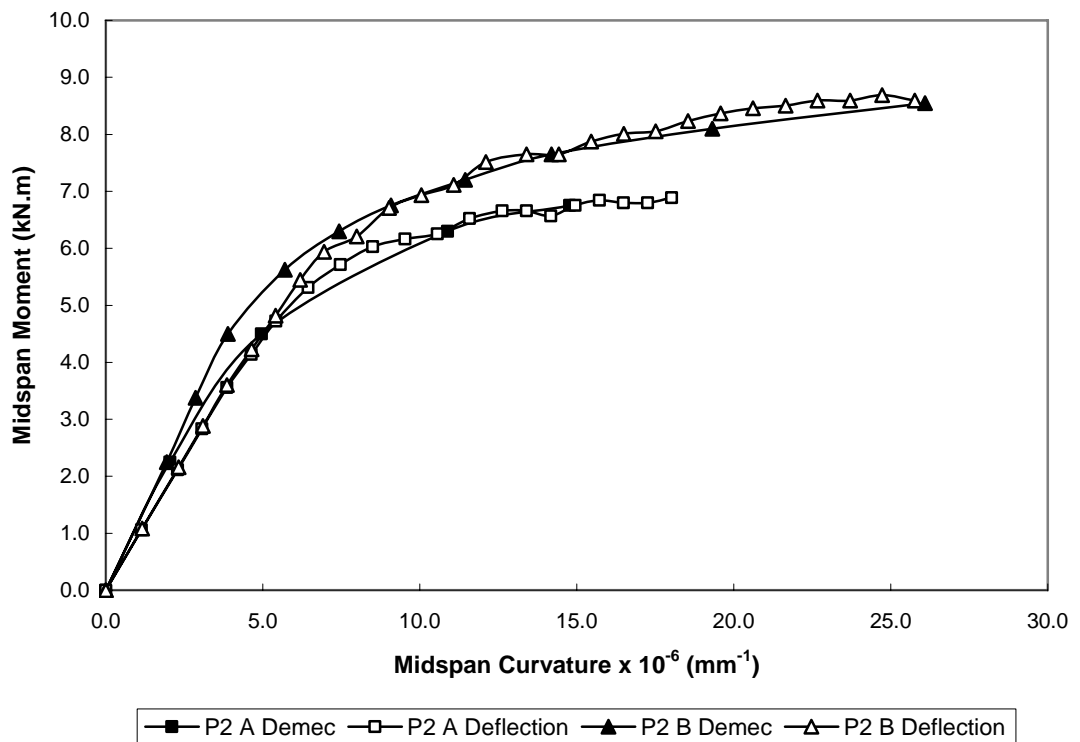


Figure 5.26: P2 moment – curvature relationship comparison

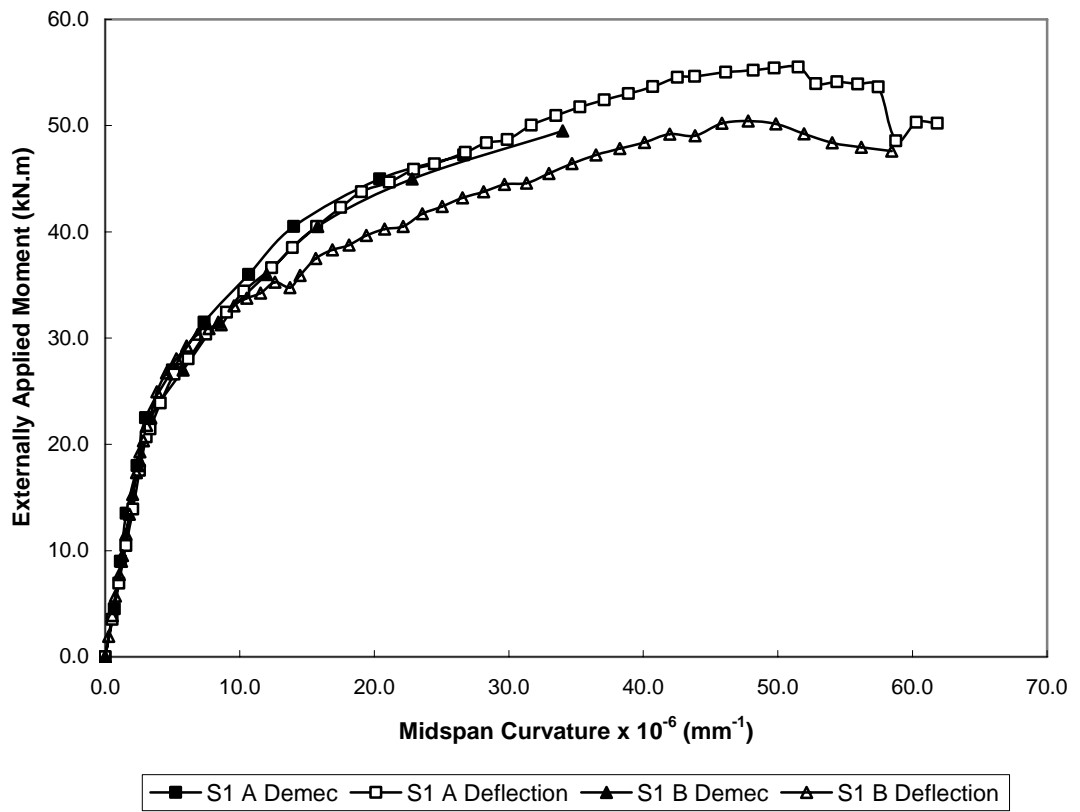


Figure 5.27: S1 moment – curvature relationship comparison

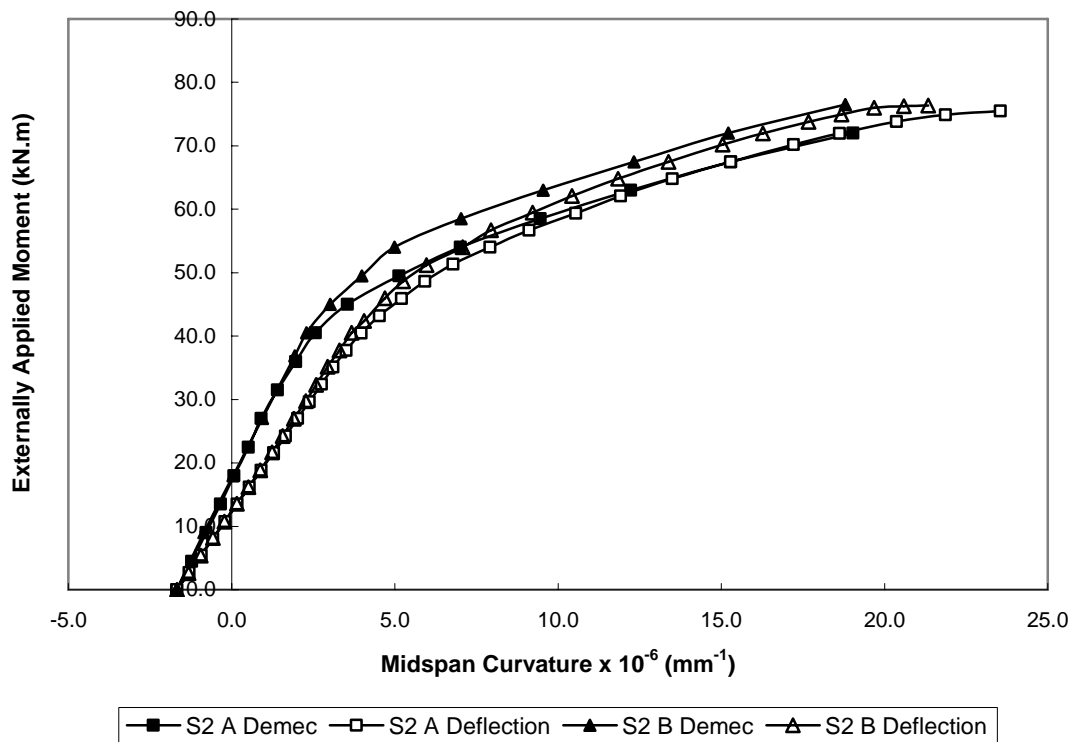


Figure 5.28: S2 moment – curvature relationship comparison

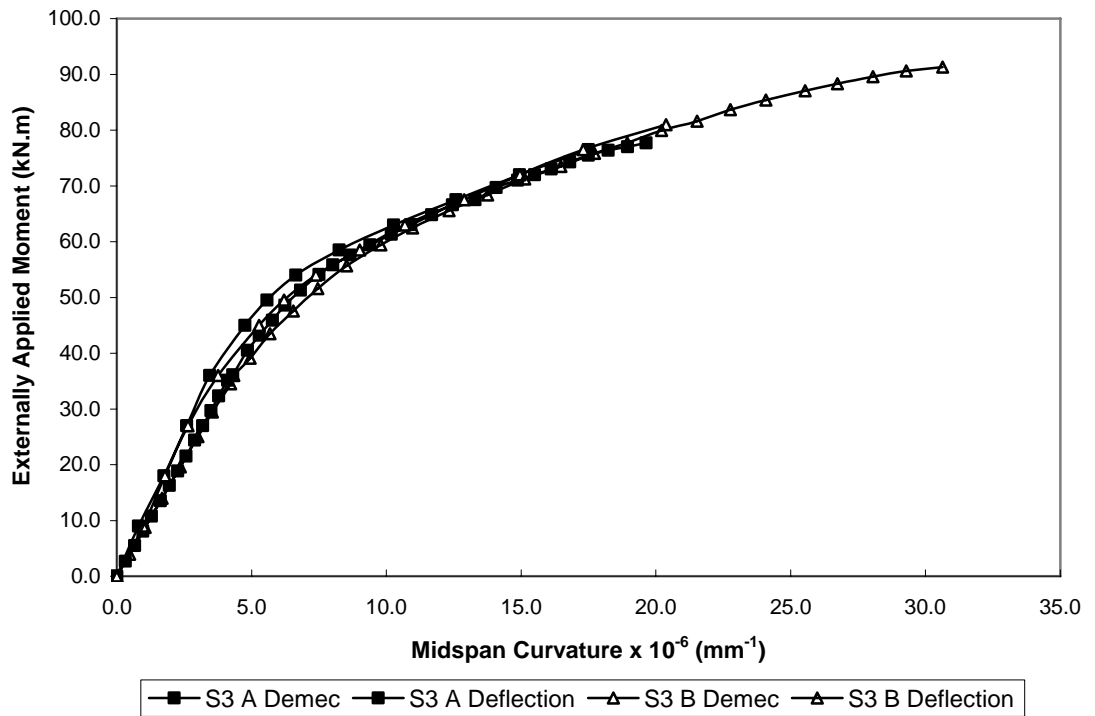


Figure 5.29: S3 moment – curvature relationship comparison

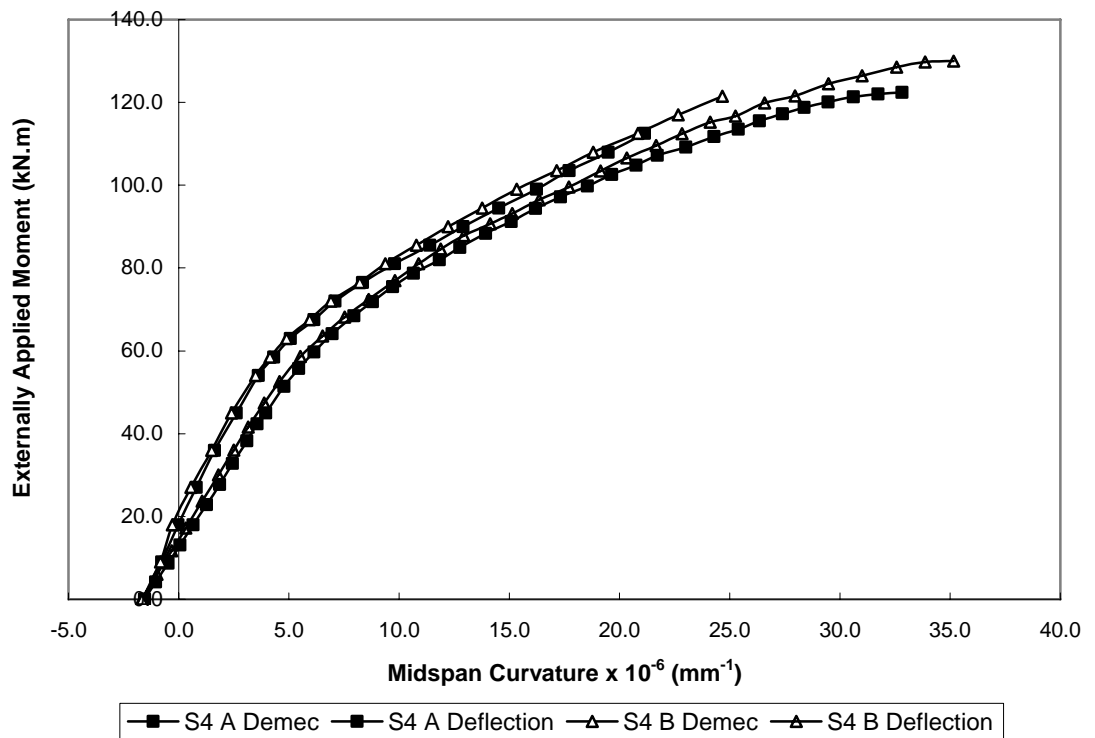


Figure 5.30: S4 moment – curvature relationship comparison

The moment-curvature relationship calculated from the midspan deflection will be identical in shape to the load-deflection relationship. The deflection calculations found in the majority of concrete design codes (e.g. AS 3600 - 2001) are based on the assumption of constant flexural rigidity of a member and not on localised curvature. All models developed to predict the moment-curvature relationships of SF-RPC beams are therefore concerned with the moment-curvature relationships based on the midspan deflection and not the localised curvature from the strain measurements.

## **5.5.2 Performance of the Current Models**

### *5.5.2.1 Plain SF-RPC Beams*

The theoretical predictions of the moment-curvature relationships for Beam Series 1 from both currently available models compared with the experimental results are shown in Figures 5.31 and 5.32. As can be seen in these figures, both current models accurately predict the effective moment-curvature relationships prior to cracking. This is to be expected as the elastic properties of SF-RPC and their effects on the moment-curvature relationship are well known. However, both models have limited success in accurately predicting the post-crack flexural behaviour of plain SF-RPC beams. The inaccuracy after cracking is the result of the large tensile strain limits adopted in both the Australian and AFGC models.

### *5.5.2.2 Prestressed SF-RPC Beams*

The theoretical predictions of the moment-curvature relationships for Beam Series 3 from both currently available models compared with the experimental results are shown in Figures 5.33 – 5.36. As can be seen from these figures, both current models accurately predict the effective moment-curvature relationships prior to cracking. Both currently available models have greater success in predicting the behaviour of prestressed SF-RPC beams than plain SF-RPC Beams. This is because the majority of the tensile capacity is now the result of the prestressing tendons and not the SF-RPC. Since the material properties of the prestressing tendons are well-known throughout its entire stress-strain curve, it is expected that current models will show improved

performance when tendons are present. Except in the case of S1 beams, the models under-predict the ultimate moment capacity of the beams tested.

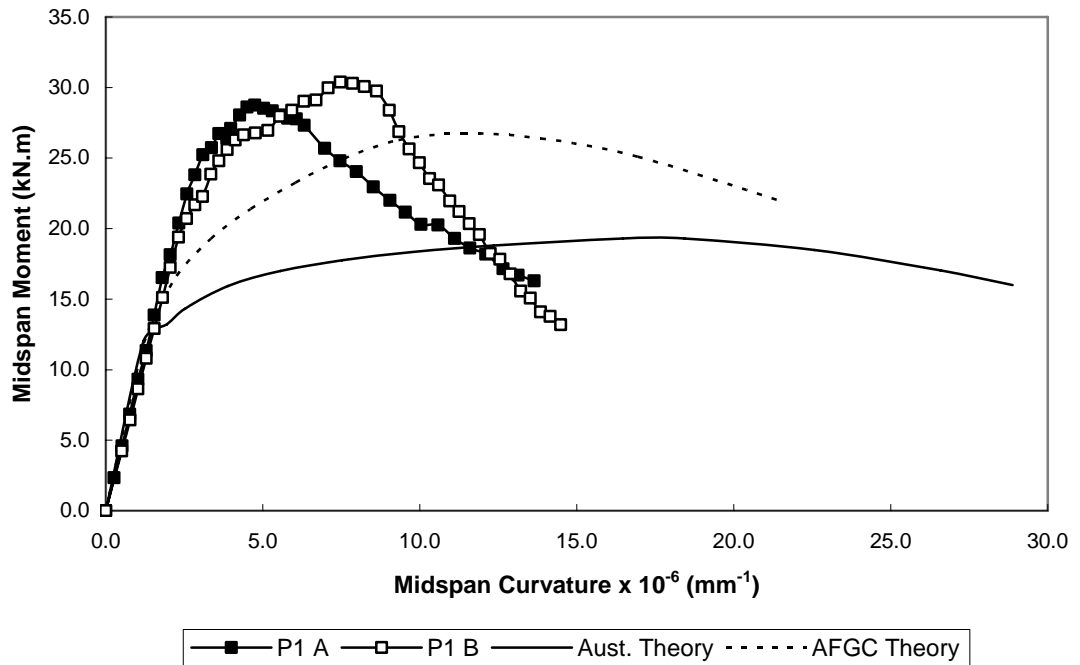


**Figure 5.31:** Predicted versus experimental moment – curvature relationships (Cross-section P1)

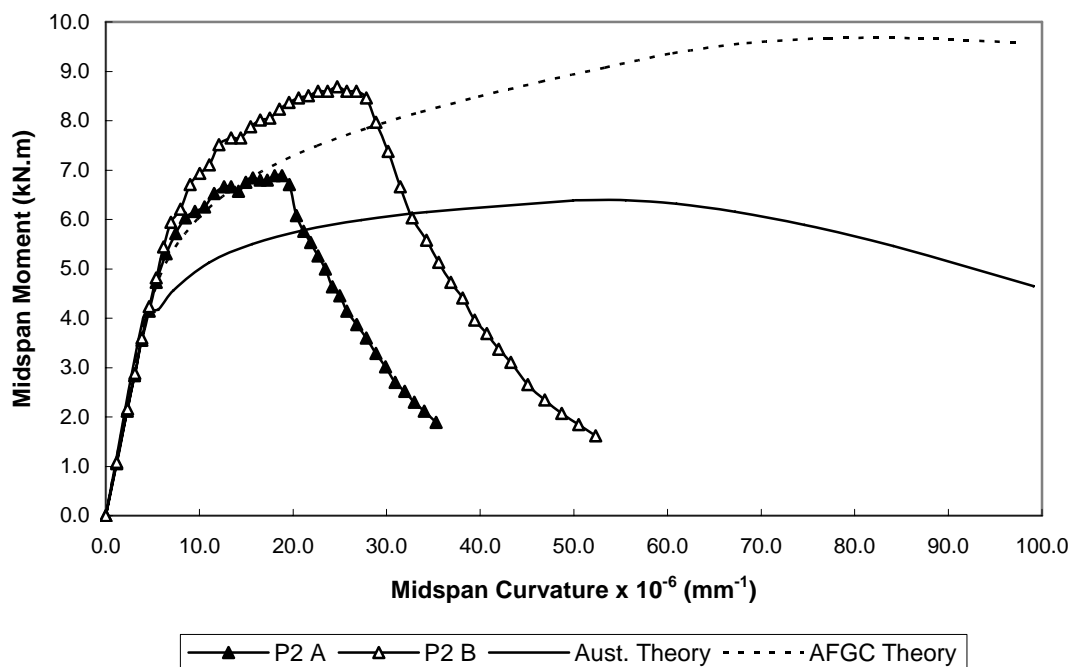


**Figure 5.32:** Predicted versus experimental moment – curvature relationships (Cross-section P2)

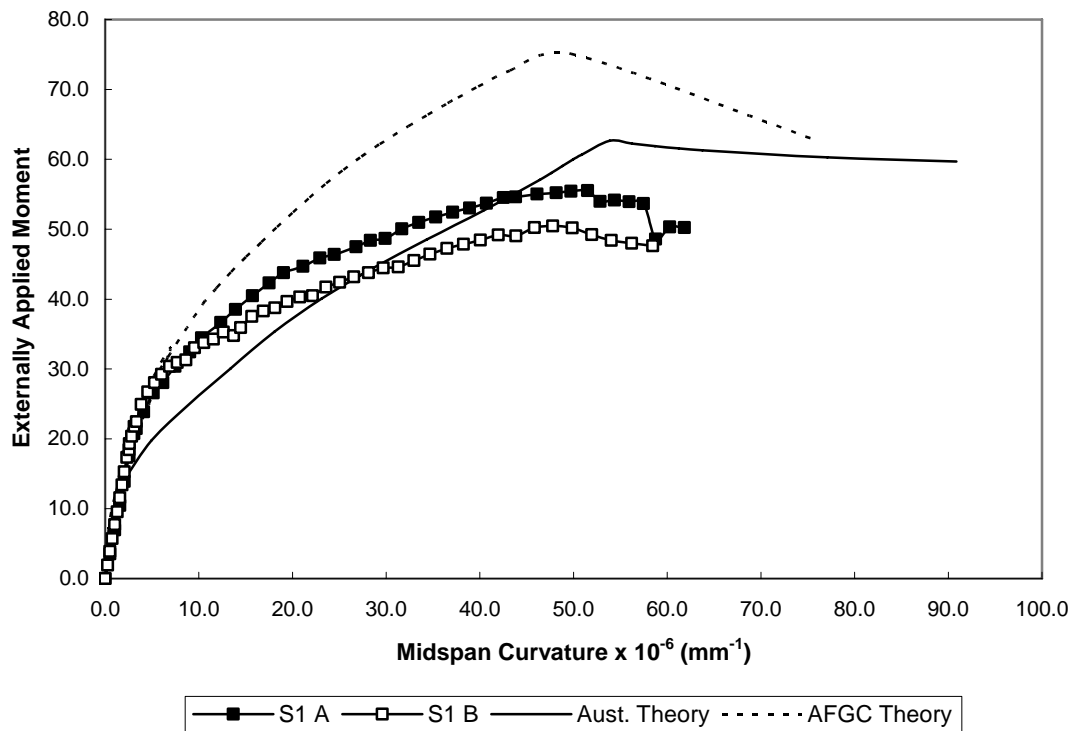


**Figure 5.33:** Predicted versus experimental moment – curvature relationships (Cross-section S1)

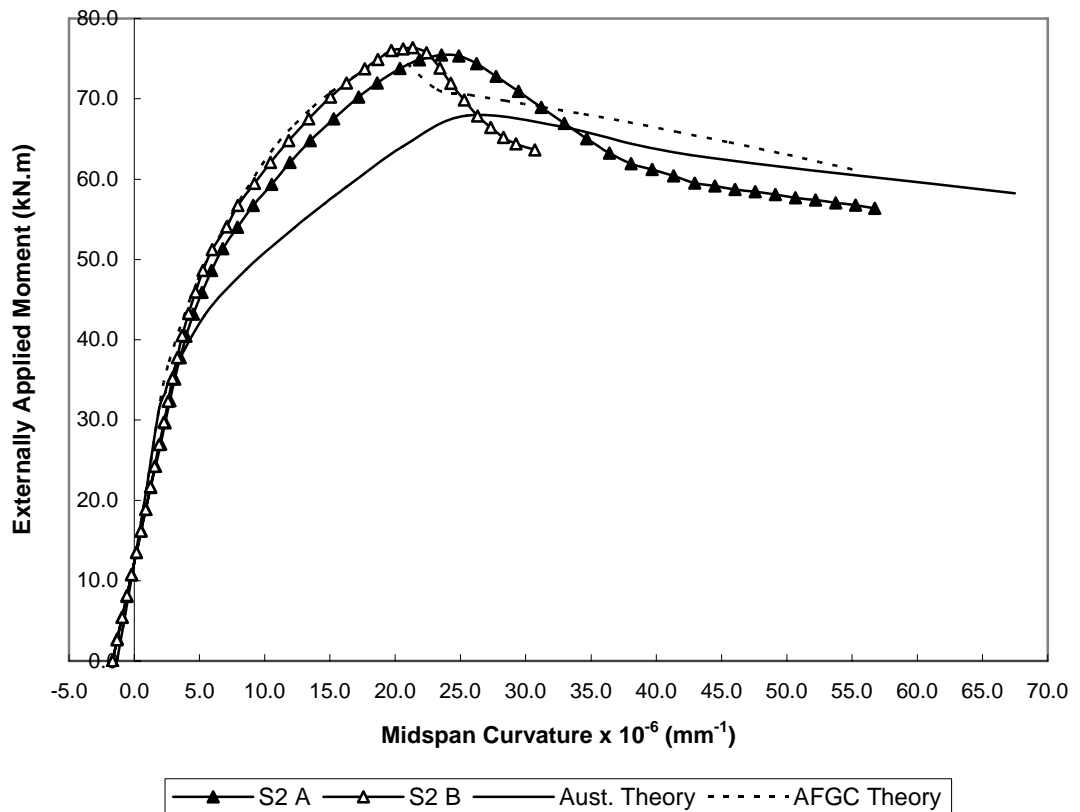


**Figure 5.34:** Predicted versus experimental moment – curvature relationships (Cross-section S2)

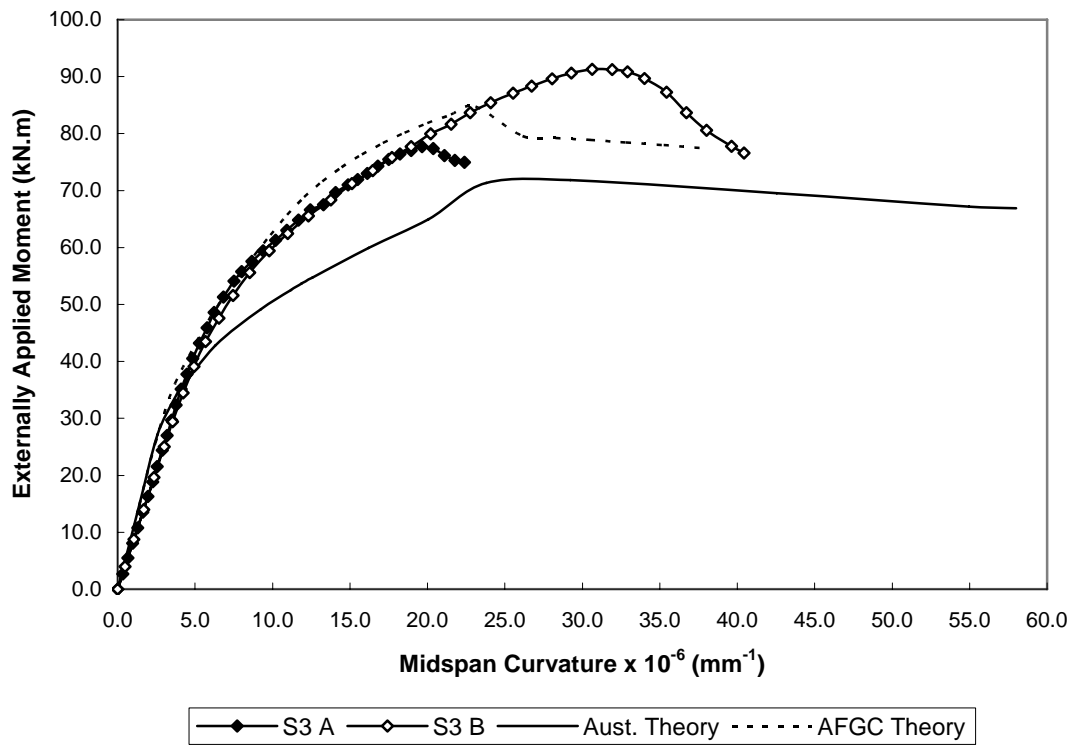


**Figure 5.35:** Predicted versus experimental moment – curvature relationships (Cross-section S3)

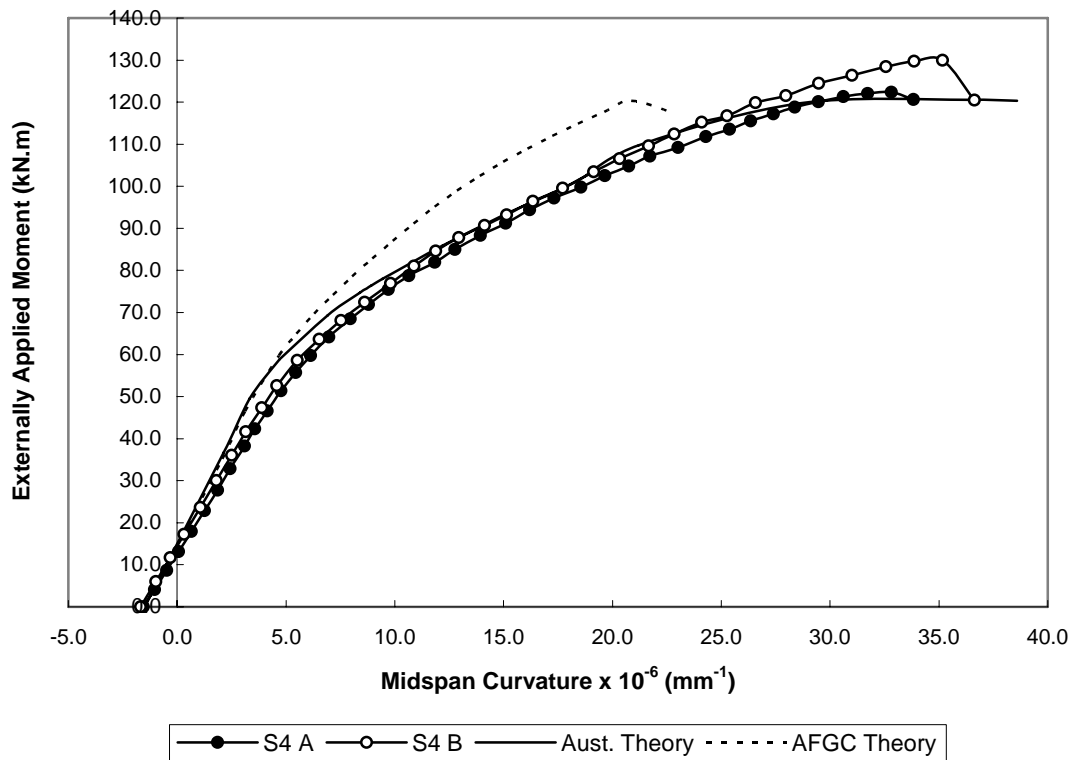


**Figure 5.36:** Predicted versus experimental moment – curvature relationships (Cross-section S4)

## 5.6 MODIFIED MODEL

The moment-curvature relationship of plain SF-RPC sections can be divided into 3 phases. The 3 phases are shown in Figure 5.37. Phase 1 is the initial linear portion of the moment-curvature relationship and the end of the phase corresponds to first crack ( $M_{cr}$ ). The second phase is similar to the strain hardening phase seen in the flexural tests and the end of the phase corresponds to the peak (or ultimate) moment ( $M_u$ ). The final phase is similar to the strain softening phase seen in the flexural tests.

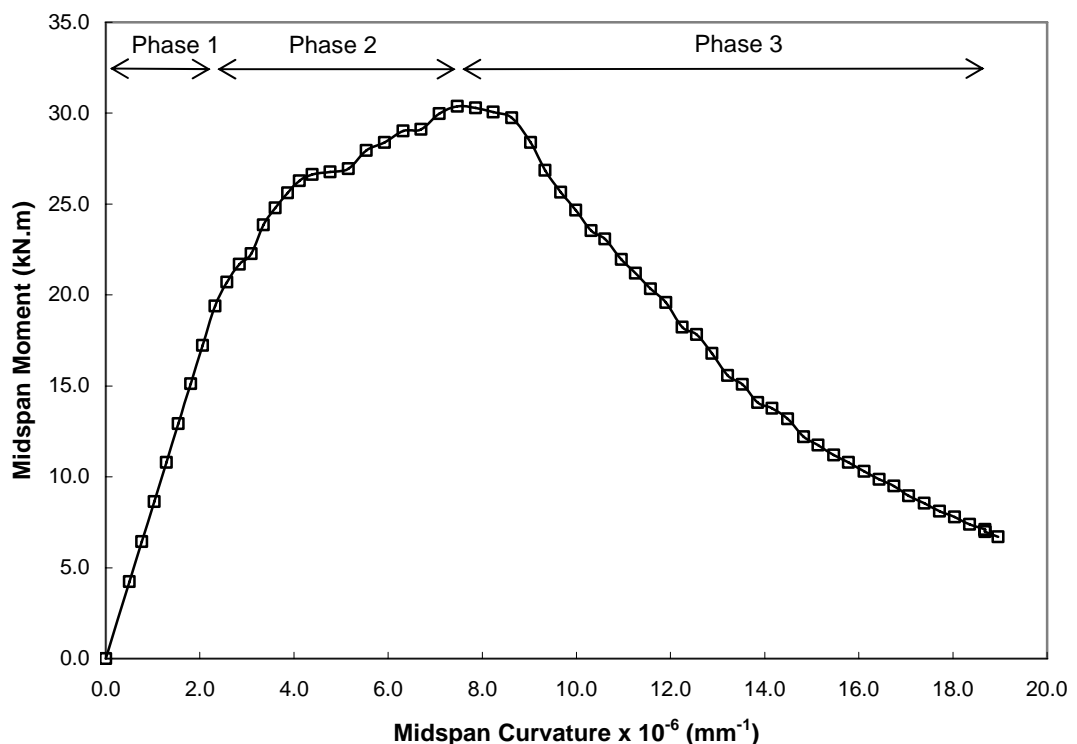


**Figure 5.37:** Moment – curvature relationship phases for plain SF-RPC sections (P1 B)

The shape of the moment-curvature relationship for plain SF-RPC beams is dependent on the tension model adopted for the concrete. Thus, the 4-phase tension model proposed by the AFGC Interim Recommendations (2002) is more appropriate than the 3-phase model proposed by the Australian Guidelines (2000) as it can predict the point of contra-flexure seen in the post-peak phase. However, although the strain values for the various parameters in the AFGC model are based on experimental data, the model tends to over-

predict the curvature for any given moment indicating that the strain values at the various stress levels are too large in the post-peak region.

The moment-curvature relationship for prestressed SF-RPC sections also consists of 3 phases. The 3 phases are shown in Figure 5.38. Phase 1 is the initial linear portion up to first crack ( $M_{cr}$ ). The second phases consists of another approximately linear portion up to the peak (or ultimate) moment ( $M_u$ ). The final phase (post-peak) phase is dependent on section geometry. If the section is under-reinforced such as S2 then a post-peak softening phase is seen. However, if the section is over-reinforced the final phase can be relatively short ending in brittle failure of the section.

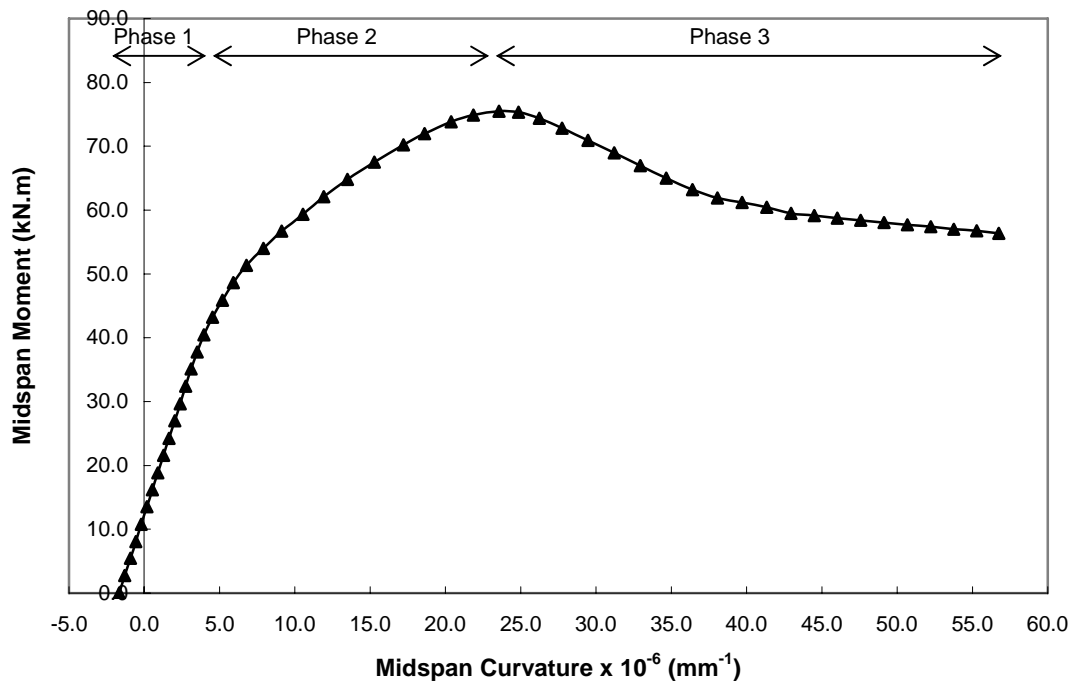


**Figure 5.38:** Moment – curvature relationship phases for prestressed SF-RPC sections (S2 A)

As shown in Section 5.5.2, the current models have some deficiencies in predicting the moment-curvature relationships of the plain and prestressed SF-RPC beams tested as part of this study, particularly the post-peak behaviour. Therefore, in order to more accurately predict the moment-curvature relationship of plain and prestressed SF-RPC beams, a modified model is proposed here.

For plain sections, the modified model consists of an upper and lower bound approach. The rationale for this is to consider the natural variations that are evident in fibre-reinforced concrete. For design purposes, the lower bound would be adopted with the application of appropriate safety factors. For prestressed sections, the lower bound tension stress-strain relationship is adopted as the tensile capacity of the concrete has minimal effect on the moment-curvature relationship of SF-RPC when prestressing tendons are present.

### 5.6.1 Adopted Stress-Strain Relationships for the Modified Model

#### 5.6.1.1 SF-RPC compressive relationship

Figure 5.39 shows the stress-strain relationship for the SF-RPC in compression that was adopted for the modified model. This is the constitutive model shown in Figure 4.16 and has been repeated here for clarity. The compressive behaviour is defined by the characteristic strength  $f_c'$  and the modulus of elasticity  $E$  with a maximum strength corresponding to  $0.85f_c'$  and a maximum strain of  $4000\mu\epsilon$ .

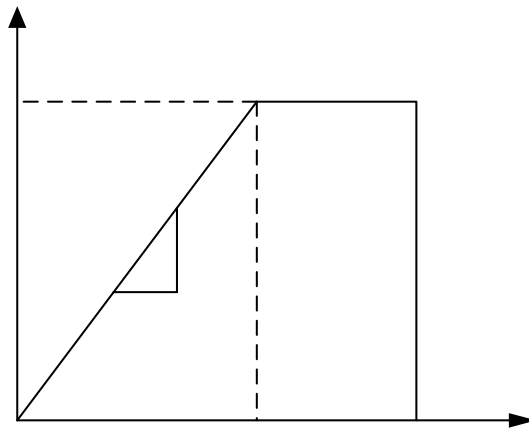


**Figure 5.39:** SF-RPC stress-strain relationship in compression

In practice, within the range of the tests conducted as part of this study, the stress plateau of  $0.85f_c'$  is not reached for plain SF-RPC beams. The compression stress plateau is more relevant for prestressed SF-RPC beams.

### 5.6.1.2 Concrete tensile relationship

Figure 5.40 shows the stress-strain relationship for the SF-RPC in tension that was adopted for the modified model. The model is based on the 4-phase tension relationship proposed by the AFGC Interim Recommendations (2002) for reasons discussed previously. The tensile behaviour is based on  $R_{ft}$  (see Section 4.3.4.1) from the flexural strength tests and uses Equation 4.6 in order to account for size effects. However,  $h$  is taken as the depth of the beam not the depth of the flexural test specimen.

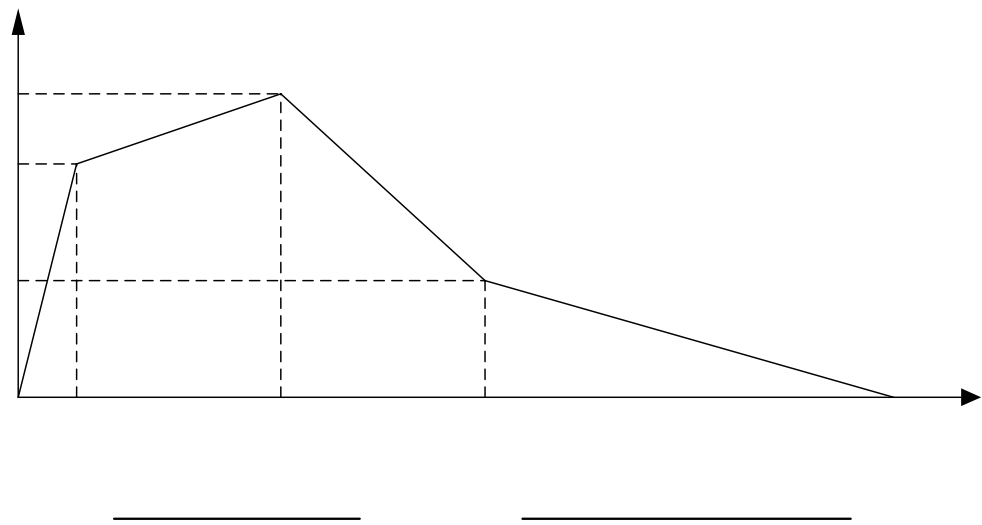


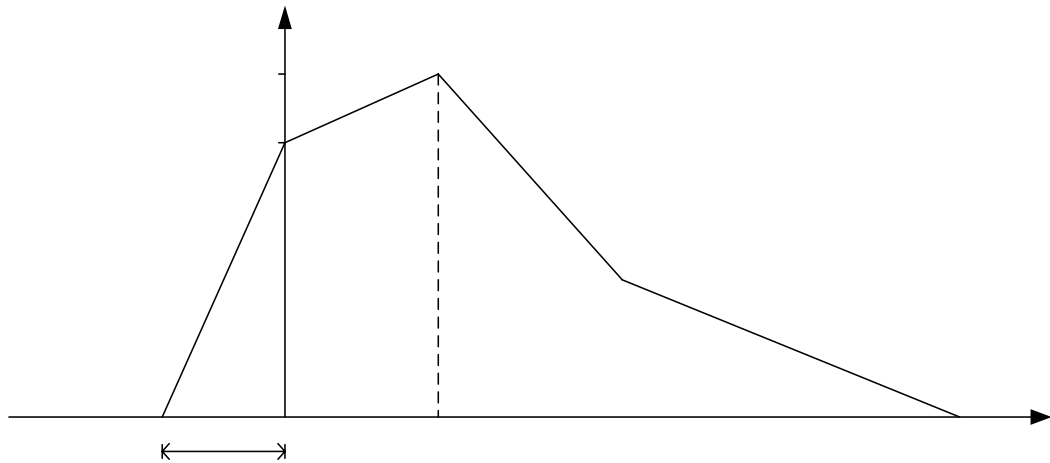
**Figure 5.40:** SF-RPC stress – strain relationship in tension

When the modified model was applied to the test results, it was found that the value of parameter  $\lambda$  was dependent on the level of confinement due to the effective prestress. The greater the level of prestress in terms of prestress/area (i.e. the greater the confinement effect), the greater the parameter  $\lambda$ . Table 5.3 contains the value of the parameter  $\lambda$  adopted for the 12 short-term sections tested.

**Table 5.3:** Parameter  $\lambda$ 

SECTION	P1, P2, S1	S2	S3	S4
Prestress Level	None	Low	Medium	High
$f_c / f_c'$ (%)	0	0 – 5	5 – 10	10+
Parameter $\lambda$	6	12	16	20

This confinement effect can be explained by considerations of the stress-crack width curve (for example, see Figure 5.41). It is common practice to model the behaviour of fibre reinforced concrete by a stress-crack width curve taken from a crack mouth opening test despite the debate about the validity of test results. The stress-crack width curve is then usually converted to a stress-strain type relationship for use in structural modelling/design considerations. This method of determining the stress-strain tensile properties is adopted by the AFGC Model.

**Figure 5.41:** Stress – crack width relationship for SF-RPC

When the stress-strain relationship for SF-RPC is considered from a perspective of stress-crack width, the implications of increasing confinement (from the effective prestress) can be seen to have direct consequences on the stress-strain relationship. The effect of confinement inhibits the growth of cracks and therefore the greater the confinement (i.e. the greater the effective prestress), the longer the same stress can be maintained. In practice, this is

seen in the increasing strain values in the tensile stress-strain relationship adopted for SF-RPC.

The general form of the stress-crack width curve has an initial linear proportion representing the initial linear stress-strain behaviour of fibre reinforced concrete prior to cracking (see Figure 5.41). The stress required to cause cracking occurs at a crack width of zero. The stress and strain values at which cracking will occur is a material property and is therefore independent of the level of confinement provided by the effective prestress. Confinement will therefore only be important after cracking has occurred and hence the factor  $\lambda$  is only applicable to strain values greater than  $\epsilon_{cr}$  (i.e. after cracking has occurred).

#### 5.6.1.3 Steel stress-strain relationship

The stress-strain behaviour of the steel tendons used was modelled using a modified Ramberg-Osgood function as given in Equation 5.3.

$$f_s = E_s \epsilon_s \left[ 0.03 + \frac{0.97}{\left(1 + (102\epsilon_s)^{10}\right)^{0.1}} \right] \leq 0.85 f_{su} \quad (5.3)$$

where

- $f_s$  is the stress in the prestressing tendon at strain  $\epsilon_s$ ;
- $E_s$  is the modulus of elasticity of the prestressing tendon; and
- $f_{su}$  is the tensile strength of the prestressing tendon.

An elastic modulus of 195GPa, tensile strength of 1840MPa and 1750MPa for 15.2mm and 12.7mm strands respectively and an ultimate strain of 4.5% were adopted for this study (Gilbert and Mickleborough, 1990).

#### 5.6.1.4 Moment-Curvature Relationship

The moment-curvature relationship can be calculated using the adopted stress-strain relationships of the materials used. Appendix C contains sample calculations for both plain and prestressed sections. The deflection for any given moment and curvature can be calculated by rearranging the equation for the curvature  $\kappa_m$  found in Figure 5.24.

## 5.6.2 Performance of Modified Model

### 5.6.2.1 Plain SF-RPC Beams

The theoretical predictions of the moment-curvature relationships for Beam Series 1 from the modified model compared with the experimental results are shown in Figures 5.42 and 5.43. As can be seen from these figures, the modified model performs agreeably with the experimental results for the plain SF-RPC beams tested as part of Series 1. By making use of a lower and upper bound approach, the modified model can predict the range of behaviour that is likely to occur when plain SF-RPC beams are tested.

### 5.6.2.2 Prestressed SF-RPC Beams

The theoretical predictions of the moment-curvature relationships for Beam Series 3 from the modified model compared with the experimental results are shown in Figures 5.44 – 5.47. As can be seen from these figures, the modified model performs agreeably with the experimental results for the prestressed SF-RPC beams tested as part of Series 3. The model behaves erratically when prestressing tendons are used with no initial prestress due to the delayed yielding of the steel present. This anomaly is only seen with the modelling of Beam S1. The smoothed curve in Figure 5.44 is more likely to be the actual beam behaviour.

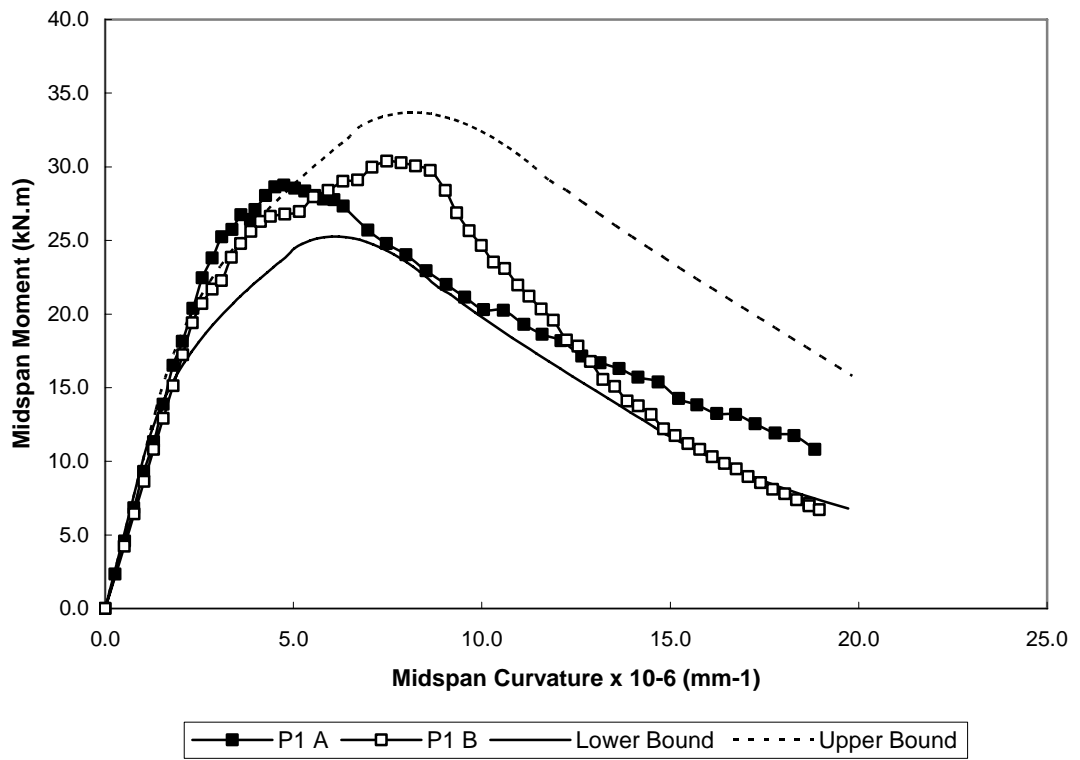


Figure 5.42: P1 modified model performance

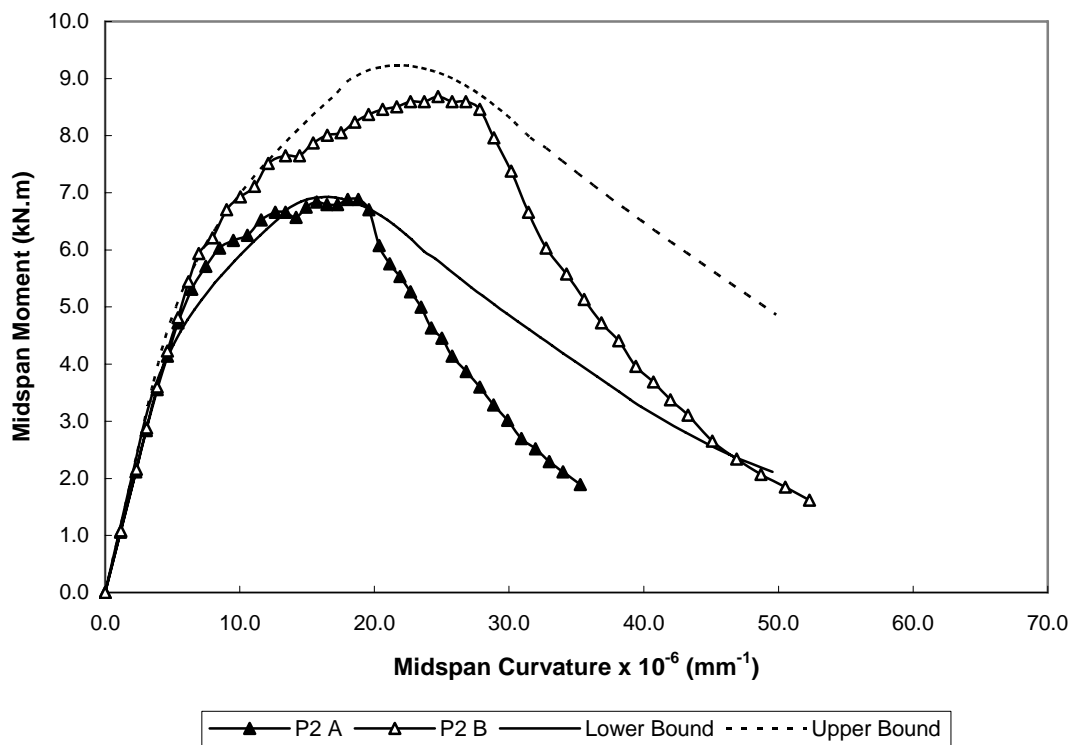


Figure 5.43: P2 modified model performance

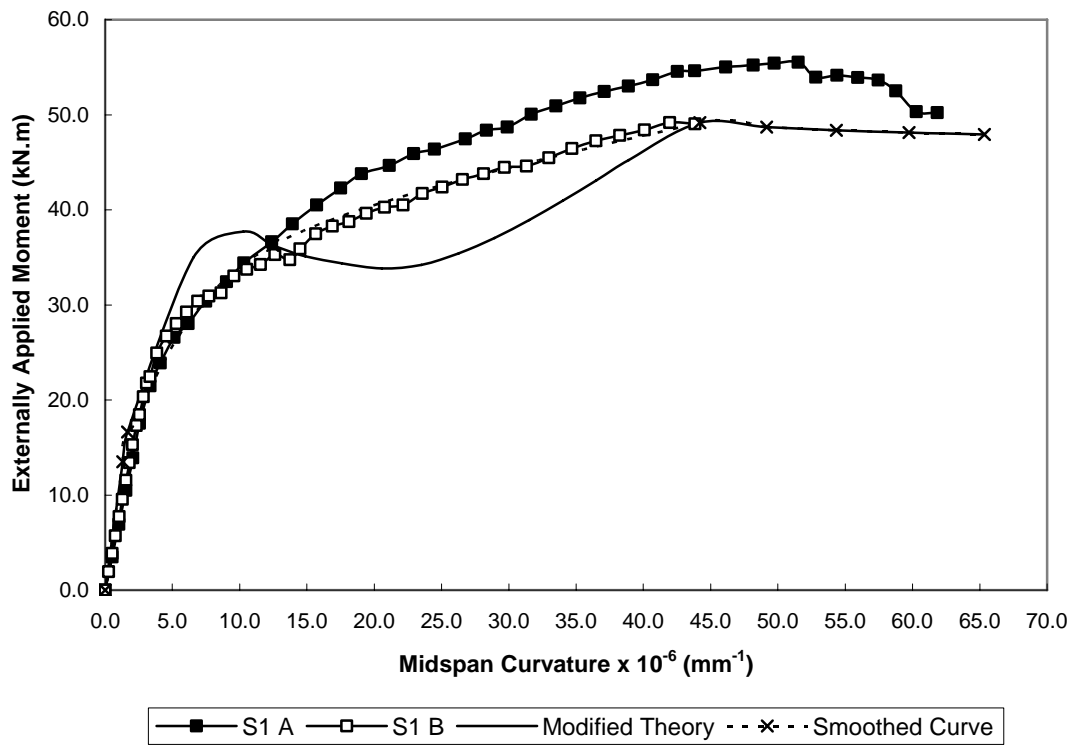


Figure 5.44: S1 modified model performance

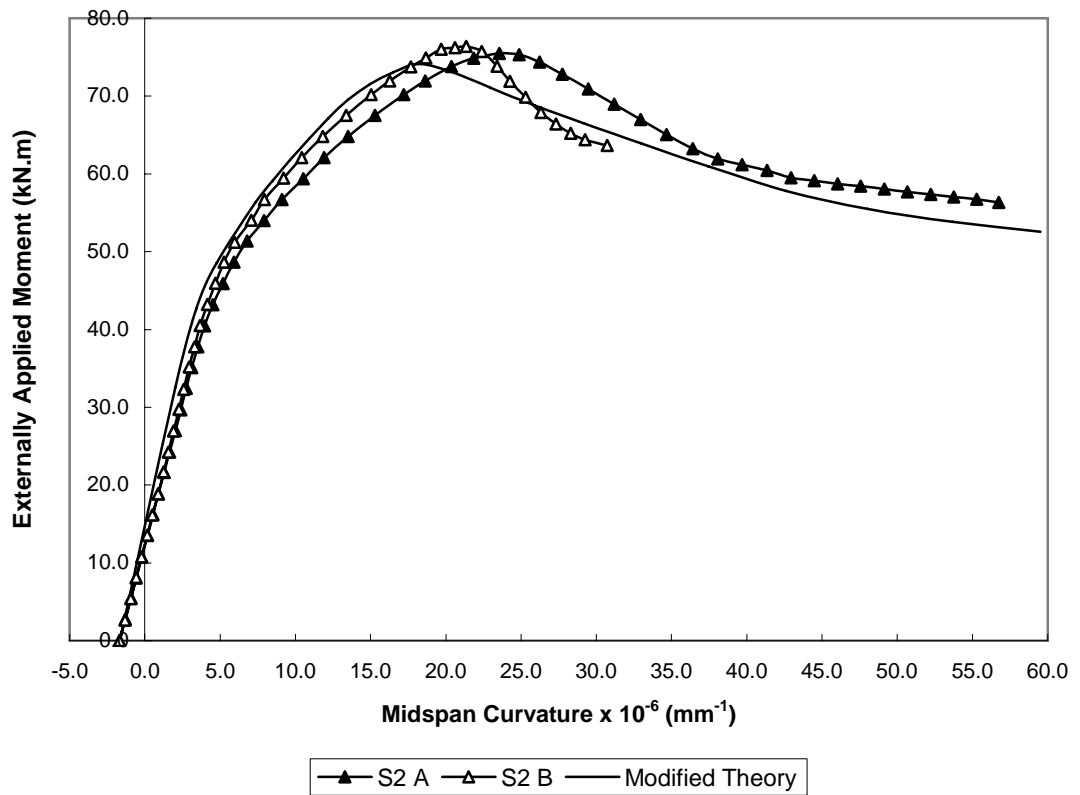


Figure 5.45: S2 modified model performance

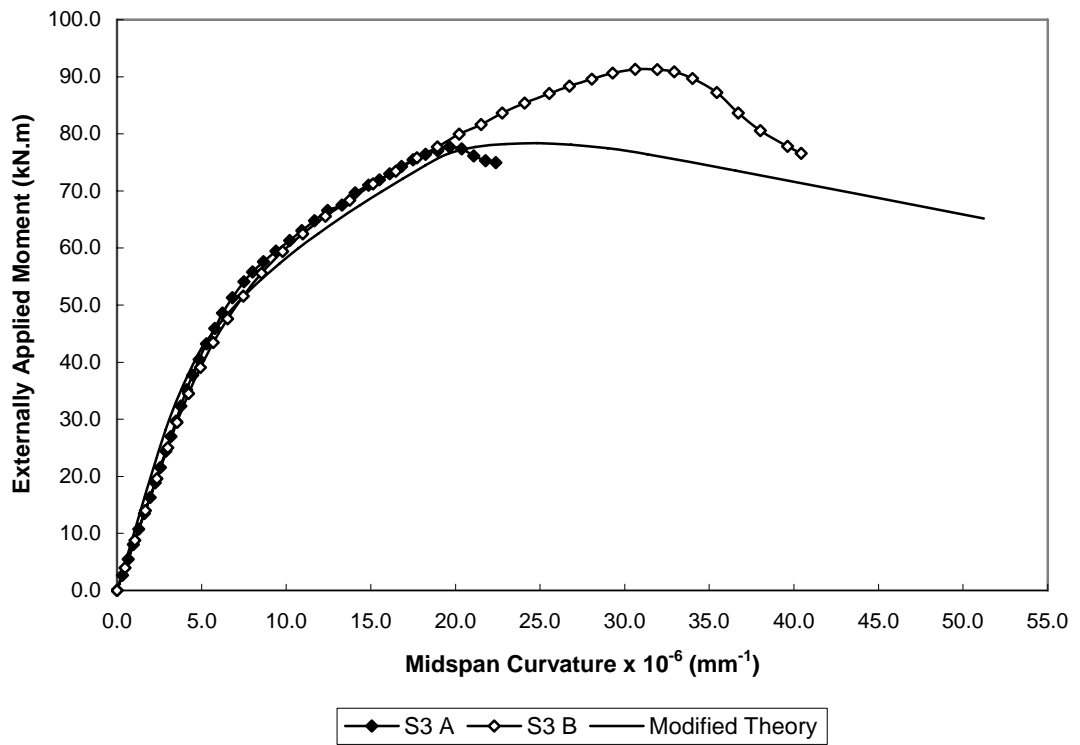


Figure 5.46: S3 modified model performance

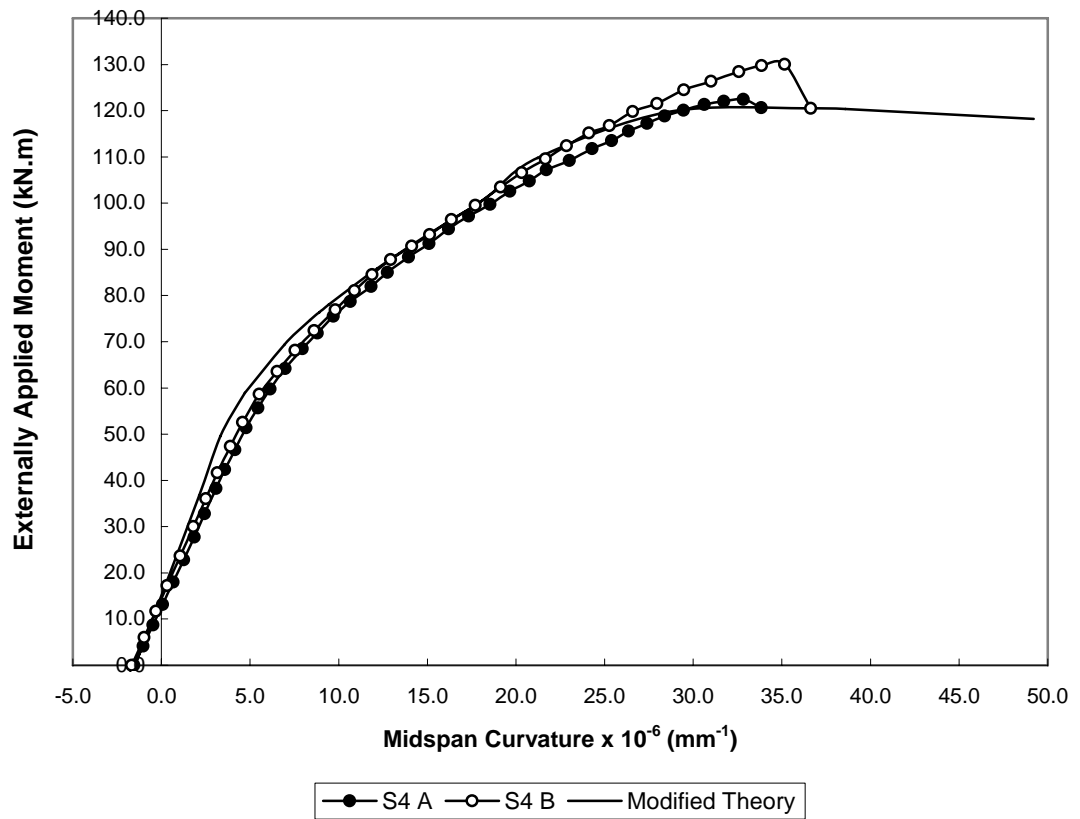
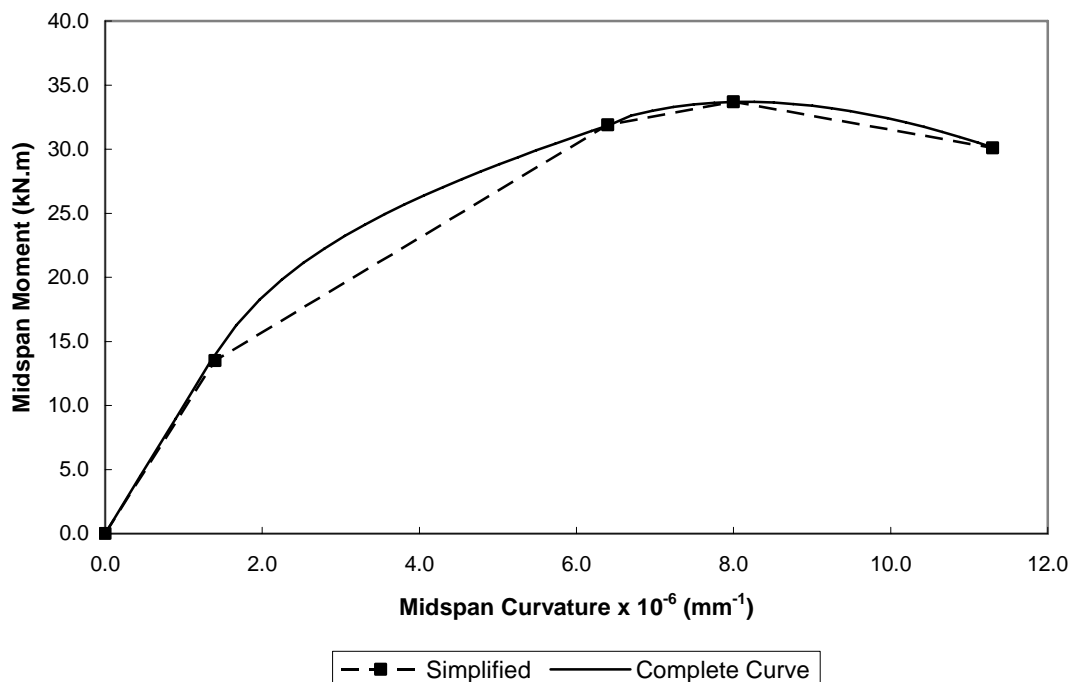


Figure 5.47: S4 modified model performance

## 5.7 SIMPLIFICATION OF THE MODIFIED MODEL

The modified model for SF-RPC plain and prestressed beams can be simplified by considering a number of key locations on the curve and using straight-line interpolation to plot the curve. For design purposes, a simplified model is needed for preliminary investigations.

For plain SF-RPC cross-sections, five key points are considered (although the simplification can be taken further if required). Point 1 corresponds to zero curvature and zero moment. Point 2 corresponds to the cracking moment and curvature. Point 3 corresponds to the moment when the tensile strain reaches  $\epsilon_t$ . Point 4 corresponds to the ultimate moment and corresponding curvature. Point 5 corresponds to the tensile strain limits  $2\epsilon_t$  imposed in the tensile stress-strain relationship. (See Appendix C for sample calculations.) Figure 5.48 compares the simplified modified model with the full modified model. As can be seen the simplification provides a reasonable estimate of the full moment-curvature relationship.



**Figure 5.48:** Simplified model – plain SF-RPC section

Simplification of the modified model for prestressed SF-RPC sections is more complex than the plain sections due to the increasing number of variations that result from the introduction of prestress. There is no set value for either the extreme compressive or tensile strain that will yield the ultimate moment and curvature. For design of prestressed SF-RPC, an iterative approach to determine the ultimate moment and curvature of a section is deemed most appropriate. (See Appendix C for sample calculations.)

From a design perspective, the application of appropriate safety factors will be required. A safety factor of 0.7 for plain SF-RPC sections and 0.8 for prestressed SF-RPC sections as adopted in the Australian Guidelines for RPC structures (2000) are deemed to be appropriate.

## 5.8 LIMITATION OF MODIFIED MODEL

Due to the preliminary nature of the study undertaken, it is important to recognize the limitations of the modified model. The model was developed from the results of 4 plain and 8 prestressed beams. Whilst the model provides a reasonable estimate of the results of the beams tested as part of this investigation, further research is recommended to determine its applicability to other cross-sectional geometries, various SF-RPC formulations and prestress levels.

The sections tested as part of this study were simple sections with rectangular cross-sections. The applicability of the model to more complex cross-sectional geometries should be investigated before application into any design models. However, from the results of the plain SF-RPC beam (Series 1), the model appears to be independent of limitations of size effects as it can provide a reasonable estimate for both the plain beam (cross-section P1) and the plain slab (cross-section P2). However, neither of these sections is a *deep* beam and therefore, further investigations into the effect of beam depth on the model need to be undertaken.

It is also important to state that the model was developed for the material properties of a fibre reinforced RPC with a specific type of fibre (i.e. straight,

0.2mm diameter, 13mm length steel fibres). The material properties of any fibre reinforced concrete are dependent on the fibre type used (Maidl, 1995). Therefore, modifications are expected to be required if alternate fibre types are used.

The parameter  $\lambda$  applied to account for the effect of confinement resulting from prestress has only been applied to the range of prestress considered in this study. No conclusive results can be drawn regarding the effect of the level of confinement on the stress-strain relationship of SF-RPC. Therefore further research in this crucial area is required.

## 5.9 CONCLUSION

1. As part of this investigation 4 plain and 8 prestressed beams were tested under four-point bending to determine their short-term flexural behaviour. The plain and prestressed beams were tested at an age of approximately 28 days under displacement control and load control, respectively.
2. The moment-curvature relationship, load-deflection behaviour, cracking behaviour and cracking and ultimate moment were determined for all beams tested.
3. The performance of the current models available for predicting the flexural behaviour of plain and prestressed SF-RPC was evaluated. These models performed well in the elastic region (i.e. prior to cracking). However, for the plain SF-RPC the models deviated considerably from the test results obtained. This deviation was minimized for the results of the prestressed SF-RPC tested as the impact of the RPC tensile stress-strain model adopted is negated by the presence of the prestressing strands.
4. The modified model proposed provides greater accuracy in predicting the flexural behaviour of the plain and prestressed SF-RPC beams tested as part of this investigation. The model adopts similar stress-strain relationships for SF-RPC in compression and tension as the currently available models but the values of the various parameters has been altered.

5. The modified model introduces the parameter  $\lambda$  to account for the effect of confinement provided by the application of prestress.
6. The modified model is based on rectangular sections only. In order to broaden the application of this model to general cross-sections, a research program containing beams of differing cross-sectional shapes, depths and prestress levels should be undertaken. In addition to this, the model should be validated for different RPC formulations particularly differing fibre types.

## **Chapter 6: Time-dependent Flexural Behaviour**

### **6.1 INTRODUCTION**

Concrete members subjected to sustained loading over a long period of time will undergo time-dependent deformations. The time-dependent deformations of a prestressed concrete member are the result of the creep and shrinkage of the concrete and relaxation of the steel used for prestressing. As the creep and shrinkage of SF-RPC are considerably less than that of conventional concrete, it follows that the time-dependent deformations of a prestressed SF-RPC member will be significantly less than the time-dependent deformations of a conventional prestressed concrete member.

Codes of practice generally rely on simple approximation methods to provide an approximate estimate of the long-term deformations of a concrete member subjected to sustained loading. The magnitude of the long-term deflections is often taken to be equal to a factored short-term deflection dependent on the level of the sustained load. This method often falls short for prestressed sections as often the sustained external load is balanced by the longitudinal effective force exerted by the tendon. Under this balanced load, the short-term deflection may be zero. Gilbert and Mickleborough (1990) present a number of approximate procedures for an estimate of the long-term deflections of a prestressed concrete member.

In addition to this, the simplified procedures specified in codes of practice for predicting the loss of prestress due to creep and shrinkage often lead to significant errors. Therefore, alternate analytical methods are needed to provide detailed time-dependent analysis of prestressed concrete members. The most widely used methods make use of the age-adjusted effective modulus method to model the effects of creep in concrete. The simple analytical procedure is discussed in detail by Gilbert and Mickleborough (1990). As the procedure calculates the time-dependent change in curvature of a cross-section, it can be used to more accurately determine the time-dependent deflections of a prestressed concrete member.

This chapter presents the experimental results and analysis of the time-dependent flexural behaviour of the prestressed SF-RPC beams tested as part of Series 3. Beam Series 3 consisted of 4 prestressed SF-RPC slabs of identical cross-section. The slabs were 300mm wide by 100mm deep. Each slab was prestressed with two 12.7mm diameter 7-wire super strands at an eccentricity of 20mm. The slabs were cast as part of Batch 7 along with a number of companion material specimens.

Included in this chapter are details pertaining to the test procedure adopted for Beam Series 3 along with a summary of the results obtained. These results include the time-dependent changes to the curvature and resulting deflections, and the cracking response of all beams tested, along with a qualitative discussion of the results. The remainder of the chapter then deals with the analysis of the results obtained. An Age-adjusted Effective Modulus Method (AEMM) has been used to analyse the time-dependent results of the prestressed SF-RPC slabs.

## 6.2 TEST PROCEDURES

The aim of Beam Series 3 was to gain some insight into the time-dependent flexural behaviour of prestressed SF-RPC slabs. The series consisted of 4 identical slabs. Details of the slab cross-section (S5) can be found in Figure 3.9. An initial prestress of 290kN was applied through two 12.7mm 7-wire super strands. At an age of 3 days, the prestressing force was transferred to the concrete by cutting the tendons at one end. After transfer of prestress, the slabs (along with companion specimens) underwent a period of hot water curing for a period of 5 days (Curing Condition 2 – see Section 3.3.2).

Upon removal from the hot water bath, the slabs were stored on the laboratory floor until testing. At an age of 26 days, one of the slabs was tested for ultimate moment capacity to characterise the full moment-curvature behaviour for the cross-section. The remaining 3 slabs were simply supported with a span of 2700mm. At an age of 28 days, these 3 slabs were then loaded with a sustained service load of between 120% and 180% of the calculated load required to cause cracking in the constant moment region of the beam. The

sustained load on each slab was maintained without adjustment for the duration of the test period (270 days). The slab designations and loading arrangement can be found in Table 3.7 and Figure 3.10 respectively.

The initial behaviour of the cross-section from casting to 28 days (application of load) was not investigated as part of this study. An approximate estimate of the deflection of the member at the midspan and under the points of application of the load was obtained prior to the commencement of sustained loading. Appendix B contains details pertaining to the approximation of the curvature and deflection at 28 days.

As this was a preliminary investigation into the time-dependent behaviour of SF-RPC members, only effective curvature values were considered. For all beams, the effective curvature was obtained from deflection measurements at midspan and under the application of equal point loads. The deflections were measured using dial gauges.

The beams were cast as part of Batch 7. A number of companion SF-RPC specimens were cast and tested to measure the short-term and time-dependent properties of the SF-RPC. These results can be found in Chapter 4.

## **6.3 TEST RESULTS**

### **6.3.1 Slab S5 A**

Slab S5 A was tested at an age of 26 days to determine the cracking behaviour and ultimate moment capacity of cross-section S5. Figure 6.1 contains the moment-curvature relationship for the cross-section. The curvature was calculated from the midspan deflection.

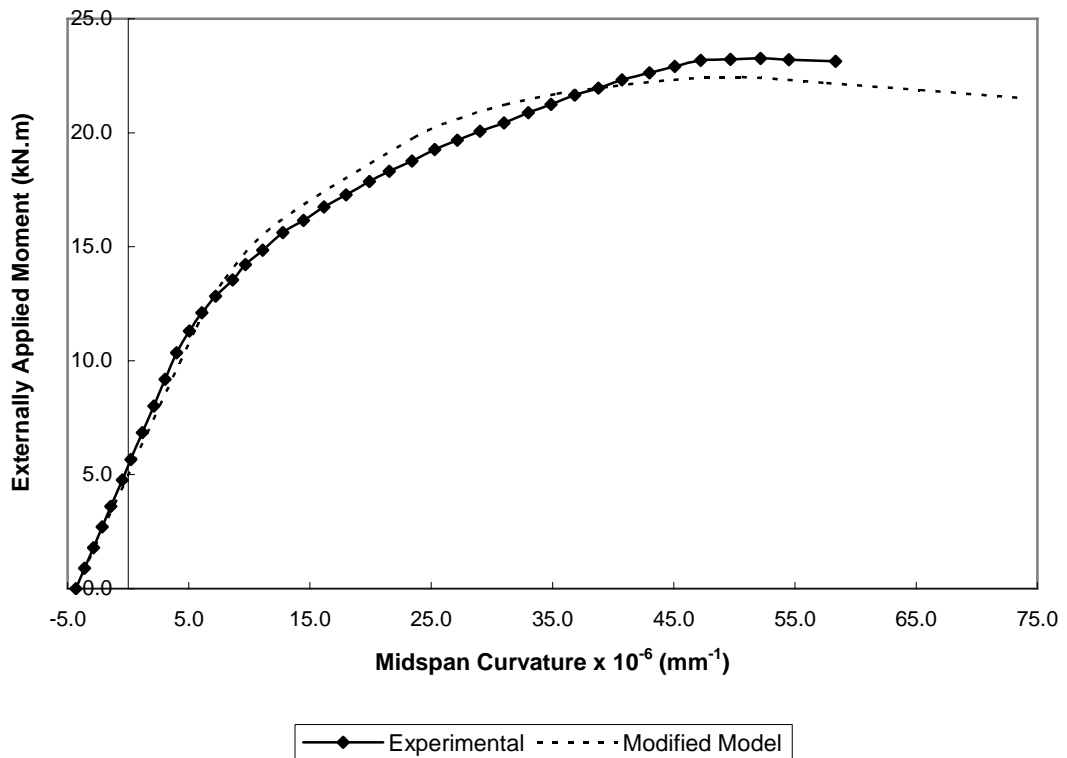


**Figure 6.1:** Moment – curvature relationship for cross-section S5

From Figure 6.1, it can be seen that the cracking moment of cross-section S5 is 11.2kNm (cracking load = 24.9kN) and the ultimate moment capacity is 23.3kNm. The curvature at first crack and ultimate were  $5.37 \times 10^{-6} \text{ mm}^{-1}$  and  $52.25 \times 10^{-6} \text{ mm}^{-1}$ , respectively (deflection 4.17mm and 40.75mm, respectively).

Figure 6.1 also shows the performance of the modified model in predicting the flexural behaviour of prestressed SF-RPC slabs. As can be seen, the model agrees with the experimental results well. Slab S5 is considered to have a medium level of prestress corresponding to  $\lambda = 12$  (see Table 5.3).

### 6.3.2 Slab S5 B

At an age of 28 days, Slab S5 B was placed under a sustained load of 30.2kN which is approximately 1.2 times the load required to cause cracking of cross-section S5. Figure 6.2 shows the change in effective curvature (see Section 5.5.1) with time. The effective curvature was calculated from the midspan deflection results. The initial negative curvature is the result of the application of prestress.

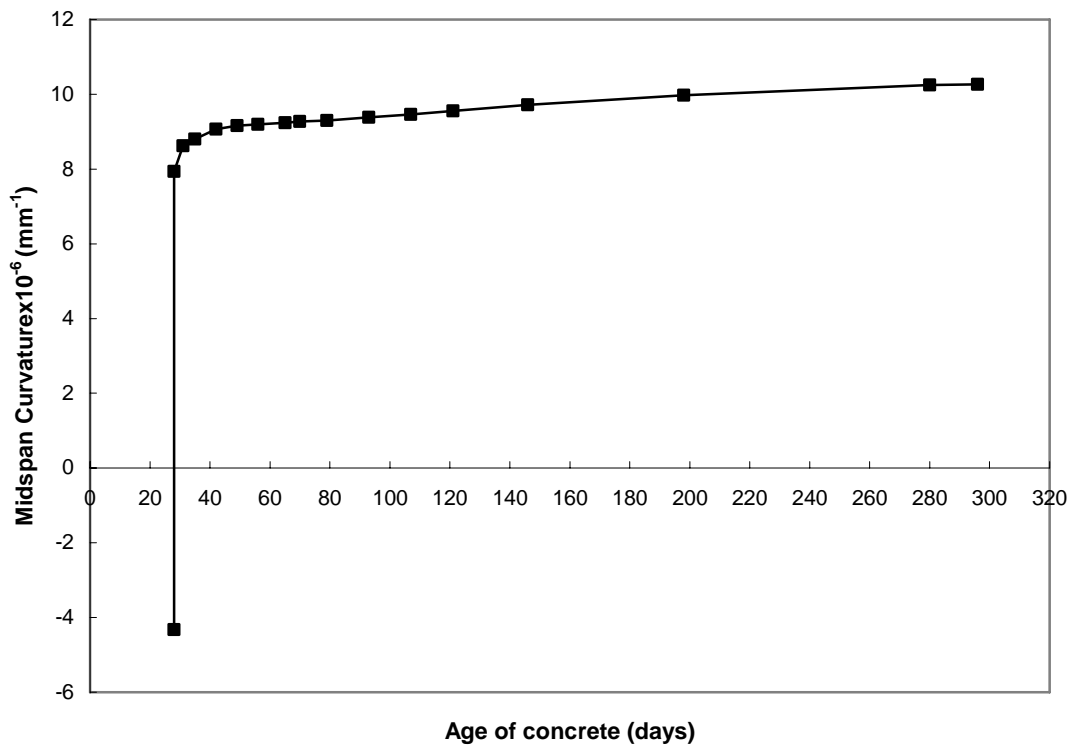


**Figure 6.2:** Change in midspan curvature with time (S5 B)

Prior to the application of load, the curvature due to prestress was approximately  $-4.32 \times 10^{-6} \text{ mm}^{-1}$ . Immediately after the application of the sustained loading, the curvature increased by  $+12.26 \times 10^{-6} \text{ mm}^{-1}$  to  $7.94 \times 10^{-6} \text{ mm}^{-1}$ . This change in curvature corresponds to a total change in deflection of 9.65mm. With time, due to the effects of creep and shrinkage, the curvature increased to  $10.26 \times 10^{-6} \text{ mm}^{-1}$  by the completion of the test period (268 days). This corresponds to a time-dependent increase in effective curvature of  $2.32 \times 10^{-6} \text{ mm}^{-1}$  (or an increase in midspan deflection of 1.83mm). Approximately 70% of the total change in effective curvature (for the test period) occurred during the first 90 days after the application of the sustained load.

### 6.3.3 Slab S5 C

At an age of 28 days, Slab S5 C was placed under a sustained load of 35.8kN which is approximately 1.4 times the load required to cause cracking of cross-section S5. Figure 6.3 shows the change in effective curvature with time.

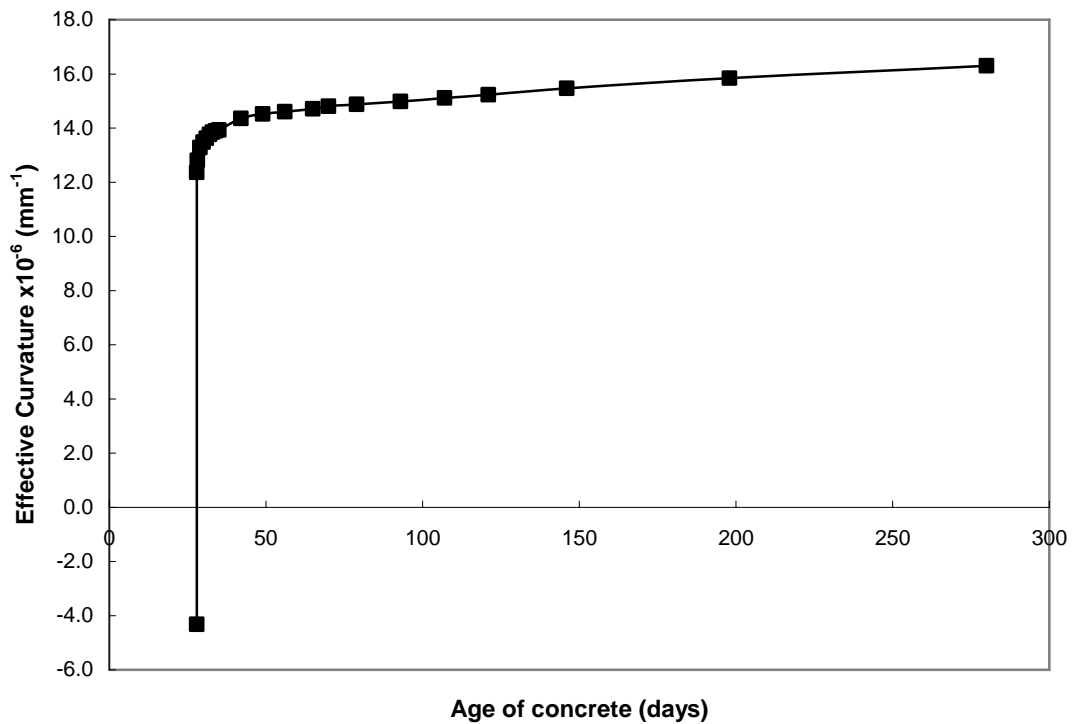


**Figure 6.3:** Change in midspan curvature with time (S5 C)

Prior to the application of load, the curvature due to prestress was approximately  $-4.32 \times 10^{-6} \text{mm}^{-1}$ . Immediately after the application of the sustained loading, the curvature increased by  $+16.68 \times 10^{-6} \text{mm}^{-1}$  to  $12.36 \times 10^{-6} \text{mm}^{-1}$ . This change in curvature corresponds to a total change in deflection of 12.95mm. With time, due to the effects of creep and shrinkage, the curvature increased to  $16.34 \times 10^{-6} \text{mm}^{-1}$  by the completion of the test period (268 days). This corresponds to a time-dependent increase in effective curvature of  $3.98 \times 10^{-6} \text{mm}^{-1}$  (or an increase in midspan deflection of 3.09mm). Approximately 70% of the total change in effective curvature (for the test period) occurred during the first 90 days after the application of the sustained load.

#### 6.3.4 Slab S5 D

At an age of 28 days, Slab S5 D was placed under a sustained load of 46.3kN which is approximately 1.8 times the load required to cause cracking of cross-section S5. Figure 6.4 shows the change in effective curvature with time.

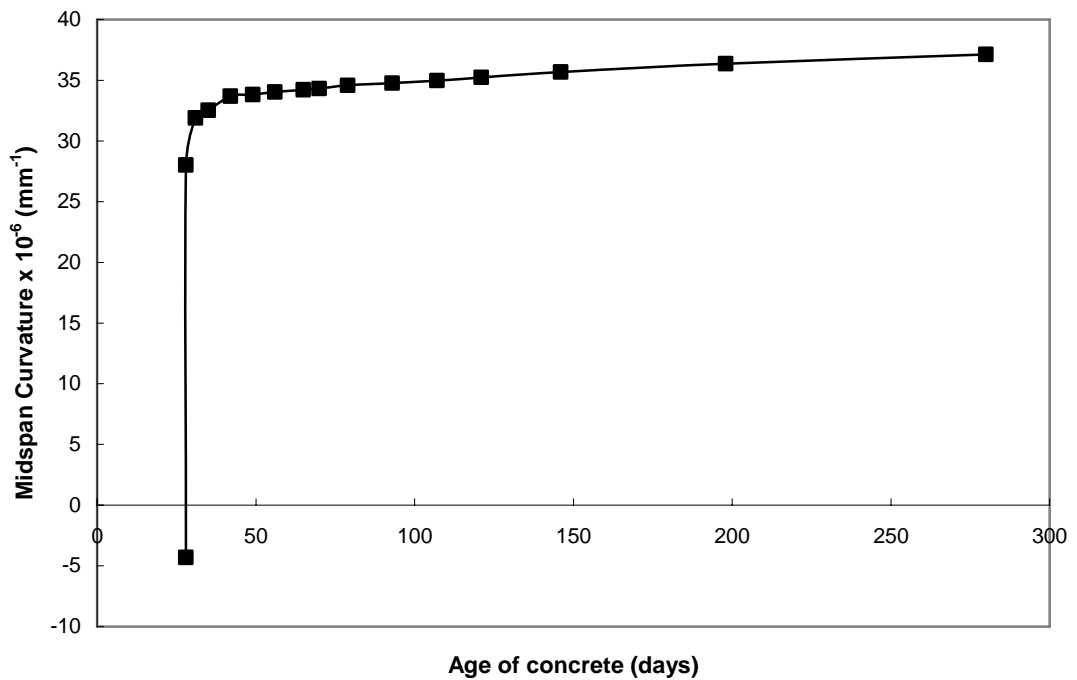


**Figure 6.4:** Change in midspan curvature with time (S5 D)

Prior to the application of load, the curvature due to prestress was approximately  $-4.32 \times 10^{-6} \text{mm}^{-1}$ . Immediately after the application of the sustained loading, the curvature increased by  $+32.33 \times 10^{-6} \text{mm}^{-1}$  to  $28.01 \times 10^{-6} \text{mm}^{-1}$ . This change in curvature corresponds to a total change in deflection of 25.1mm. With time, due to the effects of creep and shrinkage, the curvature increased to  $37.12 \times 10^{-6} \text{mm}^{-1}$  by the completion of the test period (252 days). This corresponds to a time-dependent increase in effective curvature of  $9.11 \times 10^{-6} \text{mm}^{-1}$  (or an increase in midspan deflection of 7.07mm). Approximately 80% of the measured total change in effective curvature (for the test period) occurred during the first 90 days after the application of the sustained load.

Table 6.1 is a summary of the 3 sustained load tests conducted as part of Beam Series 3. From the table, it can be seen that there is an increase in the ratio of the initial to time-dependent deflection with increasing sustained load level.

**Table 6.1:** Initial to time-dependent deflection

	<u>S5 B</u>	<u>S5 C</u>	<u>S5 D</u>
Sustained Load	1.2M <sub>cr</sub>	1.4M <sub>cr</sub>	1.8M <sub>cr</sub>
Initial change in deflection $\delta_i$	9.65	12.95	25.10
Time-dependent change in deflection $\delta_t$	11.48	16.04	32.17
$\delta_t / \delta_i$	1.19	1.24	1.28

#### 6.4 CROSS-SECTIONAL ANALYSIS METHOD

As mentioned, in order to determine the time-dependent behaviour of a prestressed SF-RPC member, a simple analytical method is needed to determine the effect of creep, shrinkage and loss of prestress with time. These effects can be quantified by the Age-adjusted Effective Modulus Method (AEMM). This section contains a brief explanation of the method. Thorough details of the method are described in Ghali et al. (2002) and Gilbert and Mickleborough (1990).

In a prestressed concrete beam, the bonded tendons (and any conventional reinforcement) provide restraint to the time-dependent shortening of concrete caused by creep and shrinkage. As the concrete creeps and shrinks, the tendons are gradually compressed. Equal and opposite tensile forces are applied to the concrete at each level of bonded reinforcement, thereby reducing the compression caused by prestress. The result of these gradually applied tensile forces at each level of bonded steel is significant time-dependent changes in curvature and deflection (Gilbert and Mickleborough, 1990).

The time-dependent analysis considered here uses the AEMM (Bazant, 1972) together with a relaxation approach (Bresler, Selna, 1964). The application was proposed by Gilbert (1988). In the relaxation approach, the strain at any point on the cross-section is initially assumed to remain unchanged during the time period being considered. If the total strain is held constant and the creep and shrinkage components change, then the instantaneous strain component must also change by an equal and opposite amount resulting in a change in the concrete stress. The concrete stress on the cross-section is therefore allowed to vary due to relaxation and as a result, the internal actions will change and

equilibrium will not be maintained. An axial force  $\Delta N$  and a bending moment  $\Delta M$  must therefore be applied to the cross-section to restore equilibrium. The actions required to restrain creep and shrinkage in the concrete and creep in the prestressing tendon are given by:

$$-\Delta N_{creep} = -\bar{E}_e \Delta \phi (A_c \varepsilon_{oi} + B_c \kappa_i) \quad (6.1)$$

$$-\Delta M_{creep} = -\bar{E}_e \Delta \phi (B_c \varepsilon_{oi} + \bar{I}_c \kappa_i) \quad (6.2)$$

$$-\Delta N_{shrinkage} = -\bar{E}_e \varepsilon_{sh} A_c \quad (6.3)$$

$$-\Delta M_{shrinkage} = -\bar{E}_e \varepsilon_{sh} B_c \quad (6.4)$$

$$-\Delta N_{relaxation} = \sum_{k=1}^m R_k \quad (6.5)$$

$$-\Delta M_{relaxation} = \sum_{k=1}^m R_k d_{pk} \quad (6.6)$$

$$-\Delta N_{total} = -\Delta N_{creep} - \Delta N_{shrinkage} - \Delta N_{relaxation} \quad (6.7)$$

$$-\Delta M_{total} = -\Delta M_{creep} - \Delta M_{shrinkage} - \Delta M_{relaxation} \quad (6.8)$$

where  $A_c$  is the concrete area  
 $B_c, \bar{I}_c$  are the first and second moment of the concrete area about the top surface of the section respectively  
 $\Delta \phi$  is the change in creep coefficient for the time period being considered  
 $\varepsilon_{sh}$  is the free shrinkage occurring during the time period being considered  
 $R_k$  relaxation in each layer of tendons  
 $\bar{E}_e$  is the age-adjusted effective modulus as defined in Equation 6.9

$$\bar{E}_e = \frac{E_c}{1 + \chi \Delta \phi} \quad (6.9)$$

where  $E_c$  Is the modulus of elasticity of the concrete  
 $\chi$  Is the aging coefficient

### Uncracked cross-section

Consider the transformed section shown in Figure 6.5. A simple cross-section containing only one layer of prestressing steel and no conventional reinforcement such as cross-section S5 is shown. The method is applicable to

any cross-section regardless of geometry and bonded reinforcement arrangement.

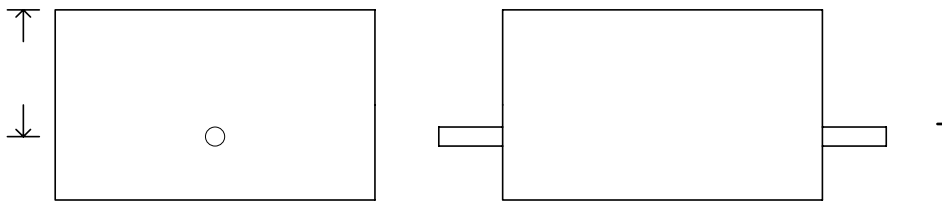


**Figure 6.5:** Actual and age-adjusted transformed section (uncracked)

The bonded reinforcement is transformed into equivalent areas of concrete i.e. an additional area of concrete equal to  $(\bar{n} - 1)A_p$  is added to the section at each bonded steel level where  $\bar{n}$  is the age-adjusted modular ratio and is given by Equation 6.10.

$$\bar{n} = \frac{E_p}{E_e} \quad (6.10)$$

where  $E_p$  is the modulus of elasticity of the prestressing steel

Figure 6.6 shows the change in strain profile with time. The initial strain profile (i.e.  $\varepsilon_{oi}$  and  $\kappa_i$ ) are determined from a short-term analysis of the cross-section. For SF-RPC, the modified model presented in Chapter 6 was used to determine the initial strain profile. The time-dependent change in strain at any depth  $y$  below the top of the cross-section ( $\Delta\varepsilon$ ) is given by:

$$\Delta\varepsilon = \Delta\varepsilon_o + y\Delta\kappa \quad (6.11)$$

where  $\Delta\varepsilon$  is the change in top fibre strain as given by Equation 6.12

$\Delta\kappa$  is the change in curvature as given by Equation 6.13

$$\Delta\varepsilon_o = \frac{\bar{B}_e \delta M - \bar{I}_e \delta N}{E_e (\bar{B}_e^2 - \bar{A}_e \bar{I}_e)} \quad (6.12)$$

$$\Delta\kappa = \frac{\bar{B}_e \delta N - \bar{A}_e \delta M}{E_e (\bar{B}_e^2 - \bar{A}_e \bar{I}_e)} \quad (6.13)$$

where  $\bar{A}_e$  is the area of the age-adjusted transformed section (see Figure 6.5)

$\bar{B}_e, \bar{I}_e$  are the first and second moments of area of the age-adjusted transformed section with respect to the top fibre

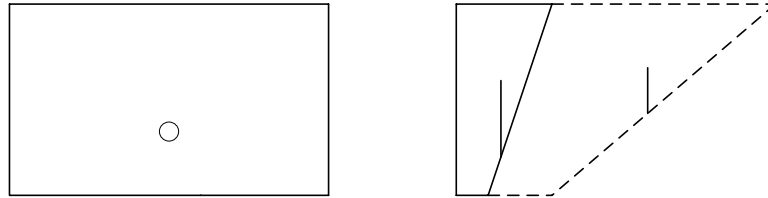


**Figure 6.6:** Time-dependent deformations

### Cracked cross-section

When a fully cracked cross-section is subjected to a period of sustained loading, creep causes a change in the position of the neutral axis. In general, the depth to the neutral axis increases with time and therefore so too does the area of concrete in compression. However, to include this in the time-dependent calculations would require an iterative solution resulting in increased complexity with little increase in accuracy. Therefore, in order to simplify calculations, it is assumed that the depth to the neutral axis remains constant with time. The assumption is actually necessary if the short and time-dependent stress and strains increments are to be calculated separately and added together to obtain the final stresses and deformations. The assumption greatly simplifies the analysis and usually results in relatively little error. (Gilbert and Mickleborough, 1990)

The depth to the neutral axis ( $d_n$ ), the initial top fibre strain ( $\varepsilon_{oi}$ ) and the initial curvature ( $\kappa_i$ ) are determined from the result of a short-term analysis (see Chapter 5). Consider the cracked section shown in Figure 6.7.

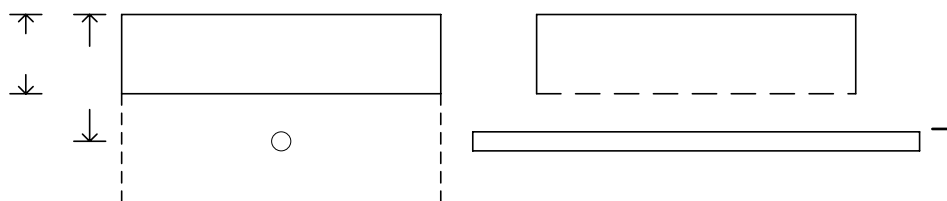


**Figure 6.7:** Actual and age-adjusted transformed section (cracked)

The restraining action,  $-\Delta N$  and  $-\Delta M$  are calculated using Equations 6.1 - 6.8 with the terms  $A_c, B_c$  and  $\bar{I}_c$  in the equations being the properties of the uncracked part of the concrete cross-section with respect to the top fibre (see Figure 6.7). The change in the strain distribution with time is calculated using Equations 6.11 – 6.13 with the terms  $\bar{A}_e, \bar{B}_e$  and  $\bar{I}_e$  being the properties of the cracked age-adjusted transformed section (see Figure 6.7).

### 6.5 AEMM APPLIED TO SF-RPC

The method described in Section 6.3 was applied to the results of the time-dependent behaviour of the slabs in Beam Series 3.

Figures 6.8 – 6.10 show a comparison between the predicted results using the AEMM and the actual effective curvature results for the three slabs tested under sustained loads. As can be seen, the method provides reasonable approximations for predicting the long-term changes in the effective curvature of SF-RPC members. For S5 B and S5 C, the method slightly over-predicts the time-dependent deformations. The method is relatively accurate for S5 D. This increased accuracy for slab S5 D is the result of the significant portion of the ultimate load that the slab is carrying. The slab was carrying 1.8 times the cracking load (or approximately 85% of the ultimate moment capacity of the section). The beam was significantly cracked throughout almost the entire span and therefore the assumption of an effective curvature (i.e. constant curvature across the span) was more accurate for slab S5 D than for either slab S5 B or S5 C.

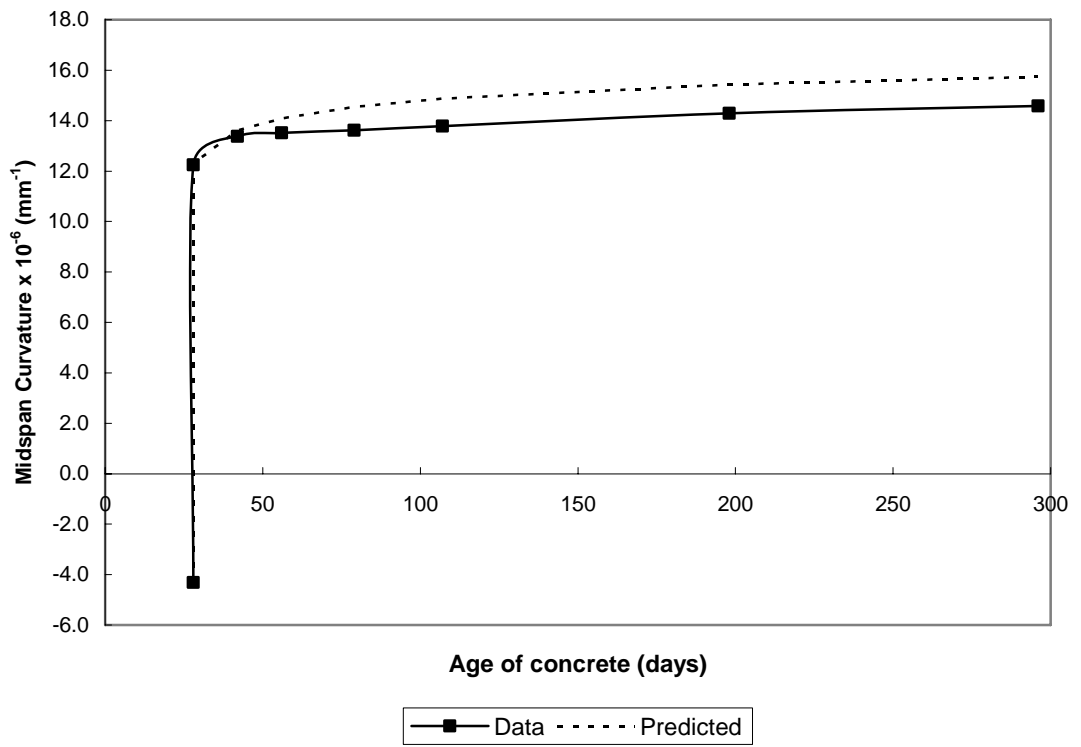


Figure 6.8: Predicted long – term deformations (S5 B)

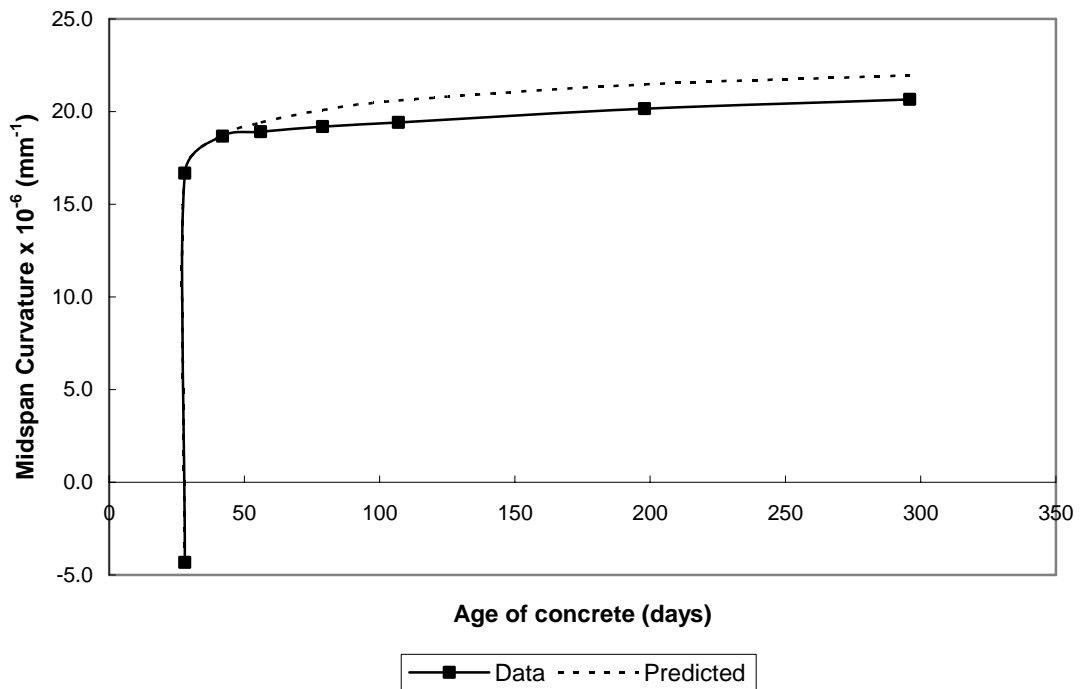
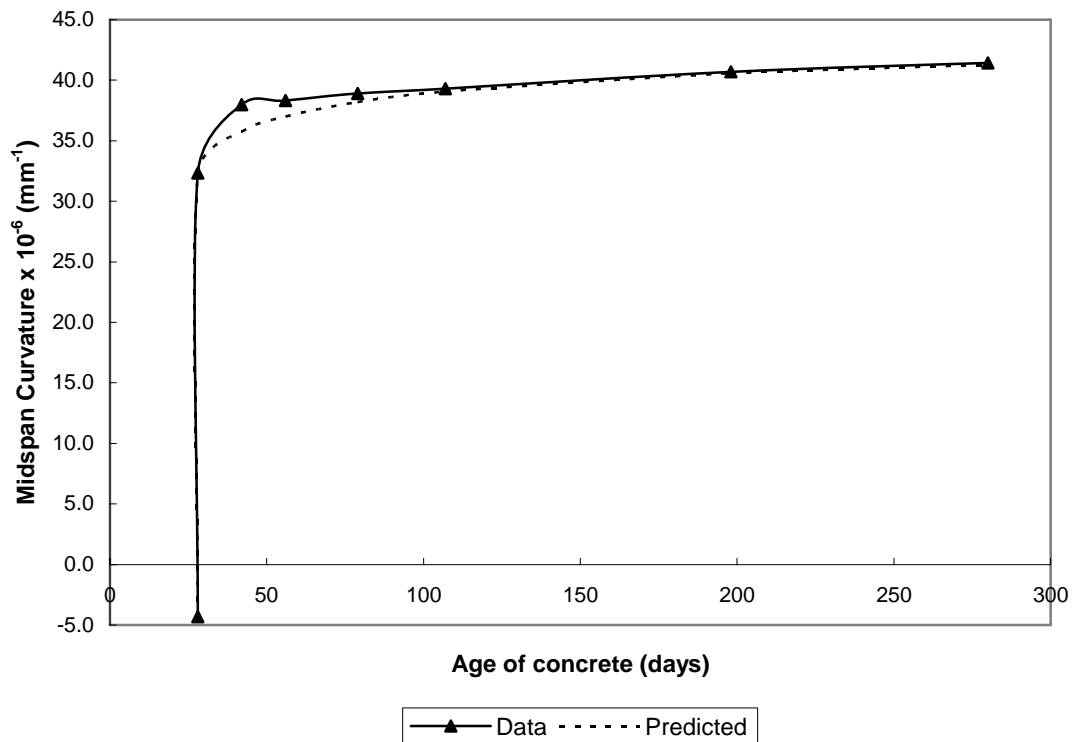


Figure 6.9: Predicted long – term deformations (S5 C)



**Figure 6.10:** Predicted long-term deformations from the AEMM (S5 D)

The AEMM may be refined further for SF-RPC by considering the depth of intact concrete (as shown in Figure 6.11) and not the depth to the neutral axis when calculating the restraining forces due to creep and shrinkage (Equations 6.1 – 6.4) and calculations pertaining to the area plus the first and second moment of area of the transformed section. This refinement is logical as any concrete that is still intact (i.e. uncracked) will be affected by creep and shrinkage and will also contribute to the stiffness of the member. However, for SF-RPC members that have undergone heat-treatment such as the slabs considered in this study, this refinement yields minimal change to the results as the long-term shrinkage strains after heat-treatment are minimal. The results of the refined AEMM are shown in Figure 6.12 – 6.14.

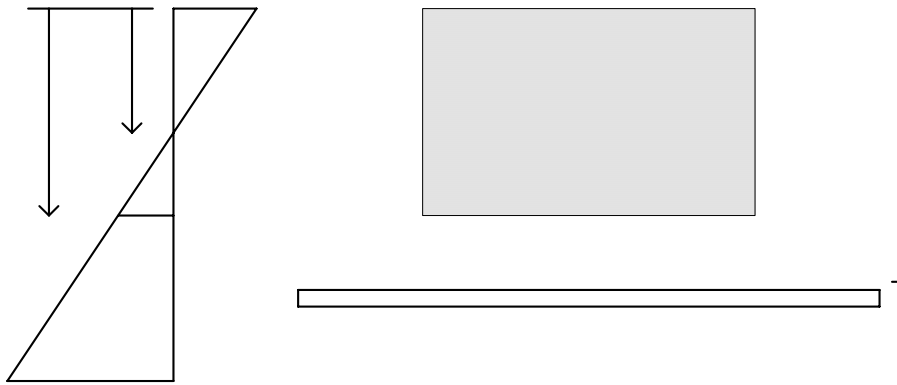


Figure 6.11: Refined age – adjusted transformed section

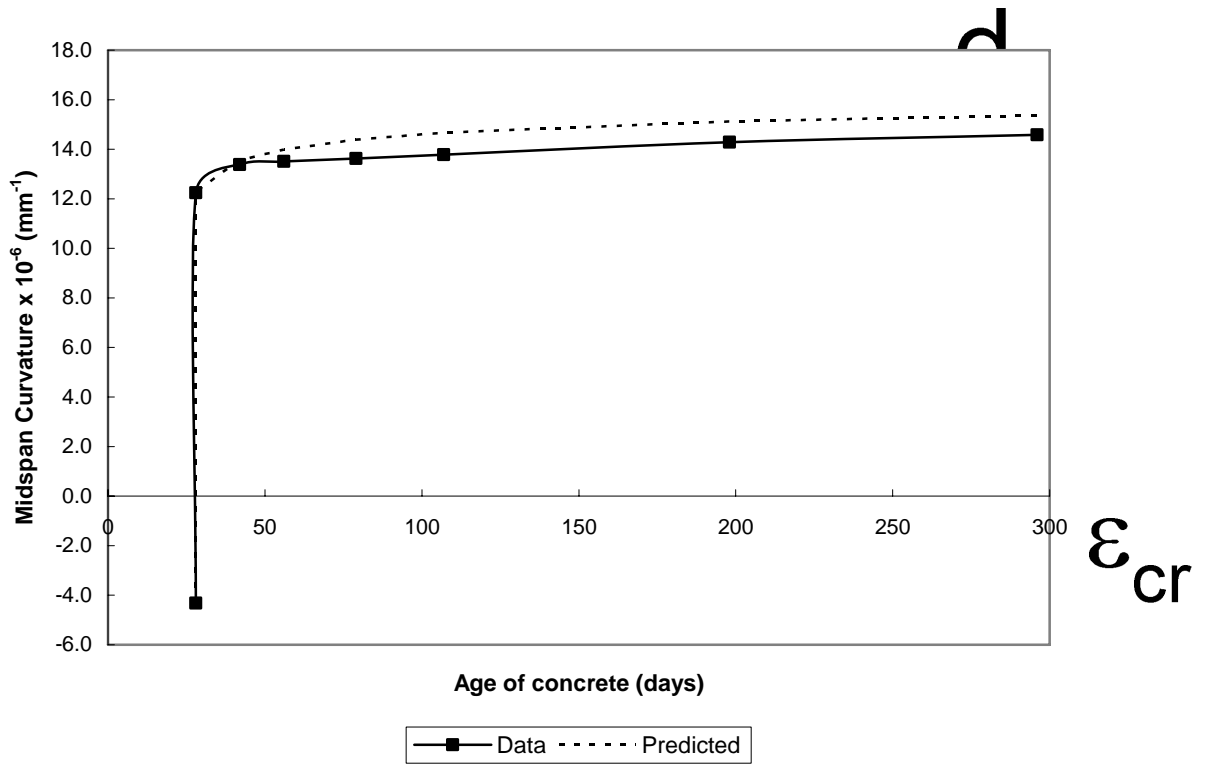
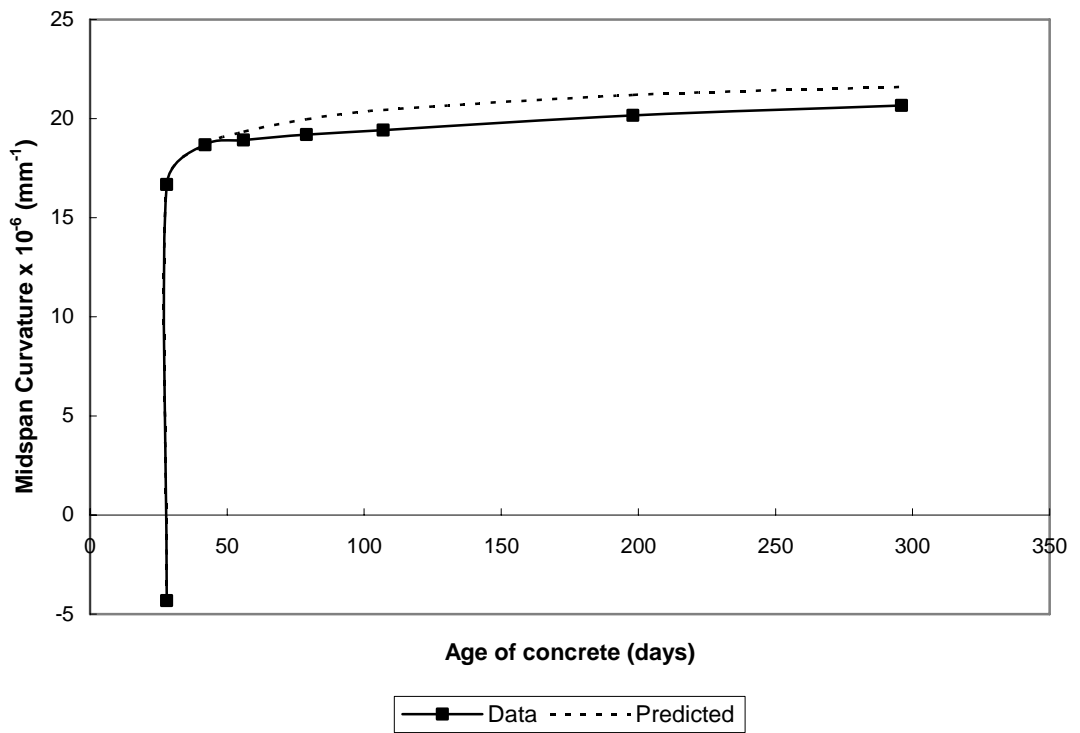
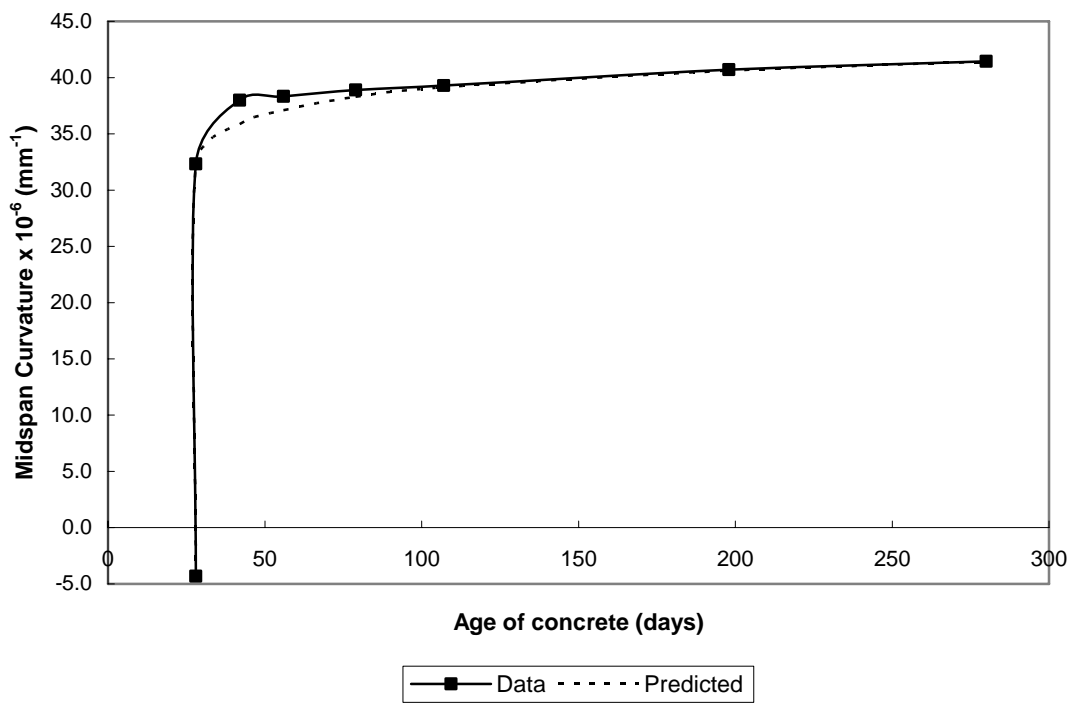


Figure 6.12: Refined predictions for long-term deformations (S5 B)

$d_n$  - depth to  
 $d_{int}$  - depth to  
 $d_{cr}$  - depth to



**Figure 6.13:** Refined predictions for long-term deformations (S5 C)



**Figure 6.14:** Refined predictions for long-term deformations (S5 D)

However, for non heat-treated SF-RPC where the long-term shrinkage is considerable, this refinement has a significant impact on the results. For example, consider a slab similar to slab S5 B but with an overall shrinkage strain of  $-400 \mu\epsilon$  occurring between 28 and 268 days (i.e. after loading). Figure 6.15 shows a comparison between the AEMM with and without the refinement of using the depth of intact concrete for restraining forces due to shrinkage and creep and calculations pertaining to the age-adjusted transformed area. Further studies are required with non heat-treated SF-RPC beams to determine whether the refinement is necessary.

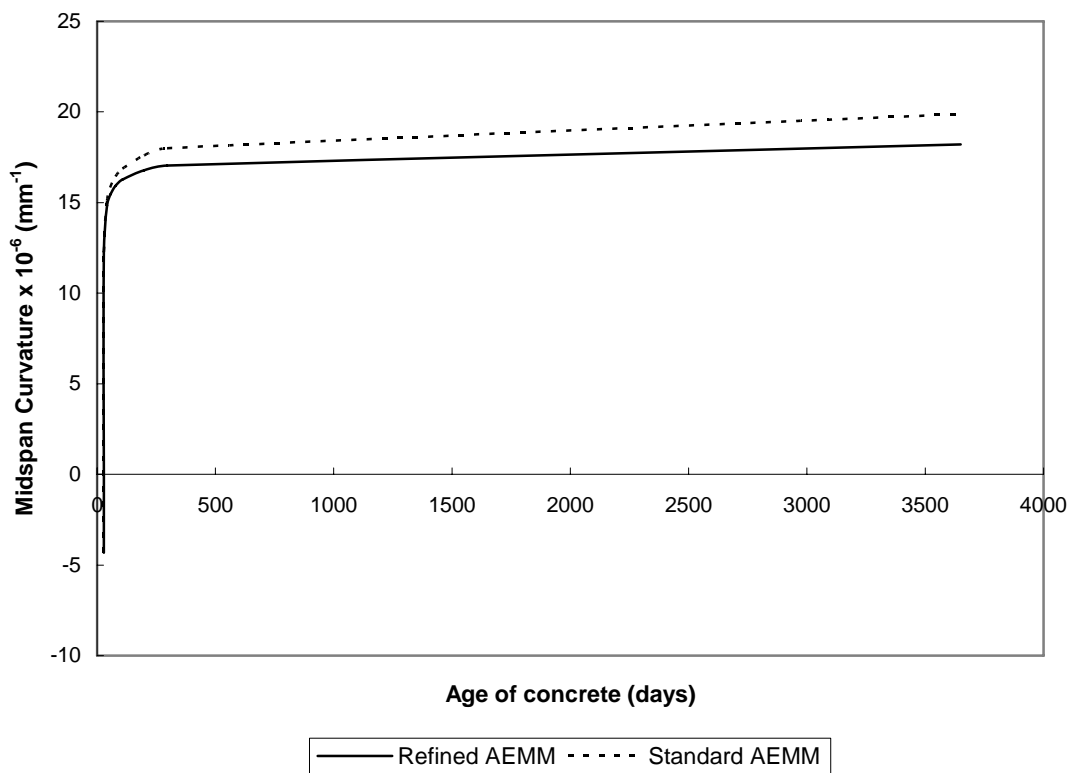


**Figure 6.15: Refined AEMM**

## 6.5 CONCLUSION

1. As part of this investigation 4 prestressed slabs were tested under 4-point bending to determine the time-dependent behaviour of prestressed SF-RPC slabs. One slab was tested for first cracking and ultimate moment capacity at an age of 26 days. The remaining 3 slabs were placed under various levels of sustained loading. The loads on each slab remained unchanged throughout the duration of the test (approximately 300 days).

2. The time-dependent moment-curvature relationship and cracking behaviour were determined for the three slabs tested.
3. The performance of an Age-adjusted Effective Modulus Method (AEMM) for predicting the time-dependent behaviour of prestressed SF-RPC slabs was evaluated. From the results of this preliminary investigation, it was shown that an AEMM can be used to provide a reasonable estimate of the time-dependent deformations of heat-treated SF-RPC slabs.
4. For conventional strength concrete, the AEMM only considers the contribution of concrete above the neutral axis for calculations pertaining to the restraining forces due to creep and shrinkage and for calculating the age-adjusted transformed section properties. Refinements can be made to the AEMM for predicting the behaviour of prestressed SF-RPC slabs to account for the increased depth of intact concrete that is the result of the increased tensile capacity of the material when compared with conventional concrete.
5. The number of long-term beam specimens tested was 3. The test duration was approximately 9 months. In order to validate the use of an AEMM to determine the time-dependent behaviour of SF-RPC members, an expanded research program should be undertaken.

## **Chapter 7: Conclusions and Recommendations**

### **7.1 CONCLUSION**

Since its introduction in 1995, Reactive Powder Concrete (RPC) has seen increasing interest and utilisation. The superior mechanical and structural properties of the material result in a concrete that is extremely versatile and durable. Throughout the world, several RPC structures have already been built including pedestrian bridges in Canada, Korea and Japan along with vehicular bridges in Australia and France.

The aim of this study was to investigate the material behaviour of a locally produced SF-RPC and to determine the flexural behaviour of plain and prestressed SF-RPC structural members. As part of this research, a detailed material investigation was undertaken to determine the short-term and time-dependent properties of SF-RPC. In addition to this, 16 plain and prestressed SF-RPC beams were produced and tested. Based on this experimental program and analytical work, the following conclusions can be drawn.

For the SF-RPC investigated with a mix design as shown in Table 3.1, from the results of the materials investigation the following conclusions can be drawn:

1. Behaviour in compression
  - a. For specimens that have undergone heat treatment, the mean 28-day compressive strength was 167.0MPa with a characteristic compressive strength of 153.0MPa. On the condition that heat treatment is provided for no less than 2 days at 90°C, the compressive strength results obtained at the end of the heat treatment process can be taken as the final compressive strength value.
  - b. For specimens that have undergone standard curing conditions, the rate of compressive strength development is greatest between 3 and 7 days. The final compressive strength is approximately 1.3 times the compressive strength at 28 days.

- c. The temperature at which heat treatment is carried out has a greater impact on the compressive strength than the duration of heat treatment.

## 2. Behaviour in flexure

- a. For specimens that have undergone heat treatment, the mean 28-day flexural strength was 23.0MPa with a characteristic flexural strength of 16.5MPa. The flexural strength results obtained at the end of the heat treatment process can be taken as the final strength.
- b. The flexural strength lies in the range of 1.5 to 2.3 times the square root of the compressive strength. For design purposes, a flexural strength value of no more than 1.5 times the square root of the compressive strength should be considered. However, due to the highly variable nature of SF-RPC, it is preferable to determine this material property experimentally.
- c. Similar to the compressive strength result of specimens that have undergone standard curing conditions, the rate of flexural strength development for standard cure specimens is greatest between 3 and 7 days. The final flexural strength is about 1.1 times the flexural strength at 28 days.
- d. For specimens with or without heat treatment, the material displays considerable ductility in the post-peak range of the load-deflection curve making it applicable for use in structural applications.

## 3. Behaviour in direct tension

- a. For specimens that have undergone heat treatment, the mean 28-day estimated tensile strength was 8.3MPa. The range of calculated tensile strengths was 6.3 to 11.1MPa.
- b. For properties that are dependent on the tensile strength of the material (i.e. direct tensile and flexural strength), the results showed a large variation indicating considerable scatter of the results. This is normal for any fibre reinforced concrete due to the natural

variations of the material as a result of the random distribution of fibres in the concrete mix.

#### 4. Modulus of Elasticity

- a. For specimens that have undergone heat treatment, the mean 28-day static chord modulus of elasticity was 45.5GPa with a characteristic static chord modulus of elasticity of 43.1GPa. The modulus of elasticity results obtained at the end of the heat treatment period can be taken as the final value.
- b. The modulus of elasticity (in GPa) lies in the range of 3.4 to 3.6 times the square root of the compressive strength (in MPa). For design purposes, a modulus of elasticity value (in GPa) of no more than 3.4 times the square root of the compressive strength (in MPa) should be considered.
- c. Similar to the compressive strength result of specimens that have undergone standard curing conditions, the rate of modulus of elasticity development for standard cure specimens is greatest between 3 and 7 days. The final modulus of elasticity is about 1.1 times the modulus of elasticity at 28 days.

#### 5. Stress-Strain Behaviour in Compression

- a. The stress-strain behaviour of SF-RPC is best determined experimentally. A conservative model for the stress-strain behaviour for design purposes may be taken as that shown in Figure 4.16.
- b. Although not investigated in this particular study, a value of 0.2 is a conservative estimate for the Poisson's Ratio of SF-RPC.

#### 6. Shrinkage

- a. For specimens that have undergone heat treatment, the majority of shrinkage is autogenous and occurs during the period of heat treatment. The autogenous shrinkage of heat-treated SF-RPC is about  $400\mu\epsilon$  with a small proportion (100 -  $150\mu\epsilon$ ) of shrinkage strain occurring after heat treatment. Like conventional concrete,

the rate of drying shrinkage for SF-RPC develops rapidly at an early age and continues to increase at a decreasing rate with time.

- b. Using the results of a regression analysis on the shrinkage results, the long-term shrinkage of SF-RPC may be as high as  $700\mu\epsilon$ .
- c. The shrinkage of specimens that have undergone standard curing conditions follows a similar pattern to that of the shrinkage of conventional concrete. The shrinkage develops rapidly at an early age and continues to increase at a decreasing rate with time. The majority of the drying shrinkage of standard cure SF-RPC specimens occurs within the first 90 days after the cessation of wet curing. Current equations available for predicting the shrinkage of concrete should be used with care as they tend to over-predict the long-term shrinkage of SF-RPC even when the 28-day shrinkage value is known.

## 7. Creep

- a. The creep of SF-RPC with or without initial heat treatment, like conventional concrete, develops rapidly at an early age and continues to increase at a decreasing rate with time.
- b. Heat treatment significantly reduces the creep of SF-RPC. For specimens that have undergone heat treatment, the basic creep coefficient ranges from 0.2 – 0.35. For standard cure specimens, the basic creep coefficient is approximately 0.6.
- c. Provided the creep-coefficient at 28-days is known, the equation given in ACI-209 (1992) gives a reasonable estimate of the long-term creep of SF-RPC. The method given in AS3600 (2001) with modified basic creep factors also provides a reasonable estimate for the creep coefficient curves of SF-RPC with time.
- d. The creep coefficients for SF-RPC with or without heat treatment are smaller than those of conventional concrete.

From the three series of beam tests conducted as part of this investigation in conjunction with the results of the materials investigation, the following conclusions can be made:

1. Short-term flexural behaviour – Current models
  - a. There are currently two available models for predicting the flexural behaviour of plain and prestressed RPC beams. The models were evaluated against the short-term flexural behaviour of plain and prestressed beams. The models performed well in the elastic region (i.e. prior to cracking).
  - b. For the plain beams in the post-cracking and post-peak ranges, the current models deviated considerably from the test results.
  - c. For the prestressed beams and slab, the deviations seen with the plain beam results were minimized. The smaller deviation noted between the current models and the test results for the prestressed beams and slab is because the impact of the tension model for the SF-RPC is largely negated by the presence of the prestressing strands.
2. Short-term flexural behaviour – Modified model
  - a. A modified model was proposed to provide greater accuracy in predicting the deflection of plain and prestressed SF-RPC beams and slabs. The model adopts similar principles for cross-section analysis as the currently available models but the material stress-strain constitutive laws have been modified.
  - b. The modified model introduces a parameter  $\lambda$  to account for the effect of confinement provided by the application of prestress. This parameter was necessary to increase the accuracy of the model when applied to the prestressed beams. The effect of confinement is the limitation of crack growth under flexural loads.
3. Time-dependent flexural behaviour
  - a. The performance of an Age-adjusted Effective Modulus Method (AEMM) for predicting the time-dependent behaviour of prestressed

slabs was evaluated. From the results of this preliminary investigation, it can be seen that an AEMM can be used to provide a reasonable estimate of the time-dependent deformations of prestressed SF-RPC slabs.

- b. For conventional strength concrete, the AEMM only considers the contribution of concrete above the neutral axis for calculations pertaining to the restraining forces due to creep and shrinkage and for calculating the age-adjusted transformed section properties. Refinements can be made to the AEMM for predicting the behaviour of prestressed SF-RPC slabs to account for the increased depth of 'intact concrete' that is the result of the increased tensile capacity of the material when compared with conventional concrete.

## **7.2 RECOMMENDATIONS**

This investigation was by no means an exhaustive study into the material and structural behaviour of SF-RPC. Further research is recommended to further enhance the fundamental knowledge of this relatively new material. There are a number of areas that have been identified from the results of this research.

1. From the material results obtained from this investigation, there appears to be some disparity between the two levels of heat treatment considered. Further studies are therefore required to determine the effect of temperature and duration of heat treatment on the material properties of SF-RPC. Knowledge of this is necessary as it is envisaged that the majority of SF-RPC members will undergo some form of heat treatment predominantly through the application of steam curing. In addition to this, studies should be undertaken to consider if there are any differences between steam curing and full hot water submersion as considered in this study.
2. As a result of the short-term flexural testing of 8 prestressed beams, there appears to be a relation between the confinement effect due to prestress

and the stress-strain relationship of SF-RPC in tension. Further studies are required to fully investigate this connection. In particular, the relationship between level of prestress (i.e. confinement) and the parameter  $\lambda$  needs to be addressed.

3. The modified model for flexural behaviour of plain and prestressed SF-RPC beams presented as part of Chapter 5 was based on a limited number of test results. From this preliminary investigation, the model could provide reasonable predictions for two depths of both plain and prestressed SF-RPC beams. However, none of the beams tested could be considered to be a 'deep beam'. Further studies are required to determine whether SF-RPC beams show similar size effects to those seen for conventional strength concrete.
4. In addition to research into size effects, research is needed to validate the findings of this study for SF-RPC beams of greater complexity i.e. differing cross-sectional shapes (e.g. I-beams), various load arrangements (e.g. distributed loading) and various levels of prestress.
5. Within the scope of this study into the flexural behaviour of SF-RPC beams, no investigations were undertaken into the behaviour at transfer or during heat treatment. Studies into the behaviour at transfer and losses of prestress due to heat treatment need to be considered in greater detail. The transfer behaviour is important as transfer of prestress takes place at an early age prior to the concrete being heat treated. The concrete is 'immature' and therefore likely to suffer increased creep due to the higher ratio of stress to strength at transfer. Losses of prestress due to heat treatment will result from the autogenous shrinkage of SF-RPC during heat treatment and the impact of increased temperature on the relaxation of steel.
6. Studies of longer duration into the creep and shrinkage properties of SF-RPC are recommended to validate the findings of this study. If SF-RPC is to be utilized in structural elements then the time-dependent deformations

- of these members will need to be determined. For this, extensive knowledge of the time-dependent material properties will be required.
7. Similarly, studies of longer duration are required to validate the preliminary findings that an AEMM is appropriate for predicting the time-dependent deformations of prestressed SF-RPC beams. These studies should be extended to cover plain members.
  8. As mentioned in Chapter 6, refinements can be applied to the AEMM when predicting the time-dependent deformation of prestressed SF-RPC beams. However, the refinement will have a greater impact on SF-RPC members that have not undergone any form of heat treatment and thus are outside the scope of this investigation. Investigations to verify the impact of this refinement are needed if SF-RPC members are to be utilized structurally without any form of heat treatment prior to loading.

The following recommendations are outside the scope of this investigation but due to their importance should be considered for further research into the material and structural properties of SF-RPC:

9. Studies dealing with fibre reinforced concrete have shown that the type of fibre used has a direct impact on the material properties. It is therefore recommended that studies involving alternate fibre types be undertaken to determine their impact on the resulting material properties and what effect this may have on the structural models.
10. Another important area of investigation that has a direct consequence on the long-term behaviour of SF-RPC is tensile creep. This property will have a bearing on the serviceability requirements (crack control, long-term deformations) and long-term strength of SF-RPC members.
11. The behaviour of SF-RPC members in shear is another important structural aspect that should be considered. As shear is a strength requirement in the design of structural members, studies into this area are critical.
12. Currently some investigations on blast and impact resistance are being undertaken. Preliminary findings indicate that steel fibre reinforced RPC

has significant potential to withstand blast and impact loading. However, a detailed investigation into this aspect of the material is recommended.

13. Finally, the ability of SF-RPC to withstand fire loading needs to be considered. Little or no information regarding this aspect of serviceability requirements has been reported indicating a lack of investigations into this area.

## APPENDIX A: Material Test Results

This appendix contains the test results of the material properties of the SF-RPC studied.

**Table A.1:** Compressive Strength Development with Age (Batch 1)

Concrete Age (days)	Strength (MPa)	
	Standard Cure	Hot Water Cure
1	4.7	
3	54.5	
7	73.0	141.7
14	84.6	135.0
28	97.2	136.6
91	114.1	148.4
182	120.2	143.0
365	128.4	141.1

**Table A.2:** Flexural Strength Development with Age (Batch 2)

Concrete Age (days)	Strength (MPa)	
	Standard Cure	Hot Water Cure
3	16.0	19.0
7	16.5	19.0
14	20.6	21.2
28	22.3	20.9
91	24.2	21.4
182	25.1	21.6
365	25.3	21.0

**Table A.3:** Modulus of Elasticity Development with Age (Batch 3)

Concrete Age (days)	Strength (MPa)	
	Standard Cure	Hot Water Cure
3	34.47	
7	38.09	44.56
14	42.24	47.48
28	44.92	45.59
91	46.35	45.73
182	46.44	44.72
365	46.48	45.42

**Table A.4:** Shrinkage Results

Concrete Age (days)	Total Shrinkage Strain ( $\mu\epsilon$ )		
	Standard Cure	Hot Water Cure	Autogenous
<b>Batch 4</b>			
2			0
3			-149
4			-133
5			-101
6			-80
7	0	394	-69
14	133	421	24
21	197	434	72
28	240	449	82
35	264	458	90
63	315	471	100
92	349	479	120
121	384	493	135
168	429	514	141
279	490	535	141
393	520	554	
<b>Batch 7</b>			
1	0		0
3	80		
4	140		
5	192		
6	228		
7	256		410
8	276		
9	288		
10	292		
14			430
22	344		446
28	360		453
56	430		478
112	480		518
204	536		538

**Table A.5:** Creep Results

Concrete Age (days)	Time since Loading (days)	Total Strain ( $\mu\epsilon$ )	Shrinkage Strain ( $\mu\epsilon$ )	Creep Strain ( $\mu\epsilon$ )
<b>Batch 4 – Standard Curing Condition</b>				
28	0	851.8	0	0
28.08	0.08	908.4	0.3	56.3
28.25	0.25	905.7	1.1	52.9
29	1	948.9	4.3	92.9
30	2	975.9	8.4	115.7
31	3	992.0	12.3	127.9
32	4	1008.2	16.2	140.2
33	5	1024.4	19.9	152.7
34	6	1051.4	23.5	176.1
35	7	1067.5	27.1	188.7
42	14	1143.1	49.2	242.2
49	21	1221.2	67.9	301.6
56	28	1276.0	84.1	340.1
110	82	1431.6	165.9	413.9
182	154	1530.4	227.0	451.7
365	337	1634.5	311.4	471.3
<b>Batch 4 - Heat treated</b>				
28	0	842.4	0	0
28.08	0.08	861.3	0.1	18.8
28.25	0.25	866.7	0.3	24.0
29	1	877.5	1.3	33.8
30	2	882.9	2.6	37.9
31	3	891.0	3.9	44.7
32	4	891.0	5.1	43.5
33	5	896.4	6.2	47.8
34	6	909.9	7.4	60.1
35	7	920.7	8.5	69.8
42	14	934.2	15.4	76.4
49	21	958.6	21.2	95.0
56	28	977.8	26.3	109.1
110	82	1028.9	51.9	134.8
182	154	1063.4	70.9	150.1
365	337	1100.8	97.3	161.3
<b>Batch 7 – Heat treated</b>				
28	0	1455.2	0	0
28.08	0.08	1514.6	0.1	59.3
28.25	0.25	1541.6	0.3	86.1
29	1	1547.0	1.4	90.5
30	2	1587.5	2.7	129.6
31	3	1606.4	4.0	147.2
32	4	1595.6	5.2	135.2

**Table A.5:** Creep Results (continued)

Concrete Age (days)	Time since Loading (days)	Total Strain ( $\mu\epsilon$ )	Shrinkage Strain ( $\mu\epsilon$ )	Creep Strain ( $\mu\epsilon$ )
33	5	1609.1	6.4	147.5
34	6	1614.5	7.6	151.7
35	7	1673.9	8.7	210.0
42	14	1731.0	15.9	259.9
49	21	1792.7	21.9	315.6
56	28	1833.2	27.2	350.8
84	56	1903.9	43.1	405.6
140	112	2008.5	63.1	490.2
237	209	2089.7	83.7	550.8
301	154	2148.3	93.1	599.1

## Appendix B: Prestressed Beam Behaviour Prior to Application of Load

### Prestress Losses – transfer to 28 days

#### 1. Jacking force

All 15.2 mm diameter super strands:  $P_j = 200$  kN (Sections S2 – S4)

All 12.7 mm diameter super strands:  $P_j = 147$  kN (Section S5)

#### 2. Initial Prestress

Assume 5% loss of prestress at transfer  $\Rightarrow P_i = 0.95 P_j$

#### 3. Effective prestress

##### a. Relaxation of steel (from transfer to 28 days)

$$R = k_1 k_2 R_{1000} \left[ \log(5.38t^{0.167}) \right] \quad \text{AS3600 - 2000}$$

For all strands:  $\sigma / f_p = 0.8 \Rightarrow k_1 = 1.5$

5 days HWB  $T_{ave} = 50^\circ\text{C} \Rightarrow k_2 = T / 20 = 2.5$

8 – 28 days  $T_{ave} = 20^\circ\text{C} \Rightarrow k_2 = T / 20 = 1.0$

Basic relaxation (Normal)  $R_{1000} = 7.0\%$  AS 3600 - 2000

$$R = 2.82\%$$

15.2 mm strands:  $R = 5.4$  kN

12.7 mm strands:  $R = 4.0$  kN

##### b. Creep and shrinkage

Shrinkage strain of companion specimens from 3 – 28 days

$$\varepsilon_{sh(3-28)} = -400\mu\varepsilon$$

$$\Delta\sigma_p = \varepsilon_{sh} E_p = -78 \text{ MPa}$$

$$\Delta P_{sh} = \Delta\sigma_p / A \Rightarrow \quad 15.2\text{mm strand: } P = 11.2 \text{ kN}$$

$$12.7\text{mm strand: } P = 7.8 \text{ kN}$$

Ignore creep

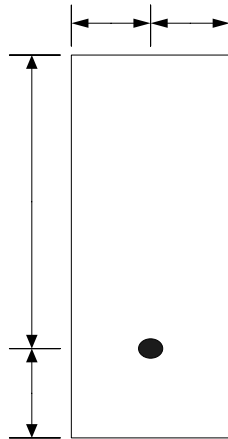
##### c. Effective prestress

15.2 mm strand:  $P_e = 173.4$  kN

12.7 mm strand:  $P_e = 128.2$  kN

**Section S1**

No initial prestress applied  $\Rightarrow$  Zero curvature and deflection at commencement of test

**Section S2**1. **Section Geometry**

1 x 15.2 mm strand  $\Rightarrow P_e = 173.4$  kN at an eccentricity of 80mm

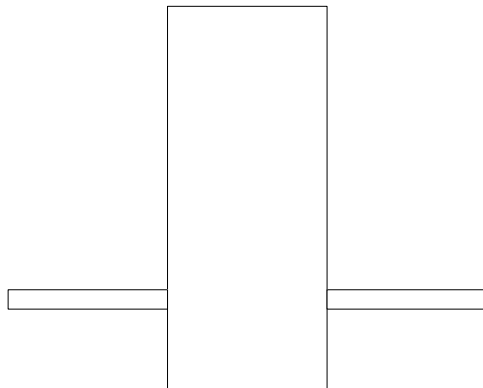
2. **Materials Properties**

Section S2 cast as part of Batch 5

$$f'_c = 157 \text{ MPa} \quad E_c = 45.9 \text{ GPa} \quad E_p = 195 \text{ GPa}$$

3. **Transformed Section**

$$n = E_p / E_c = 4.25$$



$$A = 30608 \text{ mm}^2 \quad B = 4.64 \times 10^6 \text{ mm}^3 \quad \bar{I} = 932.16 \times 10^6 \text{ mm}^4$$

4. **Forces on Section**

$$P_e = 173.4 \text{ kN} \quad \Rightarrow \quad N_i = -P_e = -173.4 \times 10^3 \text{ N}$$

$$M_o = 0 \quad \Rightarrow \quad M_i = M_o - P_e d_p = -39.9 \times 10^6 \text{ N.mm}$$

5. Predicted Top Fibre Strain and Curvature

$$\begin{aligned} \varepsilon_o &= \frac{BM_i - \bar{I}N_i}{E_c(B^2 - A\bar{I})} = +72.8 \times 10^{-6} \\ &= +72.8\mu\varepsilon \text{ (in tension but below the cracking strain)} \end{aligned}$$

$$\kappa_i = \frac{BN_i - AM_i}{E_c(B^2 - A\bar{I})} = -1.29 \times 10^{-6} \text{ mm}^{-1}$$

6. Predicted Initial Deflections

From Moment-Area Theorem

Midspan  $\delta_M = (-1.29 \times 10^{-6})(1350)(675) = -1.2 \text{ mm} = 1.2\text{mm} \uparrow$

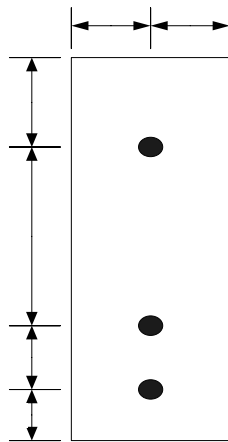
Point load  $\delta_L = -1.2 - (-1.29 \times 10^{-6})(450)(225) = -1.0\text{mm} = 1.0\text{mm} \uparrow$

**Section S3**

Initial prestress applied with no eccentricity  $\Rightarrow$  Zero initial curvature and deflection

**Section S4**

1. Section Geometry



3 x 15.2mm strand  $\Rightarrow P_e = 520.2 \text{ kN}$  at an eccentricity of 30 mm

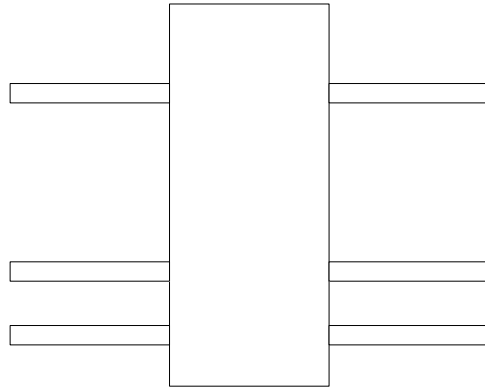
2. Material Properties

Section S4 cast as part of Batch 6

$$f'_c = 169 \text{ MPa} \quad E_c = 46.9 \text{ GPa} \quad E_p = 195 \text{ GPa}$$

3. Transformed Section

$$n = E_p / E_c = 4.16$$



$$A = 31785 \text{ mm}^2 \quad B = 4.82 \times 10^6 \text{ mm}^3 \quad \bar{I} = 969.38 \times 10^6 \text{ mm}^4$$

4. Forces on Section

$$P_e = 520.2 \text{ kN} \quad \Rightarrow \quad N_i = -P_e = -520.2 \times 10^3 \text{ N}$$

$$M_o = 0 \quad \Rightarrow \quad M_i = M_o - P_e d_p = -93.6 \times 10^6 \text{ N.mm}$$

5. Predicted Top Fibre Strain and Curvature

$$\begin{aligned} \varepsilon_o &= \frac{BM_i - \bar{I}N_i}{E_c(B^2 - A\bar{I})} = -148.8 \times 10^{-6} \\ &= -148.8 \mu\varepsilon \end{aligned}$$

$$\kappa_i = \frac{BN_i - AM_i}{E_c(B^2 - A\bar{I})} = -1.32 \times 10^{-6} \text{ mm}^{-1}$$

6. Predicted Initial Deflections

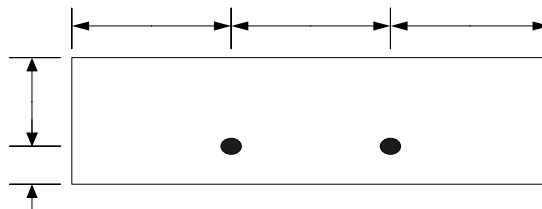
From Moment-Area Theorem

Midspan  $\delta_M = (-1.31 \times 10^{-6})(1350)(675) = -1.2\text{mm} = 1.2\text{mm} \uparrow$

Point load  $\delta_L = -1.2 - (-1.31 \times 10^{-6})(450)(225) = -1.0\text{mm} = 1.0\text{mm} \uparrow$

**Section S5**

1. Section Geometry



2 x 12.7mm strand  $\Rightarrow P_e = 256.4 \text{ kN}$  at an eccentricity of 20 mm

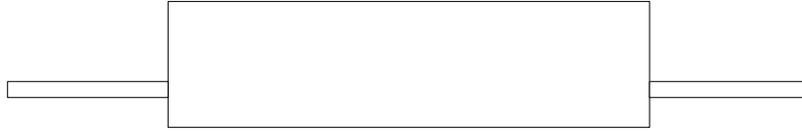
2. Material Properties

Section S5 cast as part of Batch 7

$$f'_c = 155 \text{ MPa} \quad E_c = 46.0 \text{ GPa} \quad E_p = 195 \text{ GPa}$$

### 3. Transformed Section

$$n = E_p / E_c = 4.24$$



$$A = 30848 \text{ mm}^2 \quad B = 1.56 \times 10^6 \text{ mm}^3 \quad \bar{I} = 104.16 \times 10^6 \text{ mm}^4$$

### 4. Forces on Section

$$P_e = 256.4 \text{ kN} \quad \Rightarrow \quad N_i = -P_e = -256.4 \times 10^3 \text{ N}$$

$$M_o = 0 \quad \Rightarrow \quad M_i = M_o - P_e d_p = -17.9 \times 10^6 \text{ N.mm}$$

### 5. Predicted Top Fibre Strain and Curvature

$$\begin{aligned} \varepsilon_o &= \frac{BM_i - \bar{I}N_i}{E_c(B^2 - A\bar{I})} = +35.6 \times 10^{-6} \\ &= +35.6 \mu\epsilon \text{ (i.e. in tension but below cracking strain)} \end{aligned}$$

$$\kappa_i = \frac{BN_i - AM_i}{E_c(B^2 - A\bar{I})} = -4.28 \times 10^{-6} \text{ mm}^{-1}$$

### 6. Predicted Initial Deflection

From Moment-Area Theorem

$$\text{Midspan} \quad \delta_M = (-4.28 \times 10^{-6})(1350)(675) = -3.9 \text{ mm} = 3.9 \text{ mm} \uparrow$$

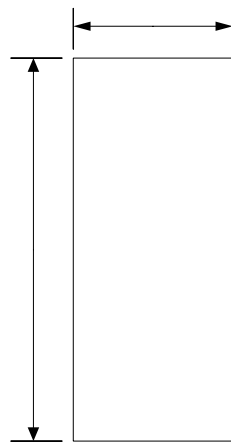
$$\text{Point load} \quad \delta_L = -1.2 - (-1.31 \times 10^{-6})(450)(225) = -3.5 \text{ mm} = 3.5 \text{ mm} \uparrow$$

### APPENDIX C: Sample Calculations – Short term Flexural Behaviour

The following appendix contains sample calculations for calculating the moment-curvature relationship for plain and prestressed SF-RPC sections. Details of the stress-strain relationships adopted for the behaviour of the SF-RPC in compression and tension can be found in Figures 5.39 and 5.40 respectively. A modified Ramberg-Osgood equation (Equation 5.3) is adopted for the tensile behaviour of the prestressing strands.

#### Plain SF-RPC Section (Cross-section P1)

##### 1. Section Geometry



##### 2. Material Properties

Cross-section P1 was cast as part of Batch 2. For full material results, see Chapter 4.

$$f'_c = 155.5 \text{ MPa}$$

$$R_{fl} = 11.1 \text{ MPa} \quad \text{Using Equation 4.6:}$$

$$h = 300 \text{ mm (Beam depth)} \Rightarrow R_t = 9.0 \text{ MPa}$$

$$E_c = 44.5 \text{ GPa}$$

Figure C1 shows the concrete stress-strain relationship adopted.

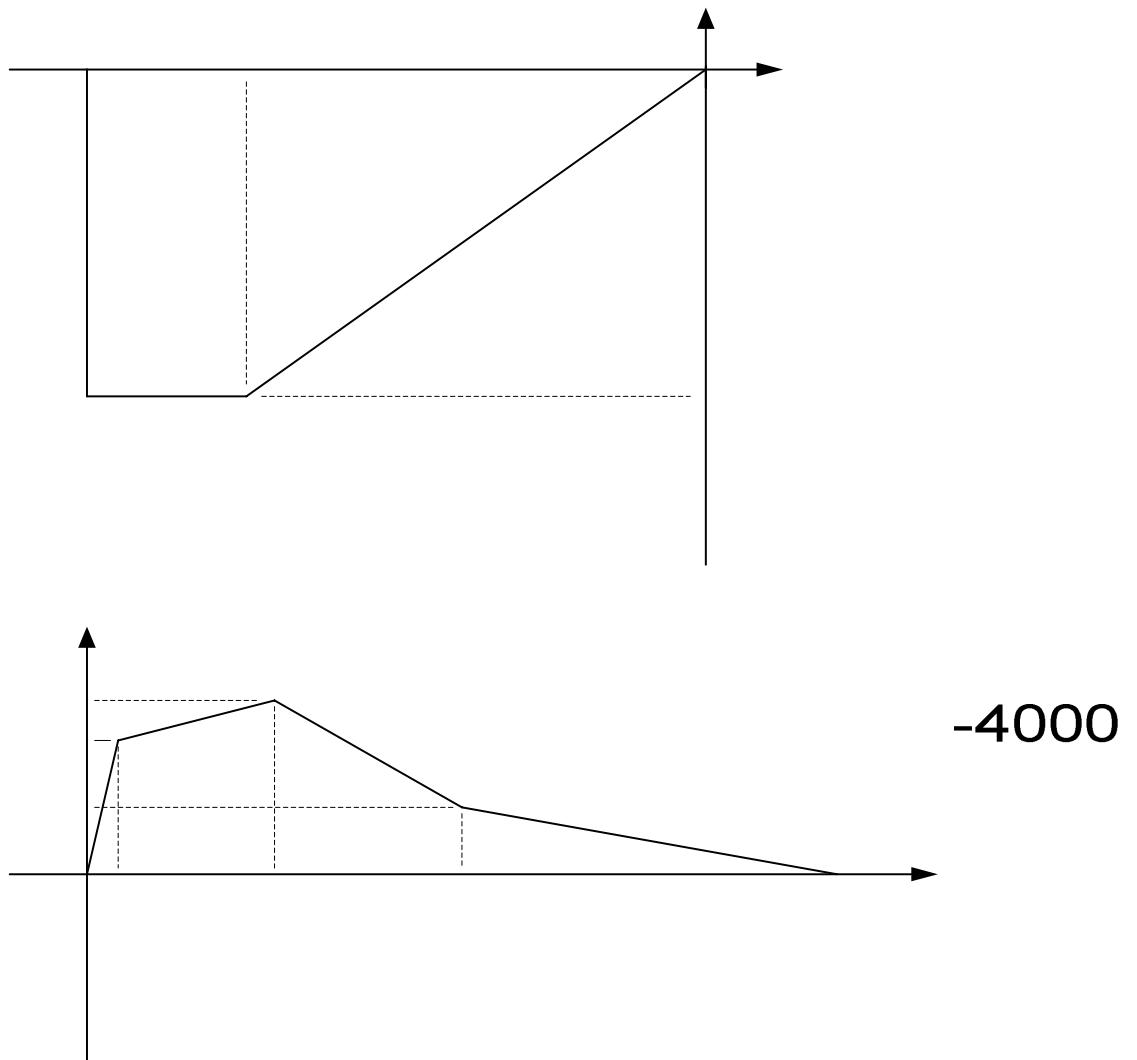


**Figure C1:** Adopted concrete stress-strain relationships

3. Cracking moment and curvature

$$I_g = \frac{bD^3}{12} = 225 \times 10^6 \text{ mm}^4$$

$$Z = \frac{bD^2}{6} = 1.5 \times 10^6 \text{ mm}^3$$

$$M_{cr} = \sigma_{cr} Z = 9 \times 1.5 = 13.5 \text{ kN.m}$$

$$\kappa_{cr} = \frac{M_{cr}}{E_c I_g} = 1.35 \times 10^{-6} \text{ mm}^{-1}$$

4. Moment and curvature at  $\epsilon_t$

Figure C2 shows the stress and strain distribution for cross-section P1 when the extreme tensile fibre strain reaches  $\epsilon_t$ .

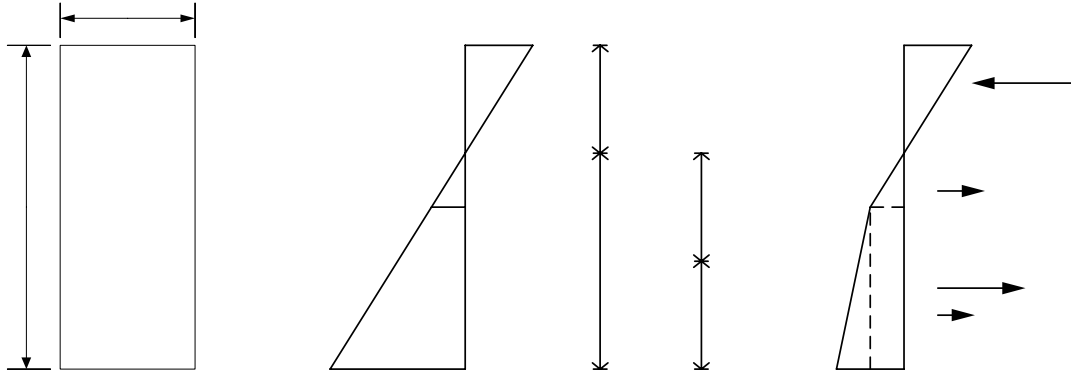


**Figure C2:** Stress and strain distribution

**SAMPLE CALCULATIONS**

*From strain compatibility*

$$\frac{\epsilon_o}{d_n} = \frac{\epsilon_t}{d_b} \Rightarrow \epsilon_o = \frac{\epsilon_t(D - d_b)}{d_b}$$

$$d_n = D - d_b$$

$$X_1 = \frac{1}{6}d_b$$

$$X_2 = \frac{5}{6}d_b$$

*Compressive and tensile stress block volumes*

$$C = 0.5\sigma_o d_n b = -2696.4 \frac{(300 - d_b)^2}{d_b}$$

$$T_1 = 0.5\sigma_{cr} X_1 b = 75d_b$$

$$T_2 = \sigma_{cr} X_2 b = 750d_b$$

$$T_3 = (\sigma_t - \sigma_{cr}) X_2 b = 225d_b$$

*Equilibrium*

$$C + T = 0 \Rightarrow 2696.4 \frac{(300 - d_b)}{d_b} + 1050d_b \overset{300}{}$$

Solving for  $d_b \Rightarrow d_b = 188.7 \text{ mm}$

Substituting for  $d_b$  gives  $C = -176.9 \text{ kN}$

100

$$T_1 = +14.2 \text{ kN}$$

$$T_2 = +141.5 \text{ kN}$$

$$T_3 = +21.2 \text{ kN}$$

$$d_n = 111.2 \text{ mm}$$

$$X_1 = 31.5 \text{ mm}$$

$$X_2 = 157.3 \text{ mm}$$

$$\varepsilon_o = -714.6 \mu\varepsilon$$

*Location of compressive and tensile forces*

$$C : y_c = \frac{1}{3}d_n = 37.1 \text{ mm below the top fibre}$$

$$T_1 : y_{T1} = d_n + \frac{2}{3}X_1 = 132.2 \text{ mm below the top fibre}$$

$$T_2 : y_{T2} = d_n + X_1 + \frac{1}{2}X_2 = 221.4 \text{ mm below the top fibre}$$

$$T_3 : y_{T3} = d_n + X_1 + \frac{2}{3}X_2 = 247.6 \text{ mm below the top fibre}$$

*Moment and Curvature*

Taking moments about the top fibre gives

$$M = Cy_c + T_1y_{T1} + T_2y_{T2} + T_3y_{T3} = 31.9 \text{ kN.m}$$

$$\kappa = \frac{-\varepsilon_o}{d_n} = 6.4 \times 10^{-6} \text{ mm}^{-1}$$

##### 5. Ultimate moment and curvature

Ultimate moment and curvature occur at a tensile strain value of approximately  $1.3 \varepsilon_t$ . Calculations similar to procedure outlined above.

$$\varepsilon_b = 1.3\varepsilon_t = 1575.6 \mu\varepsilon$$

$$M = 33.7 \text{ kN.m}$$

$$\kappa = 8.0 \times 10^{-6} \text{ mm}^{-1}$$

##### 6. Moment and Curvature at $2\varepsilon_t$

Calculations similar to procedure outlined above.

$$\varepsilon_b = 2\varepsilon_t = 2424 \mu\varepsilon$$

$$M = 30.1 \text{ kN.m}$$

$$\kappa = 11.3 \times 10^{-6} \text{ mm}^{-1}$$

7. Simplified Moment – Curvature Relationship

Figure C3 shows the simplified moment – curvature relationship for cross-section P1.

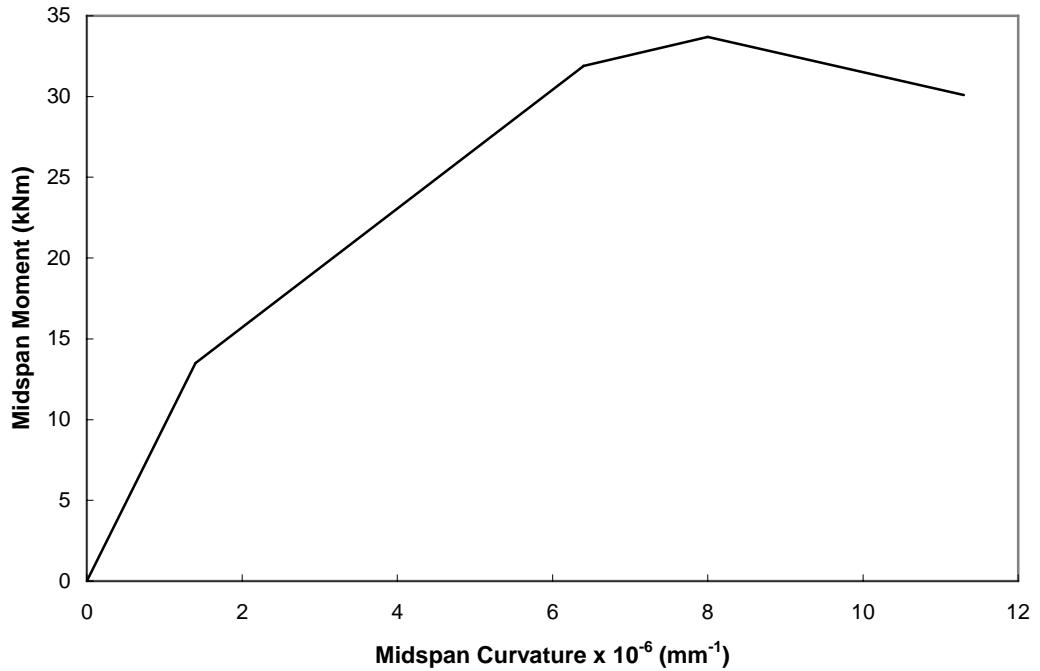
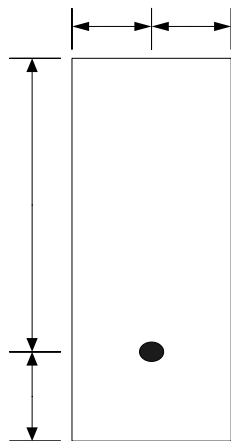


**Figure C3:** Simplified moment-curvature relationship

**Prestressed SF-RPC Section (Cross-section S2)**

1. Section Geometry



## 2. Material Properties

Cross-section S2 was cast as part of Batch 5. For full material results, see Chapter 4.

$$f'_c = 156.6 \text{ MPa}$$

$$R_{fl} = 14.4 \text{ MPa} \quad \text{Using Equation 4.6:}$$

$$h = 300 \text{ mm (Beam depth)} \Rightarrow R_t = 11.6 \text{ MPa}$$

$$\Rightarrow \sigma_{cr} = 0.75R_t = 8.7 \text{ MPa}$$

$$E = 45.9 \text{ GPa}$$

Figure C4 shows the concrete stress-strain relationships adopted.

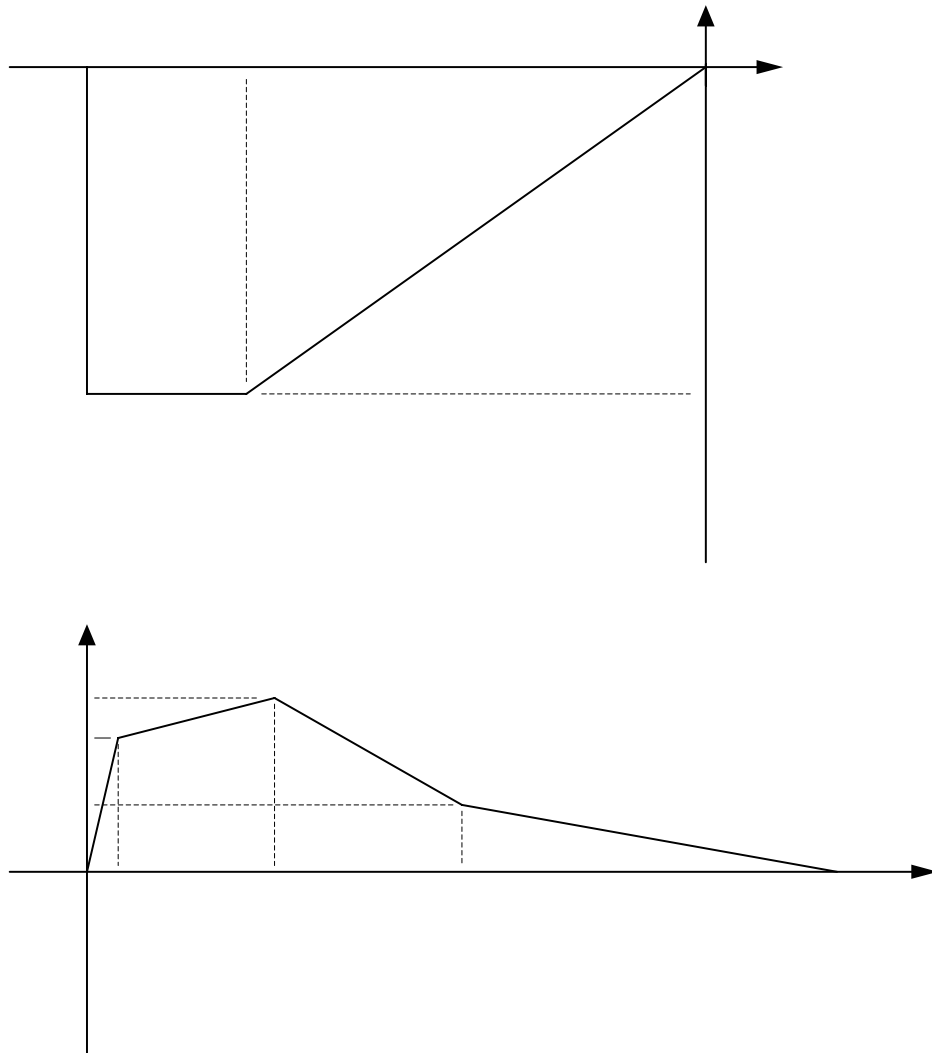


**Figure C4:** Adopted concrete stress-strain relationships

### 3. Cracking Moment and Curvature

Figure C5 shows the stress and strain distribution at cracking

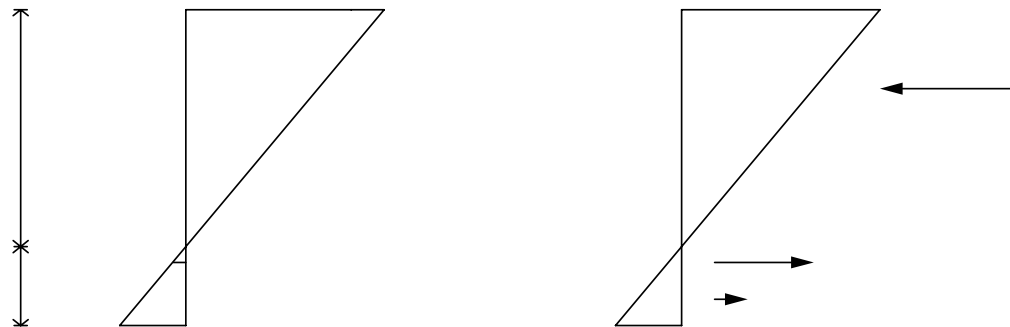


**Figure C5:** Stress and strain distribution at cracking

#### CALCULATIONS

*Initial strain in prestress cable*

$$\epsilon_{ce} = \frac{1}{E_c} \left( \frac{P_e}{A} + \frac{P_e e^2}{I} \right) = \frac{1}{45900} \left( \frac{173 \times 10^3}{30 \times 10^3} + \frac{173 \times 10^3 \cdot 80^2}{225 \times 10^6} \right) = 233 \mu\epsilon$$

$$\epsilon_{pe} = \frac{P_e}{E_p A_p} = \frac{173 \times 10^3}{195 \times 10^3 \cdot 143} = 6204 \mu\epsilon$$

*From strain compatibility*

$$\frac{\epsilon_o}{d_n} = \frac{\epsilon_b}{d_b} \Rightarrow \epsilon_o = \frac{\epsilon_b (D - d_b)}{d_b}$$

$$\frac{\epsilon_{pt}}{(d_b - 70)} = \frac{\epsilon_b}{d_b} \Rightarrow \epsilon_{pt} = \frac{190(d_b - 70)}{d_b}$$

$$\epsilon_p = \epsilon_{ce} + \epsilon_{pe} + \epsilon_{pt} = 6437 + \frac{190(d_b - 70)}{d_b}$$

*Compressive and tensile stress block volumes*

$$C = 0.5 \epsilon_o E_c d_n b = -435 \frac{(D - d_b)^2}{d_b}$$

$$T_c = 0.5 \sigma_{cr} d_b b = 435 d_b$$

*Steel force*

Assume  $\epsilon_s < \epsilon_{sy}$

$$T_p = E_p \epsilon_p A_p = 27.9 \left( 6437 + \frac{190(d_b - 70)}{d_b} \right)$$

*Equilibrium*

$$C + T_c + T_p = 0 \Rightarrow d_b = 88.7 \text{ mm}$$

$$\epsilon_b = \epsilon_{cr} =$$

Strain

*Forces on section*

$$C = -219.2 \text{ kN} \qquad y_c = \frac{1}{3}d_n = 70.5 \text{ mm}$$

$$T_c = 38.6 \text{ kN} \qquad y_{Tc} = d_n + \frac{2}{3}d_b = 270.5 \text{ mm}$$

Check  $\varepsilon_p = 6477 \mu\varepsilon < \varepsilon_{sy}$

$$\Rightarrow T_p = 180.6 \text{ kN} \qquad y_{Tp} = 230 \text{ mm}$$

*Moment and Curvature*

Taking moments about the top fibre gives

$$M = Cy_c + T_c y_{Tc} + T_p y_{Tp} = 36.5 \text{ kN.m}$$

$$\varepsilon_o = -454 \mu\varepsilon \Rightarrow \kappa = \frac{-\varepsilon_o}{d_n} = 2.1 \times 10^{-6} \text{ mm}^{-1}$$

4. Moment – curvature diagram

The moment and curvature for any given top or bottom fibre strain can be determined in a similar manner to the procedure outlined for the cracking moment by applying the adopted stress-strain relationships for concrete and steel. The moment and curvature corresponding to various values of top fibre strain are presented in Table C1. Figure C6 is the moment –curvature plot.

**Table C1**

$\varepsilon_o$ ( $\mu\varepsilon$ )	$d_n$ (mm)	$\varepsilon_b$ ( $\mu\varepsilon$ )	M (kN.m)	$\kappa \times 10^{-6}$ ( $\text{mm}^{-1}$ )
			0	-1.3
-451	211.4	190	36.5	2.1
-1000	142.6	1100	59.9	7.0
-1500	115.1	2409	73.5	13.0
-2000	87.4	4869	72.6	22.9
-2250	72.8	7028	66.8	30.9
-2500	59.2	10172	59.7	42.2
-2750	49.3	13971	55.3	55.8
-3000	42.6	18121	53.1	70.4
-3500	34.9	26549	51.3	100.16
-4000	30.8	34976	50.6	129.9

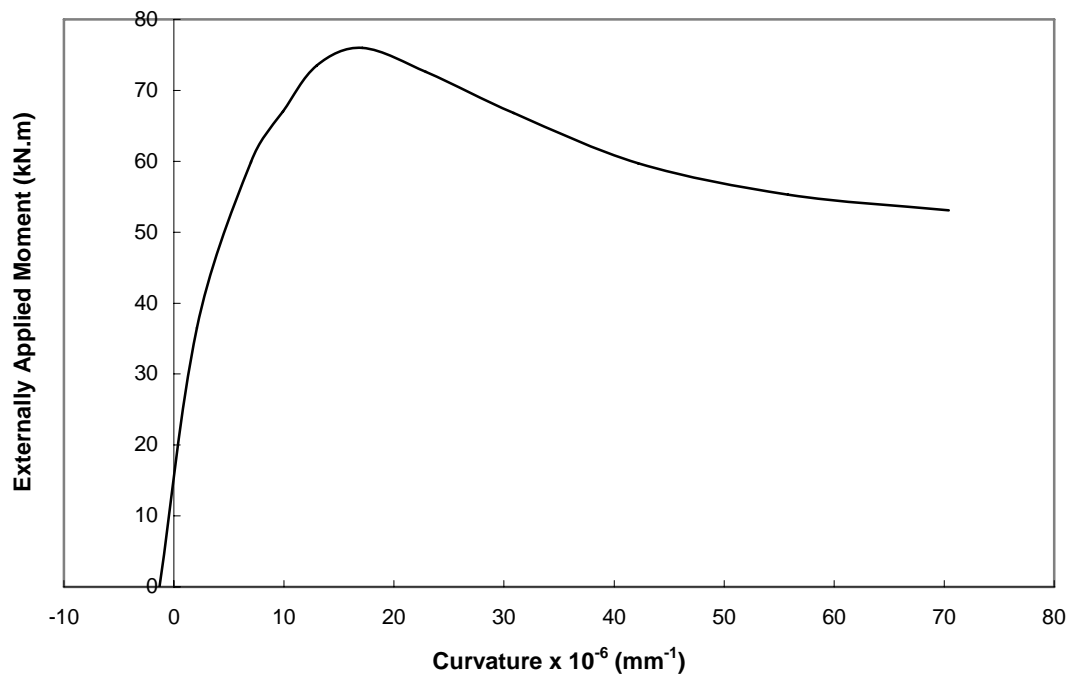


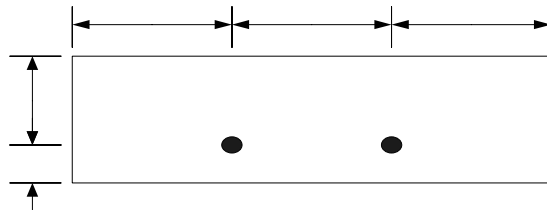
**Figure C6:** Moment-curvature plot

## APPENDIX D: Sample Calculations – Long term Flexural Behaviour

The following appendix contains sample calculations for calculating the time – dependent deformations of prestressed SF-RPC slabs tested as part of Beam series 6. Details of the Age-adjusted Modulus Method to estimate the time-dependent deformations can be found in Section 6.3.

### Sample Calculations S5 C

#### 1. Section Geometry



#### 2. Material Properties

Cross-section S5 was cast as part of Batch 7. For full material results, see Chapter 4.

$$f_c' = 154.7 \text{ MPa}$$

$$R_{fl} = 9.8 \text{ MPa} \quad \text{Using Equation 4.6:}$$

$$h = 100 \text{ mm (Beam depth)} \Rightarrow R_t = 6.5 \text{ MPa}$$

$$E = 46.0 \text{ GPa}$$

#### 3. Strain profile from short-term analysis

Curvature from prestress (See Appendix B)  $\kappa_{pe} = -4.3 \times 10^{-6} \text{ mm}^{-1}$

Externally applied load = 35.8 kN

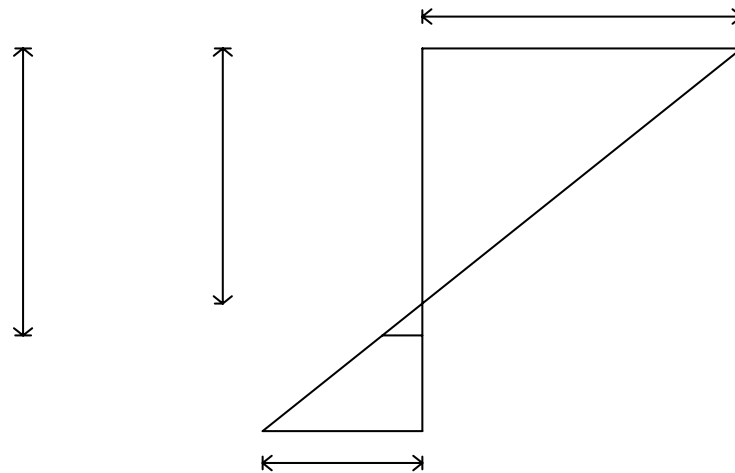
Externally Applied Moment = 16.1 kN

Figure D1 shows the strain profile after the application of external load.

$$\varepsilon_{oi} = -744 \mu\varepsilon$$

$$\kappa_i = 12.37 \times 10^{-6} \text{ mm}^{-1}$$

$$\varepsilon_b = 493 \mu\varepsilon$$



**Figure D1:** Strain profile after application of load

4. Time dependent analysis

Example: 56 days (i.e. 28 days of sustained load)

*From Batch 7 Material results*

Shrinkage  $\epsilon_{sh.28} = -400 \mu\epsilon$

$$\epsilon_{sh.56} = -427 \mu\epsilon$$

$$\Delta\epsilon_{sh} = -27 \mu\epsilon$$

Creep 
$$\phi_{cr} = \frac{1.17(t - t_o)^{0.7}}{10.65 + (t - t_o)^{0.7}} \phi_{cc.b} = 0.2$$

$$\Delta\phi_{cr} = 0.2$$

Relaxation of steel (28 – 56 days) (See Equations Appendix B)

$$R = 1.5 \text{ kN}$$

*Age-adjusted effective modulus*

Since concrete has undergone heat treatment, it has effectively reached maturity. Therefore, take the ageing coefficient  $\chi = 1.0$

$$\bar{E}_e(t, t_o) = \frac{E_c}{1 + \chi\Delta\phi_{cr}} = 38333 \text{ MPa}$$

*Restraining Forces*

1. Creep – apply to intact concrete

$$d_n = 68.8 \text{ mm}$$

$$A_c = 300 \times 68.1 = 20640 \text{ mm}^2$$

$$B_c = 300 \times 68.8 \times \frac{68.8}{2} = 710016 \text{ mm}^3$$

$$\bar{I}_c = \frac{300 \times 68.8^3}{3} = 35.57 \times 10^6 \text{ mm}^4$$

$$-\delta N_{cr} = -\bar{E}_e \Delta \phi_{cr} (A_c \varepsilon_{oi} + B_c \kappa_i) = 50.7 \times 10^3 \text{ N}$$

$$-\delta M_{cr} = -\bar{E}_e \Delta \phi_{cr} (B_c \varepsilon_{oi} + \bar{I}_c \kappa_i) = 0.97 \times 10^6 \text{ N.mm}$$

## 2. Shrinkage – apply to intact concrete

$$d_{\text{int}} = 68.8 \text{ mm}$$

$$A_{\text{int}} = 300 \times 68.8 = 20626.5 \text{ mm}^2$$

$$B_{\text{int}} = 300 \times 68.8 \times \frac{68.8}{2} = 709088.6 \text{ mm}^3$$

$$-\delta N_{sh} = -\bar{E}_e \varepsilon_{sh} A_{\text{int}} = 21.35 \times 10^3 \text{ N}$$

$$-\delta M_{sh} = -\bar{E}_e \varepsilon_{sh} B_{\text{int}} = 0.73 \times 10^6 \text{ N.mm}$$

## 3. Relaxation

$$-\delta N_{rel} = R = -1.5 \times 10^3 \text{ N}$$

$$-\delta M_{rel} = R d_p = -0.11 \times 10^6 \text{ N.mm}$$

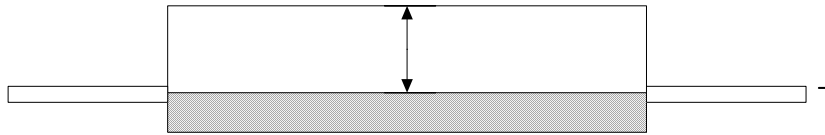
## 4. TOTAL

$$\delta N = -70.5 \times 10^3 \text{ N}$$

$$\delta M = -1.60 \times 10^6 \text{ N.mm}$$

### Transformed Section

$$\bar{n} = \frac{E_p}{E_e} = 5.1$$



$$\bar{A}_e = 300 \times 68.8 + 1017.4 = 21644 \text{ mm}^2$$

$$\bar{B}_e = 300 \times 68.8 \times \frac{68.8}{2} + 1017.4 \times 70 = 780.3 \times 10^3 \text{ mm}^3$$

$$\bar{I}_e = \frac{300 \times 68.8^3}{3} + 1017.4(70)^3 = 37.5 \times 10^6 \text{ mm}^4$$

### Change in strain and curvature with time

$$\Delta \varepsilon_o = \frac{\bar{B}_e \delta M - \bar{I}_e \delta N}{\bar{E}_e (\bar{B}_e^2 - \bar{A}_e \bar{I}_e)} = -180.3 \mu \varepsilon$$

$$\Delta \kappa = \frac{\bar{B}_e \delta N - \bar{A}_e \delta M}{\bar{E}_e (\bar{B}_e^2 - \bar{A}_e \bar{I}_e)} = -2.6 \times 10^{-6} \text{ mm}^{-1}$$

### Total predicted change in curvature from 28 days (no load) to 56 days

$$\Delta \kappa_{28-56} = (4.3 + 12.4 + 2.6) \times 10^{-6} = 19.3 \times 10^{-6} \text{ mm}^{-1}$$

**REFERENCES**

ACI 209 - 92, 1992, Prediction of Creep, Shrinkage and Temperature Effects in Concrete Structures, American Concrete Institute, Michigan

ACI 318 - 95, 1995, Building code requirements for reinforced concrete, American Concrete Institute, Michigan.

AFGC, 2002, Recommandations provisoires – Béton fibres à ultra-hautes performances, France, 152pp.

AS 1012.8, 2000, Method 8: Method for making and curing concrete compression, indirect tensile, and flexure test specimens, in the laboratory or in the field, Standards Australia, Sydney.

AS 1012.9, 1999, Method 9: Determination of the compressive strength of concrete specimens, Standards Australia, Sydney.

AS 1012.11, 2000, Method 11: Determination of modulus of rupture, Standards Australia, Sydney

AS 1012.13, 1992, Method 13: Determination of the drying shrinkage of concrete for samples prepared in the field or the laboratory, Standards Australia, Sydney.

AS 1012.16, 1996, Method 16: Determination of creep of concrete cylinders in compression, Standards Australia, Sydney.

AS 1012.17, 1997, Method 17: Determination of the static chord modulus of elasticity and Poisson's ratio of concrete specimens, Standards Australia, Sydney.

AS 3600, 1994, Australian standard for concrete structures, Standards Australia, Sydney.

AS 3600, 2001, Australian standard for concrete structures, Standards Australia, Sydney.

Bazant, Z.P., 1972, 'Prediction of concrete creep effects using age-adjusted effective modulus method', ACI Journal, Volume 69, pp. 212 – 217.

Beer, F.P., Johnston, E.R., 1992, Mechanics of Materials, McGraw-Hill Book Company, London, 736pp.

Behloul, M., 1996, Analyse et Modelisation du Comportement d'un Matrice Cimentaire Fibree a Ultra Hautes Performances (Betons de Poudres Reactives), France, 180pp.

Behloul, M., 1999, Design Rules for DUCTAL Prestressed Beams, France, 19pp.

Blais, P., Couture, M., 1999, 'Precast, Prestressed Pedestrian Bridge – World's First Reactive Powder Concrete Structure', *PCI Journal*, Volume 44, Number 5, pp. 60 – 71.

Bonneau, O., Lachemi, M., Dallaire, E., Dugat, J., Aitcin, P., 1997, 'Mechanical Properties and Durability of Two Industrial Reactive Powder Concretes', *ACI Materials Journal*, Volume 94, Issue 4, pp. 286 – 290.

BPEL 91, 1999, Reglès techniques de conception et de calcul des ouvrages et constructions béton précontraint suivante la méthode des etats limites.

Bresler, B., Selna, L., 1964, 'Analysis of time dependent behaviour of a reinforced concrete structures', *Symposium on Creep of Concrete*, ACI Special Publication SP-9, American Concrete Institute, Michigan, pp. 115 – 128

Carreira, D.J., Chu, K.H., 1985, 'Stress-strain relationship for plain concrete in compression', *ACI Journal*, Volume 83, Issue 6, pp. 797 – 804.

Cavill, B., Chirgwan, G., 2003, 'The World's First RPC Road Bridge at Shepherds Gully Creek, NSW', *Proceedings, Concrete in the Third Millennium Conference*, Brisbane Australia, 17 – 19 July, Volume 1, pp. 89 – 98.

CEB-FIP, 1990, Model Code for Concrete Structures (MC-90), English Translation, Thomas Telford, London.

Cheyrezy, M., 1999, 'Structural Applications of RPC', *Concrete (London)*, Volume 33, Issue 1, pp. 20 – 23.

- Cheyrezy, M., Maret, V., Frouin, L., 1995, 'Microstructural Analysis of RPC (Reactive Powder Concrete)', *Cement and Concrete Research*, Volume 25, Number 7, pp. 1491 – 1500.
- Chunxiang, Q., Patnaikuni, I., 1999, 'Properties of high-strength steel fibre-reinforced concrete beams in bending', *Cement and Concrete Composites*, Volume 21, Issue 1, pp. 73 – 81.
- Dalliare, E., Aitcin, P., Lachemi, M., 1998, 'High-Performance Powder', *Civil Engineering ASCE*, Volume 68, Number 1, pp. 49 – 51.
- Dauriac, C., 1997, 'Special concrete may give steel stiff competition' <http://www.djc.com/special/concrete1997/10024304.htm>.
- Dowd, W., 2000, 'Reactive Powder Concrete' <http://www.new-technologies.org/ECT/Civil/reactive.htm>.
- Ghali, A., Favre, R., Elbadry, M., 2002, Concrete Structures: stresses and deformations, Spon, London, 584pp.
- Gilbert, R.I., 1988, Time Effects on Concrete Structures, Elsevier, New York, 321pp.
- Gilbert, R.I., Mickleborough, N.C., 1990, Design of Prestressed Concrete, Unwin Hyman, London, 504pp.
- Gopalaratnam, V.S., Shah, S.P., 1987, 'Tensile fracture of steel fibre reinforced concrete', *Journal of Engineering Mechanics*, Volume 113, Issue 5, pp. 635 – 653.
- Gowripalan, N., Gilbert, R.I., 2000, Design Guidelines for RPC Prestressed Concrete Beams, Sydney, 51pp.
- Maidl, B.R., 1995, Steel fibre reinforced concrete, Ernst, Berlin.
- Lee, M.K., Barr, B.I.G., 2003, 'Strength and fracture properties of industrially prepared steel fibre reinforced concrete', *Cement and Concrete Composites*, Volume 25, pp. 321 – 332.

- Moranville-Regourd, M., 2002, 'New Cementitious Systems and Composite Materials', *Key Engineering Materials*, Volume 206 – 213, Number 3, pp. 1841 – 1846.
- Neville, A.M., 1995, Properties of Concrete, Longman, Malaysia, 844pp.
- O'Neil, E.F., Neeley, B.D., Cargile, J.D., 2002, 'Tensile Properties of Very-High-Strength Concrete for Penetration-Resistant Structures' <http://www.hdrinc/engineering/Topics/TensilePropertiesForPenetration-Resistant%20Structures.htm>.
- Richard, P., Cheyrezy, M., 1994, 'Reactive Powder Concrete with High Ductility and 200 – 800 MPa Compressive Strength', *ACI SP 144 – 24*, pp. 507 – 518.
- Richard, P., Cheyrezy, M., 1995, 'Composition of Reactive Powder Concrete', *Cement and Concrete Research*, Volume 25, Number 7, pp. 1501 – 1511.
- Roux, N., Andrade, C., Sanjuan, M.A., 1996, 'Experimental Study of Durability of Reactive Powder Concretes', *Journal of Materials in Civil Engineering*, Volume 8, Number 1, pp. 1 – 6.
- Semiloi, W.J., 2001, 'The New Concrete Technology', *Concrete international Design and Construction*, Volume 23, Number 11, pp. 75 – 79.
- Toutlemoude, F., Boulay, C., Sercombe, J., Le Maou, F., Renwez, S., Adeline, R., 1998, 'Characterization of Reactive Powder Concrete (RPC) in Direct Tension at Medium to High Loading Rates', 2<sup>nd</sup> International Conference on Concrete under Severe Conditions: Environment and Loading, CONSEC98, Tromsø, Norway, 21-24 June 1998, E&FN SPON, vol. 2, pp. 887 – 896.
- Warner, R.F., Rangan, B.V., Hall, A.S., Faulkes, K.A., 1998, Concrete Structures, Addison Wesley Longman Australia Pty Limited, Melbourne, 650pp.
- Zanni, H., Cheyrezy, M., Maret, V., Philippot, S., Nieto, P., 1996, 'Investigation of Hydration and Pozzolanic Reaction in Reactive Powder Concrete (RPC) Using <sup>29</sup>Si NMR', *Cement and Concrete Research*, Volume 26, Number 1, pp. 93 – 100.